QCD Analysis of Isolated Photon and Jet Data from ep, pp, and $p\overline{p}$ Collisions and Tests of α_s Running

Dissertation

zur Erlangung des Doktorgrades

des Department Physik

der Universität Hamburg

vorgelegt von

Oleg Kuprash

aus Kyiw und Stakhanov (Ukraine)

Hamburg

2015

Gutachter/in der Dissertation:	PD Dr. Achim Geiser Prof. Dr. Brian Foster Prof. Dr. Mark Lancaster
Gutachter/in der Disputation:	Prof. Dr. Caren Hagner Prof. Dr. Sven-Olaf Moch Prof. Dr. Christian Sander
Datum der Disputation:	10. Dezember 2014
Vorsitzender des Prüfungsausschusses:	Prof. Dr. Caren Hagner
Vorsitzender des Promotionsausschusses:	Prof. Dr. Jan Louis
Dekan des MIN-Fakultät:	Prof. Dr. Heinrich Graener

Abstract

A QCD analysis of the cross section for the production of an isolated photon with an accompanying jet in deep inelastic *ep* scattering (DIS) at HERA is presented. A description of the relevant measurement is given, made with the ZEUS detector. A fit of the Parton Density Functions (PDFs) of the proton, to isolated photon and inclusive DIS data, is done. The sensitivity to the low x composition of the quark sea is studied. The extracted ratio of the sea u and d quark PDFs at $x \to 0$ is consistent with unity, as expected by isospin symmetry. The level of presence of additional partons in a proton, apart from quarks and gluons (e.g. photons), is estimated, and found to be about or below 1%.

The running of the strong coupling constant, $\alpha_s(\mu)$, is tested in a QCD analysis using jet measurements at LHC, Tevatron and HERA in combination with inclusive DIS data. Here μ is associated with the energy scale in the process, typically with the jet transverse energy. For the α_s running test, the parameter n_f of the running, which gives the number of active quarks contributing to loop corrections of the jet and DIS cross sections, is replaced by $n_f + \Delta n_f$ at energy scales greater than $\mu > \mu_{\text{thresh}}$. A series of simultaneous $\alpha_s(M_Z) + \Delta n_f$ + proton PDF fits to world collider cross section data is done at Next-to-Leading Order QCD, for μ_{thresh} values ranging from 1 GeV to 1 TeV. The fitted Δn_f is consistent with zero at all tested scales, which gives a precise quantitative confirmation of the QCD running of α_s over 3 orders of magnitude in energy scale. The presented method also provides a new way for indirect searches of physics beyond the Standard Model (SM). Constraints are derived on models suggesting physics beyond the SM, which contain loop corrections to the jet and DIS cross sections, and for which a change of the measured configuration of the final state can be neglected.

Power pulsing studies are reported of the Mimosa26 pixel sensor, which is the first sensor prototype for the vertex detector for the International Linear Collider (ILC). The analogue and digital output of Mimosa26 are analysed. The fake hit rate is studied, as a function of time within the power "ON" phase, and is compared to the fake hit rate under a constant power supply. The studies show that power pulsing operation is possible with no discernible disadvantages.

Zusammenfassung

Eine QCD-Analyse des Wirkungsquerschnitts für die Produktion eines isolierten Photons in Begleitung eines Jets in tief unelastischer Streuung (DIS) wird vorgestellt. Die entsprechende Messung mit dem ZEUS-Detektor wird detailliert beschrieben. Eine Anpassung (Fit) der Parton-Dichte-Verteilungen (PDFs) im Proton an die isolierten Photon-Daten sowie an inklusive DIS-Daten wird durchgeführt. Die Sensitivität auf die Zusammensetzung des "Quark-Sees" bei kleinen Werten des Impulsbruchteils x wird untersucht. Der extrahierte Wert des Verhältnisses von u- und d-quark-Verteilungen am Grenzwert $x \to 0$ ist konsistent mit 1, wie aufgrund der Isospin-Symmetrie erwartet. Ein möglicher Beitrag von Partonen im Proton zusätzlich zu Quarks und Gluonen (z.B. Photonen) wird untersucht, und auf weniger als 1% eingeschränkt.

Das 'Laufen' der starken Kopplungskonstanten $\alpha_s(\mu)$ wird getestet im Rahmen einer QCD-Analyse von Jet-Daten bei LHC, Tevatron und HERA in Kombination mit inklusiven DIS-Daten. Die Skala μ wird assoziiert mit der physikalischen Skala des jeweiligen Prozesses, typischerweise dem Jet-Transversalimpuls. Für diesen Test wird der Parameter n_f, der beschreibt, wie viele Quarks aktiv zu Schleifenkorrekturen der DIS- und Jetwirkungsquerschnitte beitragen, ersetzt durch $n_f + \Delta n_f$ für Energieskalen $\mu > \mu_{\text{thresh}}$. Eine Serie von Fits in nächstführender Ordnung an die Welt-Kollider-Daten wird durchgeführt im Skalenbereich 1 GeV $< \mu_{\text{thresh}} <$ 1 TeV. Die gefitteten Δn_f-Werte sind konsistent mit 0 über den gesamten getesteten Bereich. Dies liefert eine präzise quantitative Bestätigung des Laufens der Kopplungskonstante über 3 Größenordnungen in der Energieskala. Die vorgestellte Methode erlaubt auch eine neue Art des Tests auf Physik jenseits des Standardmodells. Beiträge von Modellen neuer Physik, die Loop-Korrekturen enthalten, ohne den gemessenen Endzustand signifikant zu verändern, werden eingeschränkt.

Die Ergebnisse von "power pulsing"-Studien mit dem Mimosa26-Pixelsensor werden berichtet. Mimosa26 ist der erste Sensor-Prototyp für den Vertex-Detektor eines Experiments am zukünftigen International Linear Collider. Die analogen und digitalen Ausgangssignale von Mimosa26 werden analysiert. Die Rauschsignalrate wird untersucht als Funktion der Zeit innerhalb der sogenannten "power ON"-Phase, und verglichen mit der Rauschsignalrate im Dauerbetrieb. Die Studien zeigen, dass der "power pulsing"-Betrieb möglich ist und sich daraus keinerlei Nachteile ergeben.

Посвящается Даниилу Хармсу

Внезапная мысль блеснула в его голове.
Он поднял оброненную мадам Гороховой
ложку и твёрдыми шагами подошёл к ведру.

Contents

Introduction

The precision of experiments in high energy physics is constantly improving, allowing ever more stringent tests of theoretical models and approaches. This is also achieved at new accelerators with higher energies and intensities, where it is possible to test models in regions of phase space never investigated before. Confronting experimental results with theoretical expectations can lead to discoveries and thus to a better understanding of Nature. Such an experimental study can be done in different ways. *Precision tests* require a comparison of observables measured with high accuracy to the theoretical predictions (made with appropriate precision), while the other method is a *search* for new physics. The two methods are discussed below.

Testing the Standard Model

The Standard Model (SM) of particle physics is highly predictive and is therefore very extensively tested. The most precise tests are done in the electroweak sector, where perturbative calculations can be made with high accuracy thanks to the small values of the coupling constants in the phase space investigated. The most striking examples are measurements of the anomalous magnetic dipole moments of the electron, a_e, and muon, a_μ, which yield $a_e^{\text{exp}} = 11596521807.3(2.8) \times 10^{-13}$ [1] and $a_\mu^{\text{exp}} = 116592089(63) \times 10^{-11}$ [2], corresponding to a precision of 0.24 parts per billion and 0.5 parts per million, respectively. The difference between the measured value and the one predicted by the SM for the electron anomalous magnetic moment[1] is $\delta a_e = a_e^{\text{exp}} - a_e^{\text{SM}} = -10.6(8.2) \times 10^{-13}$, which is a great triumph of the Standard Model.

However, there are cases when measurements of the SM observables disagree with predictions, giving some hints for the incompleteness of the Standard Model. Probably the currently most significant indication is the so-called $B \to K^* \mu^+ \mu^-$ anomaly, a recently found deviation of up to 3.9σ [6] between the observables of this decay and the Standard Model predictions. It was shown in [6] that by adding effects of new physics in the theory, it is possible to obtain good agreement with the experiment. Another example of a

[1] The predicted value was calculated using the value of the electromagnetic coupling constant obtained from the precise measurements of the Rydberg constant, $\alpha^{-1} = 137.035999049(90)$ [3–5]

deviation from the Standard Model predictions is found in the muon anomalous magnetic moment, where a level of disagreement of the measurement and prediction similar to the one described above is observed [7].

The accuracy of measurements and predictions for the strong interaction, described in terms of Quantum Chromodynamics (QCD), is not as striking as for the electroweak case, however they are slowly improving in time. The most precisely measured quantity in QCD is the value of the strong coupling constant, $\alpha_s^{\text{meas}}(M_Z) = 0.1185(6)$ [8,9], measured with 5 per mil accuracy. This value is an average of many measurements performed with different methods, like extraction from lattice QCD, from particle decays, and from hadronic final states at colliders. The precision is limited either by the precision of the theoretical calculations or by the experimental uncertainties. Lattice QCD gives the most precise estimate of $\alpha_s(M_Z) = 0.1185(5)$ [8], which is obtained by calculations in the region of energy scales of a few GeV and below.

Beyond the Standard Model

Although the Standard Model seems to be extremely successful in describing a broad range of processes, there are indications (see Section 1.1) for effects that the Standard Model in its current formulation cannot explain. Currently there are a lot of searches for hints of effects beyond the Standard Model ongoing. Examples are the search for proton decay, searches for supersymmetry, searches for new particles (new gauge bosons, leptoquarks, ...), and searches for signals from extra dimensions. The searches can be classified into *direct* and *indirect*. Direct searches aim for a clear experimental observation of new effects, like the measurement of particle decays forbidden by the Standard Model or the detection of new particles. Indirect searches are sensitive to virtual effects that alter the values of the Standard Model predictions. The significance of this method can be illustrated already within the Standard Model. For instance, the Gfitter group [10], which performs global fits of the electroweak Standard Model, by comparing experimental data to theoretical predictions, which included virtual loop effects of the Higgs boson, found an estimate of the Higgs mass at $M_H = 91^{+30}_{-23}$ GeV [11][2], which is consistent with the value directly measured by the CMS collaboration, $M_H = 125.03^{+0.26}_{-0.27}(\text{stat.})^{+0.13}_{-0.15}(\text{syst.})$ GeV [12].

Indirect searches do not claim discovery but may point to the region (energy range) at which new effects could be observed directly. Indirect searches also have the attractive advantage that in virtual contributions the integration is done over the full momentum range (0 to infinity) of the particle in the loop, so that indirect searches, at least in principle, can be sensitive to new particles with very high masses, that cannot be produced in final states at current colliders due to insufficiently high centre-of-mass energy.

[2] 120^{+12}_{-5} GeV if information from direct Higgs searches is included

Aims and Thesis Overview

The aim of this thesis is to address two aspects of experimental studies, discussed above. One part of the thesis is devoted to a test of the Standard Model, presenting measurements of dijet production at high virtualities of the exchanged boson, Q^2, and isolated photon with jet production at low Q^2 in Deep Inelastic Scattering (DIS) at HERA. These measurements are also used as an input to the proton PDF fits described further in the thesis.

The second part of this thesis, which gives a test of the running of α_s, can be considered as both a test of QCD and a generic indirect search for effects beyond the Standard Model. The approach utilises the dependence of the α_s evolution on the number of active flavours, n_f, contributing to virtual loops in the gluon propagator. So far most measurements of the strong coupling were done implicitly assuming the standard variable-flavour running, where the number of active flavours changes from 3 to 4, from 4 to 5 and from 5 to 6 at the scales $\mu_R = m_c,\ m_b,\ m_t$. These scales correspond to the masses of the charm, bottom and top quarks, respectively. Therefore, the familiar plots with running α_s and experimental points at different scales do not strictly speaking prove the running of α_s. In the approach presented here, the number of flavours n_f is fitted in a broad range of scales to the world collider data, simultaneously with the proton PDFs. A simultaneous fit of the proton PDFs is needed, since their evolution depends on α_s.

The thesis is organised as follows. First, a theoretical overview is given in Chapter 1, followed by overview of the HERA collider and the main parts of the ZEUS detector used for the analyses presented here, in Chapter 2. Chapter 3 presents a description of the tools and methods used. Chapters 4 and 5 are devoted to measurements of the dijet and isolated photon plus jet production at HERA, respectively. Chapter 6 describes the inclusion of the isolated-photon data into the proton PDF fit. Chapter 7 describes tests of the running of the strong coupling constant. Chapter 8 describes power-pulsing studies of the Mimosa26 pixel sensors, made as part of the PLUME project. These studies were done as the 1-year technical task. Finally, the conclusions are given.

Chapter 1

Theoretical Overview

1.1 The Standard Model

The *Standard Model* (see e.g. [13]) is the commonly accepted and well established model of fundamental particles and their interactions. It was developed in the second half of the 20th century. The basic theoretical ideas of the Standard Model were finalised by the 1970s. The Standard Model is very successful in describing practically all experimental data from high energy experiments.

The Standard Model combines two theories of particle physics to describe the electromagnetic, weak and strong interactions - *Electroweak Theory* and *Quantum Chromodynamics* (QCD). According to the Standard Model, all matter is built from 12 fundamental spin $\frac{1}{2}$ particles and 12 corresponding anti-particles, which interact by exchange between themselves of various spin-one bosons. The fundamental particles of matter are 6 *leptons* (l) and 6 *quarks* (q). Leptons are, by definition, those spin-half particles that do not take part in the strong interactions: electron e, muon μ, τ-lepton, and three neutrinos ν_e, ν_μ, ν_τ. Quarks participate in all interactions. The spectrum of hadrons is rich (a few hundreds are currently established), however it is known that all of them are bound states of quarks and/or antiquarks. The quarks are not observed as free states (so-called QCD *confinement*). The six quarks are *up*, *down*, *strange*, *charm*, *bottom* (also called *beauty*) and *top* (also called *truth*), denoted shortly as u, d, s, c, b and t, respectively. The quarks carry a quantum number which leptons do not, called *colour*. Only coloured particles participate in the strong interaction.

As was mentioned above, the interactions in the Standard Model are understood as arising due to exchange of spin-one bosons between the fundamental matter particles. The corresponding bosons are 8 gluons (g) for the strong, W^+, W^- and Z for the weak, and the photon (γ) for the electromagnetic interaction. The number of bosons for each interaction type is fundamentally connected with the symmetry properties of the fermion field. The Electroweak theory and QCD are so-called *gauge* theories, which means that

their equations of motion are invariant under a local gauge transformation (a gauge transformation is a transformation of the fermion wave functions plus a corresponding change of the mediator field, which together leave the Lagrangian unchanged). In gauge theories the boson (mediator) field appears naturally as a consequence of the requirement of the Lagrangian invariance under local phase transition of the fermion (particle) fields. A local phase transformation can be interpreted as an action of the element of some symmetry group; the number of the generators of this group defines the number of mediator bosons. The interaction of quarks is invariant against SU(3) transformations of the quark fields in colour space. The number of group generators is given by n^2-1, where n is the dimension of the gauge group, so for SU(3) it is $3^2-1=8$, which means that there are 8 bosons (gluons) which are carriers of the strong interaction, according to QCD. Quantum Electrodynamics (QED), the theory of electromagnetic interactions, is invariant against global phase transitions of the fermion field; the Fermi theory that describes the weak interaction is not a gauge theory. However, there exists a mechanism to combine these two into a single gauge theory, invariant against SU(2)×U(1) transformations (Electroweak theory), which gives rise to $2^2-1=3$ massive (W+, W-, Z) and 1 massless (γ) boson fields. Finally, QCD and Electroweak Theory are combined into the single Standard Model of particle physics, having the group symmetry structure of SU(3)×SU(2)×U(1).

For theories containing only fermions and mediator bosons responsible for the interaction between the fermions, the gauge principle does not hold if the bosons are massive, which is the case for the electroweak interaction. This problem was resolved by applying the *Higgs* mechanism: a new field, the Higgs field, which has Yukawa couplings with the fermions, was introduced in the theory. Spontaneous symmetry breaking of the symmetry of this field gives rise to masses for the weak gauge bosons and produces a new massive particle, the Higgs boson. The Higgs mechanism naturally leads to the fact that the $W^{+/-}$ and Z bosons, as well as fermions, acquire mass. There are, however, no theoretical principles to calculate the fermion-Higgs couplings, hence the fermion masses are additional arbitrary parameters, which so far can only be constrained experimentally.

Some of the properties of the fundamental particles of the Standard Model are summarised in Table 1.1.

The family of fundamental fermions is grouped into three generations, $(u,\ d,\ \nu_e, e^-)$, $(c,\ s,\ \nu_\mu, \mu^-)$, $(t,\ b,\ \nu_\tau, \tau^-)$, the corresponding members of which share identical properties except their mass. The Standard Model gives no answer to the question of how to explain such a family structure, nor does it predict the number of generations.

Although the Standard Model describes nearly all data from existing high-energy accelerators, it can be criticised for several reasons. The SM has a relatively large number (about 20) of free parameters, which can only be measured from experiment. Moreover, the Standard Model does not pretend to be the final theory of interactions, since it doesn't contain gravitation. There are, in addition, other phenomena, apart from the generation puzzle, which the Standard Model in its current formulation can't explain:

Leptons

	l	name	mass (MeV)	charge e
First generation	e	electron	0.511	-1
	ν_e	electron neutrino	< 7 eV	0
Second generation	μ	muon	105.7	-1
	ν_μ	muon neutrino	< 0.27	0
Third generation	τ	tau	1777	-1
	ν_τ	tau neutrino	< 31	0

Quarks

	q	name	mass (MeV)	charge e
First generation	d	down	$\approx$10	$-1/3$
	u	up	$\approx$5	$2/3$
Second generation	s	strange	≈ 200	$-1/3$
	c	charm	≈ 1500	$2/3$
Third generation	b	bottom	≈ 4500	$-1/3$
	t	top	170 GeV	$2/3$

Gauge Bosons

	name	mass (GeV)	charge e
γ	photon	0	0
$W^{+/-}$	$W^{+/-}$ boson	80.2	$+/-1$
Z	Z boson	91.2	0
g	gluon	0	0
H	Higgs boson	125 GeV	0

Table 1.1: Particles of the Standard Model.

- **Neutrino oscillation** (see [14] for a review). Neutrinos created with a specific lepton flavour (electron, muon or tau) can later be measured to have a different flavour. The probability of measuring a particular flavour varies periodically (oscillates) as a neutrino propagates. This effect was first observed in the 1960's: there was a large disagreement between the predicted and measured flux of electron neutrinos from the Sun [15, and references therein]. The effect was lately explained with the neutrino oscillation mechanism[1]: part of the electron neutrinos became muon or tau neutrinos, which were not registered by the detector. Neutrino oscillation can only take place if the neutrino has a non-zero mass, while the Standard Model assumes

[1]The oscillation mechanism was first suggested by Pontecorvo [16] in the form of neutrino-antineutrino oscillations. The concept was adapted to neutrino flavour oscillations [17] after the discovery of the muon neutrino.

zero mass neutrinos. So far, explicit measurements of the neutrino masses led to upper constraints only, since only mass differences can be measured by oscillation experiments.

- **Dark Matter**. The existence of Dark Matter (DM) has been clarified by astrophysical observations. It is so named because it does not radiate electromagnetic waves and seems to be interacting with ordinary matter gravitationally and (maybe) weakly only. The first indication for Dark Matter was obtained in 1933, when Fritz Zwicky measured the velocities of galaxies in the Coma cluster (from the Doppler shift of their atomic spectra), and used this information to determine the mass of the cluster [18]. The calculated mass turned out to be 400 times larger than the mass of the visible stars in the cluster. Afterwards, the existence of Dark Matter was confirmed by measurements of the rotation curves for other galaxies. A possible explanation within the Standard Model was to consider neutrinos as candidates for the DM particles, however neutrinos were found to be much too light to contribute more than a small fraction of the DM. Most probably the DM particles are something completely new. It is generally assumed that the DM particles participate in weak interactions, therefore DM candidates are called WIMPs (Weakly Interacting Massive Particles). So far, numerous WIMP searches did not lead to their observation.

- **Dark Energy**. First data, suggesting that the expansion of the Universe is accelerating, were collected in 1998 using observations of Type Ia supernovae [19]. Before 1998, it was believed that the expansion is slowing down due to the gravitational attraction of all matter. The concept of Dark Energy, which suggests that the Universe is homogeneously filled with Dark Energy having negative pressure, can explain the accelerating expansion [20].

Nowadays the Standard Model is being extensively tested at particle colliders. Colliding experiments also provide an essential tool to measure the Standard Model parameters. Since this thesis is describing two measurements performed at the HERA electron proton collider, the physics of inelastic ep interaction is discussed further. The experimental setup will be described in Chapter 2.

1.2 Deep Inelastic ep Scattering at HERA

Deep Inelastic Scattering (DIS) is the name for inelastic scattering processes of a point-like particle (usually, lepton) on a composite particle (hadron or nucleus), when the exchanged momentum is large enough to resolve the constituents of the composite particle. For ep-scattering at HERA, the DIS term is usually used if the exchange momentum squared was

greater than 1 GeV^2. In the following we will concentrate on lepton-nucleon scattering, a particular case of which is *ep*-scattering.

In the most general case the lepton-nucleon interaction proceeds via the exchange of a virtual vector boson as depicted in Fig. 1.1. Since the lepton number has to be conserved, a scattered lepton l' arises in the final state, while the nucleon p fragments into a hadronic final state X [21],

$$lp \to l'X. \tag{1.1}$$

If the scattered lepton has the same charge as the incident one, the reaction is called Neutral Current and occurs via the exchange of a neutral boson (γ and Z^0), while if the lepton changes its charge (e.g. $e^-p \to \bar{\nu}_e X$ or $e^+p \to \nu_e X$), the reaction is called Charged Current, with the exchange of a charged (W^- or W^+) boson.

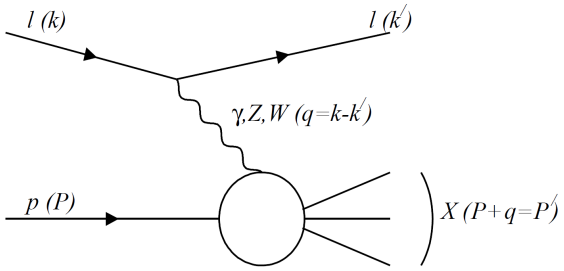

Figure 1.1: Schematic diagram describing deep inelastic lepton nucleon scattering. The four-vectors of the particles, or particle systems, are given in parentheses.

Assuming that k, k', P, P' are the four-momenta of the initial and final state lepton, of the incoming nucleon and of the outgoing hadronic system, respectively (Fig. 1.1), the usual variables describing lepton nucleon scattering are (see, e.g. [21])

$$s = (k + P)^2, \tag{1.2}$$

$$W^2 = (q + P)^2 = P'^2, \tag{1.3}$$

$$Q^2 = -q^2 = -(k - k')^2, \tag{1.4}$$

$$x = \frac{Q^2}{2P \cdot q}, \tag{1.5}$$

$$y = \frac{q \cdot P}{k \cdot P}. \tag{1.6}$$

Since all of these are obtained from the scalar products of the 4-vectors, these variables are invariant against Lorentz transformations. The variables s and W^2 are the centre-of-mass energy squared of the lepton-nucleon and intermediate boson-nucleon systems, respectively. The mass squared of the virtual boson, taken with a minus sign (so that the obtained quantity is positive), is called boson virtuality, Q^2. If $Q^2 << 1$ GeV^2 (i.e. the exchanged photon is almost real), the reaction is called *Photoproduction* (PHP). The y variable in the proton rest frame is given by $y = 1 - \frac{E'_l}{E_l}$, where E_l, E'_l are the energies of the incoming and scattered lepton, respectively. The variable x has an easy interpretation in the quark-parton model (given in the next subsection) and is also called Bjorken x, or x_{Bj}. If one ignores lepton and proton masses,

$$Q^2 = sxy, \tag{1.7}$$

so that only two of the variables Q^2, x, y are independent (s is set by the experimental conditions).

1.2.1 Quark Parton Model

According to the *Quark Parton Model* (QPM, or, sometimes, just *parton model*; for a review see e.g. [22]) developed by Feynman [23] and Bjorken & Paschos [24], the proton is conjectured to consist of point-like constituents, called partons (lately associated with quarks), from which the electron is scattered incoherently:

$$\left.\frac{d\sigma}{d\Omega}\right|_{eN} = \sum_i \left.\frac{d\sigma}{d\Omega}\right|_{eq_i} \tag{1.8}$$

This model is implemented in the infinite momentum frame of reference, in which the relativistic time dilation slows down the motion of the constituents nearly to a standstill with respect to each other. The incoming electron thus "sees" and incoherently scatters from constituents which are essentially real and non-interacting during the time the virtual boson is exchanged.

The transverse momentum of any parton, in a frame approaching the infinite momentum frame, is negligible, and the i-th parton has the momentum $P_i = x_i P$, where x_i is a fraction of the proton's momentum. If we set the quark masses to zero, as assumed by the QPM (i.e. $(x_i P)^2 = p'^2 = 0$, where p' is the four momentum of the outgoing quark), then

$$p'^2 = (x_i P + q)^2 = 2x_i P \cdot q - Q^2 = 0. \tag{1.9}$$

Comparing (1.9) with (1.5), it can be readily seen that $x_i = x$. Thus in the QPM x is the fraction of the proton momentum carried by the struck massless quark.

1.2.2 The Inclusive DIS Cross Section

In the QPM the double-differential cross section for incoherent elastic scattering of an electron off all possible types of quarks, i, with a specific value of x is [25]

$$\frac{d^2\sigma}{dxdQ^2} = \frac{2\pi\alpha^2}{xQ^4}[1+(1-y)^2]\sum_i e_i^2 xq_i(x). \tag{1.10}$$

Here α is the electromagnetic coupling constant and $q_i(x)$ is the probability that the struck quark i carries a fraction x of the hadron's momentum. The momentum distribution $xq_i(x)$ is called *parton distribution function* (PDF).

On the other hand, the general formula for inelastic lepton-hadron scattering can be expressed via the convolution of the leptonic $L^e_{\mu\nu}$ and the hadronic $W^{\mu\nu}$ tensors [25]:

$$d\sigma \sim L^e_{\mu\nu}W^{\mu\nu}. \tag{1.11}$$

If we rewrite the hadronic tensor by means of proton *structure functions* $F_1,\ F_2,\ F_3$, the inclusive Neutral Current DIS cross section for an unpolarised lepton beam will read, in the lowest order of Electroweak theory

$$\frac{d^2\sigma(l^\pm N)}{dxdQ^2} = \frac{2\pi\alpha^2}{Q^4x}\left[Y_+F_2^{lN}(x,Q^2) - y^2F_L^{lN}(x,Q^2) \mp Y_-xF_3^{lN}(x,Q^2)\right], \tag{1.12}$$

where $Y_\pm = 1\pm(1-y)^2$, $F_L = F_2 - 2xF_1$, and the "+" or "−" sign corresponds to a positively or negatively charged scattered lepton.

For charged-lepton-nucleon scattering mediated by $W^\pm$ exchange (Charged Current), the differential cross section is given by

$$\frac{d^2\sigma^{CC}(l^\pm N)}{dxdQ^2} = \frac{G_F^2}{4\pi x}\frac{M_W^4}{(Q^2+M_W^2)^2}\left[Y_+F_2(x,Q^2) - y^2F_L(x,Q^2) \mp Y_-xF_3(x,Q^2)\right], \tag{1.13}$$

where M_W is the $W^\pm$ boson mass and G_F is the Fermi coupling constant, which can be expressed as

$$G_F = \frac{\pi\alpha}{\sqrt{2}\sin^2\theta_W M_W^2}. \tag{1.14}$$

Comparing (1.12) with the parton model result of (1.10) implies that the parton model predicts

$$F_2^{lh}(x,Q^2) = \sum_i e_i^2 xq_i(x). \tag{1.15}$$

Thus the parton model predicts so-called Bjorken scaling, which means that F_2 depends only on x and not on Q^2.

The parton model also predicts,

$$F_L^{lh}(x,Q^2) = 0, \tag{1.16}$$

also known as the Callan-Gross relation [26], $2xF_1^{lh} = F_2^{lh}$, as a consequence of scattering from spin-$\frac{1}{2}$ partons.

The F_3 structure function corresponds to parity violation during the scattering, due to exchange of electroweak bosons. In the QPM model $F_3 = 0$.

The QCD expressions for F_1, F_2 and F_3 will be given in Section 1.3.5.

1.3 Perturbative Quantum Chromodynamics

This Section briefly describes the perturbative approach to QCD and its features like divergences and methods of their elimination. Different treatments of the heavy quarks (c, b) are also considered.

1.3.1 Principles of QCD

QCD (e.g. [27]) is a non-Abelian gauge theory with a quark-gluon interaction generated by the SU(3) group, as was briefly discussed in Section 1.1. Local SU(3) gauge transformations of fermion wave-functions are given by

$$\psi(x) \to \psi'(x) = e^{igt\cdot\theta(x)}\psi(x), \tag{1.17}$$

where g is the strong coupling constant and $t\cdot\theta$ represents the product of the colour group generators with a vector of space-time phase functions in colour space. The gluon field strength tensor is

$$F_a^{\mu\nu} = \partial^\mu A_a^\nu - \partial^\nu A_a^\mu + g f^{abc} A_b^\mu A_c^\nu, \tag{1.18}$$

where A_a ($a = 1,\ ...,\ 8$) are the gluon fields, f^{abc} are the SU(3) structure constants and the final term represents the interaction of the gluons amongst themselves as they also carry colour charges. Indices $\mu, \nu = 0, 1, 2, 3$ correspond to space-time dimensions. The quark spinor fields ψ_i transform as triplets under SU(3) with $i = 1, 2, 3$ running over the three colour indices. The QCD Lagrangian is given by

$$\mathcal{L}_{\mathrm{QCD}} = \sum_f \bar{\psi}_f^i (i\gamma_\mu D_{ij}^\mu - m_f)_{ij} \psi_f^j - \frac{1}{4} F_a^{\mu\nu} F_{\mu\nu}^a, \tag{1.19}$$

where m_f are the mass parameters of quarks, and the covariant derivative is

$$D_{ij}^\mu = \delta_{ij}\partial^\mu + ig(t^a)_{ij} A_a^\mu \tag{1.20}$$

and $(t^a)_{ij}$ are 3×3 hermitian matrices, which for the fundamental triplet representation of SU(3) are $(\lambda^a)_{ij}/2$, where λ^a are the Gell-Mann matrices (see e.g. [28]).

For calculations beyond the tree level, the *gauge fixing* term, L_{GF} is added to the Lagrangian [29]:

$$L_{\mathrm{GF}} = -\frac{1}{2\xi} \sum_a (\partial_\mu A_a^\mu)^2 \tag{1.21}$$

with ξ a free gauge parameter.

As a consequence of the interaction of gluons among themselves, QCD acquires two important features:

- **Asymptotic freedom.** At very short distances the QCD coupling becomes small.
- **Confinement.** The potential energy of the quark-quark or quark-antiquark interaction grows linearly with the distance. Therefore, if quarks at some moment move far enough apart, it is more energetically favourable to produce two hadrons instead of one, via the creation of an additional quark-antiquark pair.

1.3.2 Perturbative Expansion of the QCD Observables

The asymptotic freedom of QCD allows the implementation of perturbation theory for the calculation of observables: they can be expanded in a power series in the strong coupling constant, α_s. The perturbative approach works in the phase space regions where α_s is small (large energies or, equivalently, small distances), such that truncated series give a good description of the experimental data. The theoretical prescriptions for the perturbative calculations are obtained from the QCD Lagrangian after adding gauge fixing and ghost terms [30]; these prescriptions are known as the *Feynman rules*.

Shortly, the Feynman rules to calculate an order α_s^N theoretical prediction, are summarised as follows [28]:

1. Each particle is represented by a line; the interaction of particles is represented by a point (interaction vertex) in place of the connection of two lines. All conservation laws are fulfilled at vertices. If a line has points on both its ends, it is also called a propagator. External lines (those, which are attached to only one vertex) correspond to initial and final state particles. The process of interaction of particles can be displayed with Feynman diagrams, composed of lines and vertices.

2. Draw all possible topologically-independent connected diagrams with the given initial and final states (as defined by the observable). The maximum number n of gluon vertices is dictated by the order of the calculation N (i.e. $n \leq N$ for tree-like diagrams (diagrams without loops) and n always not larger than $2N$ for the diagrams containing gluons participating in loops);

3. The contribution to the matrix element coming from each diagram (an amplitude) is obtained by combining expressions corresponding to each propagator and each vertex (the rules can be found in [28]);

4. Take into account energy-momentum conservation at each vertex;

5. The integration for each loop is done over all momenta;

6. The expression for the matrix element is the square of the sum of all diagram contributions, thereby including their interference.

The prediction for the cross section σ up to the order N for an investigated process can then be expressed as:

$$\sigma = k_0 \cdot \alpha_s^0 + k_1 \cdot \alpha_s^1 + k_2 \cdot \alpha_s^2 + ... = \sum_{i=0}^{N} k_i \cdot \alpha_s^i. \tag{1.22}$$

where the coefficients k_i are evaluated from the Feynman diagrams related to the corresponding order in α_s. The first non-zero term in the series (1.22) is called *Leading Order* (LO) prediction. If the next order term is added, the prediction is said to be calculated at the Next-to-Leading order (NLO), and so on.

The application of the Feynman rules to the calculation of amplitudes with virtual and real corrections typically leads to divergences, which are discussed below, as well as methods to eliminate them. The so-called ultraviolet divergences are closely related with the renormalisation and the running of the strong coupling constant, α_s, which is tested in this thesis. The soft and collinear divergences are related to the factorisation of QCD cross sections involving hadrons in the initial state into the hard-scattering part (calculable perturbatively) and parton density functions (derived from experiment).

1.3.3 Divergences in Perturbative QCD Calculations

Different types of divergences arise during perturbative QCD (pQCD) calculations. They are listed in this subsection.

Ultraviolet divergences. *Ultraviolet* (UV) divergences appear in QCD (and in most other relativistic quantum field theories) when the continuum limit is taken, i.e. when interaction vertices approach each other in space-time [31]. The divergences are technically occur due to going to infinity momentum of a particle in a loop, Fig. 1.2. In renormalisable theories, like QCD, the UV divergences can be proved to be removed by a modification of the continuum limit, at least in perturbation theory. The renormalisation procedure and its consequences are overviewed in section 1.3.4.

Soft and collinear divergences. These two are generically called the *Infrared* (IR) divergences and emerge due to massless fields, like the gluon and the light (u, d, s) quarks, which are treated in pQCD as massless. Soft divergences occur due to the loop integration in the limit of going to zero momentum (Fig. 1.2) of the massless particle participating in the loop . Soft divergences also emerge when a massless particle is radiated at close to zero momentum. For example, if the final state quark radiates a soft gluon. This leads to an experimentally indistinguishable final state, and such radiation has to be included in the calculation, which leads to divergences. A collinear divergence (also called mass singularity) is generated if a massless particle is radiated parallel or

antiparallel with respect to an initial or final state particle (this is true for both gluon radiation by the quark and for gluon splitting into two massless quarks or into two gluons). Fortunately, in pQCD (which manipulates quarks and gluons but not hadrons) soft and collinear divergences are exactly cancelled by the corresponding soft divergence at each order of the perturbative calculations. It is, however, necessary to introduce regularisation (for example, to introduce a small artificial mass of the gluon m_g) for the purpose of making each infrared-divergent integral in the physical quantity well-defined [28]. The regularisation is removed after the cancellation is achieved. The cancellation of the IR divergences is a general property of the Standard Model theories and it is stated by the Kinoshita-Lee-Nauenberg theorem [32, 33]. The IR divergences do not occur for massive fields.

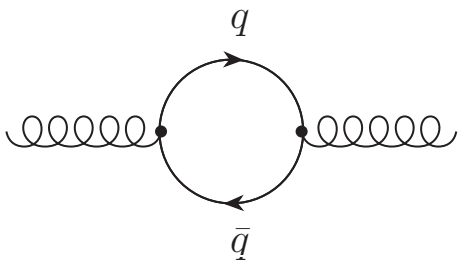

Figure 1.2: A quark-loop correction to the gluon self-energy. The diagram diverge for both zero and infinite momenta of the massless particles in the loop. The diagram is however finite for zero momentum of the massive particle in the loop.

A complication arises when considering a real physics picture of hadron collisions (pQCD treats parton level quark/gluon collisions). The cancellation of divergences appearing due to a collinear splitting in the initial state, is incomplete. However, these residual divergences can be factorised and absorbed into PDFs. More details are given in Section 1.3.5.

Non-convergent series. Divergences of this type are listed here for completeness. There are indications [34] that at asymptotically large N in (1.22), the perturbative coefficients k_i are proportional to a factorial of N, at least for some observables, and therefore the perturbative series is divergent. Strict proofs of the divergence are however still absent. A discussion and overview of the results on this point is given in [35].

1.3.4 Renormalisation and Running of the Strong Coupling

As was mentioned in subsection 1.3.3, loop integrals diverge in the limit of infinite momentum (or, equivalently, at small distances, i.e. the continuum limit). Fortunately, the divergences can be removed by applying a *renormalisation* procedure:

1. Redefine the fields, wave functions and parameters of the Lagrangian. For example, the gluon A^a_μ and quark ψ fields are usually redefined as [28] $A^a_\mu = Z_3^{1/2} A^a_{r\mu}$, $\psi = Z_2^{1/2}\psi_r$, where the constants Z_3 and Z_2 are called the gluon-field and quark-field renormalisation constants, respectively. The strong coupling constant, the masses, and the gauge parameter are redefined via the expressions $g = Z_g g_r$, $m = Z_m m_r$, and $\xi = Z_3 \xi_r$, respectively. Here, the subscript r is used for renormalised variables.

2. Rewrite the Lagrangian and re-derive the Feynman rules. The new Lagrangian will be the sum of two parts. The first will have the same form as before renormalisation, if the fields and parameters are replaced by the renormalised ones. The second part, the so-called *counter-term*, will contain all the renormalisation constants.

3. To mathematically manage the divergent integrals in the expressions corresponding to Feynman diagrams, *regularisation* needs to be performed. Among different possible regularisation schemes (see, e.g. [28]), the most widely used one is the *dimensional* regularisation, where the number of space-time dimensions is taken to be $D = 4 - 2\epsilon$. In the limit $\epsilon \to 0$, D recovers the physical value of 4. At an arbitrary number of dimensions D, the gauge coupling constant g is no longer dimensionless, it acquires a mass dimension (so that the action stays dimensionless). It is expressed as $g = g_0 \mu_R^\epsilon$, where g_0 is the dimensionless gauge coupling constant and μ_R is some mass scale, not yet determined at this step and called *renormalisation scale*.

4. Write down the expression for the Feynman diagrams. They will contain poles in ϵ and the renormalisation constants. For example the expression for the self-energy of a gluon with 4-momentum k will contain the following terms [28]:

$$\Pi^{ab}_{\mu\nu}(k) = \delta_{ab}(k_\mu k_\nu - k^2 g_{\mu\nu})\Pi(k^2), \tag{1.23}$$

$$\Pi(k^2) = \frac{g_{0r}^2}{(4\pi)^2}\left[\frac{4}{3}T_R N_f - \frac{1}{2}C_A\left(\frac{13}{3} - \xi_r\right)\right]\frac{1}{\epsilon} + Z_3 - 1 + \text{finite terms}. \tag{1.24}$$

   Here $a, b = 1, ..., 8$ are indices of the gluon field, $T_R = 1/2$ is the colour factor ("Casimir") associated with a gluon splitting into $q\bar{q}$ pair, $C_A \equiv N_c = 3$ is the colour factor associated with gluon emission from a gluon (and N_c is the number of colours).

   The first term in (1.24) is infinite when $\epsilon = 0$, but by appropriate definition of the renormalisation constant Z_3 the divergence can be removed.

5. Choose the renormalisation scheme. The renormalisation constants can be chosen in different ways, which corresponds to different renormalisation schemes. For example,

in the most widely used $\overline{\text{MS}}$ scheme, the expression for Z_3 reads

$$Z_3 = 1 - \frac{g_{0\,r}^2}{(4\pi)^2}\left[\frac{4}{3}T_R N_f - \frac{1}{2}C_A\left(\frac{13}{3} - \xi_r\right)\right]\left(\frac{1}{\epsilon} - \gamma + \ln 4\pi\right) + \mathcal{O}(g_r^4). \quad (1.25)$$

Thus, all the divergent pieces are absorbed into the definition of the renormalisation constants.

6. Perform the final calculation. The matrix elements and renormalised parameters of the Lagrangian (masses and coupling constants) will now depend on μ_R (but not on ϵ).

In the $\overline{\text{MS}}$ scheme there is no prescription of how to choose μ_R. Nevertheless, the predictions calculated to all orders of α_s should not depend on this arbitrary parameter: a change of μ_R in the matrix elements is compensated by a change of $\alpha_s(\mu_R)$. Mathematically the independence of the prediction for an observable R on μ_R is expressed by the renormalisation group equation [36],

$$\mu_R \cdot \frac{dR}{d\mu_R} = 0. \quad (1.26)$$

The renormalisation group equation is fulfilled only if the observable is calculated to all orders in α_s. If the series is truncated, as is always the case in perturbative calculations, the prediction for the observable is dependent on μ_R. Since μ_R is an arbitrary parameter in many schemes like $\overline{\text{MS}}$, several investigations were made in [37–39] for how to choose μ_R. It was suggested, that μ_R should be related to the physical scale of the studied process. For example, in inclusive DIS, the scale could be Q^2, while for inclusive jet production μ_R^2 could be a linear combination of $(p_T^{\text{jet}})^2$ and Q^2.

Equation (1.26) leads to the following equation for α_s:

$$\mu_R^2 \frac{\partial \alpha_s}{\partial \mu_R^2} = \beta(\alpha_s), \quad (1.27)$$

where the β-function describes the change of the coupling with the change of the scale and has the perturbative expansion [30]

$$\beta(\alpha_s) = -(b_0\alpha_s^2 + b_1\alpha_s^3 + b_2\alpha_s^4 + ...), \quad (1.28)$$

where

$$b_0 = \frac{11C_A - 4n_f T_R}{12\pi} = \frac{33 - 2n_f}{12\pi} \quad (1.29)$$

is the 1-loop beta-function coefficient. The 2- and 3-loop coefficients, respectively, are:

$$b_1 = \frac{153 - 19n_f}{24\pi^2}, \quad (1.30)$$

$$b_2 = \frac{2857 - \frac{5033}{9} n_f + \frac{325}{27} n_f^2}{128\pi^3}. \tag{1.31}$$

Here n_f is the number of *active* flavours, i.e. flavours with masses $m < \mu_R$. The coefficients b_0 and b_1 do not depend on the renormalisation scheme. The coefficients b_2 and b_3 are quoted here in the $\overline{\text{MS}}$ scheme. At 1-loop order, the expression for $\alpha_s(\mu_R)$ has the simple analytical form

$$\alpha_s(\mu_R) = \frac{\alpha_s(\mu_{R,0})}{1 + \frac{\alpha_s(\mu_{R,0})}{12\pi}(33 - 2n_f) \ln \frac{\mu_R^2}{\mu_{R,0}^2}}, \tag{1.32}$$

If $33 - 2n_f > 0$, which is the case in the Standard Model with $n_f = 6$ quarks, the coupling of QCD decreases with increasing μ_R and the property of asymptotic freedom emerges in the limit $\mu_R \to \infty$: $\alpha_s(\mu_R)|_{\mu_R \to \infty} \to 0$.

Alternatively, equation (1.32) can be written as:

$$\alpha_s(\mu_R) = \frac{1}{b_0 \ln(\mu_R^2/\Lambda^2)}, \tag{1.33}$$

where Λ is a constant of integration of equation (1.27) and corresponds to the scale where the perturbatively-defined coupling would diverge, i.e. it is the non-perturbative scale of QCD. As it is seen from the comparison of equations (1.32) and (1.33), the constant Λ depends on the number of flavours n_f. For five flavours, it has an experimentally measured value of $\Lambda_{\overline{\text{MS}}}^{n_f=5} = 213 \pm 8$ MeV [8].

In practice, a combination of the parameters $\mu_{R,0}$ and $\alpha_s(\mu_{R,0})$ is used instead of Λ. The scale $\mu_{R,0}$ is typically chosen to be equal to the mass of the Z boson, $\mu_{R,0} = M_Z$. The parameter $\alpha_s(M_Z)$ is a free parameter of the Standard Model and is determined experimentally.

Because the beta functions (1.29) - (1.31) depend on n_f, it follows that the slope of the α_s evolution is discontinuous when crossing a mass threshold. Beyond LO there are not only discontinuities in the slope but also in α_s itself. In N^{l}LO, the value of $\alpha_s^{(n_f+1)}$ is, at a flavour threshold, related to $\alpha_s^{(n_f)}$ by [40, 41]

$$a_s^{(n_f+1)}(k\mu_h^2) = a_s^{(n_f)}(k\mu_h^2) + \sum_{n=1}^{l} \left\{ \left[a_s^{(n_f)}(k\mu_h^2) \right]^{n+1} \sum_{j=0}^{n} C_{n,j} \ln^j k \right\} \quad l = 1, 2. \tag{1.34}$$

Here $\mu_h = m_h$ is the threshold defined on the factorisation scale and k is the ratio μ_R^2/μ_F^2 at $\mu_F = \mu_h$. For $a_s = \alpha_s/4\pi$, the coefficients C in (1.34) read

$$C_{1,0} = 0, \quad C_{1,1} = \frac{2}{3}, \quad C_{2,0} = \frac{14}{3}, \quad C_{2,1} = \frac{38}{3}, \quad C_{2,2} = \frac{4}{9}. \tag{1.35}$$

Thus, there is always a discontinuity in α_s at NNLO. At NLO, a discontinuity only occurs when the renormalisation and factorisation scales are different, $k \neq 1$ (due to $C_{1,0} = 0$).

1.3.5 Factorisation and the Parton Distribution Functions

Perturbative QCD operates with quarks and gluons at small distances, where α_s is small, and the perturbative approach is thus applicable. However, at larger distances ($r \sim 10^{-15}$ m) quarks and gluons are bound into hadrons. To relate physically measurable cross sections of hadron interactions and the results of pQCD, parton distribution functions $f_{i/h}$ must be introduced, which describe the momentum distribution of the parton type i in the hadron h.

For the DIS case, the factorisation theorem states that the structure functions can be written via a convolution of the PDFs and hard-scattering coefficients [42]:

$$F_a^{(Vh)}(x,Q^2) = \sum_{i=q,\bar{q},g} \int_x^1 \frac{d\xi}{\xi} C_a^{(Vi)}(x/\xi, Q^2, \mu_F^2, \mu_R^2, \alpha_s(\mu_R^2)) \times f_{i/h}(\xi, \mu_F), \quad (a = 1, 3) \tag{1.36}$$

$$F_2^{(Vh)}(x,Q^2) = \sum_{i=q,\bar{q},g} \int_x^1 d\xi C_2^{(Vi)}(x/\xi, Q^2, \mu_F^2, \mu_R^2, \alpha_s(\mu_R^2)) \times f_{i/h}(\xi, \mu_F). \tag{1.37}$$

Here μ_R is the renormalisation scale, μ_F is the so-called factorisation scale, and the sum runs over all partons of the proton: quarks, antiquarks and gluons. Similar theorems are stated for many QCD processes. Schematically, the statement of factorisation can be expressed as

$$\sigma = \hat{\sigma} \otimes f, \tag{1.38}$$

where σ is the prediction for some cross section (or structure function) involving hadrons in the initial state, $\hat{\sigma}$ describes the interaction of the *partons* and f are PDFs.

The PDFs $f_{i/h}(\xi, \mu_F)$ no longer have the meaning of a probability density (compare to Subsection 1.2.2), since they were redefined to absorb the non-cancelled collinear divergences. In short, the approach for factorisation with the absorption of the collinear divergences into the PDFs can be summarised as follows [31]:

1. Suppose that the W, the structure function (or cross section) under consideration, is a convolution of a partonic cross section and parton densities:

$$W = W^{\text{parton}} \otimes f^{\text{bare}}. \tag{1.39}$$

2. There are IR/collinear divergences in the parton cross section. It was shown [43,44] that the partonic cross sections are a convolution of a divergence factor, C, and a finite cross section, D:

$$W^{\text{parton}} = C \otimes D \tag{1.40}$$

3. The final factorisation formula is obtained by the use of the associativity of convolution to allow the divergences to be absorbed into a redefinition of the parton densities:
$$W = (C \otimes D) \otimes f^{\text{bare}} = C \otimes (D \otimes f^{\text{bare}}) = C \otimes f^{\text{ren}}, \tag{1.41}$$
where $f^{\text{ren}} = D \otimes f^{\text{bare}}$.

There is an ambiguity in reshuffling the divergence between the PDFs and hard scattering parts, which is removed after adopting a particular *factorisation scheme*. In a similar manner as in the renormalisation procedure, a new arbitrary parameter arises - the factorisation scale μ_F. It serves to define the separation of short-distance (calculated in the hard-scattering coefficients) from long-distance effects (absorbed into PDFs).

The hard-scattering function $C_a^{(Vi)}$ $(a = 1, 2, 3)$ of (1.36) and (1.37) is independent of long-distance effects. In particular, it is independent of the identity of the hadron h. The parton density $f(\xi, \mu_F)$ on the other hand contains all long-distance effects. They cannot be calculated perturbatively but can be measured from experiment and can be used afterwards for the prediction of other cross sections, i.e. the PDFs are believed to be universal. However, if the PDFs were measured using some specific factorisation scheme, the same scheme has to be used in all other cases where these PDFs are involved.

In an analogous way to the evolution of α_s, pQCD predicts the evolution of the PDFs with respect to μ_F. The evolution of the PDFs is usually written in terms of coupled integro-differential equations,

$$\mu_F^2 \frac{d}{d\mu_F^2} f_{i/h}(x, \mu_F) = \sum_{j=q,\bar{q},g} \int_x^1 \frac{d\xi}{\xi} P_{ij}\left(\frac{x}{\xi}, \alpha_s(\mu_R)\right) f_{j/h}(\xi, \mu_F). \tag{1.42}$$

This equation is known as the Dokshitzer-Gribov-Lipatov-Altarelli-Parisi (DGLAP) evolution equation [45–48]. The evolution kernels $P_{ij}(x)$ are given by perturbative expansions, beginning with $\mathcal{O}(\alpha_s)$. The one-loop kernels are given by $P_{ij}(x) = \frac{\alpha_s}{2\pi} P_{ij}^{(1)}$, with [42, 45]:

$$P_{qq}^{(1)}(x) = C_F \left[(1 + x^2)\left(\frac{1}{1-x}\right)_+ + \frac{3}{2}\delta(1-x)\right], \tag{1.43}$$

$$P_{qg}^{(1)}(x) = T_R \left[(1-x)^2 + x^2\right], \tag{1.44}$$

$$P_{gq}^{(1)}(x) = C_F \frac{(1-x)^2 + 1}{x}, \tag{1.45}$$

$$P_{gg}^{(1)}(x) = 2C_A \left[\frac{x}{(1-x)_+} + \frac{1-x}{x} + x(1-x)\right] + \left(\frac{11}{6}C_A - \frac{2}{3}T_R n_f\right)\delta(1-x). \tag{1.46}$$

Here $C_F = 4/3$, $C_A = 3$ and $T_F = 1/2$. Thus, the evolution of the PDFs depends on α_s.

1.3.6 Treatment of Heavy Flavours

In pQCD the light quarks u, d, s are treated as massless. For the heavy quarks, c, b, t, different treatments are possible. The treatment of charm and beauty quarks is an important ingredient in many QCD calculations, in particular for the inclusive DIS cross sections. Several heavy flavour schemes exist and are reviewed here.

Fixed Flavour Number Scheme (FFNS). In this scheme [49–51], the gluon and the light quarks and their antiquarks are considered as partons within the proton, while the massive quarks are only produced perturbatively in the final state. This scheme with $n_f = 3$ light flavours in the proton PDFs is expected to be reliable at scales $Q^2 \sim m_c^2, m_b^2$ (charm and beauty quark masses are of the same order). In fact, it was found that the fixed flavour number scheme with three flavours in the proton describes nicely HERA inclusive DIS data over a large kinematic range. At much higher scales it may break down due to the multi-scale problem[2]. However, at high scales, $Q^2 >> m_b^2$, charm and bottom quarks may be considered as light and included in the proton PDFs. The QCD theory gives strict conditions for the matching of the fixed flavour PDFs with $n_f = 3$, 4 and 5 flavours (the matching conditions can be found in [54]). In this way it is possible to extend the applicability of the FFNS to arbitrarily large scales. Together with a proper account of heavy quark masses it makes the FFNS a rigorous QCD approach.

Zero-Mass Variable Flavour Number Scheme (ZM-VFNS) [55]. The heavy quark densities are included in the proton PDFs for Q^2 values above a threshold $\sim m_{hq}^2$ (m_{hq} is the mass of a heavy quark) and they are treated as massless in both the initial and final states. This scheme is expected to be reliable only in the region with $Q^2 >> m_{hq}^2$.

General-Mass Variable Flavour Number Schemes (GM-VFNS). This scheme combines the massive and massless schemes. It converges to the FFNS ($n_f = 3$ flavours in the proton) and to the ZM-VFNS at small and large scales, respectively. In the intermediate region it performs a certain interpolation between the two schemes. The interpolation is up to some extent arbitrary and various approaches are used, like different versions of the Thorne-Roberts (RT) scheme [56–58] and a variety of versions of the Aivazis-Collins-Olness-Tung (ACOT) scheme [59–61].

1.4 Jet Physics

Similarly to the concept of the PDFs, which gives a connection between the initial state hadron and the incoming partons, the concept of *fragmentation* and *hadronisation* gives a connection between the final state partons and the hadrons, registered in the detector. Hadronisation is the transition of final state partons to colourless hadrons. Due to the self-coupling of the gluon and radiation by quarks, this process is accompanied by the

[2]The mass of the heavy quark can play a role of an additional energy scale in the process, which makes the choice of μ_R and μ_F ambiguous. The multi-scale question is addressed in [52, 53].

creation of new partons (fragmentation), radiated predominantly in the direction of the primary parton. Thus, the parton fragments into a collimated bunch of hadrons, called *jet*. The process of hadronisation cannot be calculated perturbatively. To describe the fragmentation of partons to different hadrons, the concept of fragmentation functions is introduced.

Jets are closely related to the QCD dynamics of quarks and gluons in hard scattering processes. Hence, measurements of jet cross sections allow a detailed study of the properties of the QCD interaction. Jet measurements are especially helpful in testing the QCD matrix elements and in constraining the gluon density in the proton. They also contain significant information to constrain the strong coupling constant. The latter is extensively exploited in this thesis.

1.4.1 Jet algorithms

The strict definition of jets is given by the *jet algorithm*. To compare theoretical predictions for jet production cross sections with the experimentally measured ones, the same jet algorithm should be applied in both theoretical calculations and in the measurement. To preserve the correspondence between the final state partons and the jets, the jet algorithm has to be infrared and collinear safe, i.e. the jet properties have to be insensitive to soft/collinear radiation of partons. The jet algorithms being used nowadays can be divided in two classes. Sequential recombination algorithms such as the k_t [62,63], anti-k_t [64] or Cambridge/Aachen [65] algorithm sequentially recombine close-by particles using a distance measure, defined by the user. Cone algorithms, in contrast, perform a search for regions of large energy flow.

In the analyses of the dijet and photon + jet data discussed in this thesis, the longitudinally invariant inclusive k_t algorithm [62,63] was used for the reconstruction of jets. This algorithm uses the pseudorapidity, η, the azimuthal angle, ϕ, and the transverse energy, E_T, of the input objects. The input objects can be partons, hadrons or detector level objects (tracks, calorimeter cells etc). The algorithm is performed using the following steps:

1. Two catalogues are used: a list of all measured objects, and a list of reconstructed jets which is empty at the beginning.

2. For all objects i the distance to the beam axis, $d_i = E_{T,i}^2 \cdot R_0^2$, and the distance d_{ij} to the other objects j is calculated according to $d_{ij} = \min(E_{T,i}^2, E_{T,j}^2) R_{ij}^2$, where R_{ij} is the distance in the $\eta - \phi$ plane given by $R = \sqrt{(\eta_i - \eta_j)^2 + (\phi_i - \phi_j)^2}$. The variable R_0 was set to unity in the presented in this theses jet analyses.

3. Afterwards, the smallest distance $d_{\min}$ is determined from all d_i and d_{ij}.

4. If $d_{\min}$ belongs to the list $\{d_i\}$, then a jet has been reconstructed and put into the list objects. The $d_{\min}$ is removed from the list of objects.

5. In contrast, if $d_{\min}$ belongs to the list $\{d_{ij}\}$, then the particles i and j are combined into a new particle. The particles i and j are removed from the list $\{d_{ij}\}$.

6. The procedure is repeated until all objects are clustered into jets.

The properties of resulting jets can be defined by properties of input particles using the different prescriptions, or *recombination schemes*. In this thesis, the so-called E and E_T schemes where used. The E scheme means that the 4-vector of a jet, p^{jet}, is obtained via simple addition of the 4-vectors of particles that are contained in the jet:

$$p^{\text{jet}} = \sum_i p_i. \tag{1.47}$$

In the E_T scheme, the transverse energy, pseudorapidity, and the azimuthal angle are defined respectively as:

$$E_T^{\text{jet}} = \sum_i E_{T,i}, \quad \eta^{\text{jet}} = \frac{\sum_i E_{T,i}\eta_i}{E_T^{\text{jet}}}, \quad \phi^{\text{jet}} = \frac{\sum_i E_{T,i}\phi_i}{E_T^{\text{jet}}}. \tag{1.48}$$

1.4.2 The Breit Reference Frame

The Breit frame [23, 66] is often used for the study of jets in DIS at HERA, since in this frame the factorisation of the jet cross section into the PDFs and the hard scattering part is guaranteed [67]. The Breit frame is defined by the equation $2x_{\text{Bj}}\vec{P} + \vec{q} = 0$, where $\vec{P}$ and $\vec{q}$ are the momenta of the incoming parton and the exchanged virtual boson, respectively. In this frame the parton and the virtual exchanged boson collide head-on without transferring energy from the electron to the parton.

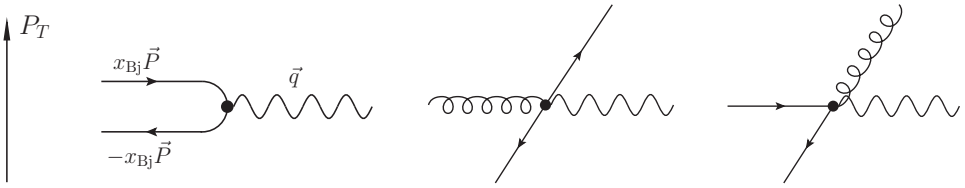

Figure 1.3: Scattering of the parton of the proton and the virtual exchanged boson in the Breit frame: quark parton model (a), boson-gluon fusion (b) QCD Compton scattering

1.4.3 Boson Gluon Fusion and QCD Compton Processes

For the QPM process in the Breit frame, Fig. 1.3(a), the transverse momentum of the scattered quark is zero, while for the lowest order processes involving QCD interaction (boson gluon fusion, Fig 1.3(b), and QCD Compton scattering, Fig. 1.3(c)) transverse momentum is present in the Breit frame. Hence, the Breit frame is useful to detect a QCD interaction in the event.

Inclusive dijet events can be characterised by the following quantities:

$$M_{\mathrm{jj}} = \sqrt{\left(\sum_{i=1}^{2} p_{i,\mathrm{B}}\right)^2},\ \overline{E_{T,\mathrm{B}}^{\mathrm{jet}}} = \frac{1}{2}(E_{T,\mathrm{B}}^{\mathrm{jet1}} + E_{T,\mathrm{B}}^{\mathrm{jet2}}),\ \eta^* = \frac{1}{2}\cdot|\eta_{1,\mathrm{B}} - \eta_{2,\mathrm{B}}|,\ \xi = x_{\mathrm{Bj}}\cdot\left(1 + \frac{M_{\mathrm{jj}}^2}{Q^2}\right).$$

Here $p_{i,\mathrm{B}}$ is the 4-momentum of the i-th jet and M_{jj} is the invariant mass of the dijet system. $\overline{E_{T,\mathrm{B}}^{\mathrm{jet}}}$ is the average transverse energy in the Breit frame. The variable η^* describes the difference of the pseudorapidities, $\eta_{i,\mathrm{B}}$, of the final state partons in the Breit frame. This difference is invariant under longitudinal Lorentz transformations. The pseudorapidity is defined as

$$\eta = -\ln\tan\frac{\theta}{2}, \tag{1.49}$$

where θ is the polar angle of the parton. The variable η^* is closely related to the angular dependent parts of the QCD matrix element. The variable ξ represents the momentum fraction of the parton entering the hard process. Thus, for a dijet system, the squared dijet centre-of-mass energy is given by

$$M_{\mathrm{jj}}^2 = (q + \xi P)^2 = (p_1 + p_2)^2 = q^2 + 2q\xi P + (\xi P)^2. \tag{1.50}$$

If one neglects the term $(\xi P)^2 \ll Q^2$, then the variable ξ is given by

$$M_{\mathrm{jj}}^2 = -Q^2 + 2q\xi P \quad \Longrightarrow \quad \xi = \frac{Q^2}{2qP} + \frac{M_{\mathrm{jj}}^2}{2qP} = x_{\mathrm{Bj}}\left(1 + \frac{M_{\mathrm{jj}}^2}{Q^2}\right). \tag{1.51}$$

The M_{jj}^2/Q^2 term is related to the additional energy needed to produce two final state partons.

1.5 Isolated Photon Production in DIS

Isolated photons in DIS are emitted either by a quark of the proton or by an incoming or outgoing lepton. The corresponding processes are called QQ and LL radiation, respectively. The leading order diagrams for photon emission by quarks are shown in Figure 1.4, while those for photon emission by a lepton are shown in Figure 1.5. The LO processes are of the order $\mathcal{O}(\alpha^3)$. QCD vertices arise in higher order corrections to the LO diagrams. The measurements of inclusive isolated photon with accompanying jet production are compared in this thesis to the NLO pQCD calculations, of the order $\mathcal{O}(\alpha^3\alpha_s)$.

When calculating the predictions, the interference between the LL and QQ mechanisms is considered, and is called the LQ contribution.

If Q^2 is calculated via the parameters of the initial and scattered electron, the resulting quantity for the LL process will not correspond to the virtuality of the exchanged boson, since the radiated photon takes away part of energy of the lepton. However, if in the theoretical calculations the Q^2 variable is defined in the same way (via the scattered electron), there is no ambiguity in the comparison of theoretical predictions with the measurement, because the definition is the same in the theoretical and experimental cross sections.

High energy photons can also be produced during the fragmentation process of the outgoing partons. This process cannot be treated perturbatively and is described in terms of the so-called quark-to-photon fragmentation function. In such processes photons are typically surrounded by additional hadronic activity and therefore are not isolated.

The definition of isolation will be given in Section 5, describing the measurement of the isolated photon with jet cross section.

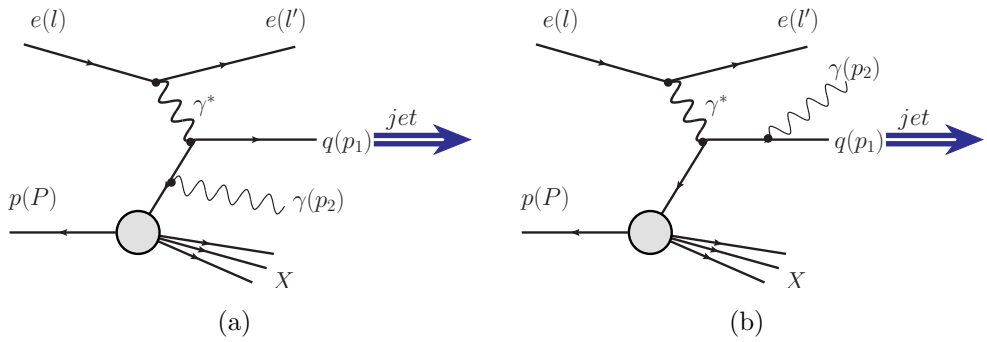

Figure 1.4: Leading order diagrams for QQ photon emission by the incoming (a) and outgoing (b) quark

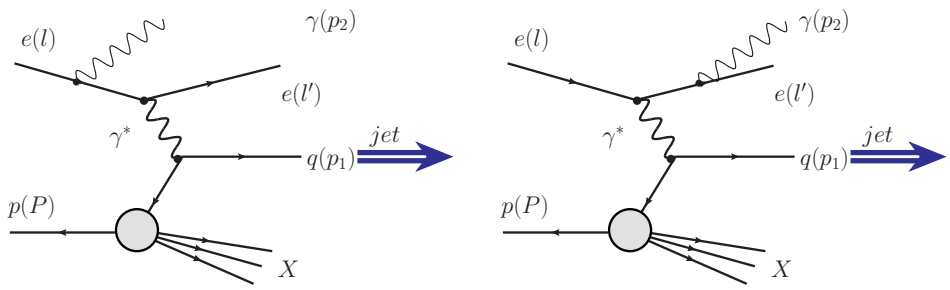

Figure 1.5: Leading order diagrams for LL photon emission by the initial (a) and final (b) state lepton

Chapter 2

The ZEUS detector at HERA

This Chapter gives a brief description of the HERA collider and of parts of the ZEUS detector which are relevant for the two measurements presented in this thesis.

2.1 DESY

The Deutsches Elektronen-Synchrotron (DESY) is a large national research centre operating particle accelerators in Hamburg, Germany. It was founded in 1959 and shortly thereafter, during 1960-1964, the DESY electron accelerator was built. During more than 50 years of successful history of the DESY centre, a lot of particle physics experiments were performed at different accelerators (DESY, DORIS, PETRA, HERA). Nowadays, the most important facilities at DESY are the free electron laser FLASH, used for photon science, and the European X-ray Free Electron Laser (XFEL, expected to be operational by the end of 2016).

DESY is also actively contributing to the ATLAS and CMS experiments at LHC and is involved in the ILC project.

2.2 HERA

The Hadron Elektron Ring Anlage (HERA) [68] collider operated at DESY between 1992-2007. It was the first and so far only accelerator which collided electrons or positrons with protons, providing the unique possibility to investigate the proton structure and to study the properties of electroweak and strong interactions.

Two collider experiments, H1 and ZEUS, and two fixed-target experiments, HERMES and HERA-B, operated at HERA. H1 and ZEUS were multi-purpose detectors. HERMES used only the electron beam to investigate the nucleon spin structure. The HERA-B experiment used only the proton beam and was optimised to study CP violation in B-meson (meson containing the b quark) systems.

The energy of the electron beam was 27.5 GeV. The proton beam energy was increased from 820 GeV to 920 GeV in 1998, which corresponds to a centre of mass energy of 318 GeV (300 GeV before 1998). During the last three months of operation of HERA, the collisions took place at reduced proton energies of 460 and 575 GeV.

HERA consisted of four straight and four arc segments with a total circumference of 6.3 km, see Fig. 2.1. Separate storage rings were used for electrons and protons with an intersection in the places where the H1 and ZEUS detectors were installed.

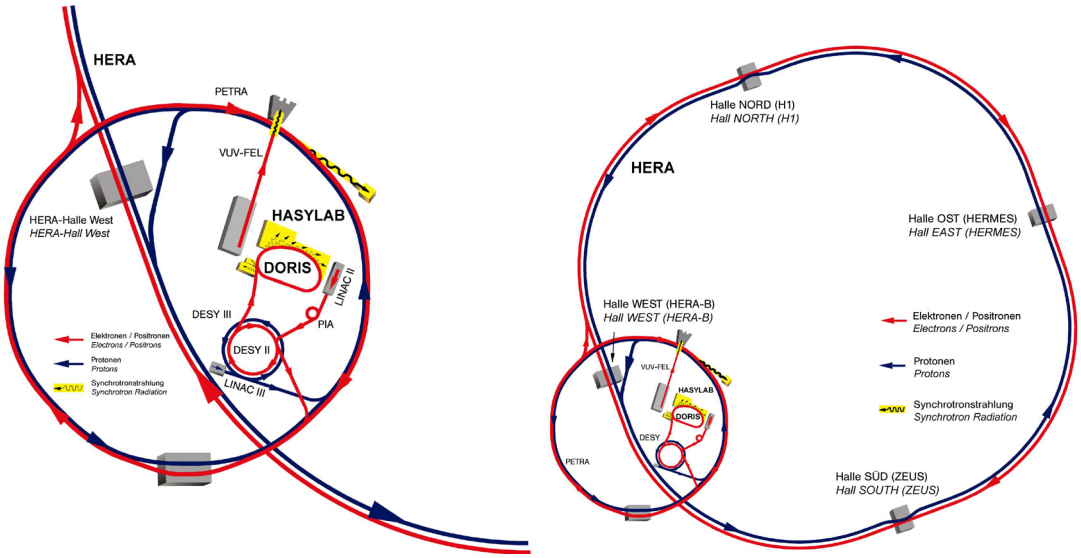

Figure 2.1: Schematic view of HERA and its preaccelerating system.

The left part of Fig. 2.1 shows the preaccelerating system of HERA. The protons were extracted from hydrogen gas. First, H_2 molecules were split into single H atoms. Then, H^- ions were produced by adding one electron. The ions were then accelerated in the LINAC III accelerator to an energy of 50 MeV and were shot into a thin aluminium foil which strips the electrons off, leaving just protons, which were injected further into DESY III. DESY III, after accelerating protons to 8 GeV, transported them to PETRA, where protons were stored and accelerated up to 40 GeV. Finally, protons were injected into the HERA proton ring, where they were accelerated to the final energy. The primary electron beam was produced in LINAC II with a pulsed DC diode gun. Electrons of energy 400 MeV accelerated in LINAC II were, when needed, used for positron production with a tungsten target at the electron-positron converter. Afterwards, the electrons/positrons were further accelerated at DESY II and transferred to the PETRA ring. The electron or positron beam then was injected into HERA at an energy of 12 GeV and accelerated there to the final energy of 27.5 GeV.

In HERA accelerated particles were grouped into a maximum of 220 bunches, each containing approximately $10^{10} - 10^{11}$ particles. The bunch spacing was 96 ns, corre-

sponding to a bunch crossing rate of about 10 MHz. In order to monitor beam related background, unpaired and empty bunches were used.

In 2000/2001 HERA was closed for a large upgrade [69,70], during which higher luminosity and longitudinally polarised lepton beams were provided for the H1 and ZEUS experiments. The experiments were equipped with additional focusing magnets and spin rotators. The instantaneous luminosity was increased from 1.5×10^{31} cm^{-2}s^{-1} to 5×10^{31} cm^{-2}s^{-1}. The spin rotators transformed the natural transverse polarisation of the lepton beam to longitudinal polarisation, thus providing the possibility to study in detail polarisation dependent electroweak effects. The transverse, TPOL, and longitudinal, LPOL, polarimeters were used to measure the lepton beam polarisation. Typical polarisations were about $30 - 40\%$. The periods of data taking before and after the upgrade are called "HERA I" and "HERA II", respectively.

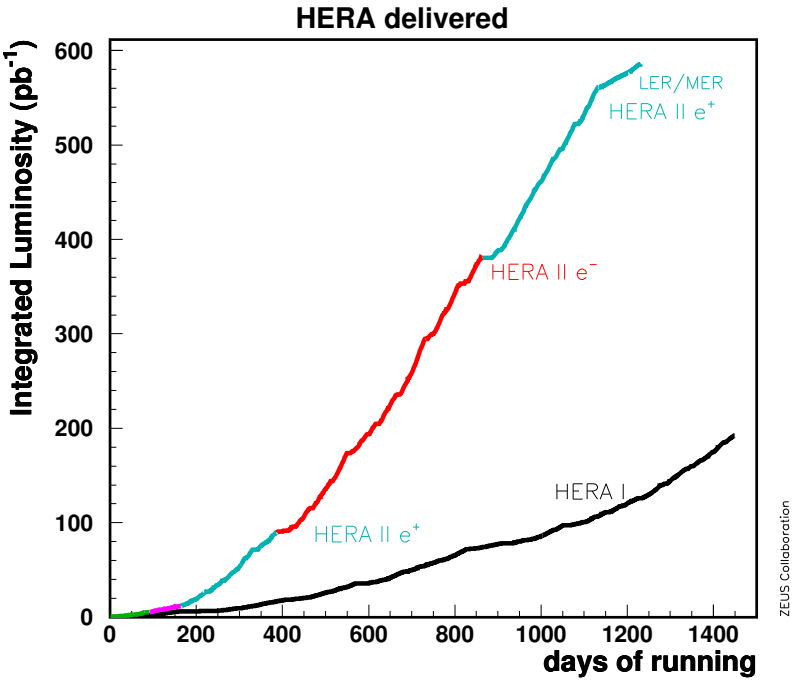

Figure 2.2: Integrated luminosity delivered by HERA as function of time, before (HERA I) and after (HERA II) the upgrade.

Fig. 2.2 shows the evolution of the integrated luminosity delivered by HERA with time. In total, the H1 and ZEUS experiments collected a set of *ep* collision data which corresponds to an integrated luminosity of 0.5 fb^{-1} per experiment.

2.3 The ZEUS Detector

The ZEUS detector [71–74] was a multi-purpose detector, covering almost the full 4π geometry, to study various aspects of ep scattering. The emphasis was put on optimising the calorimetry for hadronic measurements. The dimensions of the detector were $12 \times 11 \times 20$ m^3, the detector weight was 3600 tons. The detector is described in detail in [74].

The layout of the detector is shown in Figs. 2.3 in transverse and 2.4 in longitudinal sections. A right-handed Cartesian coordinate system is used at ZEUS, with origin at the nominal interaction point, the Z axis pointing in the direction of the proton beam, and the X axis pointing to the centre of the HERA ring.

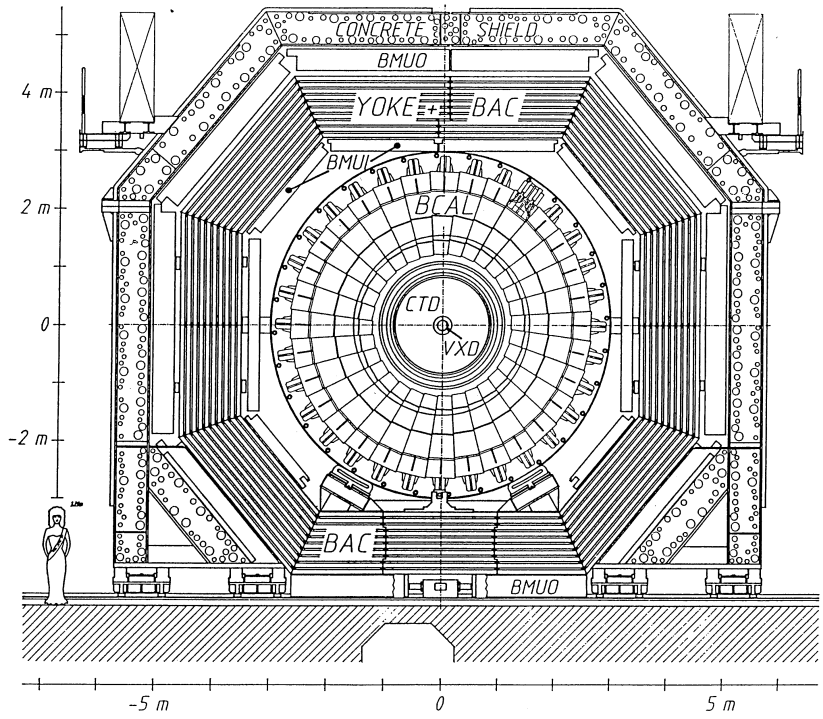

Figure 2.3: Cross section of the ZEUS detector perpendicular to the beam direction.

Due to the large asymmetry in electron and proton beam energies, most of the energy flow of the products of ep scattering is directed close to the proton beam direction. Therefore, the ZEUS detector was designed to be asymmetric, with more detecting material in the forward region than in the backward direction.

The essential elements, from innermost to outermost, are: a microvertex (MVD, from 2003) or vertex detector (VXD, before 1996), a central tracking detector (CTD), a straw tube tracker (STT, from 2003), and planar drift chambers (FTD, RTD) in the field of a thin magnetic solenoid; an electromagnetic (EMC) and a hadronic calorimeter (HAC),

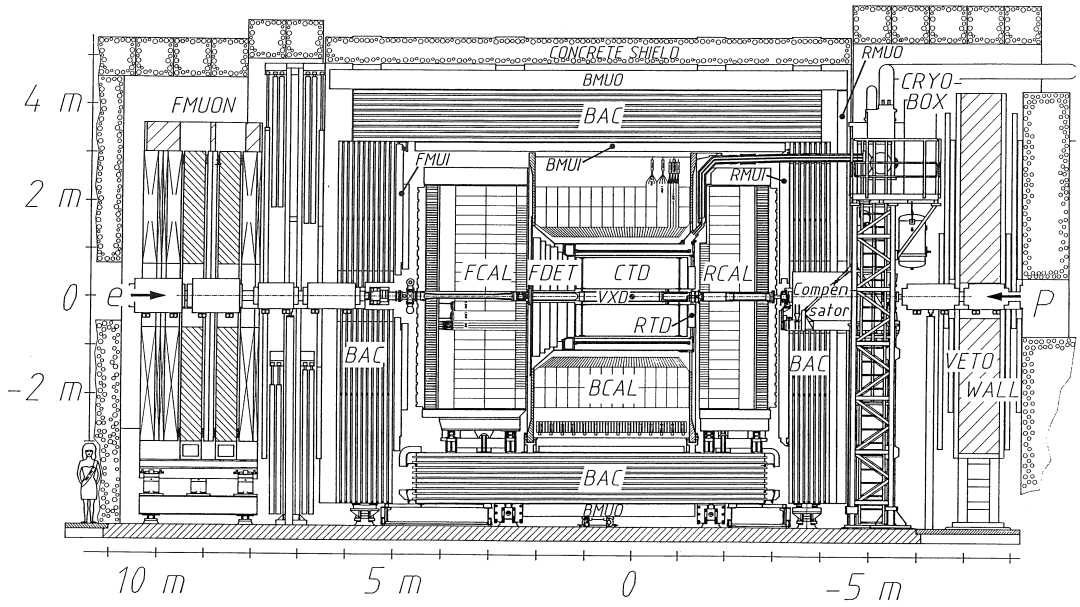

Figure 2.4: View of the ZEUS detector along the beam direction.

divided into barrel (BCAL), forward (FCAL) and rear (RCAL) parts (they are named with respect to the proton beam direction); a backing calorimeter (BAC), and muon detectors (BMUI, BMUO, RMUI, RMUO, FMUI, FMUO). In addition, photon and electron taggers located near the beam line were used for the luminosity measurement.

The microvertex detector was installed in 2001 and allowed for improved primary and secondary vertex reconstruction. Between the CTD and the barrel calorimeter, a thin superconducting solenoid coil was located, which in the inner region of the CTD produced an axial magnetic field of 1.43 T. The magnetic field allowed positively and negatively charged particles to be distinguished and the momentum measurement of charged particles. The backing calorimeter BAC was used to measure the energy of those showers which leak from the CAL. It could also distinguish between muons and hadron showers. High energy muons, which travel through CAL and BAC, were registered with the dedicated inner and outer barrel (BMUI, BMUO), forward (FMUI, FMUO) and rear (RMUI, RMUO) muon chambers. The luminosity measuring system was located outside the detector at around $Z \sim -100$ m.

In the following, the main components important for the analyses of this thesis are briefly described.

2.3.1 High Resolution Uranium Calorimeter

The CAL [75–78] is a critical part of the ZEUS detector and plays the most significant role in the analyses presented here.

High-energy particles traversing matter produce a cascade or *shower* of secondary particles of lower energy. Electromagnetic particles (e^+, e^-, γ) produce showers via e^+e^- pair production and bremsstrahlung processes, producing secondary e^+, e^- and photons, which undergo further pair production and bremsstrahlung processes. This continues until the energy of the secondary particles is low enough to lose all their energy by ionisation and absorption. The electromagnetic absorption power of matter is characterised by the *radiation length*, X_0, which is the mean distance over which a high-energy electron loses all but $1/e$ of its energy. In contrast, showers produced by hadrons arise mainly due to interaction with the nuclei of the matter they traverse, via the strong nuclear force. Such an interaction typically gives rise to multiple secondary particles, primarily pions, which proceed to develop a hadronic shower. The mean distance travelled by a hadron in matter before undergoing an inelastic nuclear interaction is called *nuclear interactions length*, λ. As a consequence of these different mechanisms, hadrons require significantly more matter to be absorbed than electrons. The showering by the incident particles is exploited by the ZEUS calorimeter to measure their energy. The shape of the electromagnetic shower is also used to identify isolated photons.

The calorimeter for the ZEUS detector was designed to give the best possible resolution for the measurement of hadronic jets and to give equal response to electrons and hadrons ($e/h = 1$). An $e/h = 1$ ratio helps to minimise the systematic error in the energy measurement of the hadronic system and to optimise the hadronic energy resolution. The equal response is achieved with depleted uranium as absorber material. Alternating layers of absorber plates with thickness of 3.3 mm and plastic scintillator with thickness of 2.6 mm were used.

The key features of the calorimeter performance were:

- ratio of response of electrons to hadrons: $e/h = 1.00 \pm 0.05$;
- hermeticity with almost full solid angle coverage (99.8% in the forward hemisphere and 99.5% in the backward hemisphere);
- energy measurement with a resolution of $18\%/\sqrt{E} \oplus 1\%$ for electrons and $\sigma(E)/E = 35\%/\sqrt{E} \oplus 2\%$ for hadrons, where E denotes energy in GeV and $\oplus$ is the quadratic sum;
- calibration of absolute energy scale to 2%;
- angular resolution for jets better than 10 mrad;
- hadron-electron separation for both isolated electrons and electrons in jets.

The CAL completely surrounds the solenoid and the tracking detectors as shown schematically in Figure 2.5. Mechanically the calorimeter is divided into three components: forward (FCAL), barrel (BCAL) and rear (RCAL). The structure of the components is similar. They are subdivided longitudinally into two parts. The inner part

constitutes the electromagnetic calorimeter (EMC) with a depth of ~ 25 X_0 ($\sim 1\lambda$) that is read out as one section. The outer part is called the hadronic calorimeter (HAC). It varies in depth from $\sim 6\lambda$ in the very forward direction to $\sim 3\lambda$ in the rear. In FCAL and BCAL the HAC is read out in two sections ($2 \times 3\lambda$ for FCAL, $2 \times 2\lambda$ for BCAL); in the RCAL there is only one HAC section with a depth of 3λ.

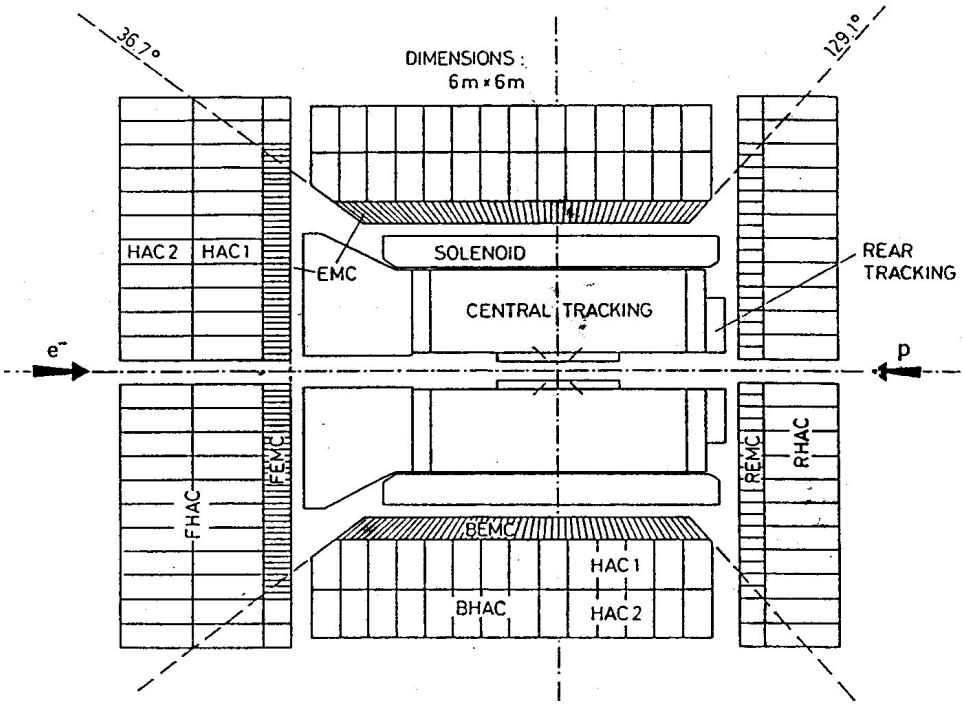

Figure 2.5: Schematic view of the ZEUS calorimeter.

In the following the barrel calorimeter, which was used for isolated photon detection, is described in more detail.

2.3.2 The Barrel Calorimeter

The BCAL [76] covers the region between $\theta = 36.7°$ and 129.1° in polar angle and 360° in azimuth. It is made of 32 wedge-shaped modules each spanning 11.25° in azimuth, and arranged coaxially with the beam, as shown in Figure 2.6. The modules extend from an inner radius $R_I = 1232$ mm to an outer radius $R_O = 2912$ mm from the beam axis. The outer radius of the active volume is 2296 mm. Each module is rotated by 2.5° around an axis parallel to the beam axis and located at a radius of 2309 mm. Such a rotation ensures that the wavelength shifter plates do not point to the beam axis, thus preventing photons from escaping undetected in the gap between modules.

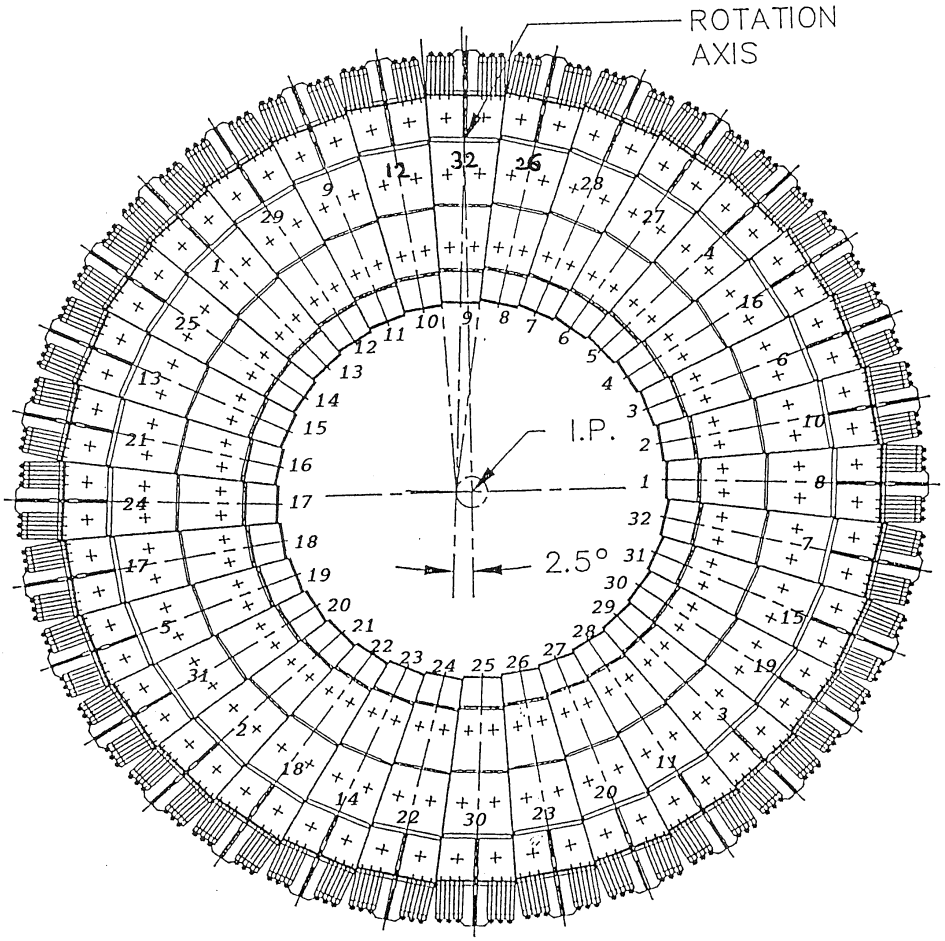

Figure 2.6: Cross section of the BCAL. The electron beam direction is into the paper.

The modules are segmented in depth into EMC, HAC1 and HAC2 sections as shown in Fig. 2.7(a). The EMC section consists of 53 towers, projective in polar angle (Fig. 2.7(b)), with front face dimensions of 5×20 mm^2. Each section contains 21 depleted Uranium plates and 22 layers of scintillator. The 14 HAC towers are non-projective, containing 49 depleted Uranium plates and 50 layers of scintillator. The total depth of the BCAL corresponds to 5 interaction lengths for normal incidence. Each EMC tower is also called a *cell*, while each HAC tower is subdivided into 2 cells (HAC1 and HAC2). Each cell was read out with two photomultipliers, connected to the cell with a wavelength shifter.

The natural radioactivity of the uranium plates, providing a stable and time independent reference signal, was used to calibrate CAL.

The angular coverage as well as some other characteristics of BCAL, FCAL and RCAL are summarised in Table 2.1.

Shower separation

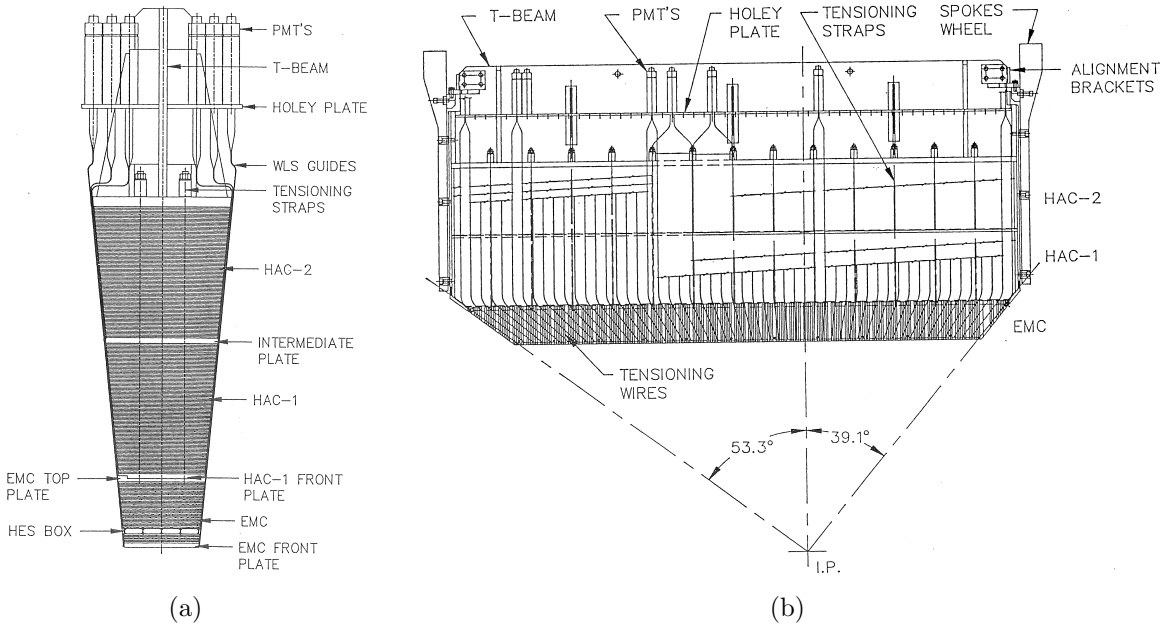

(a) (b)

Figure 2.7: Transverse (a) and longitudinal (b) cross section of a BCAL module.

The shape of the electromagnetic shower registered in the CAL can be used to identify isolated photons. The width of the electromagnetic shower is described with the *Molière radius*, R_M, which is proportional to X_0 and depends on the atomic number of the matter traversed. R_M has the meaning of the radius of a cylinder containing 90% of the energy of the shower. The value of R_M for the ZEUS BCAL, $R_M \approx 20$ mm [79], is smaller than the face dimensions of the BCAL EMC. This means that if a photon hits near the centre of a cell, its energy will be deposited mainly within this cell. The energy will however be deposited in neighbouring cells, if a photon hits near their common boundary. One of the main difficulties of isolated single photon measurements is to distinguish them from the daughter photons from neutral meson decays, mainly $\pi^0 \to \gamma\gamma$. The opening angle between the two photons, for a typical π^0 energy of 5 GeV, is 1.55°. When they reach BCAL, which is about 1.2 m away from the nominal interaction point, the displacement of points of registering these two photons will be 3.2 cm. Clearly, the probability to leave their energy in a single cell will be smaller than that for an isolated photon. Thus, the shower shape profile can be used to separate signal events from background.

2.3.3 The Central Tracking Detector and the Microvertex Detector

The CTD [80–83] was a cylindrical wire chamber located around the nominal interaction point. The chamber axis was coincident with the beam axis. The active volume of the

	FCAL	BCAL	RCAL
Angular coverage	$2.2° < \theta < 39.9°$	$36.7° < \theta < 129.1°$	$128.1° < \theta < 176.5°$
Pseudorapidity coverage	$1.01 < \eta < 3.82$	$-0.74 < \eta < 1.1$	$-3.49 < \eta < -0.72$
Maximal depth, cm	152.5	105.9	87.0
Maximal depth, λ	7.14	4.92	3.99
Maximal depth, X_0	181.0	129.0	103.0
Cell front face dimensions, cm^2	5×20	49×233	10×20
Number of electromagnetic cells	1056	1696	511
Number of hadronic cells	1116	896	642

Table 2.1: Properties of different sections of the ZEUS calorimeter.

CTD extended from $z = -100$ cm to $z = 105$ cm and from 18.2 cm to 79.4 cm in radius, with a polar angular coverage of 7.5 to 170 degrees. The CTD was located inside a superconducting solenoid which provides a 1.43 T axial magnetic field. The purpose of the CTD was to measure the momenta of charged particles, to provide dE/dx information to enhance particle identification and to provide information for the ZEUS trigger system.

The chamber was filled with an $Ar/CO_2/C_2H_6$ gas mixture at atmospheric pressure with a small addition of water vapour. The CTD was organised into 9 superlayers, which contained in total 4608 sense wires. Five of the superlayers had wires parallel to the chamber axis (0° wires) and four had small angle (about 5°) stereo wires which allow an accurate offline track measurement, see Fig. 2.8. The stereo information from the CTD provides an accurate measurement of the hit position, 1.4 mm in the Z direction, and around 280 μm in the XY-plane. For the trigger, however, a z-by-timing technique was exploited (measurement of the z-coordinate using the time difference of the signals arriving at different ends of the wire), which is much faster and gives a resolution along Z of approximately 4 cm. Such information for the trigger allows the discrimination against events with vertices lying outside the nominal electron-proton interaction region (collisions with gas in the beam pipe).

The dE/dx measurement resolution was at the level of 10%. For particles with measured hits in all 9 superlayers, the transverse momentum resolution during the years 1992-2000 was $\sigma(p_T)/p_T = 0.0058p_T \oplus 0.0065 \oplus 0.0014/p_T$, with p_T in GeV. Here the first term corresponds to the resolution of the hit position measurements, while the second and the third term arise from multiple scattering within and before the CTD, respectively.

The ZEUS microvertex detector (MVD) [84] was installed between the beam pipe and the inner radius of the CTD during the HERA I to HERA II upgrade. It replaced the VXD, which was taken out before the 1996 running (the VXD is shown in Figs. 2.3, 2.4). The MVD, which was a silicon strip vertex detector, was installed to extend the tracking acceptance, to improve the primary and secondary vertex reconstruction and to enhance the tagging capabilities for short lived particles. The barrel part of the detector was

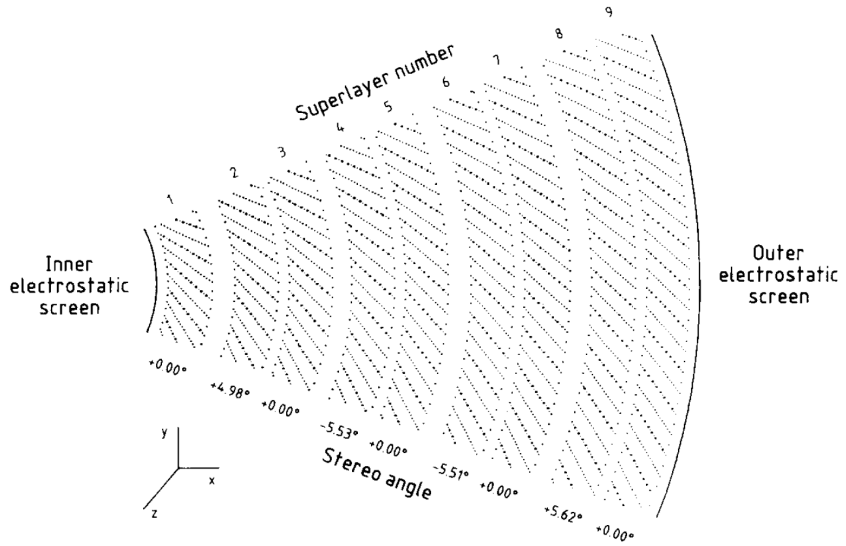

Figure 2.8: Layout of wires in the Central Tracking Detector in a 45° sector. The sense wires are indicated by the larger dots. The wire positions are shown at the end plates.

a 64 cm long cylinder with three layers of silicon sensors arranged around an elliptical beam pipe, as shown in Figure 2.9. The forward part of the MVD consisted of four disks perpendicular to the beam axis, with two sensor layers per disk. In total over 200k channels were read out, with a total silicon sensitive area of 2.9 m^2.

The MVD allowed the achievement of an impact parameter resolution of about 100 μm. The track transverse momentum resolution using combined information from the CTD and MVD, for tracks passing all 9 CTD superlayers, was $\sigma(p_T)/p_T = 0.0029p_T \oplus 0.0081 \oplus 0.0012/p_T$, with p_T in GeV.

2.3.4 The Luminosity System

The instantaneous luminosity, $\mathcal{L}$, is one of the most important characteristics of the accelerator. It is proportional to how frequently a process with a given cross section occurs. Thus, the number of events observed for a given process is:

$$N = \sigma \cdot L = \sigma \cdot \int \mathcal{L} dt, \tag{2.1}$$

where σ is the cross section of the process and L is the integrated luminosity.

The instantaneous luminosity for two oppositely directed beams of electrons and protons is given by the formula

$$\mathcal{L} = f \frac{N_e N_p}{A}, \tag{2.2}$$

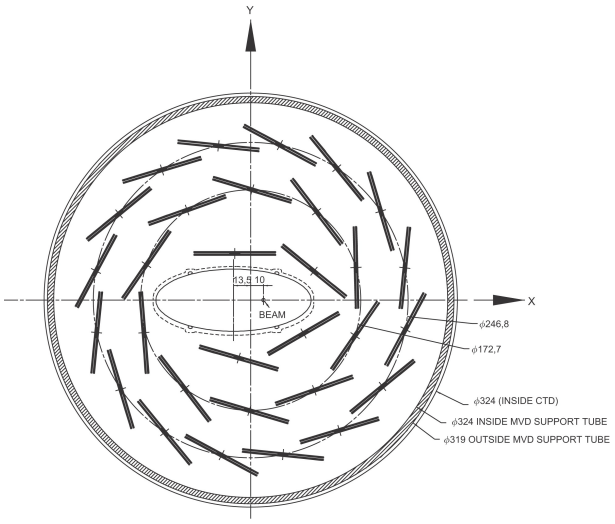

Figure 2.9: Layout of the silicon sensors in the barrel MVD, transverse cross section.

where N_e and N_p are the numbers of particles per bunch for the electron and proton beams, respectively, f is the bunch crossing frequency, and A is the cross-sectional area of the beams, assuming them to overlap completely. The formula demonstrates, that the luminosity can be increased for example by stronger focusing of the beams (reducing A), or by enlarging the beam currents. For the HERA upgrade, the first method was mainly exploited.

In practice, cross sections are measured experimentally by counting events and using equation 2.1. Thus, the accurate measurement of the luminosity is of great importance for any cross section measurement.

At ZEUS the luminosity was determined by the measurement of the event rate of the well known Bethe-Heitler process $ep \to ep\gamma$ (so-called *bremsstrahlung*), the cross section of which is high (~ 300 mb) and known with an accuracy of about 0.5%. For this measurement, the Photon Calorimeter (PCAL) [85] and the Spectrometer (SPEC) [86] were used.

The PCAL was a lead-scintillator sampling detector installed at $z = -107$ m. It measured the bremsstrahlung photons that escaped the beam pipe through a copper-beryllium window at $z = -92.5$ m.

During the HERA I to HERA II upgrade, the instantaneous luminosity was increased from 1.5×10^{31} cm^{-2}s^{-1} (very close to the original design luminosity) to 5×10^{31} cm^{-2}s^{-1}, which led to an increase of the bremsstrahlung photon rate and to an increase of synchrotron radiation. To reduce the impact of synchrotron radiation on the PCAL, additional carbon absorber blocks were installed in front of it. The SPEC detector was also installed, which allowed a permanent comparison of two independent measurements of the luminosity by two devices and helped to reduce systematic uncertainties. The SPEC

consisted of two electromagnetic calorimeters, which measured the electron-positron pair, originating from the conversion of the bremsstrahlung photon in the window of the beam pipe. The electron-positron pair was spatially split by the magnetic field of a dipole, and both particles were individually measured by two calorimeters. The layout of the ZEUS luminosity system for the HERA II period is shown in Figure 2.10. Using the information from the PCAL and the SPEC, the luminosity was measured with a systematic uncertainty of 1.7% [87].

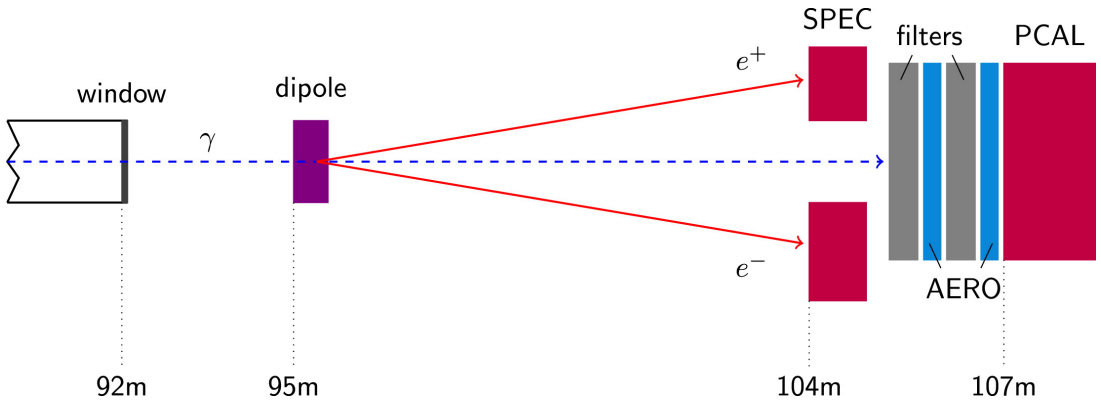

Figure 2.10: Layout of the ZEUS luminosity measurement system for HERA II. The distances are with respect to the nominal interaction point, in the negative Z direction.

2.3.5 Trigger System and Data Acquisition

In ZEUS the proton and electron bunches crossed every 96 ns, which corresponds to a 10.4 MHz rate. At the original design luminosity, the rate of ep scattering events that needed to be stored was several hundred Hz (this is the rate for photoproduction scattering, where the exchanged photon is almost real and cross sections are high. For DIS ep events, the rate was in the order of a few Hz). The rate of background interactions, such as beam gas interactions or beam halo interactions with the limiting apertures, was however much larger, of the order of $50 - 100$ kHz. The maximum rate at which events can be written to tape, was about $5 - 10$ Hz at an average event size of about 100 KB.

To select the relevant ep events, a sophisticated three level trigger system [88–91] was used at ZEUS. A schematic overview is shown in Fig. 2.11. Effective handles against background were the determination of the interaction vertex (as described in subsection 2.3.3) and signatures in the calorimeter.

All of the data in the ZEUS data acquisition system (DAQ) for each bunch crossing were pipelined for ~ 5 μs (the trigger processing was therefore *deadtimeless*), while the First Level Trigger (FLT) calculations were being performed (fast, but with reduced accuracy) and the FLT signal was propagated back to the subdetector. Only if the

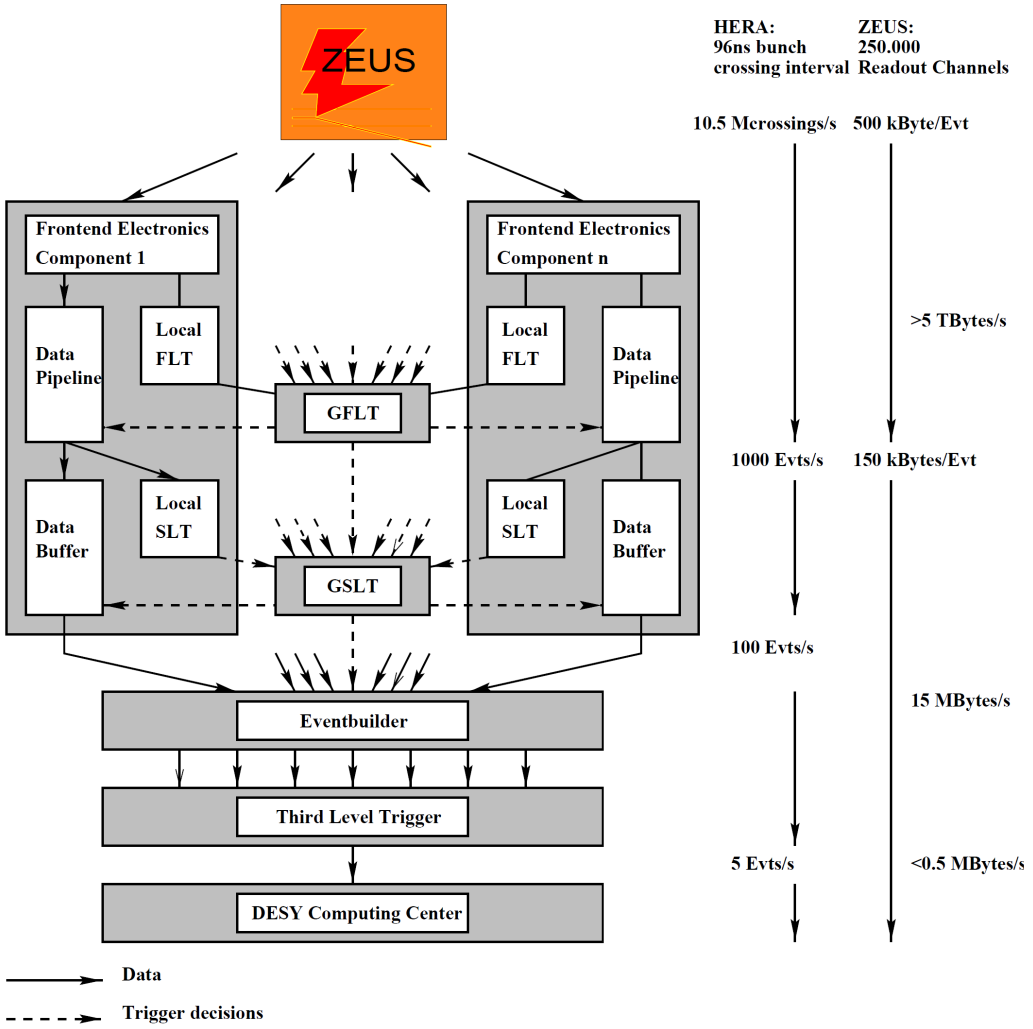

Figure 2.11: The ZEUS trigger.

event was accepted, was a small (15 μs) dead time induced in the readout to allow the components to stop the pipelines and move the data from the pipelines into the primary readout buffers. The maximum rate of the FLT accept decision was set to 1 kHz. Each detector subsystem had its own FLT, generating the information, while the decision logic was handled centrally by the Global FLT (GFLT).

The Second Level Trigger (SLT) was designed to reduce the rate from 1 kHz to 100 Hz. At this stage an array of microprocessors analysed the fully digitised data. Detailed information, such as vector energies, clustering (jet and isolated electron searches) was generated and tracking with momentum reconstruction was performed. The quantities computed were sent to the Global Second Level processor (GSLT), which made the de-

cision whether to accept the event. The GSLT had two logical decision layers. The first applied a set of vetoes to reject background events, for example, by using the time of the event reconstructed by the CAL (beam-gas events produced upstream of the detector have a different time with the respect to events from the vertex). The second layer applied a set of physics filters, designed by the physics groups.

The Third Level Trigger (TLT) used a computer farm to fully reconstruct the events and to reduce the event rate to a few Hz. Its logic was similar to the logic of the SLT: apply vetoes and physics filters. As events from the GSLT were already very clean, the TLT mainly selected the desired types of physics events. If the event was accepted by the TLT, the data were stored on tape for further offline reconstruction and analysis.

2.4 ZEUS Detector Simulation

To measure the cross section of some process, the detector response to this type of process must be known. The detector response is modelled using Monte Carlo methods. First, the interaction of the incoming particles is modelled by an event generator. The output of the event generator, which is a list of particles and their 4-momenta, is then used as input to a full simulation of the ZEUS detector.

The flow of the simulated and real data is shown in Figure 2.12.

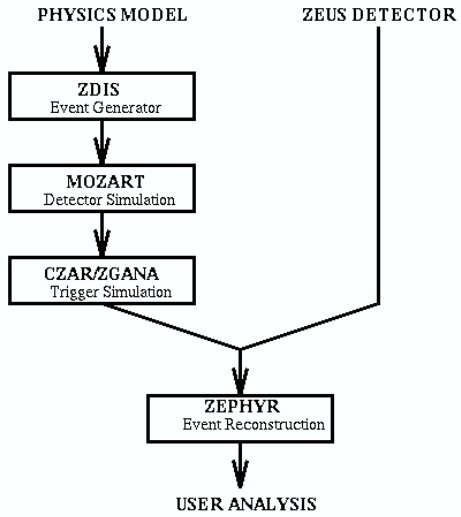

Figure 2.12: Simulated and real data flow diagram at ZEUS.

All components of the ZEUS detector were modelled using the GEANT [92] program (versions 3.13 and 3.21 for simulation of the detector for HERA I and HERA II periods, respectively). The full simulation of the ZEUS detector is called MOZART (Monte Carlo for Zeus Analysis, Reconstruction and Trigger) and includes:

- simulation of the geometry (shape, material and position of each component),
- internal generation of simple events for testing,
- propagation of particles through the whole detector taking account of processes such as particle decay, energy loss, multiple scattering and the effect of the magnetic field.

The trigger logic was simulated with the CZAR (Complete Zgana Analysis Routines) program, which is a combination of the ZGANA (ZEUS GEANTAnalysis) program, simulating the first and second level triggers, and the TLTZGANA program, simulating the third level trigger. The code for TLTZGANA is largely identical to the online code that was running during data taking.

After modelling the ZEUS response, the data were transmitted to the ZEPHYR (ZEUS Physics Reconstruction) program, which performs the reconstruction in the same way as for real data. The ZEPHYR output is available for processing with the same analysis software as used for the real data.

Chapter 3

Analysis Tools and Techniques

This Chapter gives a description of the tools and methods used in this thesis. After the explanation of event reconstruction in the ZEUS detector, a brief overview of the Monte Carlo methods used is given. Finally, methods related to the proton PDF fit are reported.

3.1 Event Reconstruction

3.1.1 Electron Identification

The accurate identification of the scattered electron in the detector is important for the reconstruction of the Neutral Current DIS variables in many *ep* collision analyses. In this thesis, electron candidates identified with the *Sinistra* algorithm [93] were used.

The Sinistra algorithm utilises the neural network approach for particle identification based on their showering properties in a segmented calorimeter. Its aim is to best identify electromagnetic particles using only the information from the uranium-scintillator calorimeter (CAL) of the ZEUS detector and to separate them from single hadrons or jets of particles for which the pattern of energy deposits in the CAL often looks quite similar especially at low energies. The algorithm first performs clustering of the CAL cells, to merge cells which belong most likely to the shower of a single particle. It is based on the idea of islands of energy, consisting of a peak of energy deposition surrounded by lower energy deposits. A selection is then applied, to reject obvious non-electromagnetic clusters (for example, clusters with a relatively large fraction of energy deposited in the hadronic sections of the CAL were rejected). Clusters contained transversely within a window of 3×3 towers were considered. Each cluster which passed the preselection cuts is now characterised by 54 values of the energy deposits in the photomultipliers (PMTs) and by the polar angle of incidence of the particles. These 55 variables were used by the neural network to assign a probability $P(e|\text{cluster})$ to each cluster, where $P(e|\text{cluster})$ is close to 1 for electromagnetic clusters and close to 0 for hadronic clusters.

In the ZEUS analyses presented in this thesis, the electron candidate with the largest probability was always assumed to be the scattered DIS electron.

3.1.2 Kinematic Reconstruction of DIS variables

While the kinematics of a DIS event is described by any two of the variables x, y, Q^2, W, the experiment measures the energy and the scattering angle of the electron, and the energy and momentum of the hadronic final state. The reconstruction of DIS variables from the experimentally measured ones can be done with different methods [21]. The methods used in the analyses presented here, are described below.

Electron method.

$$Q^2 = 2E_e E'_e(1 + \cos\theta_e), \tag{3.1}$$

$$y = 1 - \frac{E'_e}{2E_e}(1 - \cos\theta_e), \tag{3.2}$$

$$x = \frac{Q^2}{sy}. \tag{3.3}$$

Here, E_e and E'_e are the energies of the electron before and after scattering, respectively, and θ_e is the polar angle of the scattered electron. The weakness of this method is a seriously degraded x resolution at small y and large radiative corrections. The resolution is however very good at large y.

Double angle method. This method relies on the electron polar angle θ_e and the angle $\gamma_{\rm had}$ which characterises the hadronic final state and is defined via

$$\cos\gamma_{\rm had} = \frac{p^2_{t,\rm had} - \delta^2_{\rm had}}{p^2_{t,\rm had} + \delta^2_{\rm had}},\ \delta_{\rm had} = \sum_i E_i(1 - \cos\theta_i) = E_{\rm had} - p_{z,\rm had}. \tag{3.4}$$

Here E_i and θ_i are the energy and the polar angle of the i-th particle, respectively, and the sum runs over all objects of the final state excluding the electron. $E_{\rm had}$, $p_{t,\rm had}$ and $p_{z,\rm had}$ are the energy, transverse and longitudinal momenta of the final state system excluding the electron.

When these two angles are determined, the x and Q^2 variables are expressed as

$$Q^2 = 4E_e^2 \frac{\sin\gamma_{\rm had}(1 + \cos\theta_e)}{\sin\gamma_{\rm had} + \sin\theta_e - \sin(\theta_e + \gamma_{\rm had})}, \tag{3.5}$$

$$x = \frac{E_e}{E_p} \frac{\sin\gamma_{\rm had} + \sin\theta_e + \sin(\theta_e + \gamma_{\rm had})}{\sin\gamma_{\rm had} + \sin\theta_e + \sin(\theta_e - \gamma_{\rm had})}. \tag{3.6}$$

This reconstruction method has the advantage that it does not require a precise knowledge of the energy scales. It also results in small radiative corrections. However, the resolution is poor if y is very small.

Jacquet-Blondel method.

The method relies entirely on the hadronic system:

$$y = \frac{\delta_{\text{had}}}{2E_e}, \tag{3.7}$$

$$Q^2 = \frac{p_{t,\text{had}}^2}{1-y}, \tag{3.8}$$

$$x = \frac{Q^2}{sy}. \tag{3.9}$$

This method is stable against energy losses down the forward beam pipe since they contribute very little to y or p_t^2. However, it is sensitive to calorimeter noise at very small y and is sensitive to energy losses in the rear direction at higher values of y. It also requires a good understanding of energy scales and energy losses in inactive material. On the other hand, it is rather insensitive to radiative corrections. Since the Jacquet-Blondel method does not require the explicit detection of the final state lepton, it is also suited for Charged Current events and (for the reconstruction of y) for photoproduction events.

3.1.3 Jet Reconstruction

Different methods of the reconstruction of jets are possible with the ZEUS detector. The methods used in this thesis are described here.

- **Calorimeter Cells.** This method follows the one used in [94] and was used for the dijet measurement. The smallest calorimeter units are the so-called "cells" (see Section 2.3.1). After removing cells associated with the scattered electron candidate, minimum cell energy thresholds of $E_{\text{EMC cell}} > 0.05$ GeV and $E_{\text{HAC cell}} > 0.1$ GeV were required for the electromagnetic and hadronic cells, respectively, to suppress calorimeter noise. Cells with energies greater than 1.5 GeV were removed from the analysis if the energy difference between two photo-multipliers of the cell exceeded 90% of the total cell energy. This cut suppressed signals due to high-voltage discharges. Using the energy and position of the cells, a massless 4-momentum was assigned to each cell which passed the selection criteria. The list of these 4-vectors was used as an input to the jet clustering algorithm.

- **ZEUS Unidentified Flying Objects (ZUFOs).** This method was adopted for the isolated photon analysis, since it more easily allows the identification of the isolated photon candidate. The formation of ZUFOs [95] (referred to as Energy Flow

Objects, EFOs, in ZEUS publications) uses all the track and calorimeter information in a given event to build up a complete picture of the energy and charge flow.

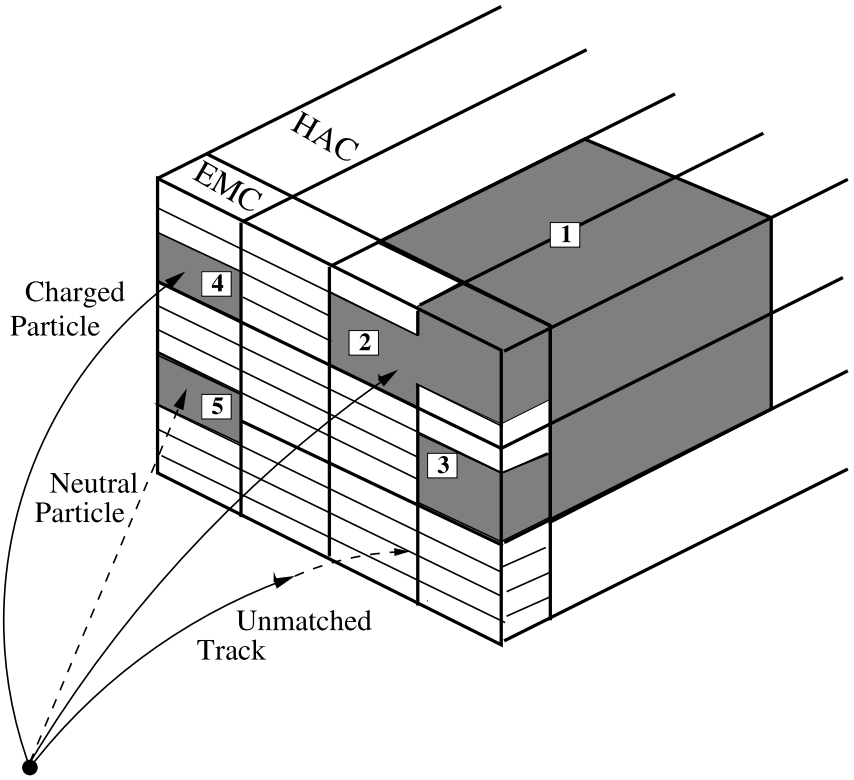

Figure 3.1: Formation of ZUFOs

The construction of ZUFOs is done in several steps. First, adjacent[1] cells in the EMC, HAC1 and HAC2 sections are clustered separately into cell islands, see Fig. 3.1. After that, the islands of the EMC and HAC sections are merged into 3-dimensional cone islands. In the next step "good" charged tracks are extrapolated to the inner surface of the calorimeter and associated with cone islands. Good tracks are those fitted to the primary vertex and which traverse at least four superlayers of the CTD; their transverse momentum must be in the range $0.1 < p_T < 20$ GeV. The maximum p_T is increased to 25 GeV for tracks which passed more than 7 superlayers. The track matches an island if the distance of closest approach is less than 20 cm, or if the distance of closest approach is less than the maximum radius of the island on the plane perpendicular to a ray drawn from the vertex to the island. The outcome of this operation are groups of matched track(s) and island(s). Finally, for each group the decision of which energy flow information to use has to be made,

[1]The "nearest neighbourhood" algorithm is used, which means that diagonal connections are not considered

i.e. from the calorimeter or from the tracking system. Depending on the matching information, a ZUFO type is assigned for each group. Different possibilities are summarised in Table 3.1. For the isolated photon candidates, ZUFOs of type 31 were used, which correspond to calorimeter islands with no associated tracks.

ZUFO type	Description	# tracks	# islands	Detector used
0	Unmatched track	1	0	CTD
1	1-to-1 match	1	1	CTD
2	2-to-1 match	2	1	CTD
3	3-to-1 match	3	1	CTD
12	1-to-2 match	1	2	CTD
22	2-to-2 match	2	2	CTD
30	Some track match	> 0	1	CAL
31	Unmatched island	0	1	CAL
37	1-to-2 match	1	2	CTD and CAL
41	1-to-1 match	1	1	CTD and CAL

Table 3.1: Different ZUFO types

The output of the energy flow algorithm is a set of ZUFOs. A four-momentum is assigned to each ZUFO, which can be used as input to the jet clustering algorithm.

3.2 Monte Carlo Simulations

The simulation of the relevant physics processes and of the detector response to them is an essential part of the analyses at high energy accelerators. The information provided by simulations is used to calculate the acceptance of the detector, i.e., how efficiently it registers particles, and to correct data for detector effects, like accounting for inactive material or backsplash corrections.

The term 'Monte Carlo' refers to the use of random number generators for the modelling of stochastic processes.

The simulation of data for the ZEUS experiment is done in two steps. First, the collision of particles is simulated with the so-called event generators. Then, the final state particles are passed through a full simulation of the ZEUS detector. While the simulation of the ZEUS detector was already described in subsection 2.4, this section gives a description of the simulation of particle collisions. Thus, subsection 3.2.1 illustrates the generation of the short-distance phenomena and subsection 3.2.2 describes the different hadronisation models used.

3.2.1 Monte Carlo Generators

The Monte Carlo event generators used in this thesis, are based on LO QCD calculations of the matrix elements. The higher order contributions are approximated via different methods, such as the *parton-shower approach* or the *colour-dipole model*, described here.

Final state parton shower algorithms [96] begin with the generation of the kinematics of the basic process, performed with a probability proportional to its LO partonic cross section, which is interpreted physically as the inclusive cross section for the basic process, followed by an arbitrary sequence of *small-angle* splittings. A probability is then assigned to each splitting sequence. Thus, the initial LO cross section is partitioned into the cross sections for a multitude of final states of arbitrary multiplicity. The sum of all these partial cross sections equals that of the primary process. This property of the parton showers reflects the KLN cancellation mentioned earlier in Section 1.3.3, and is also called "unitarity of the shower process". Shower algorithms include all leading-logarithmic corrections. In the dominant, strongly ordered region, subsequent splittings are separated by increasingly large times and distances, and this suppresses interference effects. For the *initial state*, parton showering is controlled by the evolution equations (in the leading log approximation) via a backward evolution algorithm [97]. Backward evolution is needed since the dominant logarithmic region is the collinear one, where virtualities become larger and larger in absolute value with each emission, thus the highest virtualities have to be considered first. The parton showering is thus derived from perturbative QCD by keeping only the dominant real and virtual contributions to the cross section.

An alternative formulation of QCD cascades, proposed in [98], focuses upon soft emissions, rather than collinear, as the basic splitting mechanism. It then becomes natural to consider a branching process where it is a parton pair (i.e. *a dipole*) rather than a single parton, that emits a soft parton. It is therefore called the dipole model.

For the measurement of dijets at high Q^2, following the analysis of [94], the neutral current DIS events were used as generated by the HERACLES [99] program with the DJANGOH [100] interface to the hadronisation programs of LEPTO [101] or ARIADNE [102], which implement the parton shower and the colour dipole models, respectively. The LEPTO Monte Carlo simulation was used for the extraction of the cross sections, while the ARIADNE program was used for cross checks. The HERACLES program includes radiative QED corrections such as initial- and final-state radiation, vertex and propagator terms and two-boson exchange. These QED corrections may influence the reconstruction of the event kinematics and, thus, have to be taken into account in order to describe the data. The DJANGOH program also allows the matrix element options of LEPTO to be used.

In the photon + jet analysis presented here, the same MC samples were used as in [79] (where they were used for the measurement of inclusive photon production)[2]. Signal events containing photons radiated by quarks ("QQ photons", Section 1.5), were

[2]Additional background and LL Monte Carlo events were however generated, to reduce statistical fluctuations of the MC distributions

generated with the PYTHIA event generator [103], which uses the parton shower approach to simulate final state QCD radiation. Only events containing QQ photons were simulated, while neither hard LL photons nor ISR/FSR were simulated in this sample.

The signal LL photon events were extracted from the inclusive DIS MC sample, by identifying high-p_T LL photons using parton level information. The inclusive DIS sample was prepared with the LO matrix elements by LEPTO, the QED corrections were calculated by HERACLES, and the matrix elements were interfaced by DJANGOH to the ARIADNE program. The background Monte Carlo events were those of the inclusive DIS sample after extracting events with LL photons.

3.2.2 Hadronisation

Hadronisation denotes the process by which a set of coloured partons (after showering) is transformed into a set of colour-singlet primary hadrons which can subsequently decay further. Since a first-principles solution to the relevant dynamics is absent (non-perturbative regime!), event generators use QCD-inspired phenomenological models to describe this transition.

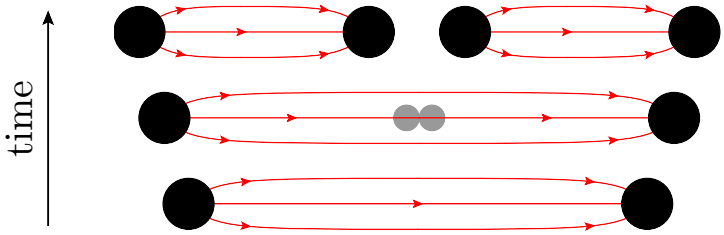

Figure 3.2: Quark pair creation in the string model [8].

For all Monte Carlo events used for the analyses presented here, the *Lund string model* [104–106] was used for the hadronisation, as implemented in the JETSET [107] program. In this model, two colour-charged quarks are connected via a colour field with each other, Fig 3.2. As the charges move apart, a potential $V(r) = kr$ is reached for large distance r (at short distances, there is a Coulomb term as well, but this is neglected in the Lund string). This potential describes a string with tension $k \sim 1$ GeV/fm ~ 0.2 GeV^2. As the string grows, the non-perturbative creation of quark-antiquark pairs can break the string via the process $q\bar{q} \to q\bar{q}' + q'\bar{q}$, illustrated in Fig 3.2. The procedure repeats until the available energy is too small for further $q\bar{q}$-pair creation.

In the following, the available information after the hadronisation procedure is called "hadron level", whereas the information directly after the parton cascade modelling and before the hadronisation is called "parton level". The fixed-order calculations (see next section) provide predictions for the partonic cross sections, therefore these predictions are also referred to as parton level predictions.

3.3 Fixed-Order Calculations

The approach of fixed-order QCD calculations was discussed in Sec. 1.3.2. During its practical implementation, difficulties arise due to soft and collinear QCD divergences. Although they are cancelled in the calculations, they have to be properly treated numerically by the computer programs. NLO calculations combine virtual one-loop corrections with the real emission contributions from unresolved partons. These two parts are usually computed separately and each is infrared divergent, while their sum is infrared finite. These infrared singularities have to be eliminated before any numerical integration can be done. There are two types of methods to effect this cancellation. The *phase space slicing* method [108–111] is based on approximating the matrix elements and the phase space integration measure in boundary regions of phase space so integration may be carried out analytically. The *subtraction method* [112–114] is based on adding and subtracting counter terms designed to approximate the real emission amplitudes in the phase space boundary regions on the one hand, and to be integrable with respect to the momentum of an unresolved parton. There exist two general formulations of the subtraction method. One is the residue approach [115], the other is the dipole formalism [116].

The phase space slicing method and the subtraction method were compared in [117] for heavy quark production in the process $\gamma^* \to Q\bar{Q}$. It was shown that the dipole method, while involving additional analytical work, is superior in efficiency and accuracy.

3.3.1 The Program NLOJet++

For the prediction of the dijet cross sections, the NLOJET++ program [118, 119] was used. NLOJET++ utilises the dipole subtraction method to cope with the appearance of divergences. The dijet cross sections were calculated to $\mathcal{O}(\alpha_s^2)$. The calculations were made in the $\overline{\text{MS}}$ renormalisation and factorisation schemes, while the number of flavours was set to five. The factorisation scale was set to $\mu_F = Q$, and the renormalisation scale was set to $\mu_R^2 = Q^2 + \overline{E}_{T,B}^{2}{}^3$, where $\overline{E}_{T,B}$ is the average transverse energy in the Breit frame of the final state partons forming the dijet or trijet system. The theoretical calculations were performed using the CTEQ6.6 parameterisation [120] of the proton PDFs. The strong coupling constant was calculated at two loops, corresponding to $\alpha_s(M_Z) = 0.118$. The k_t cluster algorithm was applied to the generated partons in the event, to obtain jet cross section predictions.

3.3.2 Theoretical Predictions for Isolated photon production

The EPGJET program [121] was used for NLO calculation of the photon plus jet cross sections to order $\mathcal{O}(\alpha^3\alpha_s)$. The calculation was performed with the help of the phase

[3] The choice of the scales was changed for the proton PDF fit which uses the dijet cross sections presented in this thesis.

space slicing method, with which it is straightforward to introduce the photon isolation requirement. The contributions from quark-to-photon fragmentation is included in the calculations and is described in terms of the quark-to-photon and gluon-to-photon fragmentation functions. HERAPDF1.0 [122] parton distribution functions for the proton were used for the calculation. The factorisation and renormalisation scales were equal to $\mu_F = \mu_R = \sqrt{Q^2 + (p_T^{\text{jet}})^2}$.

The predictions from S.P. Baranov et al. [123] (BLZ) make use of the so-called k_T factorisation approach and are based on the off-shell partonic amplitude $eq^* - > e\gamma q$, where the photon radiation from the leptons as well as from the quarks is taken into account. The unintegrated quark densities in a proton are determined using the Kimber-Martin-Ryskin prescription [124]. The predictions give a quark-radiated contribution that is enhanced relative to the leading-order collinear approximations. The uncertainties of the predictions were of the order of 20%, due mainly to the procedure of selecting jets from the evolution cascade in the k_T factorisation approach.

3.3.3 Fast NLO Calculations

The NLO calculations for the jet cross sections usually take a significant amount of time, which is not appropriate for the proton PDF fit, where many iterations are needed to be done and the cross sections are recalculated at each iteration. However, once the phase space of the measurement and binning are defined, it is possible to accelerate the NLO calculation process, by exploiting the factorisation property of the cross sections (Sec. 1.3.5). Thus, the hard scattering part can be precalculated and stored in the so-called tables of perturbative coefficients, which can be used together with arbitrary PDFs and values of α_s. To calculate the cross sections, the only thing needed is to convolve the perturbative coefficients with the PDFs, and, if needed, multiply by the coupling constant. The general idea behind the preparation of the table of perturbative coefficients lies in representation of the $\alpha_s(\mu_R)$ and the PDFs by their values at the 3-dimensional grid in x and μ_F and μ_R (calculated in points $\mu_{R,k}$, x_l, $\mu_{F,m}$ where $k = 1, ..., k_{max}$, $l = 1, ..., l_{max}$, $m = 1, ..., m_{max}$ and k_{max}, l_{max} and m_{max} represent the number of points in the corresponding dimension of the grid), whereas PDFs at arbitrary x and μ_F and α_s at arbitrary μ_R are obtained by interpolation. Thus, the PDF for the flavour i ($i = u, \overline{u}, d, \overline{d}, s, \overline{s}, c, \overline{c}, b, \overline{b}, t, \overline{t}, g$)) times α_s will read:

$$\alpha_s(\mu_R) \cdot f_i(x, \mu_F) \approx \sum_{k,l,m} \alpha_s(\mu_{R,k}) \cdot f_i(x_l, \mu_{F,m}) \cdot e^{(l)}(x) \cdot b_R^k(\mu_R) \cdot b_F^{(m)}(\mu_F), \qquad (3.10)$$

where $e^{(l)}(x)$, $b_R^k(\mu_R)$, $b_F^{(m)}$ are interpolation functions for the x, μ_R and μ_F dependence, respectively.

After that, all information of the perturbatively calculable piece (but excluding α_s and

PDFs) is fully contained in the quantity

$$\tilde{\sigma}_{n,i,k,l,m} = c_{n,i}(x, \mu_R, \mu_F) \otimes \left[e^{(l)}(x) \cdot b_R^k(\mu_R) \cdot b_F^{(m)}(\mu_F) \right]. \tag{3.11}$$

while the cross section becomes a sum of products:

$$\sigma \approx \sum_{n,i,k,l,m} \tilde{\sigma}_{n,i,k,l,m} \alpha_s^n(\mu_{R,k}) \cdot f_i(x_l, \mu_{F,m}). \tag{3.12}$$

The coefficients $\tilde{\sigma}_{n,i,k,l,m}$ need to be calculated only once, while during the fit only their convolution with the PDFs is performed.

Nowadays, basically, two projects exist which provide tools for fast fixed order calculations: FastNLO [125–127] and APPLGrid [128], which differ by the interpolation procedure and by the approach of storing the μ_F and μ_R dependence (APPLGrid allows the calculation of the theoretical predictions for arbitrary factors in front of μ_F, μ_R, while FastNLO allows only predefined values of these factors).

3.4 A HERAPDF Approach to Proton PDF Fits

A significant part of this thesis is devoted to the simultaneous fit of α_s and proton PDFs to collider data. Although obtaining the PDFs is not a goal of this thesis, the evolution of the PDFs depends on α_s, therefore if α_s running is varied during the fit, it should be accounted for by a corresponding change of the PDFs. Therefore, PDFs have to be fitted together with α_s and the parameters of its running.

Since the DGLAP evolution equations provide a connection between different μ_F values, at which PDFs are calculated, it is enough to parametrise the PDFs as a function of x at some starting scale $\mu_{F,0}$. The functional form of the parametrisation is not a priori known, therefore it can be chosen almost freely. In practice, the parameterisation is often chosen so that PDFs are zero at the boundary $x = 1$. The freedom of the choice of functional form however has to be addressed in the evaluation of the systematic uncertainties of the PDFs.

During the fit, the PDF parameters are varied and predictions are recalculated accordingly at each iteration and compared to the experimentally measured quantities (cross sections and/or structure functions) until the best description of the data is achieved. In this thesis, a minimum χ^2 method is used to obtain the best parameters of the PDFs, in a form as implemented in the HERAFitter program. This section gives a brief overview of HERAFitter, followed by description of the proton PDF fit procedure used in HERAPDF.

3.4.1 The HERAFitter Framework

HERAFitter [129, 130] is a QCD fit platform for the determination of PDFs and some parameters of the Standard Model by fits to the world high energy experiments data. Measurements of lepton-proton DIS data and of proton-(anti)proton colliders data are included currently in the HERAFitter package. They include inclusive DIS cross sections, jet and heavy quark production in ep DIS, Drell-Yan processes in pp and $p\overline{p}$ collisions, top-quark and jet production in pp and $p\overline{p}$ collisions.

Different computational techniques for the fixed order calculations can be used within HERAFitter, like a k-factor technique or fast grid techniques; the latter were discussed in Section 3.3.3. k-factors are defined as the ratio of the prediction of a higher-order (slow) QCD calculation to a lower order (fast) calculation. The k-factors have to be computed once for a given PDF with the time consuming higher-order code, before the PDF fit. However, the k-factors can be PDF-dependent, therefore after the fit they have to be re-evaluated and the fit has to be redone. The procedure may need to be repeated until input and output k-factors converge.

The HERAFitter platform allows different treatments of heavy quarks for the calculation of the proton structure functions. In fact, all options discussed in Section 1.3.6 are available.

Different parameterisation styles of the PDFs can be chosen and different representation of the χ^2 function are possible within HERAFitter. The latter, depending on the provided uncertainties and their correlation, include a covariance matrix representation (experimental uncertainties are given in a form of covariance matrix), a nuisance parameter representation (provided that systematic uncertainties are separated by sources) and a mixed-form representation (for example, when bin-to-bin statistical correlations are given in the form of a covariance matrix and the correlated systematic uncertainties are separated by sources). The systematic uncertainties can be treated as additive or multiplicative.

Apart from the DGLAP evolution equations, other evolution models are implemented in HERAFitter, like dipole models or CCFM evolution (for transverse momentum dependent PDFs).

All together they make HERAFitter a very powerful tool, which is well suited for tests of the Standard Model and beyond.

3.4.2 PDF Parameterisation

In the HERAPDF approach, PDFs are parametrised at the input scale by the generic form [122]

$$xf(x) = Ax^B(1-x)^C(1+\epsilon\sqrt{x}+Dx+Ex^2). \tag{3.13}$$

The parametrised PDFs are the gluon distribution xg, the valence quark distributions xu_v, xd_v, and the up-type and down-type anti-quark distributions, $x\overline{U}$, $x\overline{D}$. Here $x\overline{U} = x\overline{u}$,

$x\overline{D} = x\bar{d} + x\bar{s}$ at the chosen starting scale, which has to be below the charm threshold for VFN schemes.

For the HERAPDF1.0 fit [122], which used inclusive DIS HERA I data only, the optimal parametrisation[4] was obtained with the ϵ, D and E parameters set to zero, except E_{u_v}:

$$xg(x) = A_g x^{B_g}(1-x)^{C_g}, \tag{3.14}$$

$$xu_v(x) = A_{u_v} x^{B_{u_v}}(1-x)^{C_{u_v}}\left(1 + E_{u_v}x^2\right), \tag{3.15}$$

$$xd_v(x) = A_{d_v} x^{B_{d_v}}(1-x)^{C_{d_v}}, \tag{3.16}$$

$$x\bar{U}(x) = A_{\bar{U}} x^{B_{\bar{U}}}(1-x)^{C_{\bar{U}}}, \tag{3.17}$$

$$x\bar{D}(x) = A_{\bar{D}} x^{B_{\bar{D}}}(1-x)^{C_{\bar{D}}}. \tag{3.18}$$

The parameters $B_{\bar{U}}$ and $B_{\bar{D}}$ were set equal,

$$B_{\bar{U}} = B_{\bar{D}}, \tag{3.19}$$

such that there is a single B parameter for the sea distributions. The strange quark distribution is expressed as x-independent fraction, f_s, of the down-type sea, $x\bar{s} = f_s x\bar{D}$ at Q_0^2. The further constraint

$$A_{\bar{U}} = A_{\bar{D}}(1 - f_s), \tag{3.20}$$

together with the requirement (3.19), ensures that $x\bar{u} \to x\bar{d}$ as $x \to 0$. The valence B parameters were also set equal,

$$B_{u_v} = B_{d_v}. \tag{3.21}$$

Additionaly, the momentum sum rule constrained sum of the fractional momenta of all partons of the proton to 1:

$$\int_0^1 \left[\sum_i (q_i(x) + \bar{q}_i(x)) + g(x)\right] x dx = 1, \tag{3.22}$$

and the quark-number sum rules constrained the number of valence u and d quarks to 2 and 1, respectively:

$$\int_0^1 u_v(x)dx = 2, \quad \int_0^1 d_v(x) = 1. \tag{3.23}$$

[4]The optimal parameterisation means that adding more parameters does not lead to significant improvement in the fit quality.

Thus, there are 16 parameters of the PDFs in (3.14)-(3.18) and six constraints of these parameters (3.19)-(3.23). Together they make 10 fit parameters.

The optimal parameterisation for the preliminary HERAPDF2.0 fit [131] was found to be

$$xg(x) = A_g x^{B_g}(1-x)^{C_g} - A'_g x^{B'_g}(1-x)^{C'_g}, \tag{3.24}$$

$$xu_v(x) = A_{u_v} x^{B_{u_v}}(1-x)^{C_{u_v}} \left(1 + D_{u_v} x + E_{u_v} x^2\right), \tag{3.25}$$

$$xd_v(x) = A_{d_v} x^{B_{d_v}}(1-x)^{C_{d_v}}, \tag{3.26}$$

$$x\bar{U}(x) = A_{\bar{U}} x^{B_{\bar{U}}}(1-x)^{C_{\bar{U}}}(1 + D_{\bar{U}} x), \tag{3.27}$$

$$x\bar{D}(x) = A_{\bar{D}} x^{B_{\bar{D}}}(1-x)^{C_{\bar{D}}}. \tag{3.28}$$

The C'_g parameter was set to 25, and the constraint (3.21) was dropped. For the preliminary HERAPDF2.0 fits the number of fit parameters was 15.

The functional form of the χ^2 function can be found in [132].

Chapter 4

Dijet production at high Q^2

The jet cross section measurements play significant role in the α_s running tests. The jet cross sections measured at different colliders (HERA, Tevatron, LHC) and in different regions of the phase space are sensitive to α_s at broad range of energies. This chapter presents as an example a measurement of dijet production at high virtualities of the exchanged boson, made with the ZEUS detector at HERA. The measurement was done within a framework of so-called second analysis[1]. First analysis was performed by Joerg Behr and published in his PhD thesis [94]. The measured dijet cross sections were published by the ZEUS collaboration in 2010 [133]. The cross sections were included to the HERAPDF proton PDF fit and were used in the α_s running tests discussed in this thesis.

4.1 Event selection

The data used for this analysis were collected by the ZEUS detector during 1998-2000 and 2004-2007, when HERA was operating with protons of energy $E_p = 920$ GeV and electrons or positrons of energy $E_e = 27.5$ GeV (see Chapter 2). The data correspond to an integrated luminosity of 374 pb^{-1}, of which 203 pb^{-1} are electron data.

The high-Q^2 Neutral Current DIS events occur via the exchange of a photon or Z^0 boson between the electron and struck parton of the proton. Among these events, events containing at least two jets were selected, for which the cross section at leading order is proportional to α_s. The dijet measurement therefore can provide a test of the perturbative QCD and can potentially be used for the extraction of an $\alpha_s(M_Z)$ value.

All the selection criteria were applied to both data and to MC simulations at detector level. At hadron and parton level as well as for the theoretical predictions only those criteria were applied which define the phase space of the measurement. The theoretical

[1]The idea of second independent analysis is extensively used in the ZEUS experiment, to reduce probability of mistakes

predictions were obtained with the program NLOJET++ (described in Section 3.3.2) and cross checked with the DISENT program [116].

4.1.1 Phase Space

The kinematic phase space for the DIS events was chosen as follows:

- Events with high virtualities of the exchanged boson, Q^2, were selected:

$$125 < Q^2 < 20\,000 \text{ GeV}^2. \tag{4.1}$$

  At such large boson virtualities, the experimental and theoretical uncertainties are small and thus, use of the large HERA data sample can provide powerful physical constraints.

- The inelasticity, y, was required to be in the range

$$0.2 < y < 0.6, \tag{4.2}$$

  where the lower limit was chosen to reject a region with large hadronisation corrections and the higher limit rejects high-y events, for which the acceptance is typically small [94].

The dijet phase space was defined by following criteria:

- The jets were defined by the k_T cluster algorithm in the longitudinally invariant inclusive mode, applied to the final state objects in the Breit reference frame. The final state objects were assumed to be massless. The jet variables were defined according to the Snowmass convention [134].

- The two leading jet transverse energies in the Breit frame were required to be greater than

$$E_{T,\mathrm{B}}^{\mathrm{jet}} > 8 \text{ GeV}. \tag{4.3}$$

  The presence of two high-transverse energy jets in the Breit frame is an indication of a strong interaction in the event.

- The pseudorapidities of these two jets were required to be in the range

$$-1 < \eta_{\mathrm{LAB}}^{\mathrm{jet}} < 2.5. \tag{4.4}$$

- In addition, the invariant mass of the dijet system, M_{jj}, was required to be greater than

$$M_{\mathrm{jj}} > 20 \text{ GeV}. \tag{4.5}$$

  This cut was introduced to make the NLO QCD predictions for dijet production insensitive to infrared gluon radiation.

4.1.2 Inclusive DIS Event Selection

The Q^2, x_{Bj} and y variables were reconstructed with the Double-Angle method (see Section 3.1.2), since it provides the best resolution and the smallest bias over the full investigated phase space region [94]. Apart from the cuts on Q^2_{DA} and y_{DA} described in the previous subsection, several additional requirements were imposed to increase the purity of the selected DIS data sample:

- **Trigger.** A three-level trigger system was used to select events online (see Section 2.3.5). At the third level, NC DIS events were accepted on the basis of the identification of a scattered-electron candidate using localised energy deposits in the CAL. At the second level, charged-particle tracks were reconstructed online by using the ZEUS global tracking trigger which combined information from the CTD and MVD. These online tracks were used to reconstruct the interaction vertex and reject non-ep background. At the first level, only coarse calorimeter and tracking information was available. Events were selected, using criteria based on the energy and transverse energy measured in the CAL. Starting from the year 2004, additional tracking requirements were introduced to adapt the trigger rates to the higher instantaneous luminosity.

- **Data quality.** The status of all detector components was recorded for every run separately. The so-called "EVTAKE" algorithm has decided offline whether a run could be used for physics analyses. In this analysis, only runs with "EVTAKE" equal to 1 were considered.

- **The vertex position** along the beam axis, z_{vtx} was in the range that was given by the nominal vertex position plus/minus three times the width of the vertex distribution approximated by a Gaussian. Both the nominal vertex position and the width of the distribution varied between different data taking periods. The selection criteria are given in Table 4.1.

Period	lepton beam	requirement on z_{vtx}
1998-2000	e^+, e^-	$-34 < z_{\mathrm{vtx}} < 34$ cm
2004-2005	e^-	$-32 < z_{\mathrm{vtx}} < 30$ cm
2006-2007	e^+	$-29 < z_{\mathrm{vtx}} < 27$ cm

Table 4.1: Applied cuts on the vertex position along the Z axis

- **An electron candidate** was required to be found by the Sinistra algorithm (Sec. 3.1.1) with probability at least 90% and energy $E'_e > 10$ GeV. This cut suppresses background from photoproduction events in which the scattered electron escapes down

the beampipe and a false electron candidate is reconstructed instead. Furthermore, the requirement on energy ensured a high and well understood electron-finding efficiency. The total energy not associated with the electron candidate within a cone of radius 0.7 units in the pseudorapidity-azimuth ($\eta - \phi$) plane around the electron direction was required to be less than 10% of the electron energy, in order to reject events in which part of a jet was falsely identified as the scattered electron.

Moreover, if an electron candidate was registered in the acceptance region of the CTD, a matched CTD track was required. In this case, coordinates and scattering angles of the electron were reconstructed from the associated track, since the angular resolution of the tracking detectors was in general better that the angular resolution of the CAL.

- **Transverse momentum balance.** To remove cosmic-ray events and beam-related background, it was required that

$$\frac{P_{T,\mathrm{miss}}}{\sqrt{E_T}} < 2.5 \text{ GeV}^{1/2}, \tag{4.6}$$

where $P_{T,\mathrm{miss}}$ is the missing transverse momentum as measured with the CAL and E_T is the total transverse energy in the CAL.

- **Longitudinal momentum conservation.** Photoproduction events and events with large initial-state radiation were removed by applying condition

$$38 < (E - P_Z) < 65 \text{ GeV}, \tag{4.7}$$

where $E = \sum_i E_i$ is the total energy, and $P_Z = \sum_i p_{Z,i}$ is the Z-component of the momentum of the final state particles. The sum runs over all clusters of energy deposits in the CAL.

Further requirements were also applied as described in the [94], which typically had a marginal effect on the result. They included for instance the rejection of the Compton scattering events, and the rejection of events in which an electron was registered in regions of the CAL that are poorly described by Monte Carlo simulations.

Figure 4.1 shows control distributions (comparison of data and Monte Carlo distributions) of some of DIS event variables, for data taken in 2004-2006. Control plots for other data taking periods look similar.

4.1.3 Inclusive Jet Selection

The k_t cluster algorithm, described in Sec. 1.4, was applied to the CAL cells after excluding those associated with the scattered electron candidate. The jet search was performed in

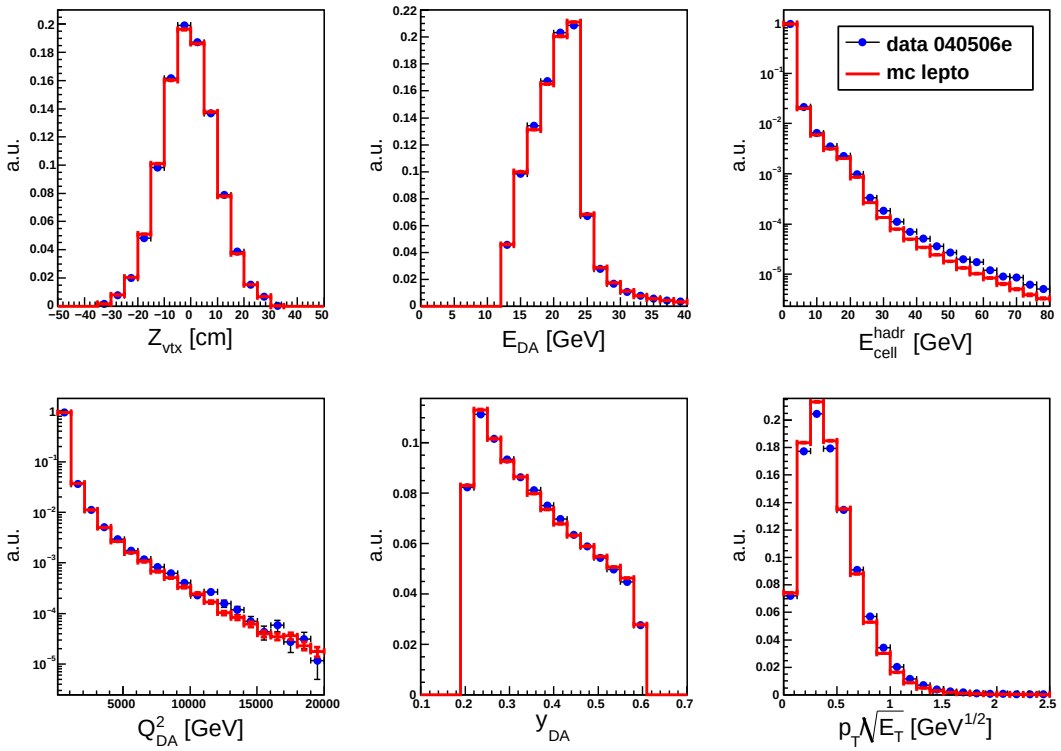

Figure 4.1: Comparison of data and Monte Carlo model predictions for inclusive DIS variables.

the $\eta - \phi$ plane of the Breit frame (Sec. 1.4). After reconstructing the jet variables in the Breit frame, the massless four-momenta were boosted into the laboratory frame. Energy corrections were then applied to the jets in the laboratory frame and propagated into the transverse jet energy in the Breit frame, to compensate for energy losses in the inactive material in front of the CAL.

The following criteria were applied to select a clean sample of high-Q^2 DIS jet events:

- Events were removed from the sample if the distance ΔR between any of the jets and the electron candidate in the $\eta - \phi$ plane of the laboratory frame was smaller than 1, $\Delta R = \sqrt{(\eta^{\rm jet}_{\rm LAB} - \eta^e)^2 + (\phi^{\rm jet}_{\rm LAB} - \phi^e)^2} < 1$. This requirement helps to improve the purity of the sample.

- Events were removed from the sample if a jet was in the backward region of the detector, $\eta^{\rm jet}_{\rm LAB} < -1$. This requirement removed events in which a radiated photon from the electron was misidentified as a jet in the Breit frame.

- The transverse energy of the jets in the laboratory frame was required to be greater

than $E^{\text{jet}}_{T,\text{LAB}} > 3$ GeV. This cut removed a small number of jets for which the uncertainty on the energy correction was large.

The dijet selection was performed by applying the dijet cuts described in Section 4.1.1 to the inclusive DIS jet event sample. Figure 4.2 shows control distributions (comparison of data and Monte Carlo distributions) of dijet variables, for data taken in 2004-2006. Control plots for other data taking periods look similar.

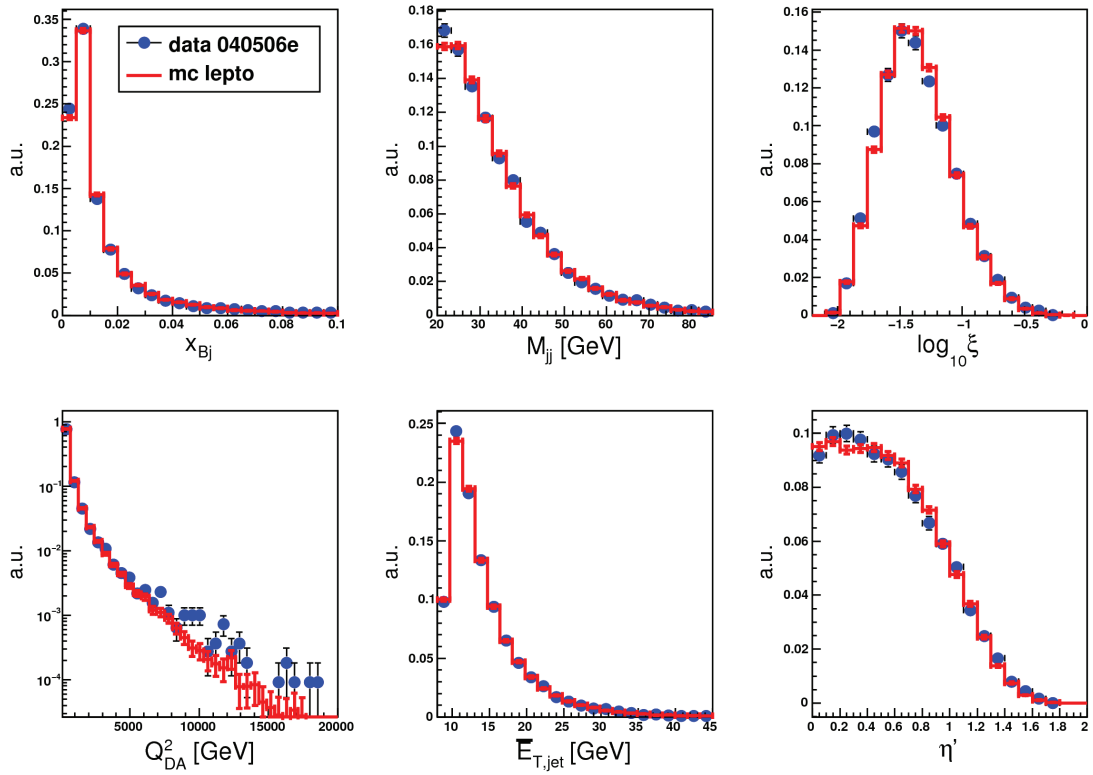

Figure 4.2: Comparison of data and Monte Carlo model predictions for dijet variables.

4.2 Corrections

Several corrections were applied to Monte Carlo and data before extracting the cross sections. The corrections were imposed for different reasons:

- Monte Carlo events were used for the determination of the bin-by-bin factors correcting detector level data to the hadron level (acceptance correction). For this approach to be valid, the uncorrected distributions of the data must be well described by the MC simulations. This condition was satisfied by both ARIADNE and

LEPTO, after reweighting the z_{vtx} and Q^2 distributions of the MC simulations to make them agree with the data and after correction of the trigger track veto efficiency of the MC, which poorly described those of the data before the correction. These corrections were defined in [94] and adopted for this analysis.

- The jet energy scale correction needed to be applied to MC simulations. This correction was obtained from an additional dedicated study of single jet events, where the scattered electron is balanced by the jet. The electron energy provided an approximately independent energy scale to correct the hadronic energy scale. This correction was performed independently in this analysis and in [94], the results agreed well.

- Additionally, a correction of the jet energies was performed, to account for inactive material which particles pass on their way to the calorimeter. The corrections were extracted using the hadron and detector level of the MC simulations, and were applied to both data and Monte Carlo. The corrections were extracted independently in this analysis and in [94], the results agreed well.

- The lepton beam in HERA was polarised, while the NLO QCD predictions don't take into account lepton beam polarisation. Since the inclusive DIS cross section depends on the polarisation, it was decided to correct the data in to be able to compare them with the predictions. The dedicated corrections were obtained with the HECTOR program [135], which allows to calculate predictions for the inclusive DIS cross sections σ_{pol} and σ_{nopol} for polarised and unpolarised lepton beams, respectively. The ratio $\sigma_{\text{nopol}}/\sigma_{\text{pol}}$ as function of Q^2 was used as data-event weights. After this correction, the data correspond to unpolarised lepton beams. This correction was described in [94] and adopted from there.

- The Monte Carlo sample used for the acceptance correction included higher-order QED processes, like initial- and final-state radiation, internal loops and running of α_{em}. In contrast, theoretical predictions did not included QED corrections. Therefore the data were corrected for QED effects.

  The MC simulations included QED effects. Hence, correction factors were obtained by using a second MC sample generated without these effects. The bin-by-bin QED correction factors were calculated as ration between MC predictions including higher-order QED effects, σ_i^{QED}, and QED Born Monte Carlo cross sections, σ_i^{Born}: $C_i^{\text{QED}} = \dfrac{\sigma_i^{\text{Born}}}{\sigma_i^{\text{QED}}}$. This correction was described in more details in [94] and adopted from there.

Theoretical predictions were corrected for hadronisation and electroweak effects [94].

4.3 Results

The single-differential[2] inclusive cross section of the observable X in bin i is obtained using the expression

$$\frac{d\sigma}{dX} = \frac{N_i}{L \cdot \Delta X_i} \cdot C_i^A \cdot C_i^{\mathrm{QED}}, \tag{4.8}$$

where N_i is the number of selected data events, L is the integrated luminosity of the data sample, ΔX_i is the bin width, C_i^A is the acceptance correction and C_i^{QED} is the correction accounting for the QED effects. The acceptance correction is defined as the ratio of the number of selected MC events on hadron level, N_i^{had}, and the corresponding number on detector level, N_i^{det}, in bin i:

$$C_i^A = \frac{N_i^{\mathrm{had}}}{N_i^{\mathrm{det}}}. \tag{4.9}$$

The acceptance corrections typically varied between 1.2 and 1.4.

The statistical uncertainty δ^{stat} of $d\sigma/dX$ was calculated with the error propagation method, taking into the account statistical uncertainties of the number of selected events, ΔN_i, and the statistical uncertainties of the acceptance correction, ΔC_i^A:

$$\delta_i^{\mathrm{stat}} = \sqrt{\left(\frac{\Delta N_i}{L \cdot \Delta X_i} \cdot C_i^A \cdot C_i^{\mathrm{QED}}\right)^2 + \left(\frac{N_i}{L \cdot \Delta X_i} \cdot \Delta C_i^A \cdot C_i^{\mathrm{QED}}.\right)^2} \tag{4.10}$$

The quantity ΔN_i was calculated as $\Delta N_i = \left(\sum_j w_j^2\right)^{1/2}$, where w_j is the weight of event j.

4.3.1 Systematic Uncertainties

The systematic uncertainties were estimated in [94] and are briefly listed here:

- the uncertainty on the absolute energy scale of the jet was estimated to be ±1% for $E_{T,\mathrm{LAB}}^{\mathrm{jet}} > 10$ GeV and ±3% for lower $E_{T,\mathrm{LAB}}^{\mathrm{jet}}$ values. The resulting uncertainty on the cross sections was about ±4% and increased to approximately ±6% in certain regions of the dijet phase space;
- the uncertainty in the absolute energy scale of the electron candidate was estimated to be ±1% [136] (±2% [137]) for the data from the years 1998–2000 (2004–2007). The resulting uncertainty was below ±1%;
- the differences in the results obtained by using either ARIADNE or LEPTO to correct the data for detector effects were typically below ±5%;

[2] A similar definition can be found for double differential cross sections.

- the analysis was repeated using an alternative technique [138] to select the scattered-electron candidate. The resulting uncertainty was typically below $\pm 1\%$;
- the $E_{T,\mathrm{LAB}}^{\mathrm{jet}}$ cut was changed to 2 and 4 GeV. The resulting uncertainty was mostly smaller than $\pm 1\%$;
- the uncertainty due to the selection cuts was estimated by varying the values of the cuts within the resolution of each variable. The effect on the cross sections was in general below $\pm 2\%$;
- the combined, luminosity-weighted systematic error on the polarisation measurement was 3.9%. The effect on the cross sections was negligible;
- the simulation of the first-level trigger was corrected in order to match the measured efficiency in the data. The systematic effect on the cross sections was typically less than 1%.

4.3.2 Single-Differential Cross Sections

The measurements of the single-differential inclusive dijet cross sections are presented in Figs 4.3 to 4.5 as functions of several kinematic and dijet variables. Single-differential cross sections are shown for Q^2, x_{Bj}, the mean transverse jet energy in the Breit frame of the two jets, $\overline{E_{T,\mathrm{B}}^{\mathrm{jet}}}$, the dijet invariant mass, M_{jj}, the half-difference of the jet pseudorapidities in the Breit frame, η^*, and the logarithm of the variable ξ. The variables Q^2 and x_{Bj} were defined in Section 1.2, while the variables $\overline{E_{T,\mathrm{B}}^{\mathrm{jet}}}$, M_{jj}, η^* and ξ were defined in Section 1.4. The data are compared to NLO QCD calculations. The relative differences between the measured differential cross sections and the NLO QCD calculations are also shown.

The single-differential dijet cross sections $d\sigma/dQ^2$ and $d\sigma/dx_{\mathrm{Bj}}$ are shown in Figs 4.3(a) and 4.3(b). The cross section $d\sigma/dQ^2$ has total experimental systematic uncertainties of the order of 5% (7%) at low (high) values of Q^2. The total theoretical uncertainty is of the order of 7% (4%) at low (high) Q^2.

For the cross section $d\sigma/dx_{\mathrm{Bj}}$, most of the data points have experimental uncertainties of less than 5%, and also the precision of the theory predictions is better than 5% over most of the x_{Bj} range.

Figures 4.4(a) and 4.4(b) show the single-differential dijet cross sections $d\sigma/d\overline{E_{T,\mathrm{B}}^{\mathrm{jet}}}$ and $d\sigma/dM_{\mathrm{jj}}$. These measurements are particularly well suited for testing the matrix elements in the perturbative calculations. Mean transverse jet energies $\overline{E_{T,\mathrm{B}}^{\mathrm{jet}}}$ (dijet invariant masses M_{jj}) of up to 60 GeV (120 GeV) are reached with this measurement. At the largest values of $\overline{E_{T,\mathrm{B}}^{\mathrm{jet}}}$ (M_{jj}), experimental uncertainties of 8% (5%) are achieved; for smaller values, the uncertainties are even smaller. The theoretical uncertainties are approximately constant over the range studied and are of the order of $(5-7)\,\%$.

The differential dijet cross-section as a function of η^* is shown in Fig. 4.5(a). The experimental uncertainties are always below 5%, the total theoretical uncertainty is also typically around 5%. The theoretical predictions for the last two η^* bins were removed from the plot due to infrared sensitivity.

The cross-section $d\sigma/d\log_{10}(\xi)$ (Fig. 4.5(b)) has similar uncertainties as the distributions described before and shows a maximum around $\log_{10}(\xi) = -1.5$. At lower and higher values, the cross section reflects the suppression by the transverse energy requirements in the selection and the decreasing quark and gluon densities, respectively.

All the measured differential cross sections are well described by NLO QCD predictions.

4.3.3 Double-Differential Cross Sections

Figures 4.7 to 4.10 show the measurements of double-differential dijet cross sections as functions of $\overline{E_{T,\mathrm{B}}^{\mathrm{jet}}}$ and $\log_{10}(\xi)$ in different Q^2 regions. These cross sections are expected to provide a valuable input for the extraction of the proton PDFs. In order to demonstrate that, Figure 4.6 show the NLO predictions for the fraction of events initiated by a gluon from the proton using the CTEQ6.6 PDFs, as a function of variable $\overline{E_{T,\mathrm{B}}^{\mathrm{jet}}}$ in different regions of Q^2. This gluon fraction ranges from about 75% at $125 < Q^2 < 250$ GeV^2 and $\overline{E_{T,\mathrm{B}}^{\mathrm{jet}}}$ values of about 10 GeV to about 5% at the highest Q^2 above 5000 GeV^2. In the lower Q^2 regions, the gluon fraction is also sizeable for larger values of $\overline{E_{T,\mathrm{B}}^{\mathrm{jet}}}$. Since the lower Q^2 region has reach statistics, precise input for the PDF fit can be expected.

The $\log_{10}(\xi)$ distributions in different Q^2 regions in Fig. 4.7 show the same behaviour as the integrated $\log_{10}(\xi)$ distribution in Fig. 4.5b, with a distinct maximum at values that increase with increasing Q^2. The data are very precise – even in the highest Q^2 bin from 5 000 to 20 000 GeV^2 the experimental uncertainties are between 10 and 15% and originate equally from the statistical and the systematical uncertainty. At lower Q^2 values, the experimental uncertainties become as small as $(2-3)$ %. Figure 4.8 shows the level of agreement between data and predictions: the theoretical uncertainties are typically between 5 and 10% and, within the combined uncertainties, the data are very well described by the theory.

The cross sections as functions of $\overline{E_{T,\mathrm{B}}^{\mathrm{jet}}}$ in different regions of Q^2, shown in Fig. 4.9, fall over 2 to 3 orders of magnitude in the range considered, with a smaller slope for higher Q^2 values. The statistical precision of the data is between 2% at the lowest $\overline{E_{T,\mathrm{B}}^{\mathrm{jet}}}$ and Q^2 and slightly above 10% at the highest values of these variables. The systematic uncertainties are mostly of the order of 3 to 5%. The theoretical uncertainties (Fig. 4.10) are approximately constant in $\overline{E_{T,\mathrm{B}}^{\mathrm{jet}}}$; they are of the order of 5 to 10%, with the smaller values at higher Q^2. Data and theory are in good agreement over the whole measured range.

4.4 Conclusions

Measurements of single- and double-differential cross sections for dijet production at high-Q^2 NC DIS were made using an integrated luminosity of 374 pb^{-1}. The measurements have very small statistical and systematic uncertainties and the description of the data by the predictions of NLO QCD is very good, giving a powerful and stringent justification of the theory. These data provide useful information for the determination of the strong coupling constant and the extraction of the proton PDFs and are included into HERAPDF fits.

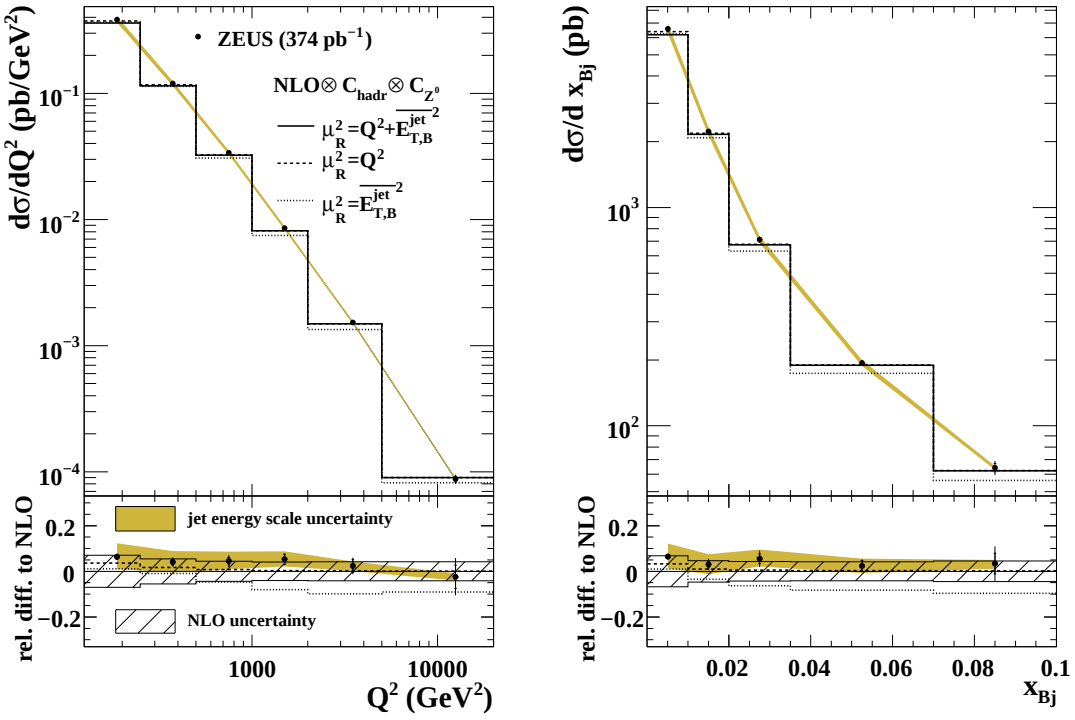

(a) (b)

Figure 4.3: The measured differential cross-sections (a) $d\sigma/dQ^2$ and (b) $d\sigma/dx_{\mathrm{Bj}}$ for inclusive dijet production with $E_{T,\mathrm{B}}^{\mathrm{jet}} > 8$ GeV, $M_{\mathrm{jj}} > 20$ GeV and $-1 < \eta_{\mathrm{LAB}}^{\mathrm{jet}} < 2.5$ (dots), in the kinematic range given by $0.2 < y < 0.6$ and $125 < Q^2 < 20\,000$ GeV^2. The inner error bars represent the statistical uncertainty. The outer error bars show the statistical and systematic uncertainties, not associated with the uncertainty on the absolute energy scale of the jets, added in quadrature. The shaded bands display the uncertainties due to the absolute energy scale of the jets. The NLO QCD calculations with $\mu_R^2 = Q^2 + \overline{E_{T,\mathrm{B}}^{\mathrm{jet}}}^2$ (solid lines), $\mu_R^2 = Q^2$ (dashed lines) and $\mu_R^2 = \overline{E_{T,\mathrm{B}}^{\mathrm{jet}}}^2$ (dotted lines), corrected for hadronisation effects and Z^0 exchange and using the CTEQ6.6 parameterisations of the proton PDFs, are also shown. The lower parts of the figures show the relative differences with respect to the NLO QCD calculations with $\mu_R^2 = Q^2 + \overline{E_{T,\mathrm{B}}^{\mathrm{jet}}}^2$. The hatched bands display the total theoretical uncertainty.

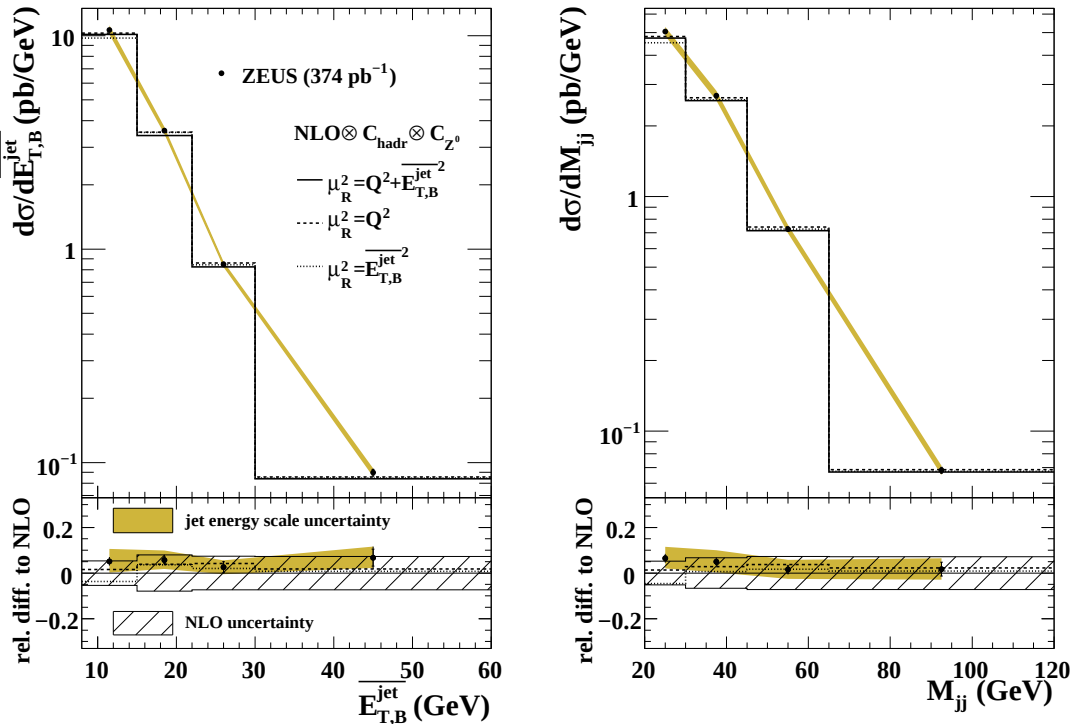

(a) (b)

Figure 4.4: The measured differential cross-sections (a) $d\sigma/d\overline{E_{T,\mathrm{B}}^{\mathrm{jet}}}$ and (b) $d\sigma/dM_{\mathrm{jj}}$ for inclusive dijet production. Other details as in the caption to Fig. 4.3.

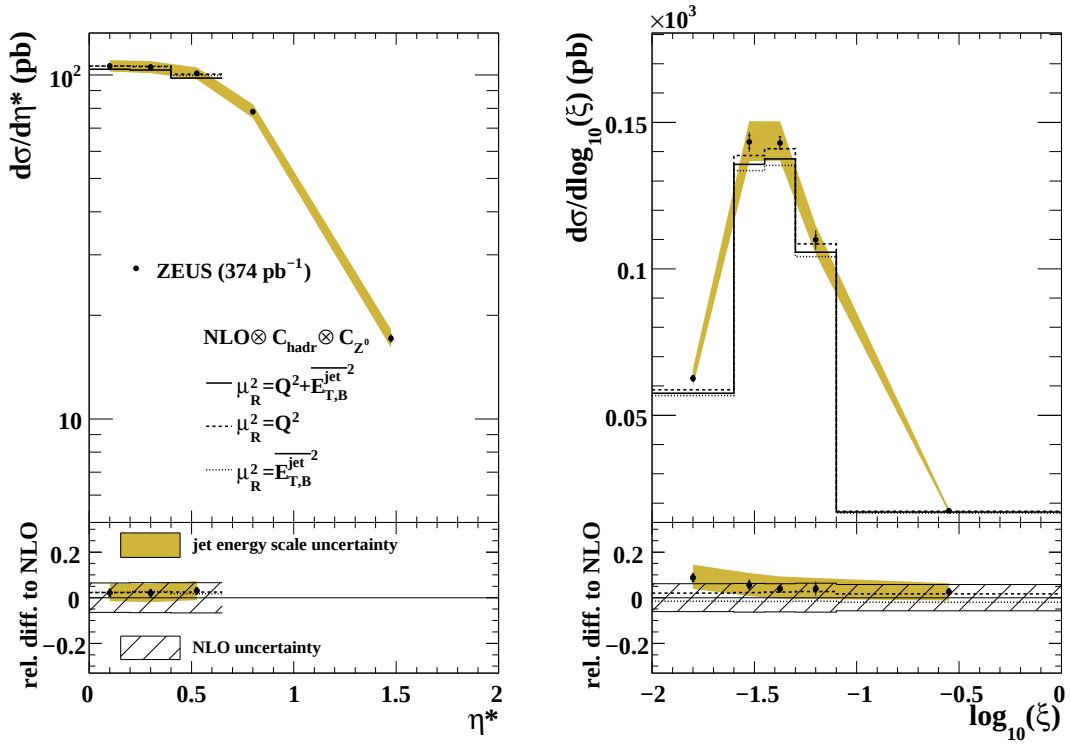

(a) (b)

Figure 4.5: The measured differential cross-sections (a) $d\sigma/d\eta^*$ and (b) $d\sigma/d\log_{10}(\xi)$ for inclusive dijet production. In the last η^* bins the NLO QCD predictions are not plotted for reasons explained in the text. Other details as in the caption to Fig. 4.3.

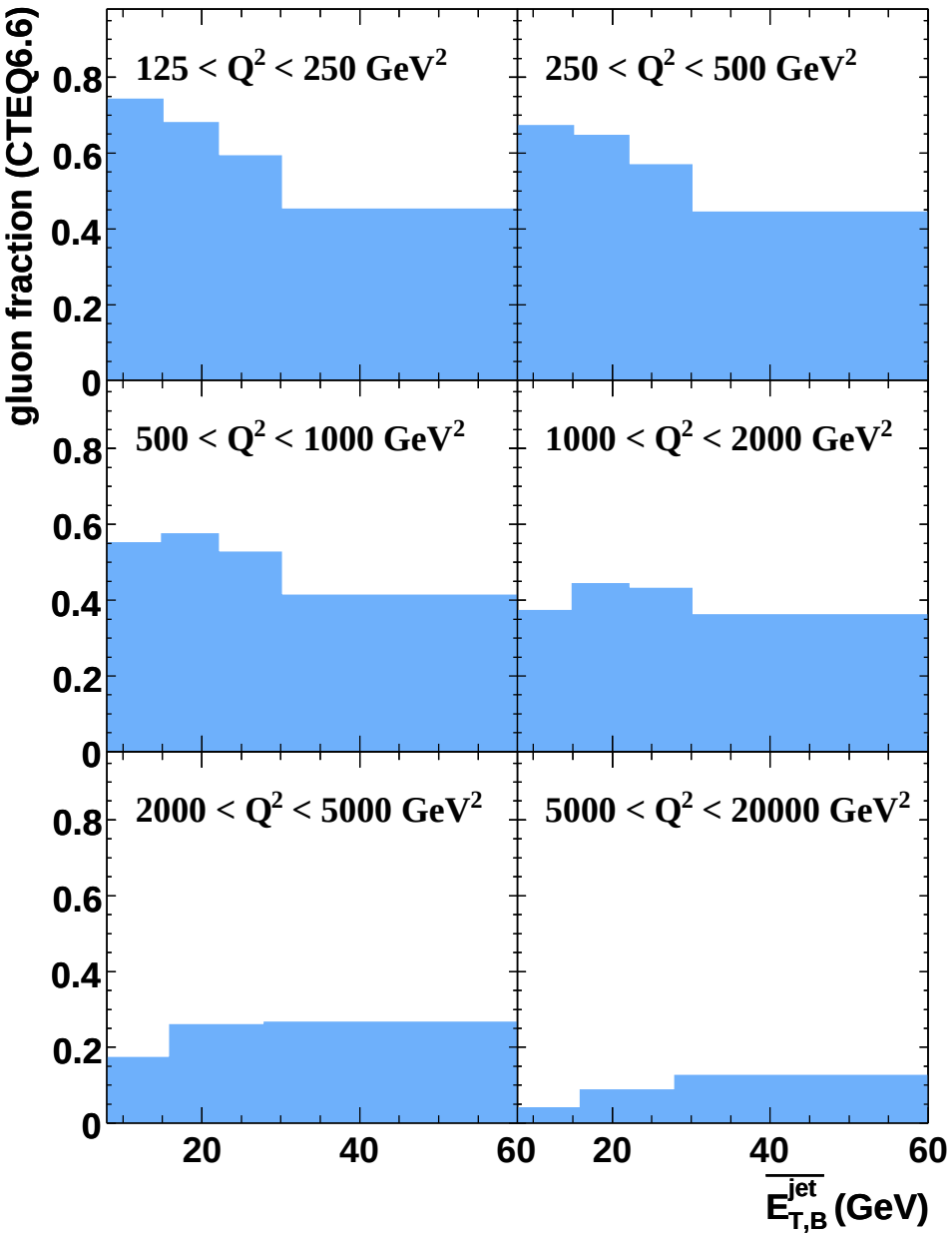

Figure 4.6: The fraction of gluon-induced dijet events as a function of $\overline{E_{T,\mathrm{B}}^{\mathrm{jet}}}$ in different regions of Q^2 as predicted by the CTEQ6.6 PDFs.

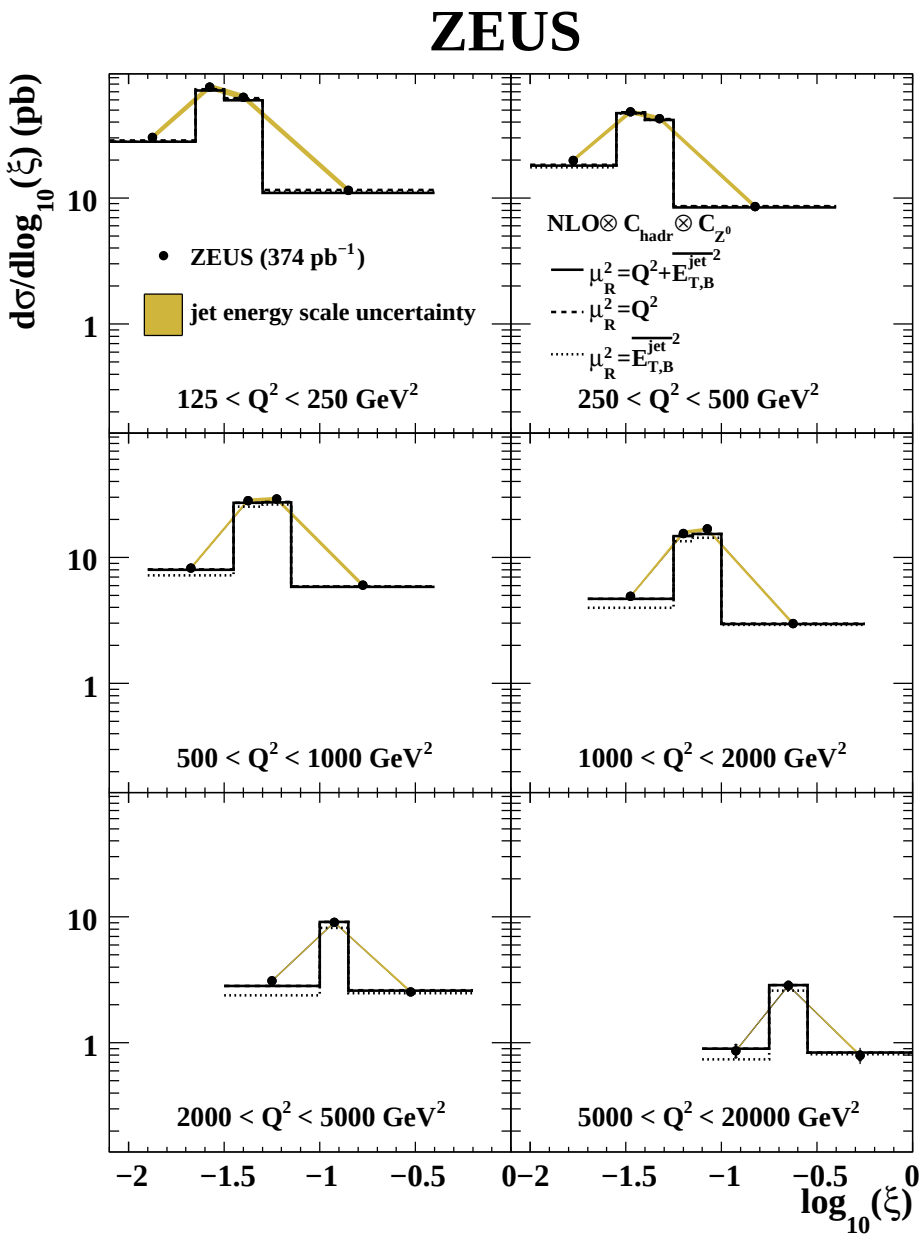

Figure 4.7: The measured differential cross-section $d\sigma/d\log_{10}(\xi)$ for inclusive dijet production in different regions of Q^2. Other details as in the caption to Fig. 4.3.

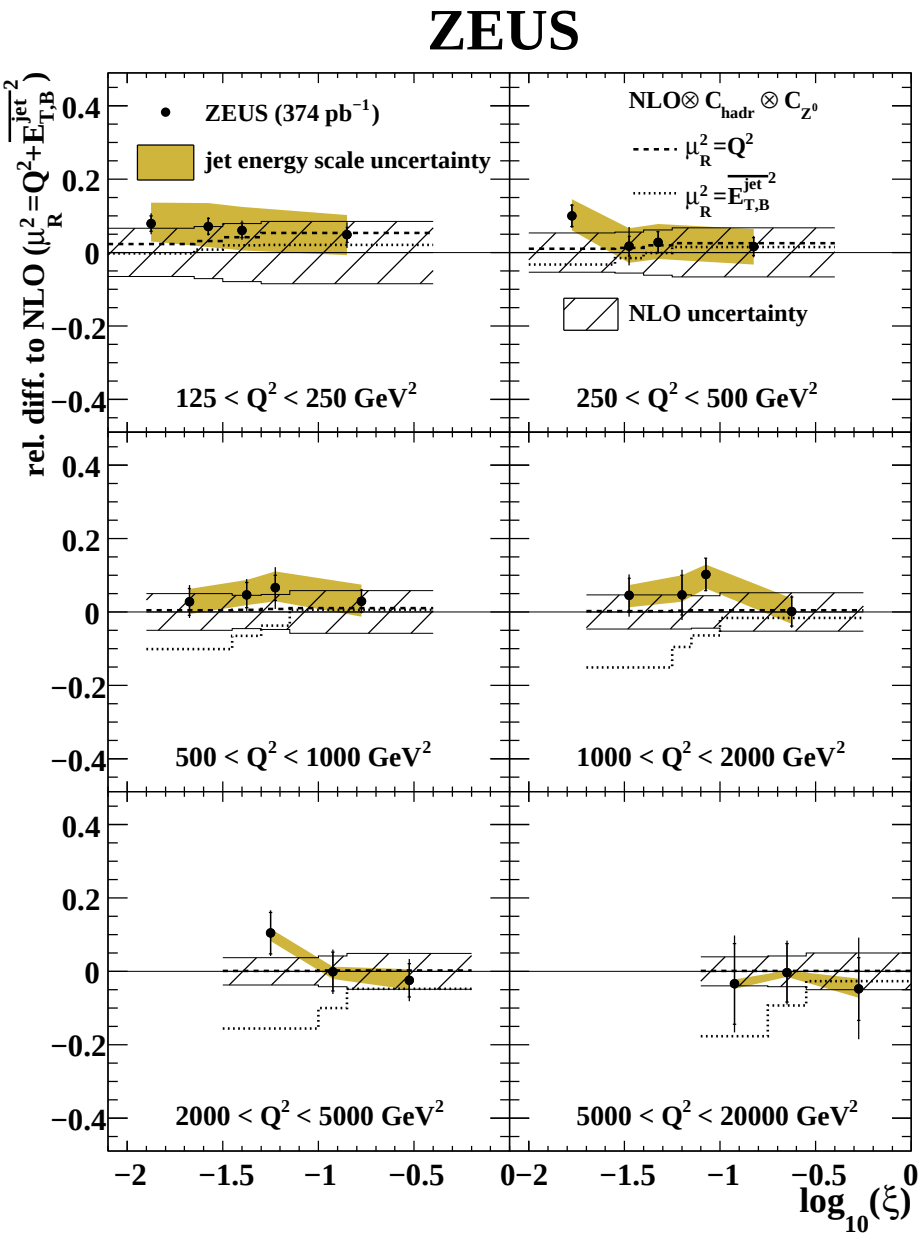

Figure 4.8: Relative differences between the measured differential cross-sections $d\sigma/d\log_{10}(\xi)$ presented in Fig. 4.7 and the NLO QCD calculations with $\mu_R^2 = Q^2 + \overline{E_{T,\mathrm{B}}^{\mathrm{jet}}}^2$. Other details as in the caption to Fig. 4.3.

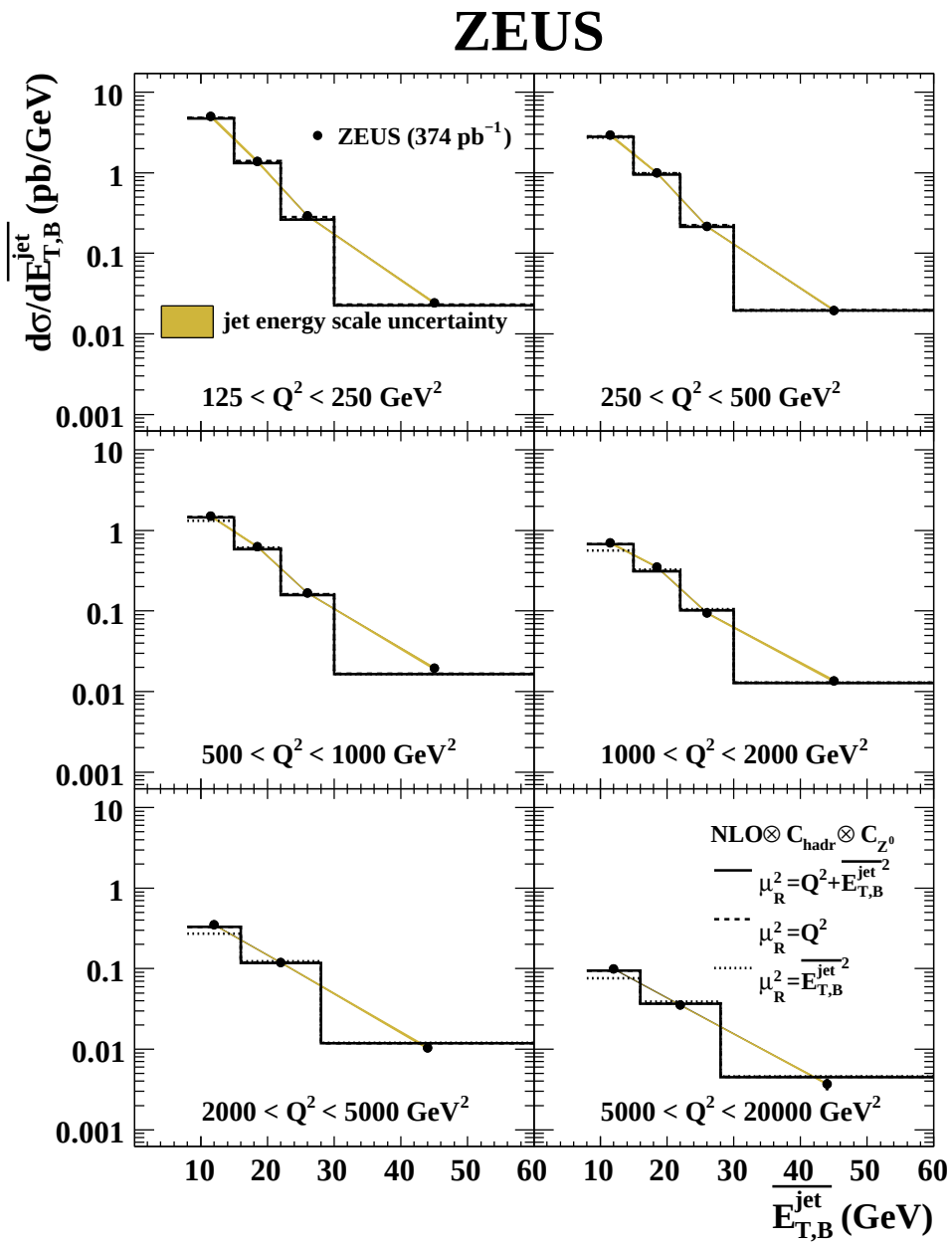

Figure 4.9: The measured differential cross-section $d\sigma/d\overline{E^{\rm jet}_{T,\rm B}}$ for inclusive dijet production in different regions of Q^2. Other details as in the caption to Fig. 4.3.

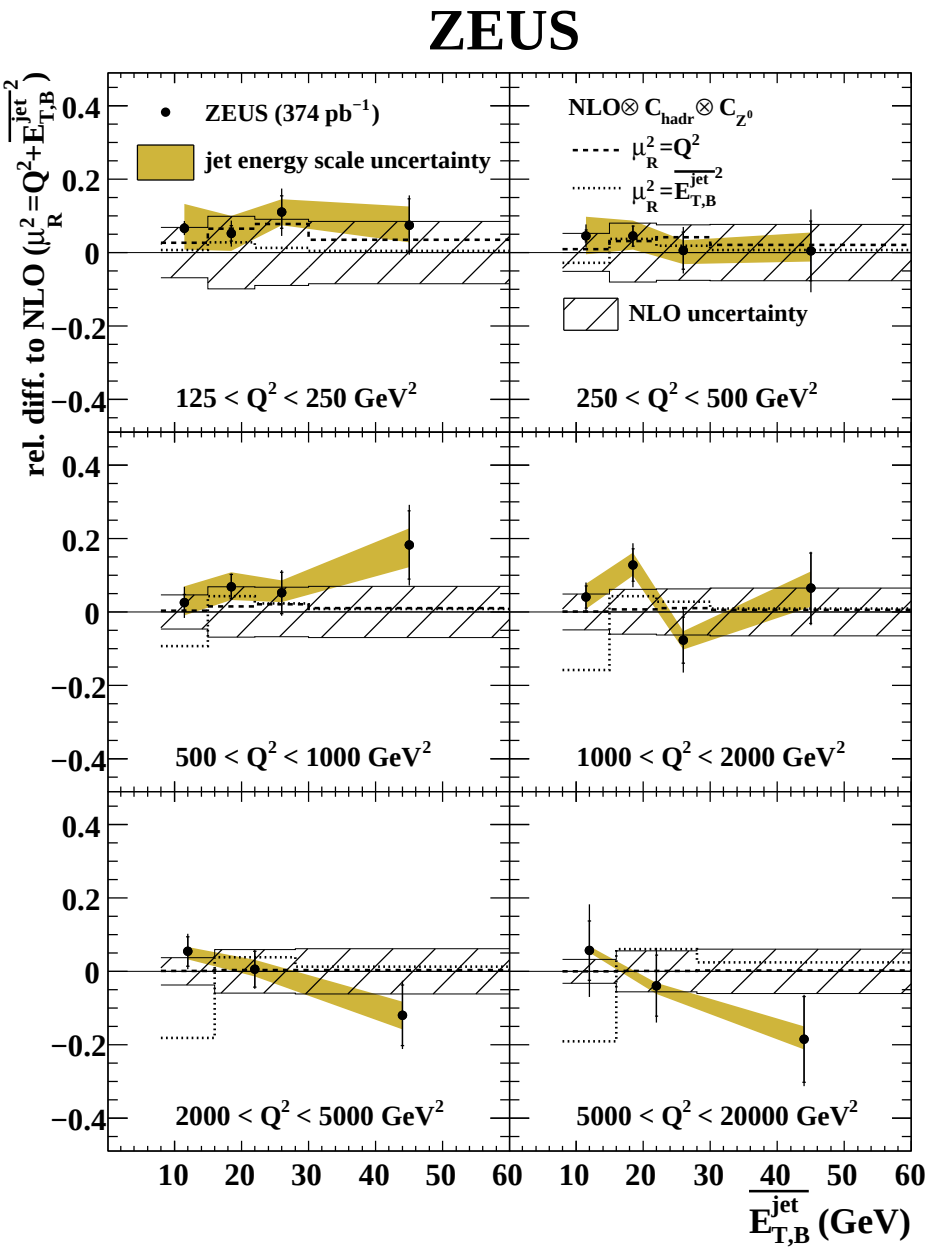

Figure 4.10: Relative differences between the measured differential cross-sections $d\sigma/d\overline{E_{T,\mathrm{B}}^{\mathrm{jet}}}$ presented in Fig. 4.9 and the NLO QCD calculations with $\mu_R^2 = Q^2 + \overline{E_{T,\mathrm{B}}^{\mathrm{jet}}}^2$. Other details as in the caption to Fig. 4.3.

Chapter 5

Isolated photon with jet production in DIS

In this Chapter, a measurement of the isolated photon with jet production made with the ZEUS detector is described. Isolated photon cross sections are expected to be sensitive to u and d PDFs in the proton and provide a possibility to test both QED and QCD. The obtained cross sections were published in 2012 [139]. A part of results was presented earlier in [140].

5.1 Event selection

The analysis is based on a data sample corresponding to an integrated luminosity of 326 ± 6 pb^{-1}, collected with the ZEUS detector during the years 2004 to 2007. The sample is a sum of 138 ± 2 pb^{-1} of e^+p data and 188 ± 3 pb^{-1} of e^-p data.

5.1.1 Phase Space

The phase space of the DIS selection was defined by the following criterion:

- the Q^2 variable reconstructed using the scattered electron was in the range

$$10 < Q^2_{\text{el}} < 350 \text{ GeV}^2. \tag{5.1}$$

Additionally, a few requirements were imposed on the scattered electron:

- The scattering polar angle was greater than

$$\theta_e > 140^\circ, \tag{5.2}$$

to ensure that the electron was registered in the RCAL. This condition together with a condition on the pseudorapidity of an isolated photon (see below) ensured

that electron and photon were separated in θ, which forbids their mutual misinterpretation.

- The energy of the scattered electron was larger than

$$E'_e > 10 \text{ GeV}, \tag{5.3}$$

to ensure good efficiency in triggering and acceptance.

In each event jets were clustered with the k_T cluster algorithm in the E-scheme in the longitudinally invariant inclusive mode [62, 63] (see Section 1.4.1), with R parameter set to 1.0. The algorithm was applied to all ZUFO objects excluding those corresponded to the scattered electron. One of the jets by construction was corresponding to or contained the isolated photon.

The isolated photon's phase space was defined as follows:

- The transverse energy was in the range

$$4 < E_T^\gamma < 15 \text{ GeV}. \tag{5.4}$$

The lower limit ensures reasonable energy resolution, while the upper is motivated by the necessity to distinguish isolated photons and photons produced by neutral meson decays: the larger the energy of the primary neutral meson, the closer are the decay products registered in the CAL (see Section 2.3.2).

- The pseudorapidity of the isolated photon was required to lie within

$$-0.7 < \eta^\gamma < 0.9, \tag{5.5}$$

which corresponds to the ZEUS BCAL acceptance region, where the shower shapes are well understood.

- Isolation from other hadronic activity was imposed by requiring that the photon possessed at least 90% of the total energy of the reconstructed jet of which it formed a part.

The accompanying hadronic jet was selected by the following criteria:

- The transverse energy in the laboratory frame was greater than

$$E_T^{\text{jet}} > 2.5 \text{ GeV}. \tag{5.6}$$

- The pseudorapidity of the jet was lying in the range

$$-1.5 < \eta^{\text{jet}} < 1.8, \tag{5.7}$$

where the ZEUS detector has reasonable acceptance for jets.

If more than one accompanying to a photon jets satisfied all the selection criteria, the one with the largest E_T^{jet} was chosen.

The phase space selection criteria listed above were applied at the detector level of data and Monte Carlo, as well as at the hadron and parton levels of the MC and for the theoretical predictions.

Additionally, several criteria were applied at the detector level of data and MC, to improve acceptance and description of the data by MC simulations. They are described below.

5.1.2 Inclusive DIS Event Selection

Apart from the requirements on Q^2_{el} and scattered electron, a few other requirements were imposed on the data and at the detector level of Monte Carlo to increase the purity of the selected DIS events:

- **The vertex position** along the Z axis was restricted to $|Z_{\text{vtx}}| < 40$ cm to suppress non-beam background and to ensure good reconstruction in the central detectors which are critical in this analysis.
- **An electron candidate** was reconstructed with the Sinistra (Sec. 3.1.1) algorithm, required to have a probability greater than 90%.
- **Box cut.** Events were rejected if the electron candidates were registered in in the region of the RCAL with $|X| < 14.8$ cm and $-14.6 < Y < 12.5$ cm, since the acceptance of the calorimeter region around the beam pipe is not well understood.
- **Longitudinal momentum conservation.** To reject non-DIS background, a condition on the difference between total energy, E, and Z-momentum, P_Z, was imposed: $35 < E - P_Z < 65$ GeV.
- **Trigger.** Events preselected with the ZEUS trigger system (Section 2.3.5) were used for the analysis. It was required that the TLT bit SPP02 was set for events taken during 2004-2005 and the TLT bit SPP09 for events taken during 2006-2007. Both bits selected low-Q^2 inclusive DIS events. They used a cut on the energy of the scattered electron, $E'_e > 4$ GeV, some loose cut on the $E - P_Z$ value, a box cut and requirements on particular bits of the second level trigger. The full description of these bits can be found in [141].

5.1.3 Isolated-Photon Candidate Selection

The isolated photon candidates were selected from the ZUFO objects (see Sec.3.1.3) of the event. The successful candidates, apart from the phase space selection, satisfied the following criteria:

- There was no matched track to the ZUFO corresponding to the isolated photon candidate, i.e. the code of the photon candidate ZUFO is 31 (Section 3.1.3);

- No tracks fitted to the primary vertex with momentum $p > 250$ MeV within 0.2 units in (η, ϕ) around the photon candidate;

- $F_{\mathrm{EMC}} = \dfrac{E^{\gamma}_{\mathrm{EMC}}}{E^{\gamma}_{\mathrm{tot}}}$: at least 90% of the photon candidate energy was registered in the EMC cells of the calorimeter, to suppress hadronic background;

5.2 Extraction of the photon signal

The event sample selected according to the criteria described in Section 5.1 was dominated by background; thus the photon signal was extracted statistically following the approach used in previous ZEUS analyses [142–146].

The photon signal was extracted from the background using the lateral width of the BEMC energy-cluster comprising the photon candidate. This was calculated as the variable $\langle \delta Z \rangle = \sum_i E_i |Z_i - Z_{\mathrm{cluster}}| \,/ (w_{\mathrm{cell}} \sum_i E_i)$. Here, Z_i is the Z position of the centre of the i-th cell, Z_{cluster} is the centroid of the EFO cluster, w_{cell} is the width of the cell in the Z direction, and E_i is the energy recorded in the cell. The sum runs over all BEMC cells in the EFO.

The global distribution of $\langle \delta Z \rangle$ in the data and in the MC are shown in Fig. 5.1(a). The MC distributions in LL and QQ have been corrected using a comparison between the shapes in $\langle \delta Z \rangle$ associated with the scattered electron in MC simulation of DIS and in real data. The $\langle \delta Z \rangle$ distribution exhibits a double-peaked structure with the first peak at ≈ 0.1, associated with the photon signal, and a second peak at ≈ 0.5, dominated by the $\pi^0 \to \gamma\gamma$ background.

As a check, an alternative method was applied in which the quantity f_{max} was employed instead of $\langle \delta Z \rangle$, where f_{max} is the fraction of the photon-candidate shower contained in the BEMC cell with the largest signal. The results (Fig. 5.1(b)) were consistent with the main analysis method and showed no significant systematic difference.

The number of isolated-photon events contributing to the data is illustrated in Fig. 5.1(a). It is determined for each cross-section bin by a χ^2 fit to the $\langle \delta Z \rangle$ distribution in the range $0 < \langle \delta Z \rangle < 0.8$, using the LL and QQ signal and background MC distributions. By treating the LL and QQ photons separately, account is taken of their differing hadronic activity (resulting in significantly different acceptances) and their differing (η, E_T) distributions (resulting in different bin migrations due to finite measuring precision).

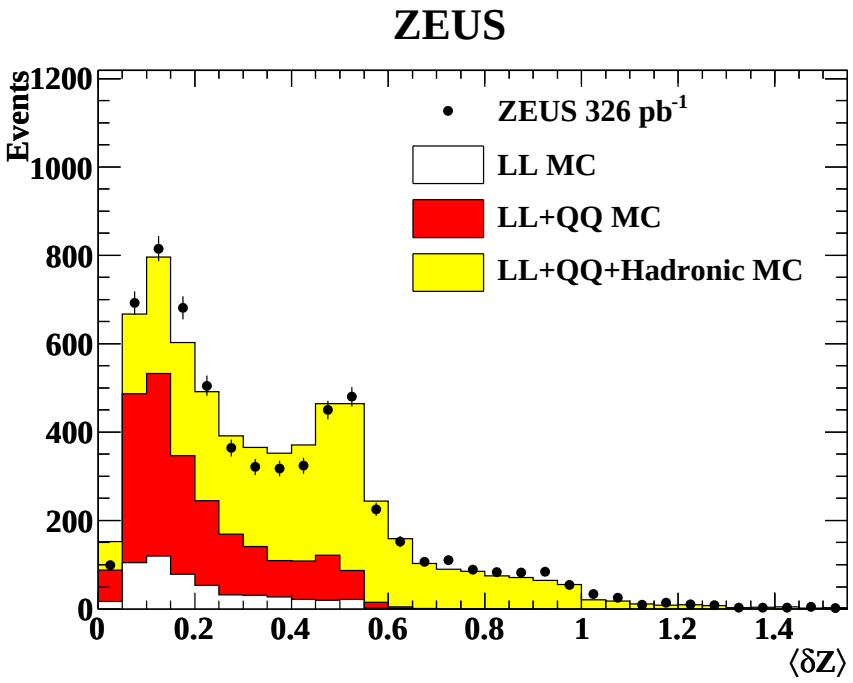

(a)

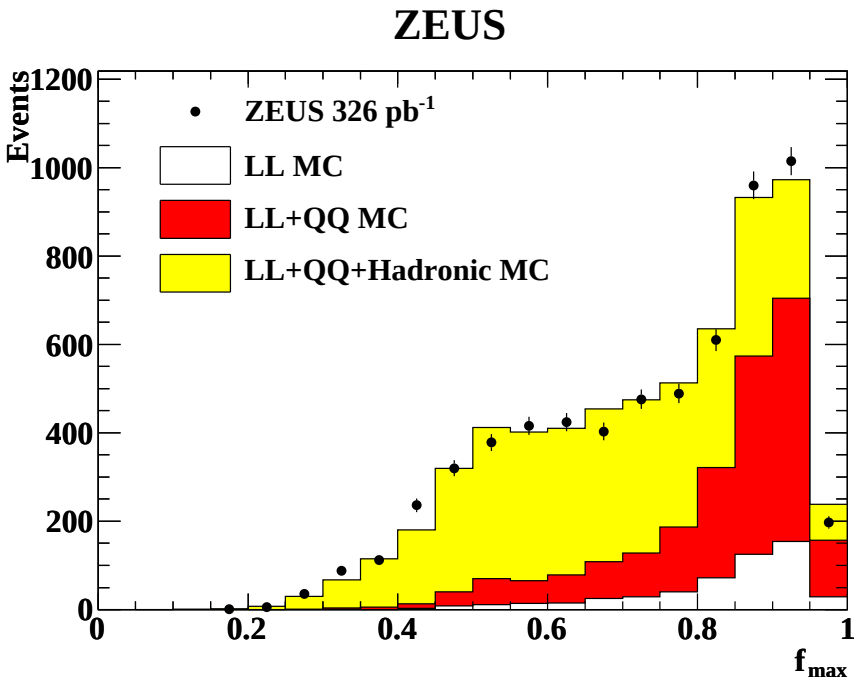

(b)

Figure 5.1: Distribution of (a) $\langle \delta Z \rangle$, (b) $f_{\max}$. The error bars represent the statistical uncertainties. The light shaded histogram shows a fit to the data of three components with fixed shapes as described in the text. The dark shaded histogram represents the QQ component of the fit, and the white histogram the LL component.

In performing the fit, the theoretically well determined LL contribution was kept constant at its MC-predicted value and the other components were varied. Of the 6167 events selected, 2440±60 correspond to the extracted signal (LL and QQ). The scale factor resulting from the global fit for the QQ photons in Fig. 5.1(a) was 1.6; this factor was used for all the plots comparing MC to data. The fitted global scale factor for the hadronic background was 1.0. In all cross-section bins, the χ^2/n.d.f. of the fits was between 0.7 and 2.3 for 14 degrees of freedom.

For a given observable Y, the production cross section was determined using

$$\frac{d\sigma}{dY} = \frac{\mathcal{A}_{\mathrm{QQ}} \cdot N(\gamma_{\mathrm{QQ}})}{\mathcal{L} \cdot \Delta Y} + \frac{d\sigma_{\mathrm{LL}}^{\mathrm{MC}}}{dY},$$

where $N(\gamma_{\mathrm{QQ}})$ is the number of QQ photons extracted from the fit, ΔY is the bin width, $\mathcal{L}$ is the total integrated luminosity, $\sigma_{\mathrm{LL}}^{\mathrm{MC}}$ is the predicted cross section for LL photons from DJANGOH, and $\mathcal{A}_{\mathrm{QQ}}$ is the acceptance correction for QQ photons. The value of $\mathcal{A}_{\mathrm{QQ}}$ was calculated using Monte Carlo from the ratio of the number of events generated to those reconstructed in a given bin. It varied between 1.0 and 1.5 from bin to bin. To improve the representation of the data, and hence the accuracy of the acceptance corrections, the Monte Carlo predictions were reweighted. This was done globally as a function of Q^2 and of η^γ, and bin-by-bin as a function of photon energy; the three reweighting factors were applied multiplicatively.

5.3 Reweighting of Q^2, η^γ and E_T^γ MC Distributions

Control plots showing distributions of the Q^2 and x variables in data and Monte Carlo and the data-to-MC ratio are given in Figure 5.2. The data Q^2 distribution is not very well described by the sum of MC distributions, therefore it was decided to reweight the Monte Carlo. The Monte Carlo distribution is given by a sum of three components: LL, QQ and background. The LL component was not reweighted, since it is expected to be well theoretically understood and properly modelled. To decide which of two remaining components (QQ or background) should be reweighted, the Q^2 distribution was investigated in two regions of the $\langle \delta Z \rangle$, Figure 5.3(a): in the region with $\langle \delta Z \rangle < 0.35$, which is signal-enhanced, (Figure 5.1(a)) the data distribution was compared to the QQ Pythia Monte Carlo, while in the background-enhanced region with $\langle \delta Z \rangle > 0.35$ the data distribution was compared to the background Ariadne Monte Carlo. As seen from Fig. 5.3(a), both Monte Carlos need to be reweighted.

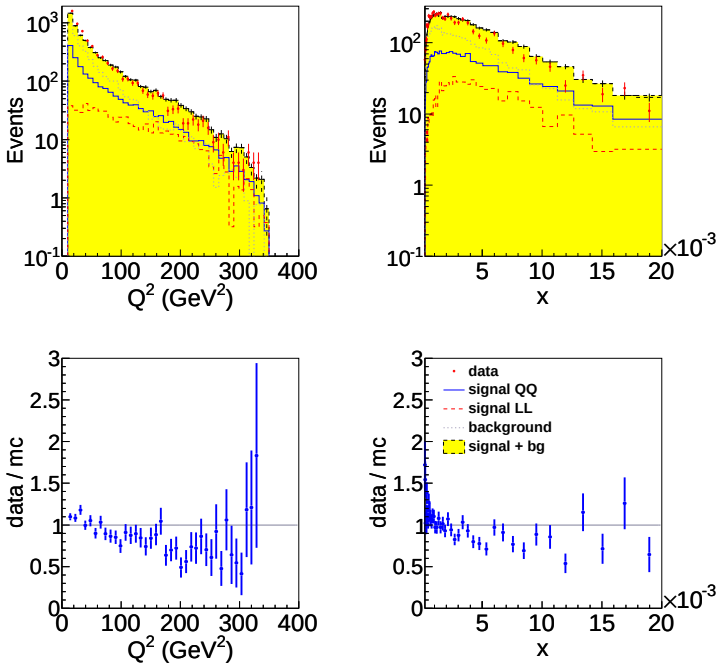

Figure 5.2: The Q^2 and x distributions for isolated photon + jet events before the Q^2 reweighting of the Monte Carlo.

The reweighting procedure was performed as follows:

1. A data-to-Monte Carlo ratio of the Q^2 distributions was fitted with

$$f_{\mathrm{Pythia}} = a_0 + a_1 \cdot \frac{Q^2}{\mathrm{GeV}^2} \quad \text{or} \quad \mathrm{f_{Ariadne}} = \mathrm{c_0} + \mathrm{c_1} \cdot \frac{\mathrm{Q^2}}{\mathrm{GeV^2}} + \mathrm{c_2} \cdot \left(\frac{\mathrm{Q^2}}{\mathrm{GeV^2}}\right)^2, \qquad (5.8)$$

   for the signal and background enhanced regions, respectively. The fitted functions are shown in Figure 5.3(a).

2. Weights $f_{\mathrm{Pythia}}(Q^2)$ and $f_{\mathrm{Ariadne}}(Q^2)$ were assigned to each signal and background Monte Carlo event, respectively, as a function of the Q^2 variable calculated at the hadron level. This weight was used for filling all the Monte Carlo histograms.

The reweighted distributions are shown in Figure 5.3(b). The agreement between Q^2 distributions of data and MC is much better after the Q^2-reweighting.

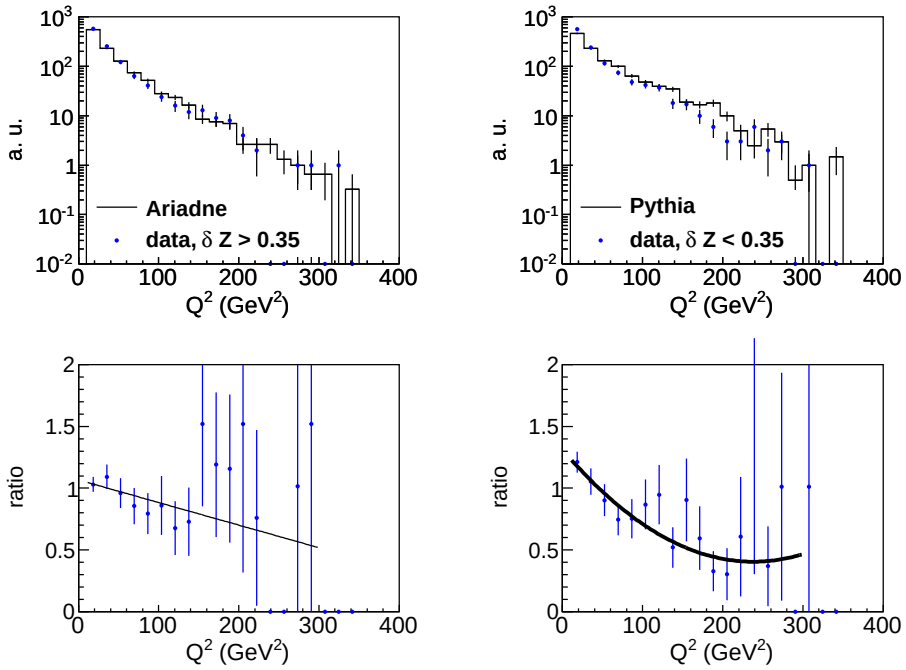

(a)

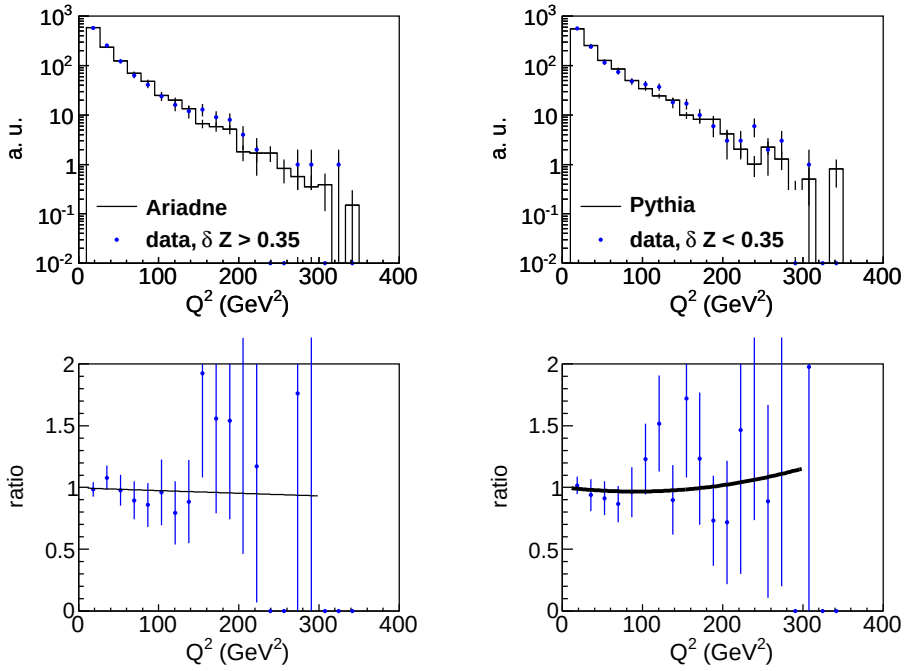

(b)

Figure 5.3: The Q^2 distribution for isolated photon + jet events, compared to the QQ Pythia Monte Carlo in the region dominated by signal events ($\langle \delta Z \rangle < 0.35$) and compared to the background Ariadne Monte Carlo in the region dominated by background ($\langle \delta Z \rangle > 0.35$). The Monte Carlo distributions are normalised to the data and are shown (a) before and (b) after the reweighting.

The pseudorapidity of the photon candidate was reweighted using a similar procedure. The energy of the photon candidate was reweighted using the weights determined by bin-by-bin ratio of data and Monte Carlo histograms. The three obtained weights were used multiplicatively.

5.3.1 Control Distributions after Monte Carlo Corrections

The distribution of the DIS event variables, of the photon candidate variables, and of the jet variables (jet energy was corrected to the hadron level), are shown in Figs 5.4, 5.5, and 5.6, respectively. After the Monte Carlo was reweighted, as described above, a reasonable agreement between data and the Monte Carlo model is found.

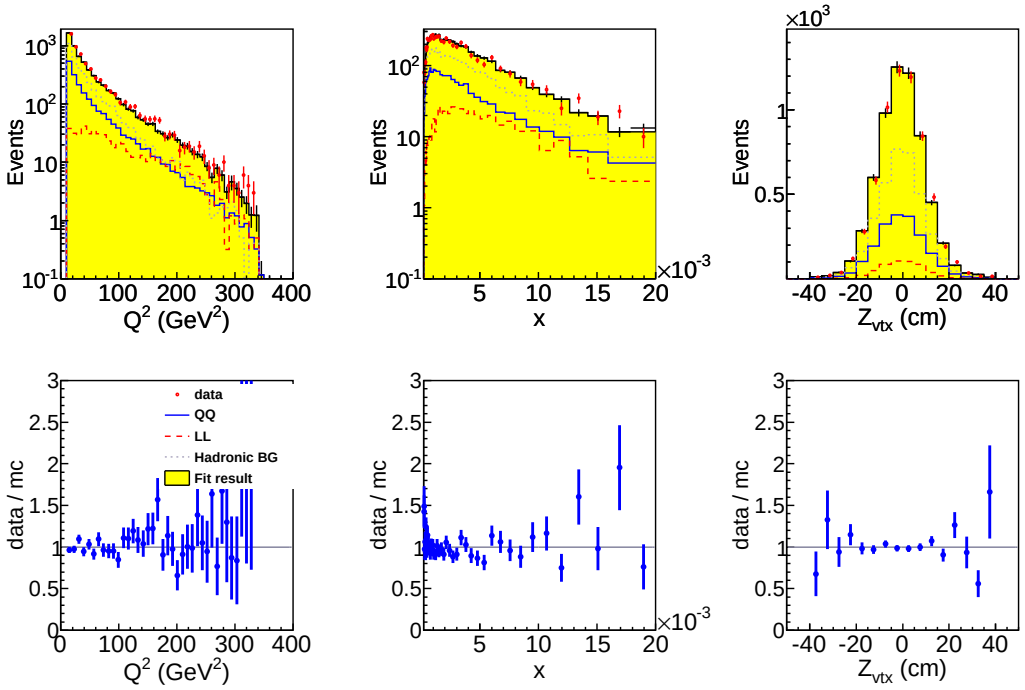

Figure 5.4: The Q^2, x and Z_{vtx} distributions for isolated photon + jet events compared to the reweighted MC model.

5.4 Results

5.4.1 Systematic Uncertainties

The following sources of systematic uncertainty due to the energy scale were taken into account:

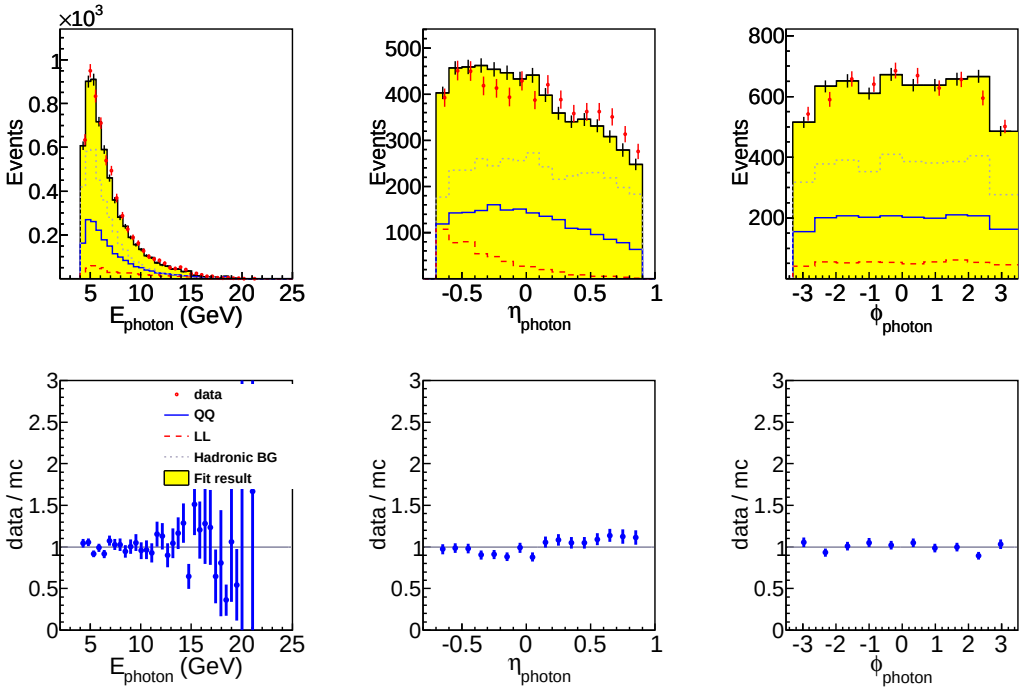

Figure 5.5: The E^γ, η^γ and ϕ^γ distributions for isolated photon + jet events compared to the reweighted MC model.

- the energy of the measured scattered electron was varied by its known scale uncertainty of $\pm 2\%$ [137], causing variations in the measured cross sections of up to $\pm 5\%$;

- the energy of the photon candidate was similarly varied by $\pm 2\%$, causing variations in the measured cross sections of up to $\pm 5\%$;

- the modelling of the jets, and in particular the energy scale, was first studied for jets with $E_T^{\rm jet} > 10$ GeV by selecting ZEUS DIS events having one jet of this type and no photon or other jets with $E_T^{\rm jet} > 10$ GeV. Using the scattered electron, and requiring transverse-momentum balance, a prediction was made for the transverse energy of the jet, which was compared to the values obtained in the data and in the MC events. In this way, an uncertainty on the energy scale of $\pm 1.5\%$ was established for these jets. For jets with $E_T^{\rm jet}$ in the range [2.5, 10] GeV, DIS events were selected containing one jet in this range and one jet with $E_T^{\rm jet} > 10$ GeV. Using the scattered electron and the well measured high-energy jet, again requiring transverse-momentum balance, a prediction was made of the lower jet $E_T^{\rm jet}$ value, which was compared to the values obtained in data and in MC. In this way, the uncertainty on the jet energy scale was evaluated as $\pm 4\%$ and $\pm 2.5\%$ in the energy

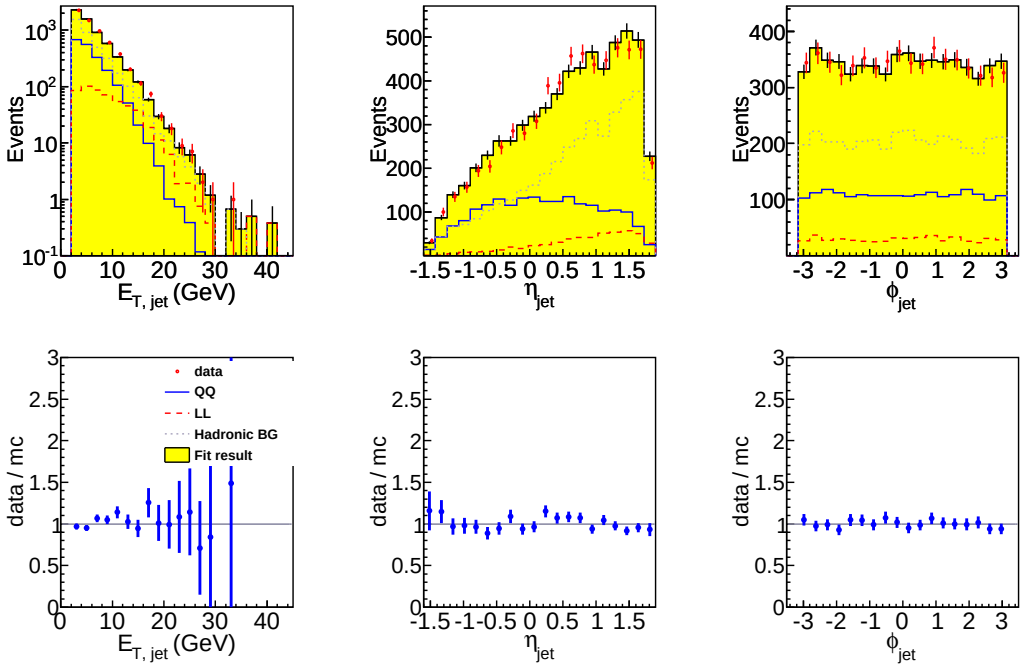

Figure 5.6: The E^{jet}, η^{jet} and ϕ^{jet} distributions for isolated photon + jet events compared to the reweighted MC model

ranges [2.5, 6] and [6, 10] GeV, respectively. The resulting systematic uncertainty on the cross section was typically around ±2%, ranging to ±10% at the highest E_T^{jet} values.

Since the photon and jet energy scales were calibrated relative to that of the scattered electron, all three energy-scale uncertainties were treated as correlated. The three energy scales were simultaneously varied by the uncertainties described above, and the resulting change in the cross sections was taken as the overall systematic energy-scale uncertainty. Further systematic uncertainties were evaluated as follows:

- the dependence on the modelling of the hadronic background by ARIADNE was investigated by varying the upper limit for the $\langle \delta Z \rangle$ fit in the range $[0.6, 1.0]$, giving variations that were typically ±5% increasing to +12% and −14% in the most forward η^γ and highest-x bins respectively;

- uncertainties in the acceptance due to the modelling by PYTHIA were accounted for by taking half of the change attributable to the reweighting as a systematic uncertainty; for most points the effect was small.

The background from photoproduction events at low Q^2 was found to be negligible. Other sources of systematic uncertainty were found to be negligible and were ignored [79, 146]: these included the modelling of the ΔR cut, the track momentum cut, the cut on $E - p_Z$, the Z_{vtx} cut, the cut on the electromagnetic fraction of the photon shower, and a variation of 5% on the LL fraction. These were found to generate systematic effects of at most 1-2% apart from a 2.5% effect in the highest-x bin.

The major uncertainties were treated as symmetric and added in quadrature. The common uncertainty of 1.8% on the luminosity measurement was not included in the figures.

The breakdown of the systematic uncertainties due to sources described above can be found in Appendix A.

5.4.2 Cross Sections

Differential cross sections in DIS for the production of an isolated photon and at least one additional jet, $ep \to e'\gamma + \text{jet}$, were measured in the kinematic region defined by $10 < Q^2 < 350$ GeV^2, $E'_e > 10$ GeV, $\theta_e > 140°$, $-0.7 < \eta^\gamma < 0.9$, $4 < E_T^\gamma < 15$ GeV, $E_T^{\text{jet}} > 2.5$ GeV and $-1.5 < \eta^{\text{jet}} < 1.8$ in the laboratory frame. The jets were formed according to the k_T-clustering algorithm with the R parameter set to 1.0, and photon isolation was imposed such that at least 90% of the energy of the jet-like object containing the photon belongs to the photon. No charged particles with momentum greater than 250 MeV was allowed within a cone around the photon of radius 0.2 in η, ϕ.

Initially, the theoretical predictions were provided at the parton level, while the measured cross sections correspond to the hadron level. Therefore, the theoretical predictions were corrected to the hadron level using the correction factors obtained from the ratio of histograms at the hadron and parton levels of the Monte Carlo.

The differential cross sections as functions of Q^2, x, E_T^γ, η^γ, E_T^{jet} and η^{jet} are shown in Fig. 5.7. As expected, the cross section decreases with increasing Q^2, x, E_T^γ, and E_T^{jet}. The modest dependence of the cross section on η^γ and η^{jet} can be attributed to the LL contribution. The predictions for the sum of the expected LL contribution from Djangoh and a factor of 1.6 times the expected QQ contribution from Pythia agree well with the measurements, and this model therefore provides a good description of the process.

The theoretical predictions described in Section 3.3.2 are compared to the measurements in Fig. 5.8. The predictions from GKS [147] describe the shape of all the distributions reasonably well, but the rise seen at low Q^2 and at low x is underestimated. The cross section as a function of η^γ and η^{jet} is underestimated by about 20%. This was also observed in the earlier inclusive photon measurement [146]. The theoretical uncertainties are indicated by the width of the shaded area. The calculations of BLZ [148] also describe the shape of the data reasonably well, except mayby for the jet quantities, but the predicted overall rate is too high by about 20%. The worse description of the jet variables by the BLZ predictions may be due to absent prescription in k_T factorisation approach of

how to set the pseudorapidity of the jet originating from the evolution cascade.

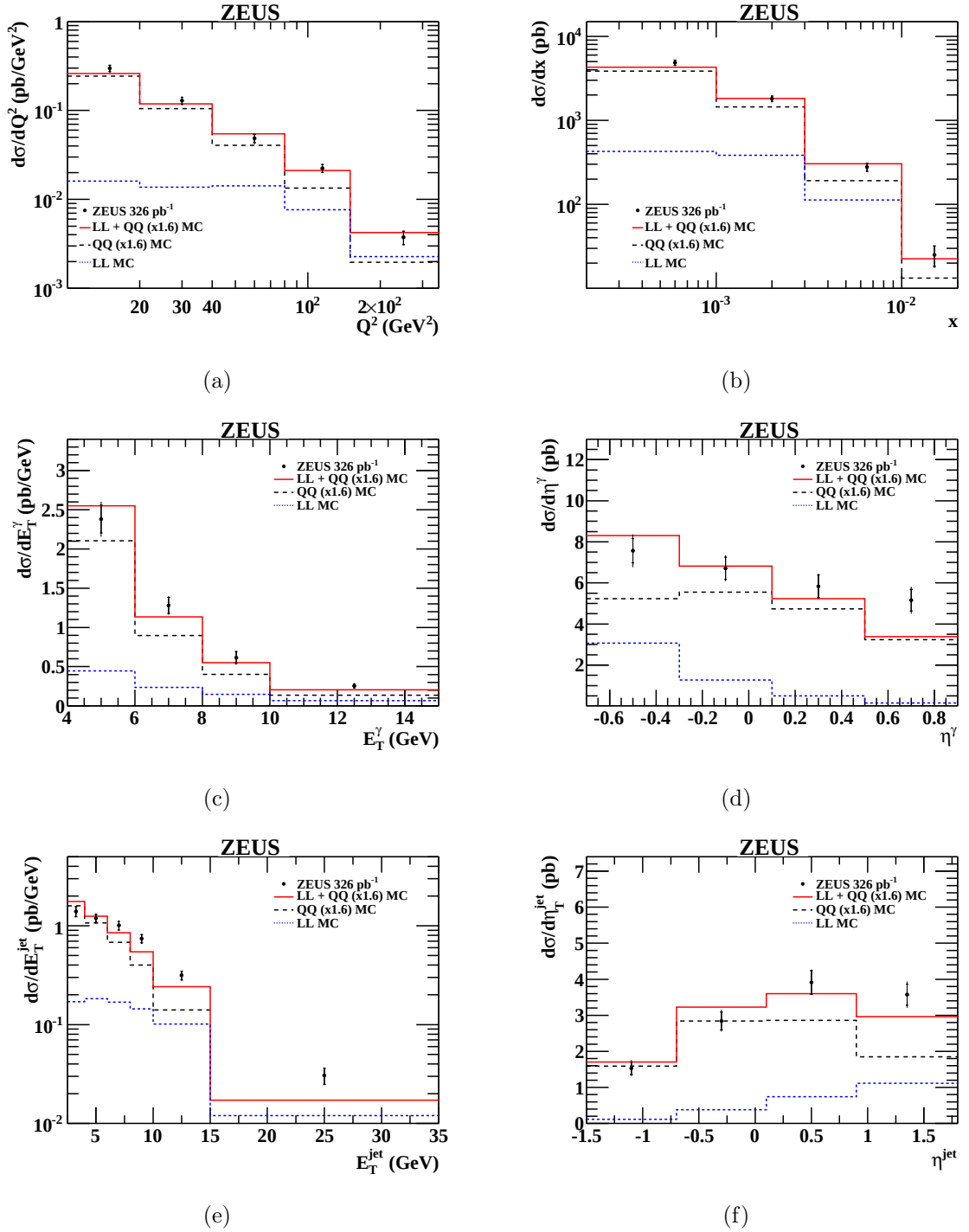

Figure 5.7: Isolated photon differential cross sections in (a) Q^2, (b) x, (c) E_T^γ, (d) η^γ, (e) E_T^{jet}, and (f) η^{jet}. The inner and outer error bars show, respectively, the statistical uncertainty and the statistical and systematic uncertainties added in quadrature. The solid histograms are the reweighted Monte Carlo predictions from the sum of QQ photons from PYTHIA normalised by a factor 1.6 plus DJANGOH LL photons. The dashed (dotted) lines show the QQ (LL) contributions.

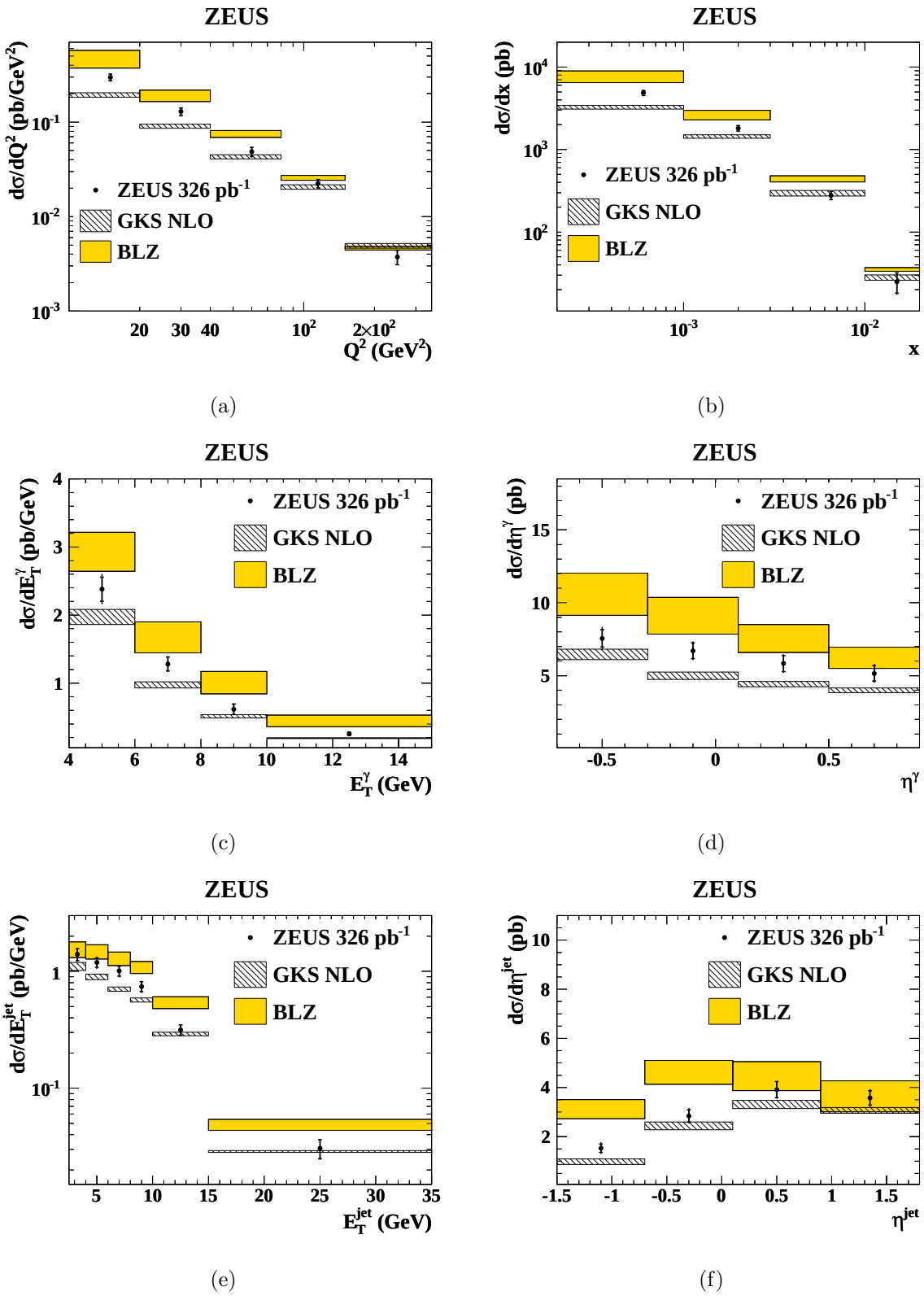

Figure 5.8: Data points as shown in Fig. 5.7. Theoretical predictions from Gehrmann-De Ridder *et al.* (GKS) [147] and Baranov *et al.* (BLZ) [148] are shown, with associated uncertainties indicated by the shaded bands.

Chapter 6

QCD analysis of the isolated photon + jet data

The following Chapter presents a QCD analysis of the isolated photon + jet cross sections, measurement of which was described in the previous Chapter. The proton PDF fit was performed with several different parameterisations, which allow a test of different assumptions. The fit was performed to the isolated photon cross sections and to the inclusive DIS HERA I data. The HERA I data were used, and not combined HERA I and HERA II, since the combination of the HERA I + HERA II DIS data was not ready yet when the studies presented here were performed.

6.1 Datasets

The QCD analysis is based on 4 datasets of inclusive DIS data and a dataset corresponding to the isolated photon + jet data, the measurement of which was described in Chapter 5 and published in [139]. The inclusive DIS datasets are combined results of the ZEUS and H1 data collected during the HERA I running period [122] and corrected to a common centre-of-mass energy corresponding to $E_p = 920$ GeV . These datasets include Charged and Neutral Current interaction for both e^+p and e^-p collisions. The total number of data points used in the fit was 596. The phase space coverage of all the used datasets is summarised in Table 6.1. It can be seen from the table, that the photon data correspond to the low x, low Q^2 region.

[1]The lower x limit is $4.32 \cdot 10^{-5}$ for a cut $Q^2 \geq 3.5$ GeV^2.
[2]Among them 379 data points with $Q^2 \geq 3.5$ GeV^2.

Dataset	x range		Q^2 range, GeV^2		n points	Reference
NC e^+p inclusive DIS	[1]$6 \cdot 10^{-6}$	0.65	0.045	30 000	528[2]	[122]
NC e^-p inclusive DIS	0.0013	0.65	90	30 000	145	[122]
CC e^+p inclusive DIS	0.008	0.4	300	15 000	34	[122]
CC e^-p inclusive DIS	0.013	0.4	300	30 000	34	[122]
Isolated Photons + Jets	0.0002	0.02	10	350	4	[139]

Table 6.1: Datasets used for the QCD analysis of the isolated photon + jet data

6.2 Theoretical Predictions

Theory predictions are essential parts of the QCD analysis. This section gives a brief description of the technical implementation of the NLO predictions for the isolated photon with jet production and for the inclusive DIS, as used during the PDF fit.

6.2.1 Fast Calculation of the NLO Predictions for Photon Plus Jet Production

The original predictions [121] for isolated photon with jet production, shown on the cross section plots in Chapter 5 (and published in [139]), were provided by the authors of [121]. The program for the calculation of theoretical predictions is called EPGJET. The EPGJET program code with documentation was provided by its authors [149], to enable the possibility to use it for the proton PDF fit described in this thesis.

The original EPGJET code was modified in order to account for higher-order QED effects in the following way. The predictions are proportional to the third power of the electromagnetic coupling, α (due to a virtual photon exchange between the quark and the lepton and a real photon emission). The original predictions used the constant value of the electromagnetic coupling constant, $\alpha_0 = 1/137.0359895$. The predictions thus corresponded to the Born-level QED approximation. However, as will be shown further, in the energy range typical for the measurement presented here, the higher order QED corrections are large and should be taken into account.

Loop corrections to the photon propagator will lead to a running of the α. The effect of replacing the constant α_0 with the running one can be estimated from Figure 6.1, where the running of α is shown as a function of the energy scale describing the photon emission. For the isolated photon with jet measurement presented here, the typical values of the isolated photon transverse energy are $4 < E_T^\gamma < 15$ GeV and typical values of the exchanged photon virtuality are $10 \lesssim Q^2 \lesssim 350$ GeV^2. It is seen from Fig. 6.1 that the difference between the α_0 and the running α at the few GeV energy scale is about 2-3%. Therefore, the expected difference between the predictions using the constant and the running α is 6-9%, since the predictions are proportional to the third power of α.

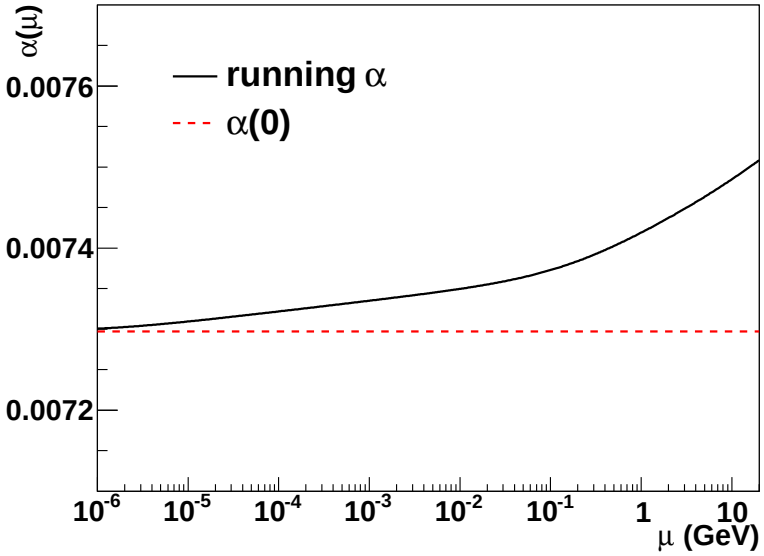

Figure 6.1: The running electromagnetic coupling constant compared to its low-energy value, $\alpha_0 = 1/137.0359895$. The running curve is evaluated with the ALPHAQED program [150].

It was decided to replace the constant α_0 with the running $\alpha(\mu)$, in order to at least partially take into account the higher order QED effects. The running of $\alpha(\mu)$ was implemented within the EPGJET program using the program ALPHAQED [150] by F. Jegerlehner [151]. The virtuality of the exchanged photon was used as an argument of the running of $\alpha(\mu)$. The change of the cross sections with the replacement of α_0 with the running $\alpha(\mu)$ is shown in Figure 6.2. The cross section increased by up to 10%.

Following the choice made in [139], the factorisation and renormalisation scales were set to $\mu_F = \mu_R = \sqrt{Q^2 + (p_T^{\text{jet}})^2}$.

6.2.2 Predictions for Inclusive DIS Cross Sections and QCD Settings

The inclusive DIS cross sections are constructed from the proton structure functions (described in Section 1.2.2), which in turn are a convolution of the proton PDFs with the hard-scattering coefficient functions. The proton PDFs are obtained by expressing them as function of x at the starting scale $Q_0^2 = 1.9$ GeV^2 and by solving the DGLAP evolution equations at NLO in the $\overline{\text{MS}}$ scheme with the renormalisation and factorisation scales set to Q^2. The starting scale is chosen so that it is below the charm mass threshold, $Q_0^2 < m_c$. The evolution of the PDFs was done by the QCDNUM program [41]. The

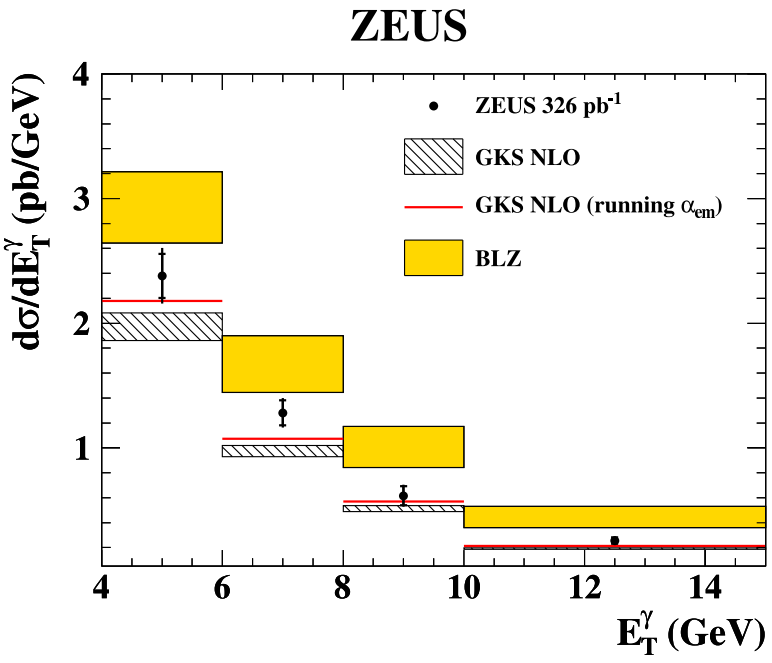

Figure 6.2: Change of the theoretical predictions if the fixed electromagnetic coupling $\alpha(0)$ is replaced with the running coupling (red line). Other details are as in Figure 5.8

light quark coefficient functions were also calculated in QCDNUM, while the heavy quark coefficient functions were calculated in the general mass variable flavour number scheme, as implemented by R. Thorne and R. Roberts [56–58] (RT scheme). The heavy quark masses $m_c = 1.4$ GeV and $m_b = 4.75$ GeV, and the strong coupling constant value $\alpha_s(M_Z) = 0.1176$ were chosen following [122].

As in [122], a minimum Q^2 cut of $Q^2_{\min} > 3.5$ GeV^2 was imposed to remain in the kinematic region where perturbative QCD should be applicable.

As a starting point, the PDFs were parameterised using 10 parameters, following the choice of [122]:

$$xg(x) = A_g x^{B_g}(1-x)^{C_g}, \tag{6.1}$$

$$xu_v(x) = A_{u_v} x^{B_{u_v}}(1-x)^{C_{u_v}}\left(1 + E_{u_v}x^2\right), \tag{6.2}$$

$$xd_v(x) = A_{d_v} x^{B_{d_v}}(1-x)^{C_{d_v}}, \tag{6.3}$$

$$x\bar{U}(x) = A_{\bar{U}} x^{B_{\bar{U}}}(1-x)^{C_{\bar{U}}}, \tag{6.4}$$

$$x\bar{D}(x) = A_{\bar{D}} x^{B_{\bar{D}}} (1-x)^{C_{\bar{D}}}. \tag{6.5}$$

Here $x\bar{U}$ and $x\bar{D}$ are the sums of the up-type and down-type sea quark densities, respectively. At the chosen starting scale they equal $x\bar{U} = x\bar{u}$, $x\bar{D} = x\bar{d} + x\bar{s}$. The valence u and d quarks densities are expressed via xu_v and xd_v, respectively. The normalisation parameters A_g, A_{u_v}, A_{d_v} are constrained by the quark number sum rules and momentum sum rule. The momentum sum rule was also tested separately. The B parameters for sea quarks were set equal, $B_{\bar{U}} = B_{\bar{D}}$, such that there is a single B parameter for the sea distributions. The strange quark density was expressed as an x-independent fraction (f_s) of the d-type sea, $x\bar{s} = f_s x\bar{D}$ at Q_0^2. The strange fraction was chosen to be $f_s = 0.31$, following [122]. To ensure that $x\bar{u} \to x\bar{d}$ as $x \to 0$ (isospin symmetry), the further constraint $A_{\bar{U}} = A_{\bar{D}}(1 - f_s)$ was applied. This constraint can be dropped to test the assumption $x\bar{u} \to x\bar{d}$ at $x \to 0$.

6.3 Proton PDF fit

Isolated photons are emitted either by a quark of the proton or by an incoming or outgoing lepton. The case in which the photon is emitted by a quark in the proton gives sensitivity to the proton PDFs. The isolated photon data have different sensitivity to up-type and down-type quark densities due to different charges of these quarks. As seen from Table 6.1, the isolated photon data correspond to the low x, low Q^2 region. Therefore, the photon data should be mainly sensitive to the up-type sea quark distribution (since it dominates the valence quark densities at low x). However, via the sum rules, the effect of adding the isolated photon data can be propagated to other parton densities.

This section presents the effect of adding the isolated photon data into the inclusive DIS data only proton PDF fit. As a reference, the fit result to inclusive HERA I DIS data only is used. Different PDF parameterisations were tried. Firstly, the standard 10-parameter version, the same as for HERAPDF1.0 [122], was used. Secondly, the constraint on normalisation of the sea quark densities $A_{\bar{U}} = A_{\bar{D}}(1 - f_s)$ was dropped, to test the assumption $\lim_{x\to 0}(x\bar{u} - x\bar{d}) = 0$. Finally, the proton momentum sum rule was tested, by removing the corresponding constraint and summing up the momenta of the fitted PDFs with and without including the photon data.

6.3.1 Impact of the Isolated Photon Data Using the Standard PDF Parameterisation

The impact was first tested using the same 10-parameter parameterisation, as was used for HERAPDF1.0, to see how well the photon data are fitted together with the HERA I inclusive DIS data. The result of the fit to the isolated photon + jet data is shown in

Figure 6.3. The partial χ^2 values for each dataset for two versions of the fit (with and without the photon data) are summarised in Table 6.2.

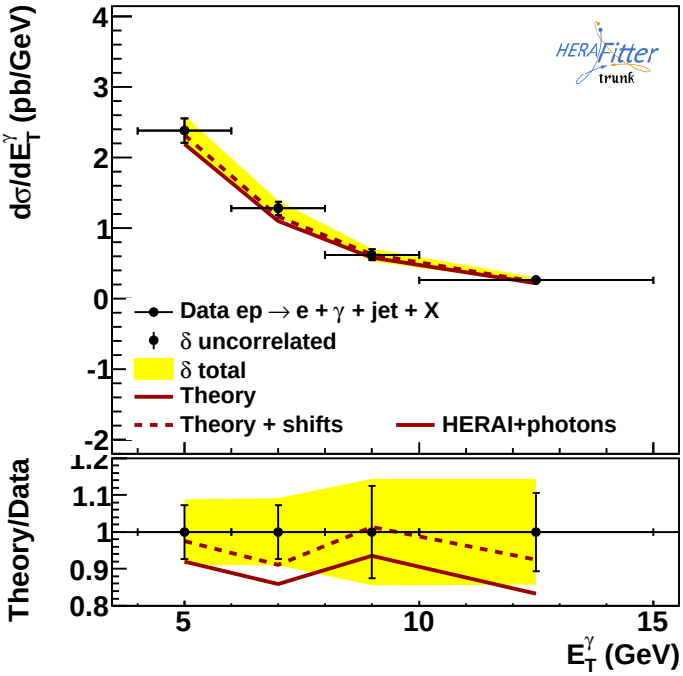

Figure 6.3: The result of the proton PDF fit to the isolated photon + jet data using the 10p parameterisation of [122].

In both cases the total χ^2/dof has reasonable value and corresponds to a fit probability of 0.57. The HERA I inclusive DIS data are fitted equally well, independently of whether the isolated photon data were added or not. The partial χ^2 per number of data points for the isolated photon dataset is $\chi^2/n_{\text{points}} = 2.1/4$. The isolated photon data are therefore very nicely consistent with the inclusive DIS data.

The fitted $x\bar{U}$ PDF with the fit uncertainties is shown in Figure 6.4(a) at the starting scale $Q_0^2 = 1.9$ GeV^2, and the ratio of the $x\bar{U}$ PDFs, extracted with and without the photon data included, is shown in Fig. 6.4(b). The PDF and its uncertainty looks practically identical, except in the very high x region, where the central value of the PDF differs, however in this region the uncertainties are anyway much larger than the observed effect. The fitted parameters of the PDFs are summarised in Table 6.3. The parameters and their uncertainties are very close in the two cases.

From this study one can conclude that the isolated photon data measured in [139] are consistent with the inclusive DIS HERA I data of [122], and that using the 10p parameterisation, the effect of adding the isolated photon data on the PDFs is marginal.

Dataset	χ^2/n_{points}	
	HERA I	HERA I + isolated photon data
NC e^-p inclusive DIS	107/145	107/145
NC e^+p inclusive DIS	419/379	419/379
CC e^-p inclusive DIS	20/34	20/34
CC e^+p inclusive DIS	29/34	29/34
ZEUS isolated photons with jets	-	2.1/4
Correlated χ^2	-	1.7
Total χ^2/dof	575/582	579/586

Table 6.2: Partial and total χ^2 values for proton PDF fits to the HERA I inclusive DIS and to the isolated photon data, using the 10p parameterisation of [122].

6.3.2 Test of the Assumption $\lim_{x\to 0}(x\bar{u} - x\bar{d}) = 0$

For the fit to the inclusive DIS data performed in [122], the following constraints on the parameters of the sea $\bar{U}$ and $\bar{D}$ quark distributions were applied: $B_{\bar{U}} = B_{\bar{D}}$ and $A_{\bar{U}} = A_{\bar{D}}(1 - f_s)$. These constraints were made to ensure that $x\bar{u} \to x\bar{d}$ as $x \to 0$. The latter requirement was introduced by hand, since it was assumed that the inclusive DIS data alone don't allow its test. This requirement is justified in theory, were the u and d quarks are both treated as massless, and therefore the gluon inside the proton, generating the quark sea, splits with equal probabilities to $u\bar{u}$ and $d\bar{d}$ quark pairs (isotopic spin invariance). However, in reality, the u and d quarks have small but non-zero masses of 2.3 MeV and 4.8 MeV, respectively [8][3]. Since the mass of the d quark is larger than the mass of the u quark, the production of $d\bar{d}$ pairs might be suppressed compared to $u\bar{u}$ pairs. Moreover, the proton contains two valence u quarks and one d quark. Therefore, the Pauli principle could potentially suppress the sea u quark constituents of the proton[4].

Since the isolated photon data have different sensitivity to the up- and down-type sea distributions, the attempt was made to test the assumption of equality of the u and d quarks seas of the proton at $x \to 0$. For this the constraint $A_{\bar{U}} = A_{\bar{D}}(1-f_s)$ was dropped. In this way the normalisations of the U and D seas are varied independently during the fit. The sea C parameters were set equal for this study, $C_{\bar{U}} = C_{\bar{D}}$, to keep the same number of parameters. Previous study showed that the $C_{\bar{U}}$ and $C_{\bar{D}}$ parameters were close within the uncertainties (see Table 6.3).

The variable r_{UD} was constructed,

$$r_{UD} = \frac{A_{\bar{U}}}{A_{\bar{D}}(1 - f_s)}, \tag{6.6}$$

[3]These are the running $\overline{\text{MS}}$ masses evaluated at a renormalisation scale $\mu = 2$ GeV.

[4]One should note that the Pauli principle will act only very slightly at low x, since the densities of the valence quarks in this region are very small.

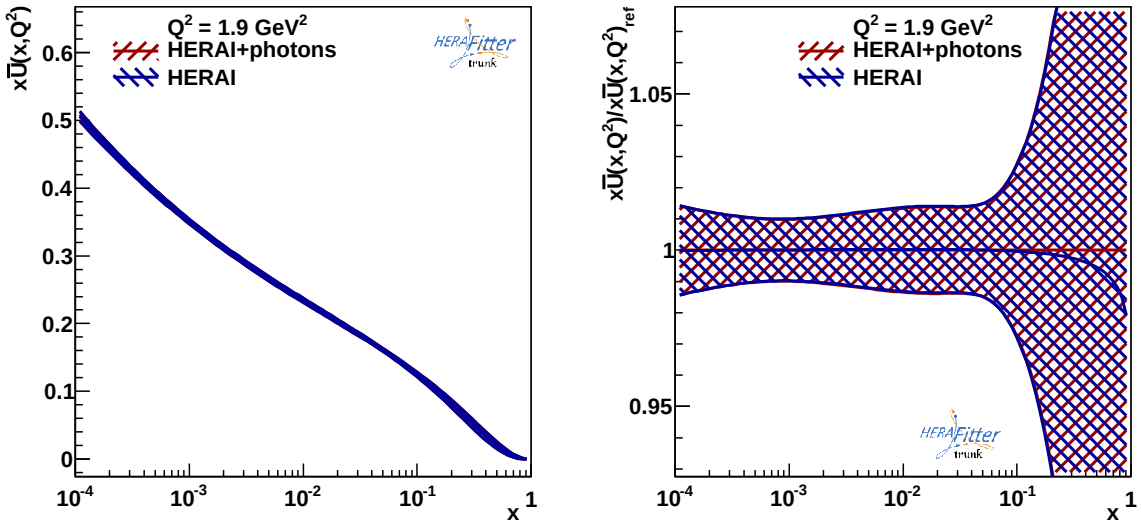

(a) (b)

Figure 6.4:

to quantise the difference between normalisations of the $\bar{U}$ and $\bar{D}$ densities. In the HERAPDF1.0 fit this variable was equal to 1 by definition.

The results of the proton PDF fits to the HERA I inclusive DIS data with and without the photon data included are summarised in Figures 6.5, 6.6 and in Tables 6.4, 6.5. Figure 6.5 shows the fit result to the isolated photon plus jet cross section. The partial and the total χ^2 values (Table 6.4) are reasonable and are very close to those obtained in previous subsection.

The $\bar{U}$, $\bar{D}$ and gluon PDFs are shown in Figure 6.6. It is seen that the fit prefers slightly more of the $\bar{U}$ sea and slightly less of the $\bar{D}$ sea in the proton, when the isolated photon data are added. The gluon shape is also slightly changed. The change of the PDF uncertainties is negligibly small. The valence distributions (not presented here) almost don't change when the photon data are added.

The ratio of the normalisations of the $x\bar{U}$ and $x\bar{D}$ distributions, changes from

$$r_{UD} = 1.06 \pm 0.18, \tag{6.7}$$

to

$$r_{UD}^{\text{phot}} = 1.09 \pm 0.19, \tag{6.8}$$

when the isolated photon data are added to the fit. One can conclude that the isolated photon data prefers slightly suppressed $\bar{D}$ sea. In general, both fits are consistent with isospin symmetry ($r_{UD} = 1$).

Parameter	HERA I	HERA I + isolated photon data
B_g	0.214 ± 0.032	0.214 ± 0.032
C_g	9.02 ± 0.8	9.02 ± 0.8
B_{u_v}	0.667 ± 0.027	0.667 ± 0.026
C_{u_v}	4.65 ± 0.19	4.65 ± 0.19
E_{u_v}	9.6 ± 1.9	9.7 ± 1.9
C_{d_v}	4.27 ± 0.58	4.26 ± 0.58
$C_{\bar{U}}$	2.62 ± 0.49	2.61 ± 0.48
$A_{\bar{D}}$	0.1633 ± 0.0074	0.1632 ± 0.0074
$B_{\bar{D}}$	-0.1647 ± 0.0058	-0.1648 ± 0.0058
$C_{\bar{D}}$	2.44 ± 0.78	2.44 ± 0.78

Table 6.3: Fitted parameters of the PDFs for the fits with and without isolated photon data included, using the 10p parameterisation of [122]. The uncertainties are Hessian fit uncertainties.

6.3.3 Test of the Proton Momentum Sum Rule

As the next step it was decided to test the proton momentum sum rule. This sum rule constrains the sum of fractional momenta of all partons of the proton to 1:

$$\int_0^1 \left[\sum_i \left(q_i(x) + \bar{q}_i\right) + g(x) \right] x dx = 1. \tag{6.9}$$

This constraint was introduced by hand in the fits described in previous subsections. However, if one releases this constraint, the data could give an answer to the question, whether the data prefer some additional constituents in the proton (for example, a photon PDF in the proton, as suggested by some recent developments, see e.g. [152]).

In the study presented in this subsection, the constraint was dropped and a new fit variable p_{proton} was introduced, $p_{\text{proton}} = \int_0^1 \left[\sum_i \left(q_i(x) + \bar{q}_i\right) + g(x)\right] x dx$. The PDFs were parameterised in the same manner as in subsection 6.3.2, allowing an independent variation of the normalisations of the U and D sea quark PDFs. Therefore, the total number of fit parameters in this case was 11.

The fits converged with reasonable χ^2 values (summarised in Table 6.6), again very similar to those obtained in the two previous subsections, which already means that the data prefer fulfilment of the proton momentum sum rule. It is confirmed by Table 6.7, where the values of the fitted parameters are given. The variable p_{proton} recovers to values $p_{\text{proton}} = 1.000 \pm 0.012$ and $p_{\text{proton}} = 0.998 \pm 0.012$, for the fits to the inclusive DIS data only and to the inclusive DIS + isolated photon data, respectively. These results are consistent with the assumption that only quarks and gluons are the constituents of the proton, but allow e.g. a photon contribution of order 1%.

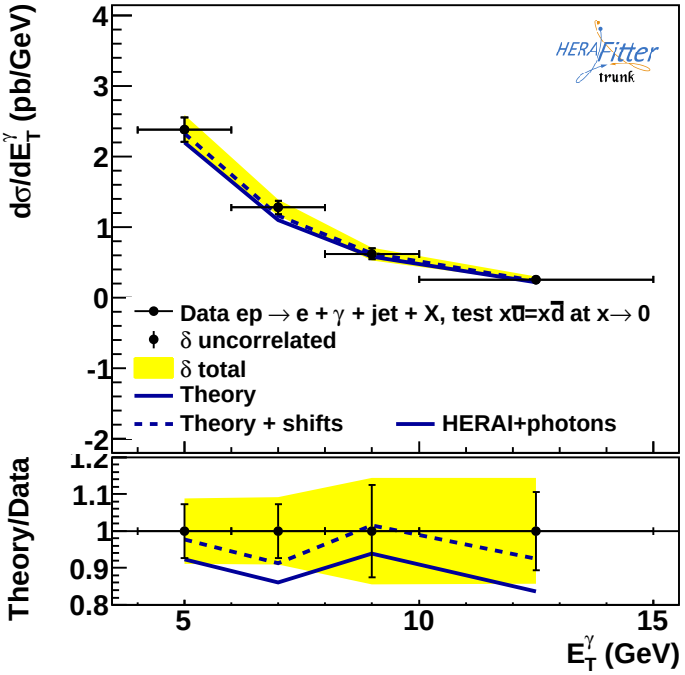

Figure 6.5: The result of the proton PDF fit to the isolated photon + jet data, using the parameterisation which allows a test of the $x\bar{u} \to x\bar{d}$ at $x \to 0$ assumption.

6.4 Conclusions

A proton PDF fit was made to the inclusive DIS ep data and to the isolated photon + jet data. It is the first attempt to use the isolated photon + jet data from ep collider. The fits showed that the isolated photon data are consistent with the inclusive DIS data. It was also shown that the isolated photon data are sensitive in principle to the low x dependence of the sea quark distributions, however it was not possible to make strong statements of the composition of the sea at low x, since only a small number (4) of the isolated photon data points could be used, and the data precision was considerably limited by statistics. There are many other measurements of isolated photon production, inclusively and with a jet, by both the ZEUS and H1 experiments. More data can be included in the fit in the future, providing stronger constraints on the PDFs.

It was shown that the proton flavour composition at low x is consistent with isospin invariance, and that a possible non-QCD contribution to the proton PDF, e.g. from photons, is limited to $\mathcal{O}(1\%)$.

Dataset	χ^2/n_{points}	
	HERA I	HERA I + isolated photon data
NC e^-p inclusive DIS	107/145	106/145
NC e^+p inclusive DIS	419 / 379	420 / 379
CC e^-p inclusive DIS	20 / 34	20 / 34
CC e^+p inclusive DIS	29 / 34	29 / 34
ZEUS isolated photons with jets	-	2.1/4
Correlated χ^2	-	1.6
Total χ^2/dof	575/582	579/586

Table 6.4: Partial and total χ^2 values for proton PDF fits to the HERA I inclusive DIS and to the isolated photon data, using the parameterisation which allows a test of the $x\bar{u} \to x\bar{d}$ at $x \to 0$ assumption.

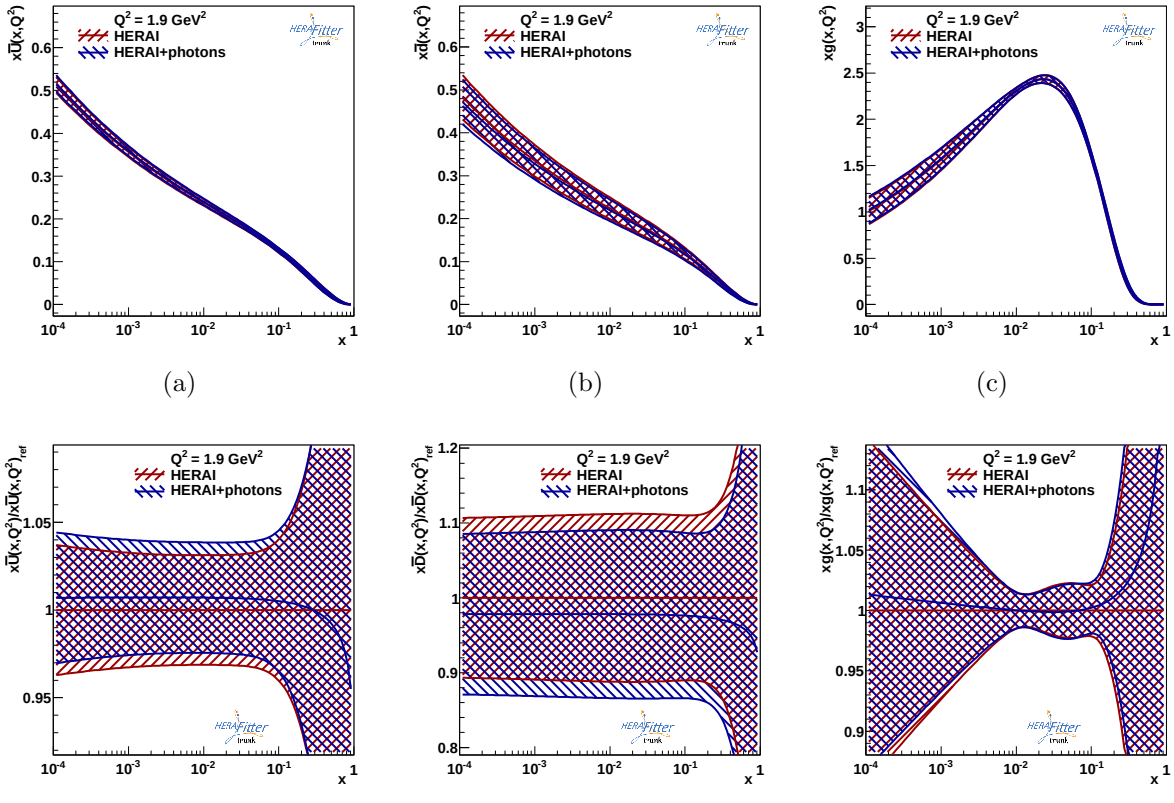

(a) (b) (c)

(d) (e) (f)

Figure 6.6:

Parameter	HERA I	HERA I + isolated photon data
B_g	0.202 ± 0.036	0.199 ± 0.036
C_g	8.63 ± 0.85	8.53 ± 0.84
B_{u_v}	0.665 ± 0.028	0.664 ± 0.029
C_{u_v}	4.64 ± 0.17	4.64 ± 0.17
E_{u_v}	9.9 ± 2.0	9.9 ± 2.0
C_{d_v}	4.04 ± 0.47	3.99 ± 0.45
$A_{\bar{U}}$	0.1149 ± 0.0081	0.1158 ± 0.0082
$A_{\bar{D}}$	0.157 ± 0.021	0.153 ± 0.021
$B_{\bar{D}}$	-0.1641 ± 0.0062	-0.1641 ± 0.0062
$C_{\bar{D}}$	2.68 ± 0.54	2.70 ± 0.55

Table 6.5: Fitted parameters of the PDFs for the fits with and without isolated photon data included, using the parameterisation which allows a test of the $x\bar{u} \to x\bar{d}$ at $x \to 0$ assumption. The uncertainties are Hessian fit uncertainties.

Dataset	χ^2/n_{points}	
	HERA I	HERA I + isolated photon data
NC e^-p inclusive DIS	107/145	106/145
NC e^+p inclusive DIS	419 / 379	419 / 379
CC e^-p inclusive DIS	20 / 34	20 / 34
CC e^+p inclusive DIS	29 / 34	29 / 34
ZEUS isolated photons with jets	-	2.0/4
Correlated χ^2	-	1.6
Total χ^2/dof	575/581	579/585

Table 6.6: Partial and total χ^2 values for proton PDF fits to the HERA I inclusive DIS and to the isolated photon data, using the parameterisation which allows a test of the $x\bar{u} \to x\bar{d}$ at $x \to 0$ assumption, and with the momentum sum rule dropped.

Parameter	HERA I	HERA I + isolated photon data
B_g	0.202 ± 0.036	0.200 ± 0.036
C_g	8.63 ± 0.93	8.59 ± 0.93
B_{u_v}	0.665 ± 0.028	0.664 ± 0.028
C_{u_v}	4.64 ± 0.17	4.64 ± 0.17
E_{u_v}	9.9 ± 2.0	9.9 ± 2.0
C_{d_v}	4.04 ± 0.48	4.01 ± 0.47
$A_{\bar{U}}$	0.1149 ± 0.0081	0.1161 ± 0.0081
$A_{\bar{D}}$	0.157 ± 0.027	0.151 ± 0.026
$B_{\bar{D}}$	-0.1641 ± 0.0061	-0.1643 ± 0.0061
$C_{\bar{D}}$	2.68 ± 0.56	2.67 ± 0.55
p_{proton}	1.000 ± 0.012	0.998 ± 0.012

Table 6.7: Fitted parameters of the PDFs for the fits with and without isolated photon data included, using the parameterisation which allows a test of the $x\bar{u} \to x\bar{d}$ at $x \to 0$ assumption and with the momentum sum rule dropped. The uncertainties are Hessian fit uncertainties.

Chapter 7

α_s Running Tests

This Chapter presents tests of the running of α_s, based on a QCD analysis of world collider inclusive DIS and jet cross section data. First, the motivation is given with an overview of the related literature. Then, the variant of the Fixed-Flavour Number Scheme used is described. Different variants of the FFNS and VFNS are compared by making fits to DIS and jet data. After that, tests of the running of α_s are presented, made within the adopted variant of the FFNS. A discussion of the results is given afterwards.

7.1 Motivation and the Idea

In Section 1.3.4 the formula for the running of α_s with the energy scale μ_R was given to leading order. We quote it here one more time for convenience:

$$\alpha_s(\mu_R) = \frac{\alpha_s(\mu_0)}{1 + \frac{\alpha_s(\mu_0)}{12\pi}(11N_c - 2n_f)\ln\frac{\mu_R^2}{\mu_{R,0}^2}}. \tag{7.1}$$

The running of α_s depends on the theory parameters $\alpha_s(\mu_{R,0})$[1], the number of flavours contributing to virtual loops, n_f, and the number of colours, N_c. Contributions from heavy flavours to virtual loops are enabled at the energy scales (switching points) related to the masses of the corresponding heavy quarks. This scale is taken to be equal to the heavy quark mass, m_h ($h = c,\ b,\ t$), so that:

$$n_f(\mu_R) = \begin{cases} 3, & \mu_R < m_c \\ 4, & m_c \leq \mu_R < m_b \\ 5, & m_b \leq \mu_R < m_t \\ 6, & \mu_R \geq m_t \end{cases} \tag{7.2}$$

[1] $\mu_{R,0}$ is typically set to the mass of the Z boson, $\mu_{R,0} = M_Z$. Thic choice is used also in this thesis.

Such a step-like change of n_f leads to a sudden change of the slope (appearance of "kinks") of the running. In contrast, a variation of the $\alpha_s(M_Z)$ value moves the whole running α_s curve up or down. At NLO, the $\alpha_s(\mu_R)$ curve is continuous when $\mu_F = \mu_R$, while its derivative with respect to μ_R has jumps at the switching points (see formula (1.34) Section 1.3.4).

Fixing $N_c = 3$ (SU(3) gauge group), the parameters n_f and $\alpha_s(M_Z)$ can be measured by making a fit to the cross section data. Since the evolution of the PDFs depends on α_s, the PDFs have to be fitted simultaneously with $\alpha_s(M_Z)$ and n_f. Therefore, the most appropriate data for the extraction of n_f and $\alpha_s(M_Z)$ are cross sections of inclusive deep inelastic lepton-proton scattering and cross sections of jet production. Inclusive DIS data constrain the PDFs, while jet data are strongly sensitive to α_s (at LO, the cross section of inclusive jet production in pp scattering is proportional to the second power of α_s) and span over a large region of energy scales; jet transverse energies in recent measurements by the LHC experiments reach values of a few TeV (see e.g. [153]).

A measurement of $\alpha_s(M_Z)$ is motivated by the fact that $\alpha_s(M_Z)$ is one of the free parameters of the Standard Model, while the motivation for a measurement of n_f^{loops} requires an additional discussion. In this work, the number of real flavours appearing in the initial and final state, n_f^{real}, is not varied, as it would lead to a significant modification of the theoretical calculations. Allowing $n_f^{\text{loops}} \neq n_f^{\text{real}}$ for massive particles participating in the loops does not break the cancellation of the IR and collinear divergences, since IR loop contributions and collinear splittings involving massive particles are separately finite. Physically, the appearance of a heavy particle in loops but not in legs of Feynman diagrams could correspond for example to one of the following cases:

- **Measurements just below the heavy particle production threshold.** The centre-of-mass energy squared of the collision, s, must be greater than $s > 4m_{hq}$ for production of e.g. a heavy quark-antiquak pair to be possible, were m_{hq} is the mass of the heavy quark. At the same time, the loop contribution from the heavy quark to α_s running is starting at a scale $\mu_R = m_{hq}$ (according to formula (7.2)). Therefore, at scales $m_{hq} < \mu_R < 4m_{hq}$, the heavy quarks contribute to loop corrections but don't appear in legs of the Feynman diagrams.

- **Contribution of the top quark to inclusive jet cross sections at LHC.** The top quark decays almost exclusively into a W boson and a bottom quark, and the W boson decays mainly hadronically, into a $q\bar{q}$-pair. Therefore the energy of the initial t and $\bar{t}$ quarks of the $t\bar{t}$-pair after their decays is typically distributed between many jets of lower transverse energy [154]. For the inclusive jet cross section as function of jet transverse energy at LHC it means, that jets from $t\bar{t}$ events are spread in the lower part of the E_T spectrum (where the jet cross section is much higher than at higher E_T), while at the higher part of the spectrum the change in the cross section due to top-quark loop corrections in the α_s evolution starts to be distinguishable.

It was recently confirmed with dedicated Monte Carlo studies that jets from top decays have a marginal effect on inclusive jet cross sections measured with the CMS detector [155].

Speaking more generally, the approach for indirect searches for new physics presented in this thesis is limited to those possible models beyond the SM, that alter the α_s running and mainly do not lead to production of high-energetic jets (for instance, a pair of particles decays into invisible states or to many low-energetic jets).

The measurement of n_f^{loops} presented in this Chapter can be interpreted in two different ways, which are discussed below.

7.1.1 Test of the Running

The running of α_s and measurements of $\alpha_s(\mu_R)$ made at different energy scales, $\mu_R = Q$, are presented in Figure 7.1 [156]. As can be seen from the plot, these measurements are consistent with the QCD running of α_s.

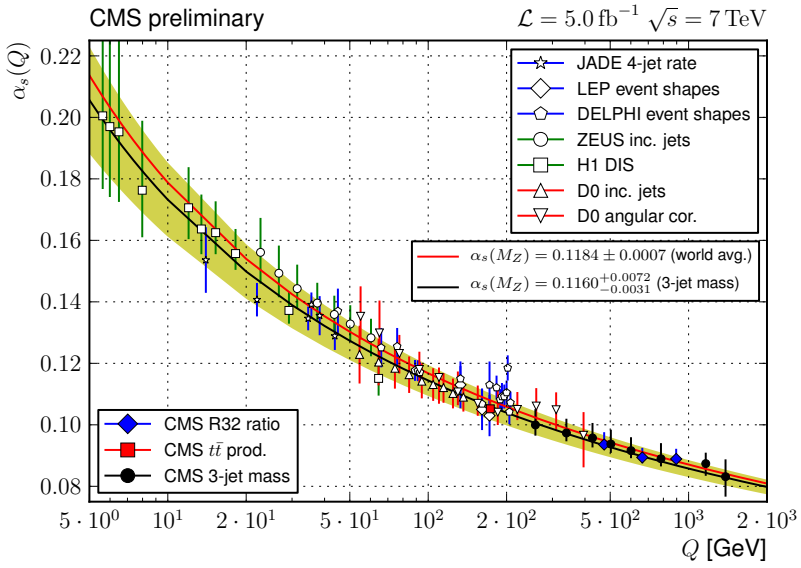

Figure 7.1: Comparison of the $\alpha_s(Q)$ evolution as determined in [156] (curve with uncertainty band) to the world average (upper curve). In addition, measurements of the running strong coupling constant $\alpha_s(Q)$ from e^+e^-, ep, pp and $p\bar{p}$ collider experiments are shown.

However, during the extraction of $\alpha_s(Q)$ at different Q, the running was implicitly assumed, at least for some of the measurements. For instance, in Ref. [156], α_s values were extracted from the measurement of the mass of 3-jet systems at LHC, using the following procedure:

1. A set of theory predictions was prepared, corresponding to different values of $\alpha_s(M_Z)$. For each prediction, the appropriate MSTW2008-NLO PDF set was used, obtained with the corresponding $\alpha_s(M_Z)$ value (range of available $\alpha_s(M_Z)$ from 0.110 up to 0.130 in steps of 0.001).

2. A χ^2 test was performed, comparing the 3-jet cross sections in different regions of the 3-jet mass to the set of theoretical predictions.

3. The best value of $\alpha_s(M_Z)$ was found for each 3-jet mass bin, this value was evolved to that corresponding to the measurement energy scale using the QCD running of α_s at NLO.

4. The energy scale corresponding to the measurement (chosen renormalisation scale) was defined as $\mu_R = m_3/2$, where m_3 is the mass of the 3-jet system. The position of the point on the plot in Fig. 7.1 along the X axis was defined as a cross-section weighted average of μ_R corresponding to a given bin, where the cross section was given by the theory prediction using the MSTW2008 PDF set with NLO evolution.

It is obvious that the running of α_s is not varied in this procedure: the standard QCD running was assumed in steps 1, 3, 4. Only the overall position of the α_s curve is changed when the $\alpha_s(M_Z)$ is varied.

To quantitatively state whether the QCD running is preferred by the data, one could allow different variants of the running and perform a comparison to experimental data, which would determine the best variant, according to e.g. a χ^2 test. Such a variation can be obtained by variation of the n_f^{loop} parameter, introduced at different energy scales (accessible at particle colliders).

7.1.2 Sensitivity to Effects of New Physics

Loop corrections due to SUSY particles near the production threshold. Supersymmetry (SUSY) is a proposed extension of the Standard Model that aims to fill some of the gaps of the SM. It predicts a partner particle (also called *sparticle*) for each particle of the Standard Model. The new particles would interact through the same forces as Standard-Model particles, but they would have different masses.

In Ref. [157, 158] the one-loop virtual-sparticle corrections to QCD jet cross sections were calculated. Such calculations may be appropriate in a case when the centre-of-mass energy, s, is below the threshold of production of the sparticle pairs, $s < 4m^2_{\text{sparticle}}$, where $m_{\text{sparticle}}$ is the sparticle mass, or if the new final states would not manifest themselves significantly in the jet cross section as outlined in the introduction of this section; so that sparticles would manifest themselves only via virtual corrections to the cross sections. It was shown, that one-loop sparticle corrections to the Born-level approximation for the jet production in $p\bar{p}$ collisions can be as large as several per cent.

The first two coefficients of the beta-function in the presence of virtual-sparticle loops are given by [159]:

$$b_0 = \frac{33 - 2n_f - 6n_{\bar{g}} - \frac{1}{2}n_{\bar{f}}}{12\pi}, \tag{7.3}$$

$$b_1 = \frac{1}{24\pi^2}\left(153 - 19n_f - 48n_{\bar{g}} - \frac{11}{2}n_{\bar{f}} + \frac{13}{2}n_{\bar{g}}n_{\bar{f}}\right), \tag{7.4}$$

where $n_{\bar{g}}$ is the number of gluino generations, and $n_{\bar{f}}$ is the number of squark flavours. If one puts $n_{\bar{g}} = n_{\bar{f}} = 0$, the standard QCD formulae (1.29), (1.30) are recovered.

Figure 7.2 [160] shows the effect of the sparticle loops on the evolution of α_s. The evolution slows down above the switching point of the sparticle contribution. Qualitatively the same effect is obtained in other works on the topic [161] and [159] and is presented in Fig. 7.3.

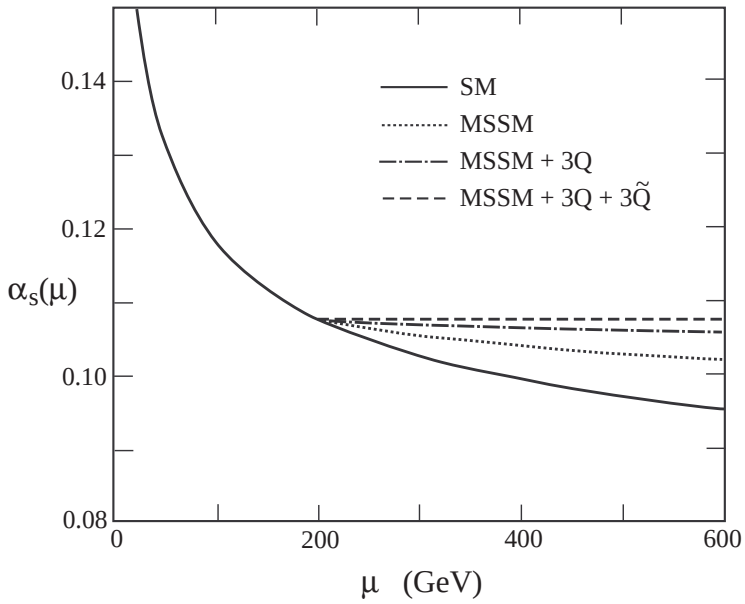

Figure 7.2: The one-loop evolution of $\alpha_s(\mu)$ versus μ compared to various SUSY scenarios normalised to $\alpha_s(M_Z) = 0.12$ [160]. The solid curve is the SM prediction; the dotted curve is the MSSM prediction with a common squark/gluino threshold at $\mu = 200$ GeV; the dot-dashed curve shows the effect of three singlet quarks with common mass $m_Q = 200$ GeV. The dashed curve shows the further effect of three singlet squarks if $m_{\bar{Q}} = 200$ GeV.

The effects of sparticle loops are also studied in [161] where the references mentioned above are discussed as well. The authors argue that the loop corrections appear in different parts of calculations:

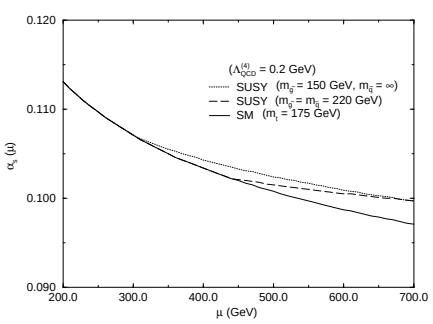

(a)

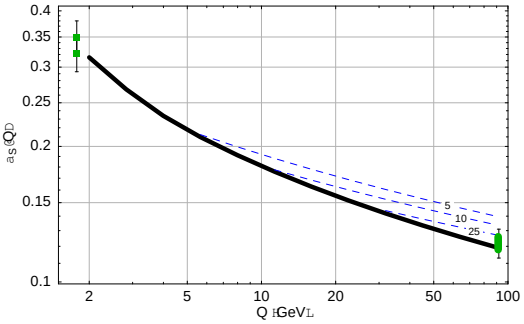

(b)

Figure 7.3: (a): The one-loop evolution of α_s versus μ for the SM (solid line) and SUSY cases [161]; (b): The evolution of α_s for SM (solid line) and for a series of scenarios for gluino masses $m_{\tilde{g}} = 5$, 10, and 25 GeV (without squark contributions) [159].

(a) In the PDFs evolution;

(b) In the α_s evoultion;

(c) In the additional virtual corrections of matrix elements (those that are not included in the α_s evolution).

Thus, in [157, 158] (b) and (c) are considered, while in [160] only (b) is considered.

The studies presented in this thesis correspond to the case when contributions (a) and (b) are considered, and not (c). Inclusion of contribution (c) would mean considerable change of details of theoretical predictions for the jet production and for the inclusive DIS cross sections, which is outside the scope of this thesis but in principle could be done in the future.

The studies of this thesis are not limited to the SUSY case and can be considered to be more general. We allow not only integer changes of the number of flavours in loops, but also fractional (both positive and negative) ones, which could be interpreted as a loop contribution of a particle of whatever origin with couplings different from those of the standard QCD multiplet.

Some further models that possibly can be tested with the presented method are briefly reviewed in Appendix B.1.

Model-independent search.

As outlined in the introduction to this section, one could imagine a scenario in which for different reasons, new particles contribute to virtual corrections of the jet cross sections but do not manifest themselves as high-energetic jets. For instance, when each member of new particle-antiparticle state decays invisibly or produce many low-energetic jets (similarly to the top quark example given earlier in this Section). The approach presented in this thesis allows constraints of such scenarios.

7.2 Heavy Flavour Treatment

In order to perform the α_s studies presented here, an appropriate scheme for the heavy quark treatment in the proton structure functions has to be adopted. There are many schemes on the market, mentioned in Section 1.3.6. However, not all of them are well suited for our purpose. We believe that the best option for the QCD analysis of the DIS and jet cross section data, involving tests of the α_s running is the Fixed-Flavour Number Scheme, since this scheme has a clear and unique formulation and the quark mass effects are treated consistently. In this scheme, the number of (light) quark flavours in the proton PDFs is kept constant, and the remaining heavy quarks are produced perturbatively in the matrix elements. Therefore, at low energy scales, E, of the order of the heavy quark mass, M, $E \sim M$, the scheme is expected to describe the data. At very large energies, large logarithms of type $\ln^n(E^2/M^2)$ may need to be resummed [50, 162–165] to give the correct behaviour of the structure functions (in the Variable Flavour Number Schemes the heavy quarks are included as active partons in the proton, which serves to resum these potentially large logarithms [166]).

VFN schemes (see Section 1.3.6) are not suitable for our approach also due to a fundamental reason. VFN schemes use the massless approach at large energy scales, while the studies presented here can be interpreted as a search for appearence of new heavy states. Since we modify the n_f parameter only in virtual corrections but not in the final (or initial) state, for a massless approach this would lead to non-cancellation of the soft and collinear divergences (Section 1.3.3).

7.2.1 FFNS A and FFNS B

Nowadays the FFN scheme is mostly used with an α_s evolution, that has a constant value of the parameter n_f (the same as the number of flavours in the PDFs) over the full evolution scale. However in this approach the contributions from heavy quark loops are not considered during the PDF evolution. In contrast, if one uses the evolution of α_s with changing n_f as a function of the scale (formula (7.2), as used for instance in Ref. [167], it will allow to at least partially resum possible large logarithms $\ln^n(E^2/M^2)$ via the inclusion of heavy-quark loops in the evolution of PDFs.

In this subsection these two variants of the FFN scheme are compared, by making a PDF fit to world collider data. The version of the FFN scheme with a constant n_f in α_s evolution will be referred to as "FFNS A", while the other, with variable n_f, as "FFNS B".

In a first step, a fit to the combined HERAI and HERAII inclusive DIS data of [168] was performed. The datasets are summarised in Table 7.1. The fits were performed in the FFNS A and FFNS B and were compared to results of the fit made within a GMVFN scheme as implemented by R. Thorne [58] (RT OPT scheme). The Fixed-Flavour Number Schemes were used with 3 flavours (u, d, s) in the proton. The code of

the OpenQCDRad [169] program, interfaced to HERAFitter, was used for calculating the heavy flavour contributions to the structure functions.

The PDFs were parameterised using 15 parameters, following the choice of [131], the parameterisation is given by formulae (3.24)-(3.28). $\alpha_s(M_Z)$ was fitted simultaneously with the PDFs.

Table 7.2 gives partial and total χ^2 values. It is seen that FFNS A gives as good a fit as the RT OPT scheme, while FFNS B gives a 16 χ^2 units better description than FFNS A.

Dataset	x range		Q^2 range, GeV^2		n points
CC e^+p 318 GeV	$8 \cdot 10^{-3}$	0.4	300	30 000	39
CC e^-p 318 GeV	$8 \cdot 10^{-3}$	0.65	300	30 000	42
NC e^-p 318 GeV	$8 \cdot 10^{-4}$	0.65	60	50 000	159
NC e^+p 300 GeV	$6.21 \cdot 10^{-7}$ $(5.73 \cdot 10^{-5})$	0.4	0.045	30 000	112 (70)
NC e^+p 318 GeV	$5.02 \cdot 10^{-6}$ $(4.06 \cdot 10^{-5})$	0.65	0.15	30 000	485 (377)
NC e^+p 225 GeV	$3.48 \cdot 10^{-5}$ $(8.12 \cdot 10^{-5})$	0.65	1.5	800	210 (204)
NC e^+p 252 GeV	$2.79 \cdot 10^{-5}$ $(6.51 \cdot 10^{-5})$	0.65	1.5	800	260 (254)

Table 7.1: The combined datasets of HERA I and HERA II inclusive DIS cross sections, measured by the ZEUS and H1 experiments. The bracketed numbers denote the corresponding values, when cut $Q^2 > 3.5$ GeV^2 is applied, which was used for the fits presented in this thesis.

Dataset	FFNS A	FFNS B	RT OPT
CC e^+p 318 GeV	39 / 39	39 / 39	39 / 39
CC e^-p 318 GeV	52 / 42	51 / 42	52 / 42
NC e^-p 318 GeV	228 / 159	224 / 159	223 / 159
NC e^+p 300 GeV	70 / 70	71 / 70	72 / 70
NC e^+p 318 GeV	447 / 377	440 / 377	452 / 377
NC e^+p 225 GeV	229 / 204	227 / 204	225 / 204
NC e^+p 252 GeV	230 / 254	230 / 254	230 / 254
Correlated χ^2	89	83	86
Total χ^2 / dof	1369 / 1129	1353 / 1129	1370 / 1129
$\alpha_s^{n_f=5}(M_Z)$	0.108671	0.1067	0.10495

Table 7.2: The comparison of the χ^2 values for the proton PDF+$\alpha_s(M_Z)$ fits to combinde HERA data [168] made with different treatment of the heavy quarks for the proton structure functions.

Dataset	$\mu_F = \mu_R$ choice	range of the relevant energy scale	n points	Reference
Charm cross section H1-ZEUS combined	$Q^2 + 4m_c^2$	$5 < Q^2 < 2000$ GeV^2	47	[170]
ZEUS inclusive dijet 98-00/04-07	$\frac{Q^2 + \overline{E_{T,\mathrm{B}}^{\mathrm{jet}}}^2}{2}$	$125 < Q^2 < 20\,000$ GeV^2, $8 < E_{T,\mathrm{B}}^{\mathrm{jet}} < 60$ GeV	22	[133]
H1 inclusive jet 99-00	$\frac{Q^2 + (P_T^{\mathrm{jet}})^2}{2}$	$150 < Q^2 < 15\,000$ GeV^2, $7 < P_T^{\mathrm{jet}} < 50$ GeV	24	[171]
H1 low Q2 inclusive jet 99-00	$\frac{Q^2 + (P_T^{\mathrm{jet}})^2}{2}$	$5 < Q^2 < 100$ GeV^2, $5 < P_T^{\mathrm{jet}} < 80$ GeV	28	[172]
ZEUS inclusive jet 96-97	$\frac{Q^2 + (E_{T,\mathrm{B}}^{\mathrm{jet}})^2}{2}$	$5 < Q^2 < 100\,000$ GeV^2, $8 < E_{T,\mathrm{B}}^{\mathrm{jet}} < 100$ GeV^2	30	[173]
CDF inclusive jets	P_T^{jet}	$62 < P_T^{\mathrm{jet}} < 527$ GeV	72	[174]
D0 pp jets	P_T^{jet}	$50 < P_T^{\mathrm{jet}} < 665$ GeV	110	[175]
BCDMS F2p 100 GeV	Q^2	$7.5 < Q^2 < 75$ GeV^2	83	[176]
BCDMS F2p 120 GeV	Q^2	$8.75 < Q^2 < 99$ GeV^2	91	[176]
BCDMS F2p 200 GeV	Q^2	$17 < Q^2 < 137.5$ GeV^2	79	[176]
BCDMS F2p 280 GeV	Q^2	$32.5 < Q^2 < 175$ GeV^2	75	[176]
ATLAS jets $0 \leq \lvert y \rvert < 0.3$	P_T^{jet}	$20 < P_T^{\mathrm{jet}} < 1\,500$ GeV	16	[177]
ATLAS jets $0.3 \leq \lvert y \rvert < 0.8$	P_T^{jet}	$20 < P_T^{\mathrm{jet}} < 1\,500$ GeV	16	[177]
ATLAS jets $0.8 \leq \lvert y \rvert < 1.2$	P_T^{jet}	$20 < P_T^{\mathrm{jet}} < 1\,500$ GeV	16	[177]
ATLAS jets $1.2 \leq \lvert y \rvert < 2.1$	P_T^{jet}	$20 < P_T^{\mathrm{jet}} < 1\,200$ GeV	15	[177]
ATLAS jets $2.1 \leq \lvert y \rvert < 2.8$	P_T^{jet}	$20 < P_T^{\mathrm{jet}} < 600$ GeV	12	[177]
ATLAS jets $2.8 \leq \lvert y \rvert < 3.6$	P_T^{jet}	$20 < P_T^{\mathrm{jet}} < 310$ GeV	9	[177]
ATLAS jets $3.6 \leq \lvert y \rvert < 4.4$	P_T^{jet}	$20 < P_T^{\mathrm{jet}} < 160$ GeV	6	[177]
CMS inclusive jets 2011	P_T^{jet}	$114 < P_T^{\mathrm{jet}} < 2116$ GeV	133	[153]
CMS electron Asymmetry rapidity	-	-	11	[178]
CMS Z Boson rapidity	-	-	35	[179]

Table 7.3: The datasets used for the comparison of FFNS A and FFNS B proton PDF fits.

Dataset	FFNS A $F_L\mathcal{O}(\alpha_s^2)$	FFNS B $F_L\mathcal{O}(\alpha_s^2)$	FFNS B $F_L\mathcal{O}(\alpha_s)$	RT OPT $F_L\ \mathcal{O}(\alpha_s^2)$
Charm cross section H1-ZEUS combined	50 / 47	49 / 47	49 / 47	43 / 47
ZEUS dijets	14 / 22	16 / 22	17 / 22	14 / 22
H1 high Q2 jets	12 / 24	12 / 24	12 / 24	11 / 24
H1 low Q2 jets	18 / 28	18 / 28	18 / 28	22 / 28
ZEUS inclusive jets	27 / 30	28 / 30	28 / 30	25 / 30
CDF inclusive jets	120 / 72	110 / 72	112 / 72	97 / 72
D0 pp jets	75 / 110	76 / 110	76 / 110	83 / 110
BCDMS F2p 100GeV	89 / 83	93 / 83	96 / 83	100 / 83
BCDMS F2p 120GeV	69 / 91	70 / 91	72 / 91	70 / 91
BCDMS F2p 200GeV	85 / 79	86 / 79	88 / 79	85 / 79
BCDMS F2p 280GeV	63 / 75	68 / 75	68 / 75	65 / 75
CC e^+p 318 GeV	61 / 39	57 / 39	56 / 39	60 / 39
CC e^-p 318 GeV	47 / 42	48 / 42	48 / 42	57 / 42
NC e^-p 318 GeV	232 / 159	232 / 159	231 / 159	228 / 159
NC e^+p 300 GeV	73 / 70	73 / 70	74 / 70	76 / 70
NC e^+p 318 GeV	548 / 377	512 / 377	495 / 377	484 / 377
NC e^+p 225 GeV	220 / 204	221 / 204	220 / 204	222 / 204
NC e^+p 252 GeV	223 / 254	225 / 254	222 / 254	225 / 254
ATLAS jets $0 \leq \lvert y\rvert < 0.3$	15 / 16	17 / 16	17 / 16	17 / 16
ATLAS jets $0.3 \leq \lvert y\rvert < 0.8$	7.6 / 16	7.2 / 16	7.3 / 16	5.9 / 16
ATLAS jets $0.8 \leq \lvert y\rvert < 1.2$	6.8 / 16	7.5 / 16	7.6 / 16	6.8 / 16
ATLAS jets $1.2 \leq \lvert y\rvert < 2.1$	5.8 / 15	6.9 / 15	7.0 / 15	6.6 / 15
ATLAS jets $2.1 \leq \lvert y\rvert < 2.8$	3.7 / 12	3.6 / 12	3.6 / 12	4.0 / 12
ATLAS jets $2.8 \leq \lvert y\rvert < 3.6$	2.7 / 9	2.8 / 9	2.7 / 9	3.0 / 9
ATLAS jets $3.6 \leq \lvert y\rvert < 4.4$	0.39 / 6	0.44 / 6	0.44 / 6	0.40 / 6
CMS inclusive jets	107 / 133	109 / 133	109 / 133	104 / 133
CMS electon Asymmetry rapidity	9.4 / 11	8.9 / 11	8.9 / 11	13 / 11
CMS Boson rapidity	54 / 35	51 / 35	52 / 35	52 / 35
Correlated χ^2	211	187	177	177
Total χ^2 / dof	2450 / 2060	2396 / 2060	2372 / 2060	2358 / 2060
$alpha_s^{n_f=5}(M_Z)$	0.118	0.118	0.118	0.118

Table 7.4: Partial and total χ^2 values for PDF fits made within different schemes for the heavy quark treatment.

	χ^2 DIS 2073 pts	χ^2 ftDY 199 pts	χ^2 jets 186 pts	$\alpha_s^{n_f=5}(M_Z)$
MSTW2008	1876	242	170	0.1202
MSTW2008 (DIS only)	1845		(193)	0.1197
MSTW $n_f = 3$ (DIS only)	1942		(>300)	0.1187
MSTW $n_f = 3$ (jets)	2010	269	177	0.1222

Table 7.5: The χ^2 values for DIS data, fixed target Drell Yan (ftDY) data and Tevatron jet data for various NLO fits performed using the GMVFNS used in the MSTW 2008 global fit and using the $n_f = 3$ FFNS for strucutre functions. The bracketed numbers denote the χ^2 values for jet data when not included in the fit. The data are taken from Ref. [180].

As a next step, it was decided to include jet cross section data in the fit. The used datasets included inclusive lepton-proton DIS data from HERA and jet production at HERA, Tevatron and LHC. They are summarised in Table 7.3.

Readily available predictions for the jet production cross sections exist only in the massless scheme and don't include electroweak effects. Since all of the jet data used correspond to energy scales that are well above the bottom quark mass, it was decided to use the theoretical predictions for them together with 5-flavour PDFs. The contribution from the top quark to the cross sections was included indirectly, only via virtual loops, that lead to the change of n_f^{loop} parameter to 6 above the top mass threshold in the α_s evolution, since the top contribution to jet final states is negligible, as outlined earlier.

The 5-flavour PDFs were obtained from the 3-flavour ones using the QCD matching conditions, as explained in [54] and implemented in the OpenQCDRad program (a similar scheme was developed by independent theorists [181, 182]). The necessary modifications of the HERAFitter code were carried out by the author of this thesis; the modifications included implementation [183–185] of parts of the OpenQCDRad program (matching of the 3-, 4- and 5-flavour PDFs and their evolution) within HERAFitter.

Table 7.4 summarises the χ^2 values (total and partial per dataset) resulting from the fit. The quality of the fit in FFNS B is considerably (47 χ^2 units less) better that those in FFNS A, while the RT OPT works somewhat better (14 χ^2 units) than FFNS B. Additionaly it was shown that by lowering the order of the predictions for the F_L structure function to the same order, as used for the F_2 and F_3 (column "FFNS B $\mathcal{O}(\alpha_s)$"), better description of the data can be achieved.

These results can be qualitatively[2] compared to results of Ref. [180]. There, a comparison of fits is given, made in the GMVFNS and FFNS A. Part of the results of this reference are quoted in Table 7.5.

[2]The comparison is only qualitative, since different input data were used.

Thus, in [180] it was shown that the proton PDF fit in the GMVFN scheme is considerably better than in the FFNS A (about 100 χ^2 units better), when the inclusive DIS data only are fitted. This result is to be compared with Table 7.2. We do not confirm the conclusion of [180] and additionally we show that by switching from FFNS A to FFNS B a sizeable improvement in the description of the data is achieved.

A similar conclusion can be made for the fits to inclusive DIS and jet data, however in this case FFNS B gives a somewhat worse description than RT OPT (38 χ^2 units worse for 2060 degrees of freedom). Compared to FFNS A, FFNS B gives a better description of the data by 54 χ^2 units. The results of Ref. [180] show a much larger difference between FFNS A and RT OPT than in our studies. The reason for this remains to be investigated.

7.2.2 Conclusions of the Section

- FFNS B and GMVFNS perform similarly well describing the DIS and jet collider data. FFNS B gives a somewhat better description than GMVFNS if only DIS data are fitted and somewhat worse if jet data are included.

- FFNS B gives a significantly better description than FFNS A for both DIS data and DIS plus jet data.

7.3 Tests of the α_s Running

7.3.1 The Approach

As was argued earlier in Section 7.1, the n_f parameter of the running $\alpha_s(\mu_R)$ can be used to parametrise the effects of new physics. In this Chapter, an extraction of this parameter from the world cross-section data is described. In the used approach, the n_f parameter is replaced by $n_f + \Delta n_f$, starting from some scale $\mu_R > \mu_{\rm thresh}$, and Δn_f is fitted. Depending on the value of $\mu_{\rm thresh}$, the number of flavours used in the running of α_s during the fit will be equal to

$$n_f = \begin{cases} n_f(\mu_R), & \mu_R < \mu_{\rm thresh} \\ n_f(\mu_R) + \Delta n_f, & \mu_R \geq \mu_{\rm thresh} \end{cases} \tag{7.5}$$

where $n_f(\mu_R)$ is given by (7.2). The scale $\mu_{\rm thresh}$ is fixed during the fit. A series of fits with different $\mu_{\rm thresh}$ is performed. A non-zero Δn_f can indicate possible effects beyond the Standard Model, which start to contribute at an energy scale around $\mu_{\rm thresh}$. Examples of such effects were discussed in Section 7.1.2. The value of $\mu_{\rm thresh}$ was chosen to be greater or equal than $\mu_{\rm thresh} \geq 1$ GeV. Thus, for $\mu_R < 1$ GeV always three flavours in the running of α_s was used. The parameter $\alpha_s(M_Z)$ and the proton PDFs were fitted simultaneously with Δn_f.

7.3.2 Settings of the Fit

For the fit, 25 datasets were used, corresponding to the inclusive DIS *ep* (H1 and ZEUS) and μp (BCDMS) scattering data and to the jet production data at HERA, Tevatron and LHC. The inclusive DIS data from HERA are described in Table 7.1, while the BCDMS and jet data are summarised in Table 7.3. The choice of the renormalisation and factorisation scales is given in the tables as well.

Additionaly to measurements made at colliders, the extracted value of α_s obtained in [186] by methods of lattice QCD was used as an input of the fit. The α_s value in [186] is quoted at 5 GeV and obtained with 3-flavour calculations (u, d, s), $\alpha_s^{n_f=3}(5\text{ GeV}) = 0.2034(21)$. For the fits described here, this value was evolved backwards with the 3-flavour QCD evolution at two loop order (NLO) to the scale of 0.99 GeV which is below the mass of the charm quark. Thus, the α_s value of $\alpha_s^{n_f=3}(0.99\text{ GeV}) = 0.452(12)$, where the bracketed number gives the uncertainty, was used as an additional input "measurement" and helps to stabilize the fit.

The 3-flavour proton PDFs were parameterised at the starting scale of $Q_0^2 = 1.9\text{ GeV}^2$ with 15 parameters, and the strange quark fraction, f_s, was set to $f_s = 0.4$ as in [131]. The Fixed Flavour Number Scheme (FFNS B) was used for the calculation of the proton structure functions, combined with modified α_s running, as explained above. The inclusive DIS data from HERA and BCDMS were treated using 3-flavour PDFs (u, d, s). The jet data from HERA and all data from Tevatron and LHC were treated using the 5-flavour PDFs (u, d, s, c, b), since these data are typically well above the bottom quark production threshold. The 5-flavour PDFs were obtained from the 3-flavour ones by using the QCD matching conditions, through the chain of 2 matchings: $3 \to 4$ and $4 \to 5$, performed at scales $\mu_{\text{matching}} = m_c,\ m_b$, respectively. For the matching and evolution of the PDFs, the OpenQCDRad package [169] was used, interfaced to HERAFitter. The same package was used for calculation of the proton structure functions, needed for the calculation of the predictions for inclusive DIS cross section.

The pole masses of charm, bottom and top quarks were set to $m_c = 1.67$ GeV [8], $m_b = 4.78$ GeV [8] and $m_t = 177$ GeV [187].

The corresponding HERAFitter steering files are given in Appendix B.2.

7.3.3 Results

An $\alpha_s(M_Z)$ + PDF fit was performed first, with Δn_f fixed to 0, to get a reference value of χ^2. The result of the fit is shown for the CMS jet data in Figure 7.4, for the CDF jet data in Figure 7.5, and for the ZEUS dijet data (Chapter 4) in Figure 7.6[3]. The partial values of χ^2 per dataset are summarised in Table 7.6. The total χ^2 value of the fit is

[3]Since there are 26 data sets in total which were used for the fit, for practical reasons only a comparison to most relevant data sets is presented.

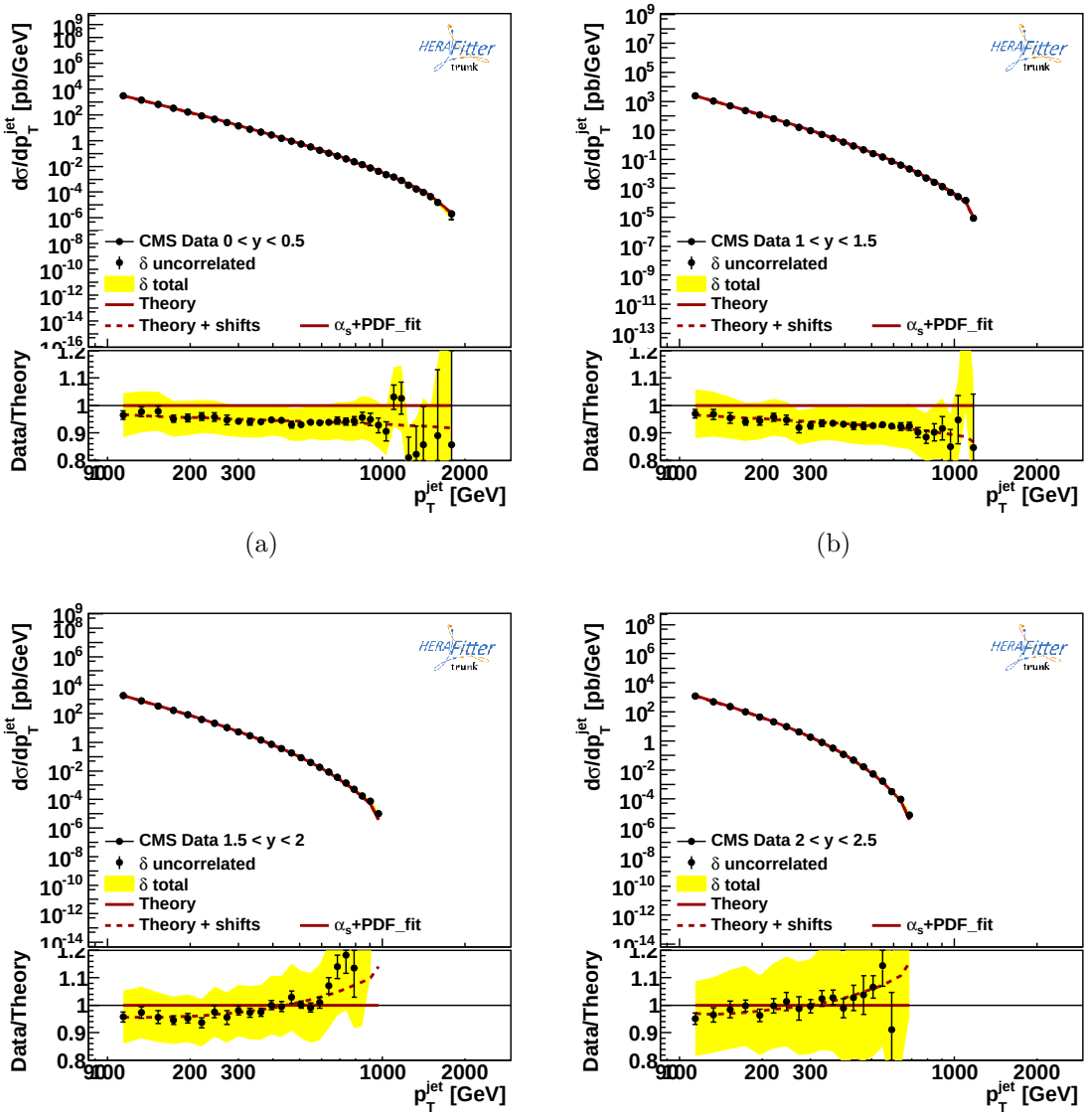

Figure 7.4: Comparison of the differential cross section of inclusive jet production as a function of the jet transverse momentum, as measured by the CMS collaboration [153], to the fitted theory predictions in different bins of the absolute jet rapidity. Error bars of the data points represent the uncorrelated uncertainty, while the yellow filled area represent the total uncertainty. The fitted theory predictions are shown before (continuous line) and after (dashed line) the shift due to systematic uncertainties of the data. The size of the shift is determined from the fit and the corresponding penalty is added to the expression for χ^2. In the legend, "Theory" and "α_s+PDF_fit" refer to the same fit result on the plots.

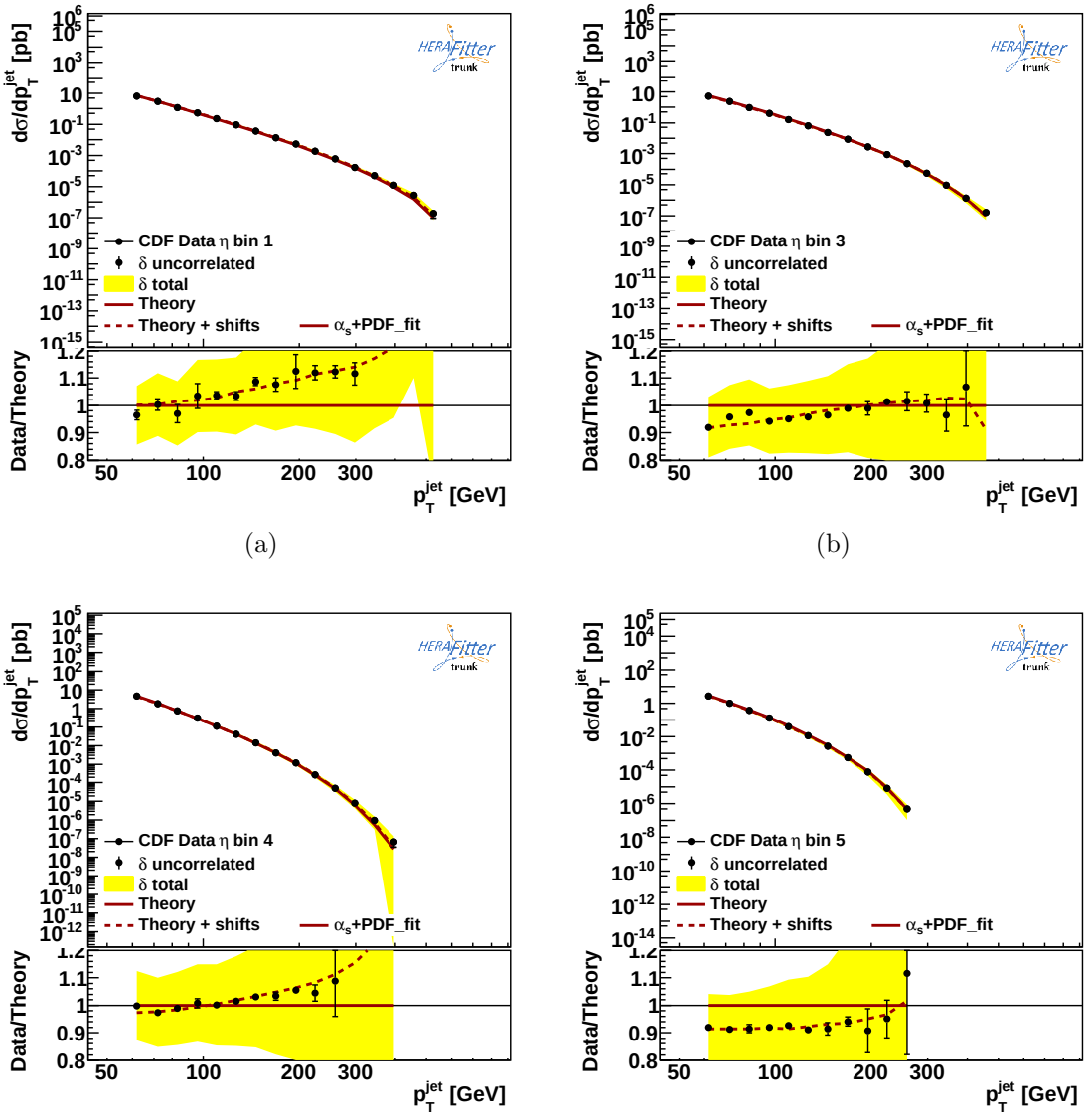

Figure 7.5: Comparison of the differential cross section of inclusive jet production as a function of the jet transverse momentum, as measured by the CDF collaboration [174], to the fitted theory predictions in different bins of the jet rapidity. The other details are as in the caption for Figure 7.4.

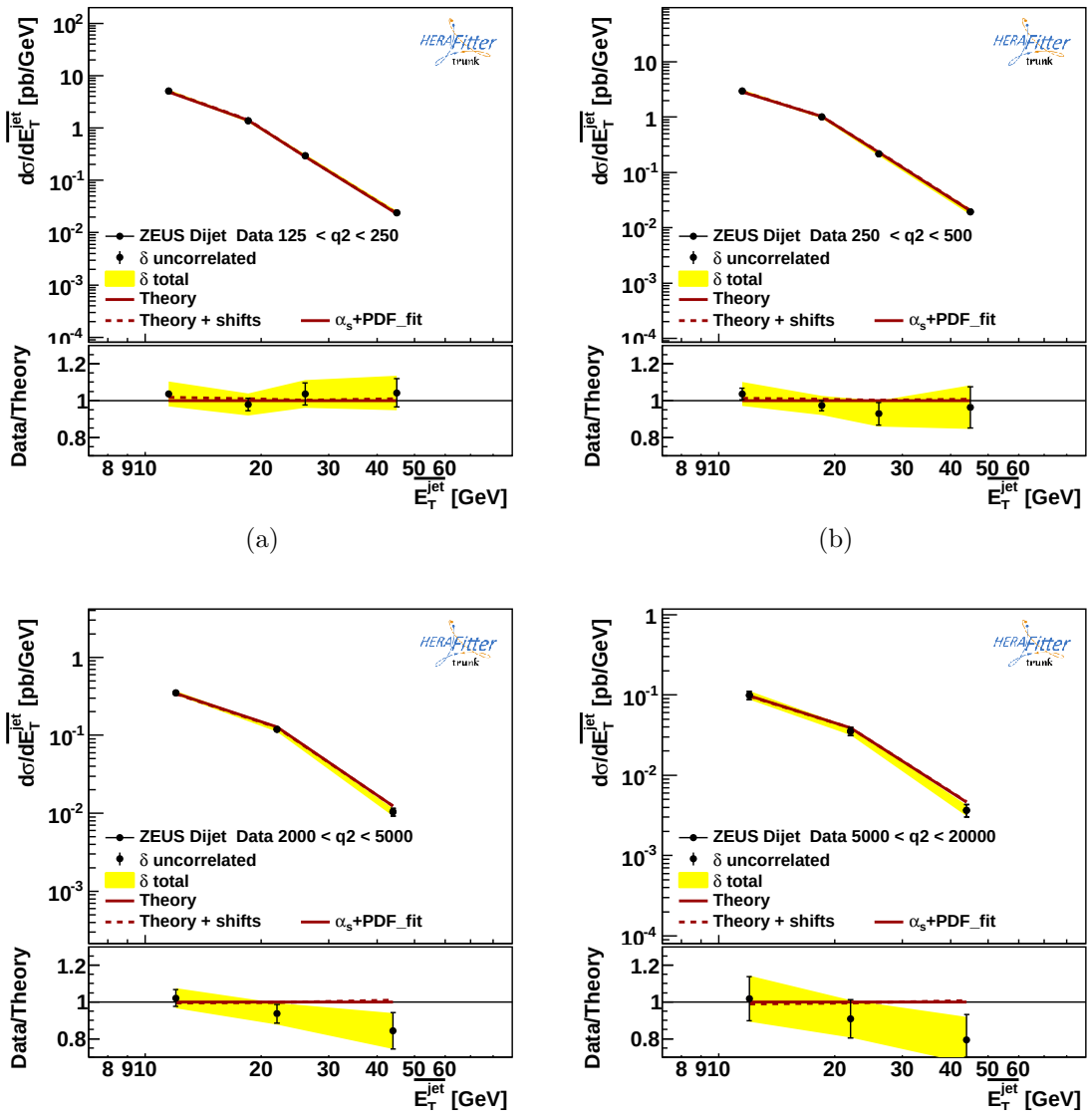

Figure 7.6: Comparison of the differential cross section of inclusive dijet production as a function of the mean transverse energy of the two jets in the Breit frame, as measured by the ZEUS collaboration [133], to the fitted theory predictions in different bins of Q^2. The other details are as in the caption for Figure 7.4.

Dataset	$\chi^2/N_{\text{data points}}$
HPQCD lattice alphas 2010	0.17 / 1
ZEUS inclusive dijet 98-00/04-07 data	19 / 22
H1 inclusive jet 99-00 data	12 / 24
H1 low Q2 inclusive jet 99-00 data	18 / 28
ZEUS inclusive jet 96-97 data	32 / 30
CDF inclusive jets	108 / 72
D0 pp jets	79 / 110
BCDMS F2p 100GeV	92 / 83
BCDMS F2p 120GeV	70 / 91
BCDMS F2p 200GeV	86 / 79
BCDMS F2p 280GeV	67 / 75
CC e^+p 318 GeV	55 / 39
CC e^-p 318 GeV	47 / 42
NC e^-p 318 GeV	231 / 159
NC e^+p 300 GeV	73 / 70
NC e^+p 318 GeV	523 / 377
NC e^+p 225 GeV	221 / 204
NC e^+p 252 GeV	225 / 254
ATLAS jets $0 \leq \|y\| < 0.3$	17 / 16
ATLAS jets $0.3 \leq \|y\| < 0.8$	6.6 / 16
ATLAS jets $0.8 \leq \|y\| < 1.2$	7.1 / 16
ATLAS jets $1.2 \leq \|y\| < 2.1$	6.6 / 15
ATLAS jets $2.1 \leq \|y\| < 2.8$	3.5 / 12
ATLAS jets $2.8 \leq \|y\| < 3.6$	2.8 / 9
ATLAS jets $3.6 \leq \|y\| < 4.4$	0.44 / 6
CMS inclusive jets 2011	105 / 133
Correlated χ^2 (326 sources)	177
Total χ^2 / dof	2286 / 1967
$\alpha_s^{n_f=5}(M_Z)$	0.1177(5)

Table 7.6: Partial and total χ^2 values for the PDF + α_s fit to the DIS and jet collider data. The fitted value of $\alpha_s(M_Z)$ is quoted with the fit uncertainty only.

$\chi^2_{\text{central}} = 2286$ for 1967 degrees of freedom. Apart from the DIS HERA Neutra Current data at $\sqrt{s} = 318$ GeV and CDF jet data, the partial χ^2 per number of data points are close (typically smaller) to unity. The fitted value of $\alpha_s(M_Z)$ is $\alpha_s^{n_f=5}(M_Z) = 0.1177(5)$, where the number in brackets is the fit uncertainty (only), it is consistent with the input lattice QCD measurement of $\alpha_s^{n_f=3}(5\text{ GeV}) = 0.2034(21)$; the latter corresponds

to $\alpha_s^{n_f=5} = 0.1174(7)$. The fit uncertainties were estimated using the conventional χ^2 tolerance, $\Delta\chi^2 = 1$.

The Δn_f parameter was released at the next step. A series of fits with different values of $\mu_{\rm thresh}$ was performed, as explained above. Fits converged properly for $3 < \mu_{\rm thresh} < 100$ GeV , while for lower values of $\mu_{\rm thresh}$ only the central values of the parameters were reliable. More effort is needed to estimate uncertainties there. However, the situation at higher scales is more intriguing, therefore they were studied separately. For higher values, $\mu_{\rm thresh} > 100$ GeV, the χ^2 scan was done with respect to Δn_f (PDFs and $\alpha_s(M_Z)$ were fitted at each iteration of the scan), made at fixed values of $\mu_{\rm thresh} = 150$, 200, 300, 400, 600, 800 and 1000 GeV. The result of this scan (χ^2 profiles) is given in Figure 7.7.

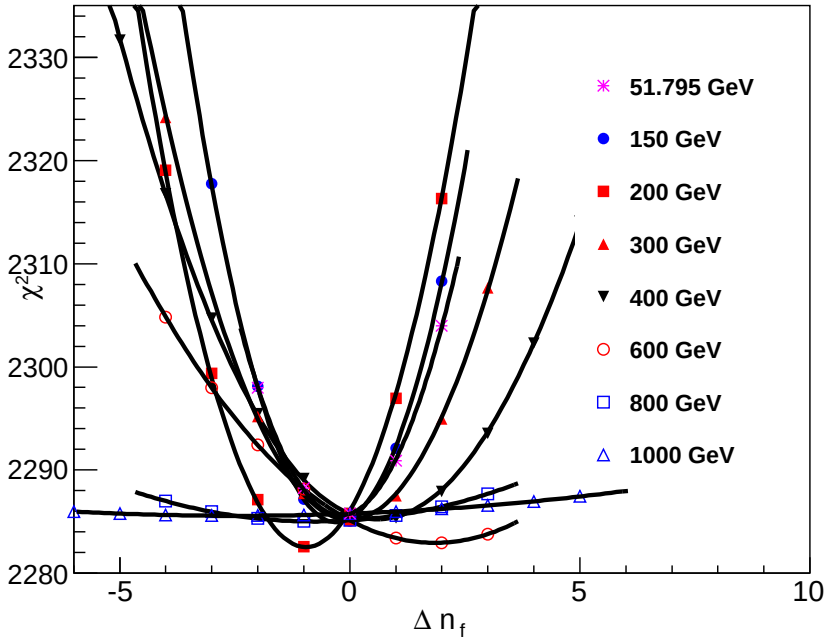

Figure 7.7: χ^2 scan against Δn_f at different thresholds $\mu_{\rm thresh}$. The scan at $\mu_{\rm thresh} = 51.795$ GeV was done for a cross check with the fit; χ^2 scan result: $\Delta n_f = -0.19 \pm 0.51$, fit result: -0.17 ± 0.52.

Additionaly, a series of fits was performed for a simultaneous variation of the factorisation and renormalisation scales by a factor 2 up and down, $\mu_F = \mu_R = 2\mu_0$, or $\mu_F = \mu_R = 0.5\mu_0$. The scales were varied for the jet data only. Since again not all fits converged, the following procedure was chosen. The largest deviation of Δn_f from the

fit with $\mu_F = \mu_R = \mu_0$ was determined. It was symmetrised and used as a systematic uncertainty of Δn_f at all values of μ_{thresh}, which is expected to be a conservative estimate.

The summary of these fits is given by the dependence of $n_f + \Delta n_f$ on the μ_{thresh} value in Figure 7.8. The fit uncertainty and the total uncertainty are shown separately on the plot. The total uncertainty was obtained as a square root of the sum of squared fit and scale uncertainties. Within the total uncertainties, Δn_f is consistent with 0, which supports the QCD running of α_s.

Figure 7.9 shows the dependence $\chi^2 - \chi^2_{\text{central}}$ on μ_{thresh}. The open circles correspond to the fits for which the central value of the parameters was determined but not the uncertainties.

It was checked that the fitted values of the $\alpha_s^{n_f+\Delta n_f}(M_Z)$ are consistent with the value of $alpha_s$ extracted by lattice methods in [186], which was used as an input to the fit. The plot with the dependence of $\alpha_s^{n_f+\Delta n_f}(M_Z)$ on μ_{thresh} is given in Appendix B.3.

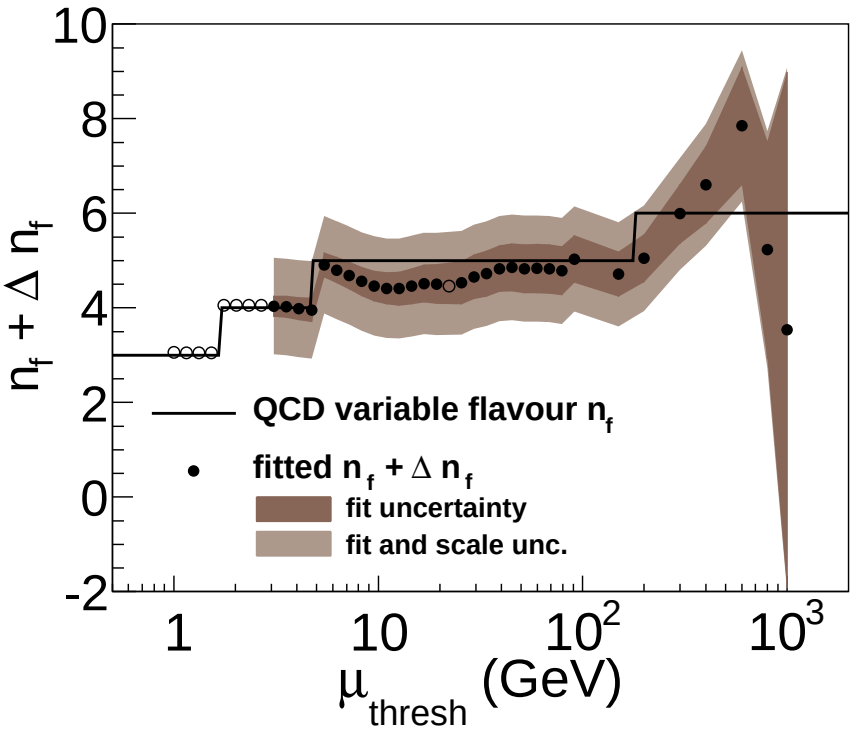

Figure 7.8: Measurement of Δn_f at different energy scales. The open circles corresponds to the fits for which only centra value of the parameters was determined but not the uncertainties.

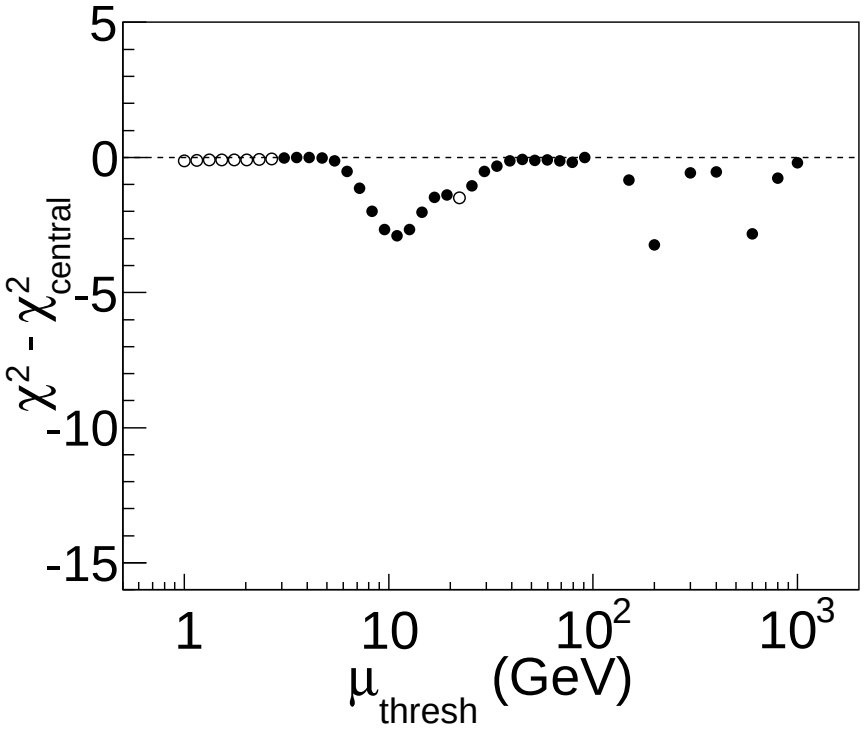

Figure 7.9: Dependence of the difference $\chi^2 - \chi^2_{\text{central}}$ on μ_{thresh}. $\chi^2_{\text{central}} = 2286$ corresponds to the fit with Δn_f set to zero. The open circles corresponds to the fits for which only centra value of the parameters was determined but not the uncertainties.

7.3.4 Comparison to Other Results and Exclusion Limits

At the finishing stage of the thesis compilation, an arXiv preprint was detected [188], in which a group of theorists (D. Becciolini et al.) utilise a similar, however less sophisticated approach to analyse the R_{32} ratio of the trijet to dijet cross section at the LHC, measured by the CMS collaboration [189]. The authors of Ref. [188] parametrised the effects of new physics (Supersymmetry in their case) with the n_{eff} parameter:

$$\frac{\alpha_s(Q)}{\alpha_s^{SM}(Q)} \approx 1 + \frac{n_{\text{eff}}}{3\pi}\alpha_s(m_X)\log\frac{Q}{m_X}, \quad \text{for Q} \geq \text{m}_\text{X}. \tag{7.6}$$

In this formula, $\alpha_s^{SM}(Q)$ is the Standard Model running α_s and $\alpha_s(Q)$ corresponds to the modified running due to replacement of n_f with $n_f + n_{\text{eff}}$ at scales $Q \geq m_X$, where m_X is the mass of a new heavy state. Surprisingly enough, there is a direct correspondence between the parameters m_X and n_{eff} of Ref. [188] and the parameters μ_{thresh} and Δn_f of this thesis.

The differences between the approach of Ref. [188] and the approach used in this thesis is that in Ref. [188] the LO order α_s running is considered and effects on the proton PDFs are neglected (the authors argue that they cancel in the R_{32} ratio). Also, some SUSY-specific parameters were varied in Ref. [188], however the effect of the variation was small. In this thesis, NLO running is used, the effect of the α_s running on the proton PDFs evolution is taken into account and much more data are used for the fit, which cover a broad range of energies, from very low, 3.5 GeV, to very high, up to about 2 TeV. The test of the α_s running is therefore performed in a considerably larger region than in Ref. [188].

The results of the two approaches were compared. Figure 7.10 taken from Ref. [188] shows the exclusion region of n_{eff} as a function of m_X. The two approaches are depicted together in Fig. 7.11. The approach presented in this thesis gives much stronger constraints than those of Ref. [188].

Since in this thesis the effects on Δn_f were probed at a broader range of μ_{thresh}, a further exclusion plot was produced, Figure 7.12. As an additional example, a star at ($\mu_{\text{thresh}} = 177$ GeV, $\Delta n_f = 2$) is placed. It would correspond to the appearance of a 4th quark generation, with the masses of both quarks of the new generation equal to the top quark mass. As can be seen from the figure, this assumption is excluded at 95% confidence level. Other scenarios considered in [188], are also indicated on the figures. They are significantly constrained.

To summarise, a method was presented which allows for indirect searches for effects of new physics by analysing jet cross sections at high energies. The developed approach is limited to those possible models beyond the SM, that alter the α_s running and mainly do not lead to production of high-energetic jets (for instance, a pair of particles decays into invisible states or to many low-energetic jets). We would like to note that the method developed in this thesis needs a somewhat more strict theoretical justification (for instance in a consideration of loop corrections of the matrix elements that are not taken into account by the α_s evolution). Under the assumption that the most important effects are treated consistently (PDF evolution with modified α_s running, chosen heavy flavour scheme etc), the method can give supplementary information in the indirect searches for new physics, as was demonstrated in this thesis. By adding further jet data, which is straightforward with the readily available tools (HERAFitter, FastNLO etc), it would be possible to make ever more strong constraints on new physics. By further improvement of the method and a more detailed study of the respective theory models, a more broad set of models can be tested.

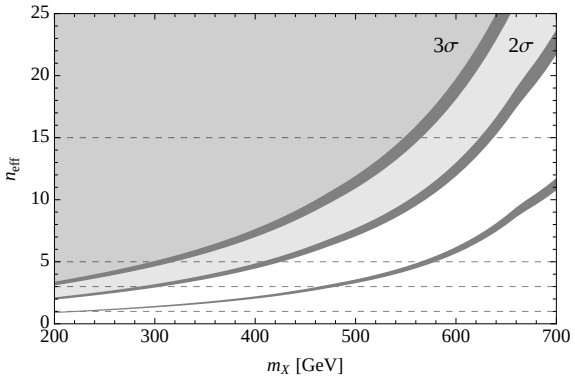

Figure 7.10: Figure from [188]. The shaded regions indicate the upper bounds on $n_{\rm eff}$ at 2σ and 3σ confidence levels, assuming the scale of new physics m_X is unknown. They are delimited by grey bands whose width show the effect of varying the Casimir C_X. As further indications, the third band shows a 1σ limit. To guide the eye, the dashed horizontal lines indicate vlaues of $n_{\rm eff}$ corresponding to one fundamental, one adjoint, one two-index symmetric and one three-index symmetric fermion.

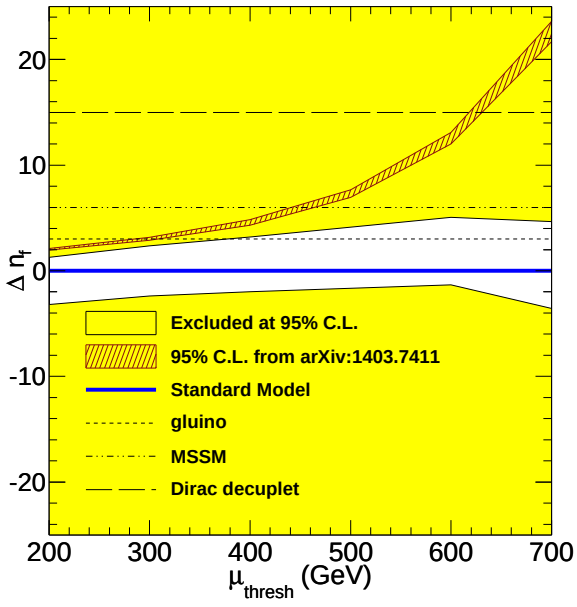

Figure 7.11: The shaded region indicate the bounds on Δn_f at 95% confidence level, assuming the scale of new physics $\mu_{\rm thresh}$ is unknown. The hatched line correspond to an upper bound at 95% C.L. obtained in a similar analysis [188]. Horizontal lines represent values of Δn_f corresponding to different models as discussed in [188] ($\Delta n_f = 0$ corresponds to the Standard Model).

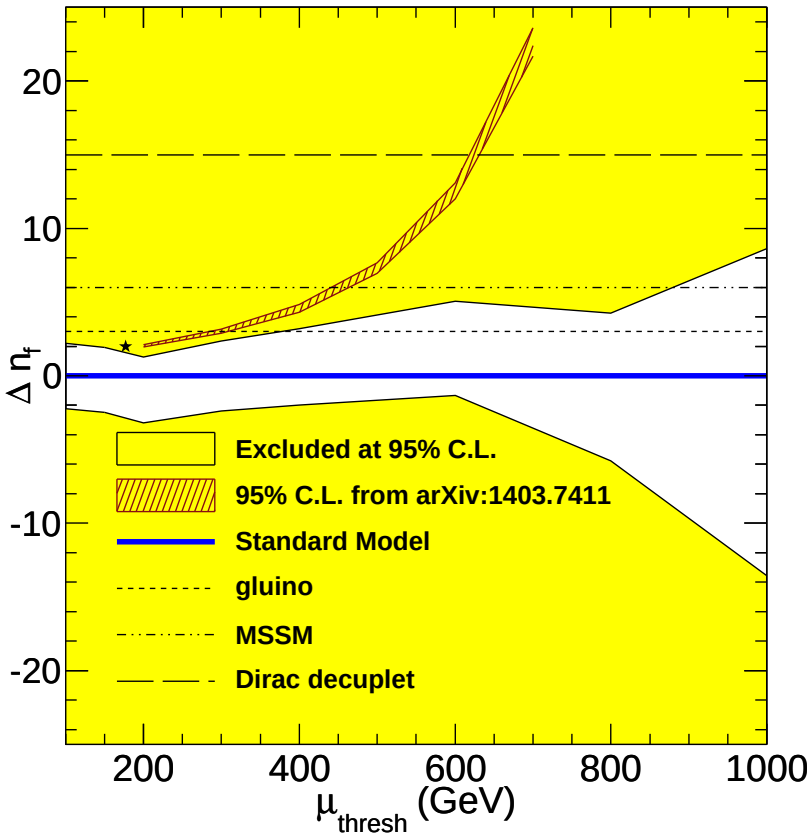

Figure 7.12: The same details as in Figure 7.11, except broader energy scale. The star at ($\mu_{\text{thresh}} = 177$ GeV, $\Delta n_f = 2$) would correspond to the appearance of 4th quark generation, with the masses of both quarks of the new generation equal to the top quark mass. As can be seen from the figure, this assumption is excluded at 95% confidence level.

Chapter 8

Power Pulsing Studies for the PLUME Project

In this chapter laboratory power pulsing studies of the silicon pixel sensor Mimosa26 are presented. The studies were done in the context of the research phase for the vertex detector for the future International Linear Collider (ILC). The power pulsing studies are performed using the digital (nominal) output of the Mimosa26 sensor. Additionally, an analogue output (test mode) was investigated, when the sensor is illuminated with a laser. Temperature studies of the sensor during power pulsing conditions are also summarised here.

Investigations of the Mimosa26 sensor under power pulsing conditions were done by studying both the fake hit rate and the hit rate when the sensor is irradiated with a ^{55}Fe radioactive source. Some results from these studies were reported in [190].

8.1 Introduction

8.1.1 International Linear Collider

One of the possible energy-frontier accelerators in the post-LHC era is the International Linear Collider[1] (ILC) [191]. At the ILC, it is planned to collide electrons and positrons at a centre-of-mass energy of 200-500 GeV (extendable to 1 TeV). Information from the ILC experiments could shed light on some of the areas of particle physics, where the Standard Model is incomplete as the theory of nature. These include unknown reasons for electroweak symmetry breaking, candidates for dark matter particles and the mechanism to generate the baryon-antibaryon asymmetry of the Universe. It is expected that all of these three problems can be solved by experiments at the TeV energy scale. The search for new phenomena is not the only goal for the ILC. It is also planned to reach a new

[1] Other projects, namely CLIC and FCC, are being extensively developed.

level of precision in measurements of the properties of already known phenomena. The properties of the recently found Higgs boson as well as properties of W- and Z-bosons, such as mass, width, and couplings, could be measured with high precision at the ILC. The corresponding physics analyses will require accurate reconstruction of secondary vertices arising from heavy quark decays. Since the Higgs coupling is proportional to a particle mass, it is important to measure the Higgs branching ratio. To measure the branching ratio of $H \to b\bar{b}$ and $H \to c\bar{c}$, the best possible performance of vertexing and flavour tagging is required. The ILC detectors will improve on the detectors built for LEP, HERA and LHC in the precision of their tracking and calorimetry.

8.1.2 Vertex Detector for the International Large Detector

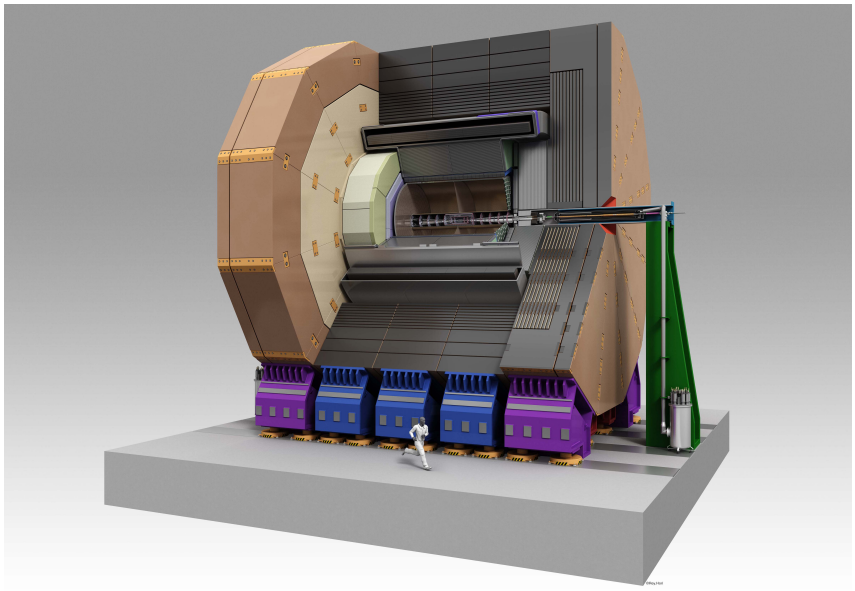

Figure 8.1: International Large Detector [192].

The International Large Detector (ILD) [192], Fig. 8.1 is a project for a multi-purpose detector for the ILC[2]. It has been designed for optimal performance of the particle-flow algorithm [193]. The inner-detector system is highly granular, and provides a detailed three-dimensional reconstruction of the events. The high-precision vertex detector (VTX) is composed of several multi-layers of pixel detectors. It will consist either of three superlayers each comprising two layers, or of 5 single layers (see Fig. 8.2). The accurate measurement of energy in the calorimeters by the particle-flow method requires as thin

[2]The other project is the Silicon Detector (SiD) [191]. It is planned that each detector can be alternately moved to the beam line.

tracker as possible, to minimise interactions before the calorimeters. The final pixel sensor technology for the VTX is not yet chosen. Several different technologies are investigated such as CCD [194], CMOS [195, 196] or DEPFET [197] sensors and others. The PLUME project [198], which aims at the development of the structure unit for the VTX (three superlayer version), uses CMOS pixel sensors.

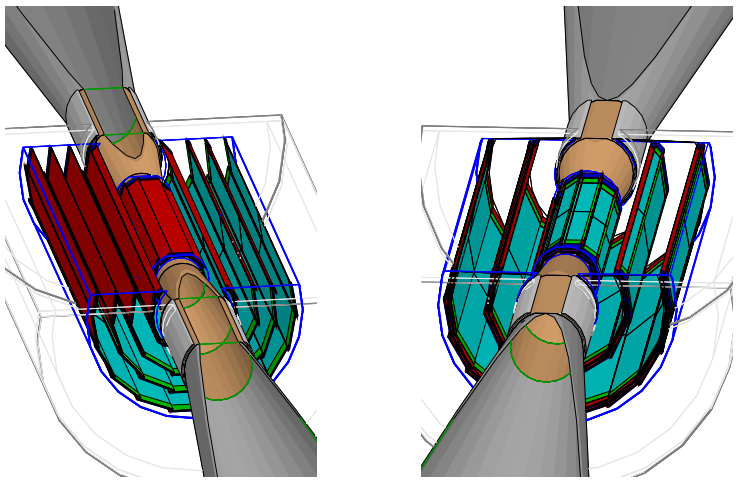

(a) (b)

Figure 8.2: Vertex detector geometries of the two design options: 5 single layers (a) and 3 double layers (b) [192].

8.1.3 PLUME Project

The PLUME (Pixelated Ladder with Ultra-low Material Embedding) collaboration [198], whose members are Institut Pluridisciplinaire Hubert Curien (IPHC, Strasbourg), Bristol University and DESY (Hamburg), is developing ultra-light ladders for a vertex detector for ILC. The PLUME ladder has a double-sided layout, which consists of two sensor layers separated by the support structure. Each layer has six Mimosa26 chips. A traversing particle produces two hits in the two ladder sensors. The hits are separated by approximately 2 mm (thickness of the ladder) and can be used to construct a mini-vector, resulting in a better reconstruction of tracks, compared to single-sided layout [198]. The schematic view of a ladder with its dimensions in longitudinal section is shown in Fig. 8.3. The material budget for the first PLUME prototype including two sensors, a kapton-metal flex cable and silicon carbide foam stiffener was $0.60\%X_0$. The aim of the collaboration is to reduce the material in the double-sided ladder further to about 0.3% of a radiation length.

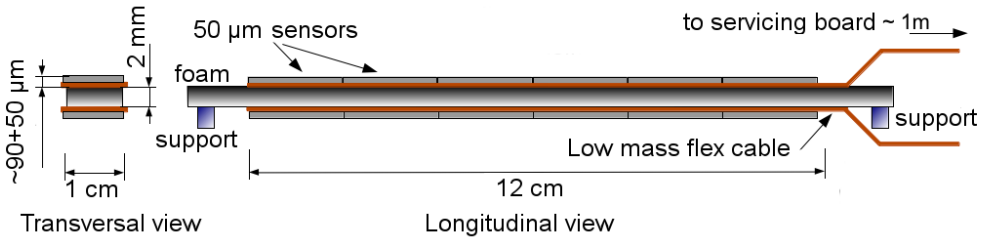

Figure 8.3: The schematic view of the double-sided PLUME ladder in the longitudinal section [198].

8.1.4 Power Pulsing

The ILC will operate, nominally, in 5 Hz mode with a 1 ms beam pulse (10 Hz mode is also considered), see Fig. 8.4. This means that in the nominal case, each 1 ms of intense collisions will be followed by 199 ms without collisions. The sparse filling of the beam allows a periodic reduction of the power to the minimum operating level for many sub-detectors, i.e. they will work in the so-called power pulsing regime. Thus, the heat load will be significantly reduced and it will be possible to use forced air for cooling. The need for cooling pipes and their supporting systems inside the detector will be reduced. The latter is a great advantage, since the requirements on track momentum resolution in the vertex detector and energy measurement in the calorimeter both demand light-weight low-material support structures, in order to have the minimal possible amount of the dead material inside the detector. In this sense, the three superlayer version for the VTX is preferable, since it requires fewer support structures than the 5 layer version.

The design of power-pulsed detector systems is a non-trivial challenge and such systems need to be thoroughly tested during the R&D phase of the ILC. Since power pulsing means pulsing of the currents, additional studies in high magnetic fields are also necessary.

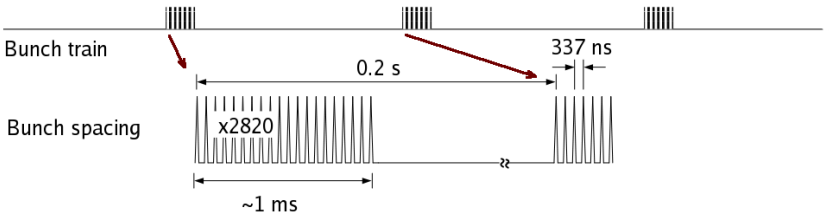

Figure 8.4: Schematic view of the bunch structure at the ILC.

It is planned that the complete set of laboratory tests of the PLUME ladder will

include power pulsing of the full ladder. As a preparation step, power pulsing studies of the single Mimosa26 pixel sensor have to be performed. Such studies using the analogue output of Mimosa26 were already started [199]. The results presented in this thesis extend previous studies using the analogue output and provide a first look at the digital output of the single Mimosa26 sensor under power pulsing conditions.

8.2 Experimental Setup

8.2.1 The Mimosa26 Pixel Sensor

Mimosa26[3] [200] is a monolithic active pixel sensor (MAPS) with fast binary readout and integrated zero suppression developed by IPHC (Strasbourg) & IRFU (Saclay) as the final sensor chip for the EUDET (Detector Research and Development toward the International Linear Collider) beam telescope for ILC vertex detector studies [201]. The chip is built in a CMOS 0.35 μm technology. The thickness of the epitaxial layer ranges from 14 to 20 μm (depending on the version), the sensor itself is thinned down to about 50 μm. The sensor matrix is composed of 576×1152 square pixels of 18.4 μm pitch. The size of the chip is 13.7×21.5 mm^2. The signals of 1152 pixels from a selected row are transferred to the bottom of the chip matrix, where 1152 column-level discriminators perform the analogue to digital conversion. The binary output of the discriminator is transferred to a zero suppression logic which only stores the addresses of those pixels which were fired. It allows the reduction of the transferred data a by factor 10 to 1000, depending on the hit density. The nominal clock frequency for the digital readout is 80 MHz. The chip readout time is 115.2 μs; it operates in the so-called rolling shutter mode, with rows being read one by one.

Amplification and correlated double sampling (CDS) are performed in each pixel. The CDS means that during the readout of the sensor, two samples are taken. The first sample is subtracted from the second in order to search for possible signals. It is a very efficient process for the noise suppression [202].

The layout of the sensor is shown on Fig. 8.5. On the top part of the sensor the analogue readout part is located (200 μm wide band). The analogue readout is introduced for test purposes only and can be removed for real vertex detector applications. In the case of analogue readout, correlated double sampling and zero suppression are not performed. The output data contain the raw signal from each pixel. The optimal readout frequency for the analogue readout mode is 20 Hz.

The Mimosa26 sensor was not designed to work under power pulsing; there is no on-chip standby mode logic. Moreover, the sensor has to be programmed using the embedded JTAG (Joint Test Action Group) controller before acquiring data. The JTAG

[3]MIMOSA stands for Minimum Ionising MOS Active pixel sensor, and (C)MOS is for (Complementary) Metal-Oxide-Semiconductor.

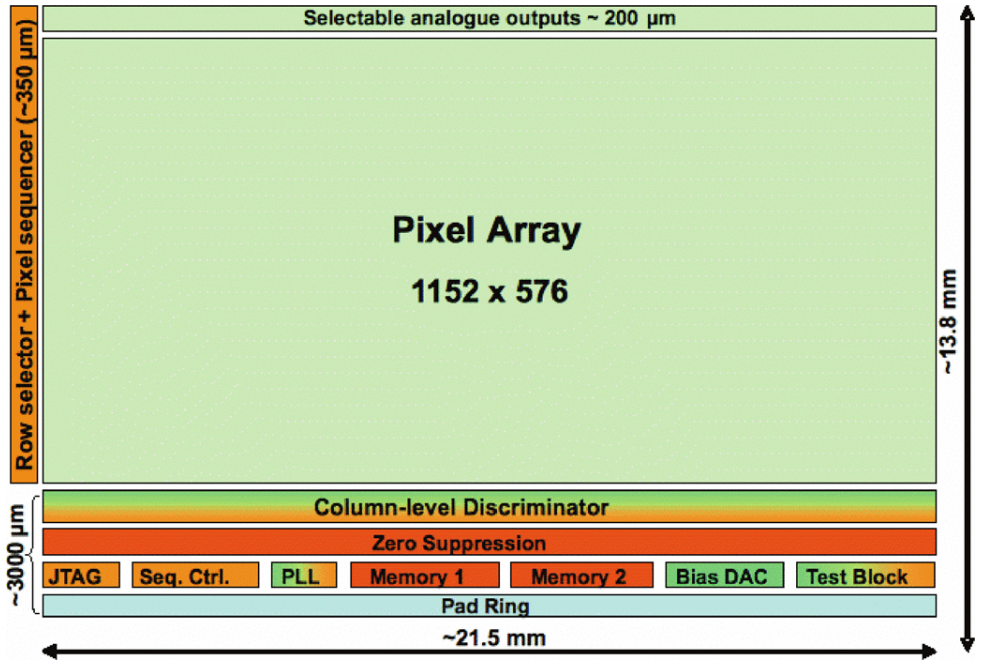

Figure 8.5: Schematic view of the Mimosa 26 sensor displaying the different functional blocks [200].

programming procedure takes a few tens of ms; this delay is not constant, because the slow control is done by software. Therefore, periodically switching the sensor off and on is not appropriate. The easiest way to power pulse the sensor is thus to reduce the voltage periodically to the minimal operating level. The minimal voltage is defined by the necessity to maintain the content of the configuration registers and the continuous clock with synchronisation signals used by the DAQ.

8.2.2 Setup for the Analogue Readout

The layout of the test setup for the Mimosa26 analogue readout studies is shown on Fig. 8.6 [203]. The main parts of the setup were:

- a Mimosa26 pixel sensor;
- a JTAG interface board for the programming of the Mimosa26 registers;
- a digital auxiliary board, used for powering and controlling the digital part of the Mimosa26 chip;
- an analogue auxiliary board, exploited for powering the analogue line, receiving the data from the chip and sending it to the imager boards;

- two USB imager boards which have four analog-to-digital converters (ADC) each, used for the conversion of the signal and for transferring it to a computer via the USB protocol. The boards were installed in a VME crate for powering;

- an analogue power cycling control module. This was used for setting the timing parameters of the power pulsing. The module also allows the voltages of the analogue and digital readout circuits of Mimosa26 to be set during the power on and power off phases;

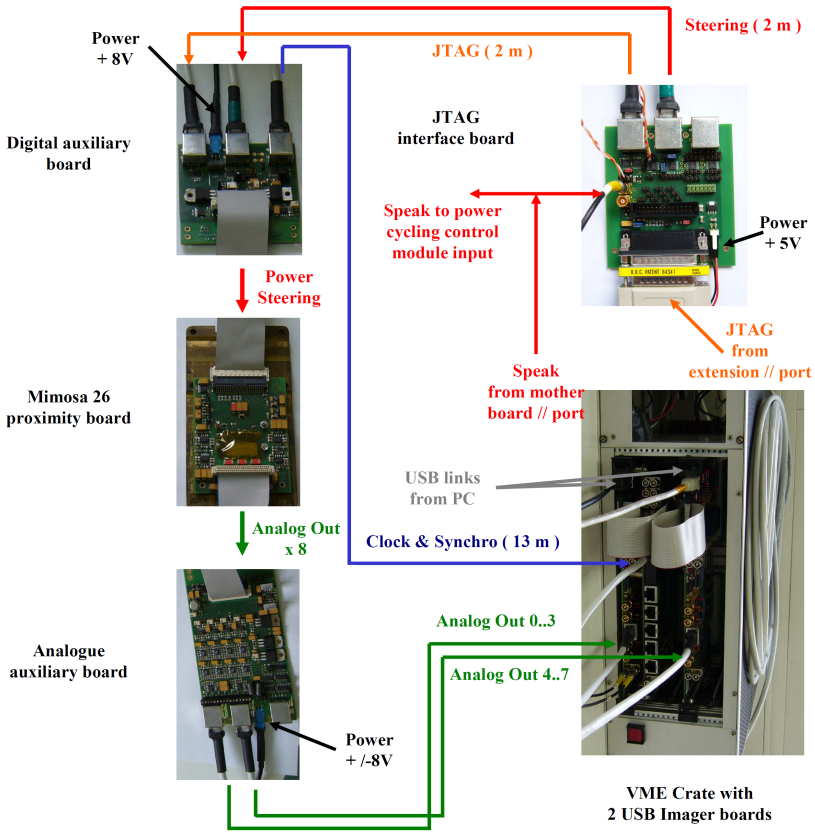

Figure 8.6: The setup for the Mimosa26 studies using the analogue readout.

- an oscilloscope, used to monitor the signals and to measure the time parameters of the power cycling;

- an external generator of the 20 MHz clock signal;

- a personal computer, used for JTAG programming and data acquisition (DAQ);

- a significant part of the measurements was done using a laser which was illuminating the surface of the sensor in a precisely defined position.

The Mimosa26 sensor was shielded from ambient light with an opaque polyethylene film. The JTAG controller was used to set on-chip programmable biases as well as voltage references and to select the test mode.

The data acquisition system was able to store up to 256 K × rows/event (due limitation of the imager boards). Since the Mimosa26 matrix has 576 rows, it is possible to store $256 \times 1024/576 = 455$ frames per event. To read 455 frames at 20 MHz clock frequency, about 209.7 ms are needed. This acquisition time is enough to study the recovery of the sensor during power cycling with an $\approx$ 200 ms period, which is needed at ILC. After the reading of 455 frames, the stored signals are sent to the computer to be saved on a hard disk drive (HDD). The next 455 frames are taken after the writing of the previous event is finished. Thus, the event frequency is limited by the speed of writing to the HDD. Since only eight ADCs are present in two image boards, there is a choice either to scan the whole Mimosa26 matrix with a step of eight columns, or to read the same eight columns for each frame. The last 8 columns of the sensor were used for studies described here. The start of the data acquisition event and the start of the power off/on cycle were synchronised using a common 'speak' (starting) signal sent by the DAQ system. The 'speak' signal was also used to synchronise the laser pulses with the readout of the chip. The analogue power cycling control module was used to set the delay of the power on/off cycle with respect to the 'speak' signal and the duration of the power ON phase. It was possible to change both the delay and the duration within the range 20 to 200 ms.

Typical values of the voltage supply and current consumption for the digital and analogue parts during the power ON and power OFF phases are summarised in Table 8.1. The digital power supply was not switched off in order to preserve the content of the JTAG registers, the clock and the synchro signal. It is seen from the table that the overall power consumption is reduced approximately by a factor of 4.

State	I_d [mA]	I_a [mA]	V_d [V]	V_a [V]	P [mW]
ON	70.7	171	3.31	3.19	779
OFF	49.7	20.9	3.34	1.26	192

Table 8.1: Comparison of voltage and current consumption by the analogue and digital parts of the chip during the ON and OFF phases, for studies using the analogue output.

One of the extensions of these power pulsing studies compared to the previous ones is to study the response of Mimosa26 illuminated by a laser. The laser was mounted on the precision moving stages in front of the sensor, the beam was focused on the surface of the sensor. It was possible to set the position of the laser with a precision of 5 μm and 2.5 μm in the parallel and perpendicular direction respectively, with respect to the sensor plane.

It was also possible to vary the frequency and intensity of the laser pulses. In order to independently monitor the intensity of the pulses, the laser beam was divided into two beams using a beam splitter: one beam illuminated the Mimosa26 and the other a photo-diode. The signal from the photo-diode was stored independently. The characteristics of the laser were as follows:

- wavelength: 904 nm;
- bandwidth: 3.5 nm;
- pulse duration (FWHM): 10 nm;
- rise time: ≤ 1 ns, fall time: ≤ 18 ns;
- maximal frequency of the pulses: 10 kHz for full power, 20 kHz for half-power;
- focal length: 20.1 mm;
- diameter of the focused beam: ≈ 5 μm.

8.2.3 Setup for the Digital Readout

The digital readout needs a setup which differs from the analogue one, since the readout data are already digitised and the chip works under its normal operational 80 MHz mode. The parts of the setup for the digital readout are the following [204]:

- a Mimosa26 pixel sensor;
- a JTAG interface board;
- a digital auxiliary board;
- a power pulsing control module. This was used to set the timing parameters of the power pulsing. The module also allows the voltages of the analogue and digital readout circuits of Mimosa26 to be set during the power on and power off phases;
- a power pulsing marker board was used to produce trigger signals which correspond to the beginning and to the end of the power off phase. These signals are stored with the DAQ system in order (during the analysis stage) to separate the data taken during power off phases from the data taken during the power on phases;
- an oscilloscope was used to monitor the signals and to measure the time parameters of the power cycling;
- a National Instruments (NI) crate with the PC unit was used for JTAG programming and data acquisition (DAQ).

The layout which describes the connection of all the boards is shown in Fig. 8.7.

The Mimosa26 sensor was mounted in an aluminium box, in which the temperature was kept constant (18 C$^\circ$) using water cooling. The box had a window for illumination

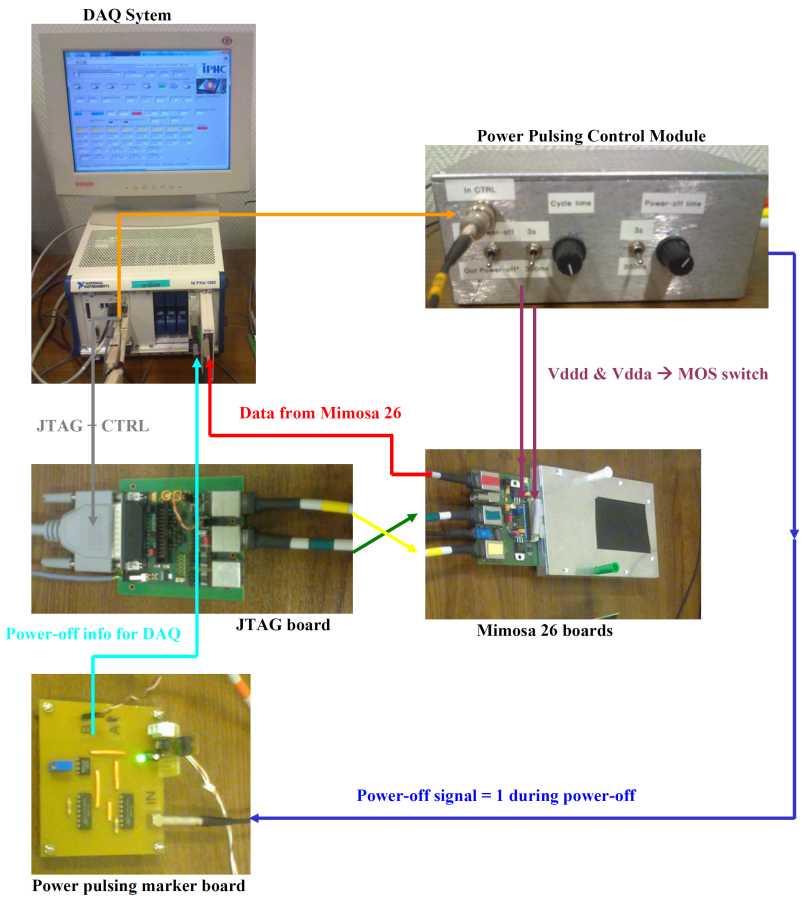

Figure 8.7: The setup for the Mimosa26 power pulsing studies with the digital readout.

with a radioactive source; the window was shielded from ambient light with an opaque polyethylene film.

Typical values of the voltage supply and current consumption for the digital and analogue parts during the power ON and power OFF phases are summarised in Table 8.2. They slightly differ from the numbers quoted in Table 8.1, because during the power pulsing studies with analogue output, the digital part of the sensor was not power pulsed. For the studies using the digital output, both the analogue and digital parts were power pulsed, therefore the power reduction factor increases to

$$f_{\text{reduction}} = \frac{P_{\text{ON}}}{P_{\text{OFF}}} = \frac{818\ \text{mW}}{129\ \text{mW}} \approx 6.34. \tag{8.1}$$

State	I_d [mA]	I_a [mA]	V_d [V]	V_a [V]	P [mW]
ON	80.	168	3.3	3.3	818
OFF	7.83	62.0	1.85	1.85	129

Table 8.2: Comparison of the voltage and current consumption by the analogue and digital parts of the chip during ON and OFF phases, for studies using the digital output.

8.2.4 Data Analysis

Analogue Readout

The method of data analysis of the analogue output of Mimosa26 is similar to the one described in [199]. A brief description is as follows.

- **Pedestal estimation.** Even when there is no particle registered, the output signal in a given pixel differs from 0 because of the leakage current and thermal noise. Usually such a signal is Gaussian-distributed around some non-zero pedestal, which has to be subtracted for the data analysis. Figure 8.8 shows as an example the distribution of the signal in one pixel. In this case the pedestal equals -7.8 ADC counts and the noise is about 4.2 ADC counts. The pedestal correction was done for each pixel separately.

- **Clusters formation.** Since the signal from an ionising particle is distributed within several neighbouring pixels, the total signal should be calculated as the sum of the signals of these pixels. The pixels were combined into clusters for this purpose. The clustering procedure is as follows:

  1. Subtract the pedestals as described above.
  2. Find all the pixels with a signal greater than $S > N \times$ noise, where N is typically set to 5. All such pixels are called "clusters".
  3. If two clusters have a common border (pixel border), they are combined into one cluster.
  4. The clusters are combined until there are no clusters with common borders left.

- **Signal extraction.** The signal due to an ionising particle is calculated as the total signal in a given cluster and is denoted as A in the following text.

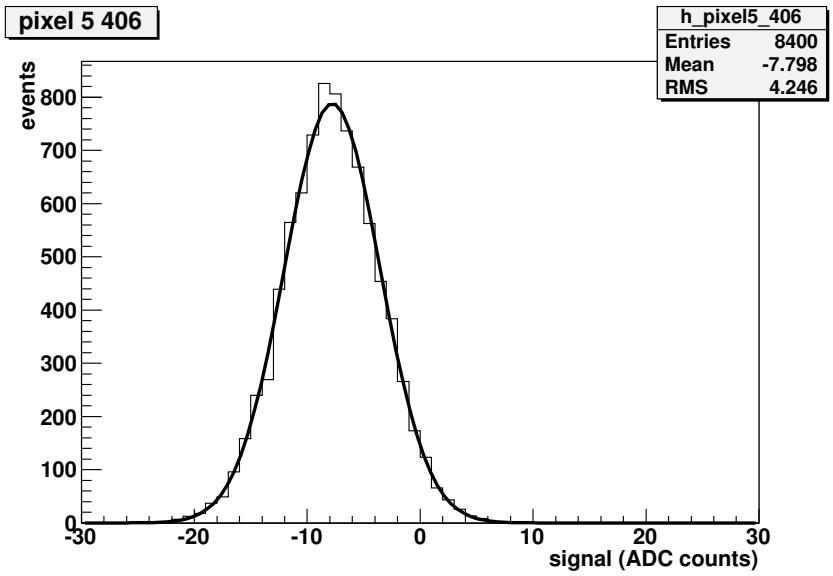

Figure 8.8: Distribution of the signal in one pixel, when the chip is not illuminated with any source. The black line is the result of a Gaussian fit.

Digital Readout

The data analysis of the digital output from Mimosa26 was performed using the TAPI analysis framework (TAF) [205]. This is the package created by IPHC (Strasbourg) to analyse CMOS pixel and strip sensor data. The framework was supplemented by the author with the subroutines needed for the preparation of the histograms related to the power pulsing studies, presented below.

8.3 Studies Using the Analogue Output of Mimosa26

The analogue output of the Mimosa26 sensors is used for test purposes only. The nominal operational mode is digital, when the only information available is whether a given pixel was fired or not (1 or 0). The advantage of the analogue output is that the signal measured in a given pixel can be quantified in ADC units with enough precision for detailed studies, such as an accurate measurement of the hit position and the time dependence of the measured signal.

This section consist of two parts. In the first, measurement of the spectrum of a radioactive X-ray source is given, which is done to establish the methodology of the data analysis. The second part presents studies of the Mimosa26 output when the sensor is illuminated by a laser. All measurements were performed in the laboratory.

8.3.1 Spectrum of a ^{55}Fe Source

A ^{55}Fe X-ray source has two emission lines, K_α with energy $E = 5.89$ keV and emission probability $P = 24.4\%$, and K_β with $E = 6.49$ keV and $P = 3.4\%$. Figure 8.9 shows the spectrum of the ^{55}Fe source taken with the Mimosa26 sensor. The spectrum represents the distribution of the charge collected in a cluster of pixels, reconstructed as described above. Data were taken with the signal-to-noise ratio of $S/N = 10$. The spectrum was fitted with a sum of two Gaussians and a parabolic background. The position of the peaks corresponding to the emission lines of ^{55}Fe provide information needed to calibrate the sensor (conversion between ADC counts and the energy of a registered particle).

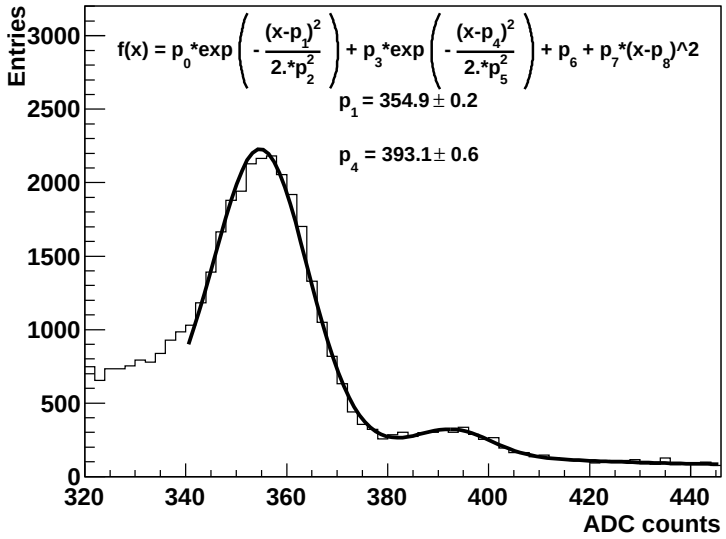

Figure 8.9: The spectrum of a ^{55}Fe X-ray source. The line corresponds to a fit with a double-Gaussian function plus parabolic background. Two peaks correspond to K_α and K_β emission lines, with energies 5.89 keV and 6.49 keV, respectively.

In silicon the energy required to produce an electron-hole pair is 3.6 keV. Therefore, K_α (K_β) photon produces approximately 1640 (1830) electron-hole pairs.

8.3.2 Studies With a Laser

The laser studies were done in order to estimate the recovery time of the Mimosa26 sensor and to cross check its response to the laser shot with the response of a light-sensitive diode. For all the measurements presented here, the pedestal was subtracted for each pixel, as described in Section 8.2.4. The response of the Mimosa26 sensor to a single laser shot is shown in Fig. 8.10. The signal is mainly contained in a cluster of 3x3 pixels. Such a large size of the cluster (compare the pixel size 18.4×18.4 μm^2 to the diameter of the focused

laser beam of 5 μm) is explained by those fact that the created by a rigesterd particle charge is shared between neighbouring pixels (since MAPS like Mimosa26 collect their signal charge by means of thermal diffusion, which causes a significant charge sharing).

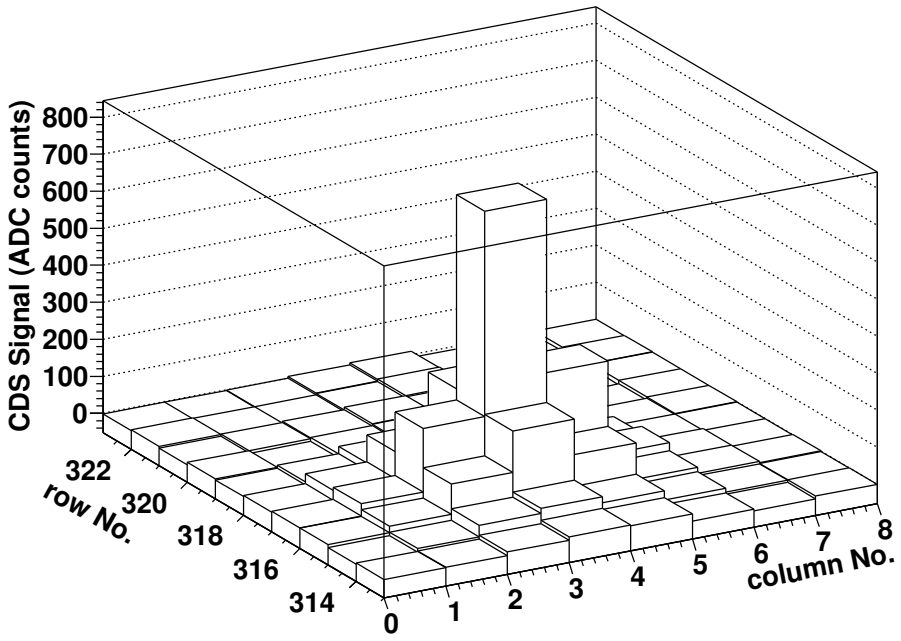

Figure 8.10: Response of the Mimosa26 pixel sensor to a single laser shot.

In order to effectively use the laser pulses, they should satisfy the following requirements:

1) the laser pulses have to be properly synchronised with the readout of the sensor (and also with the start of the power ON phase during power pulsing);

2) the ability to vary the laser pulse frequency;

3) the ability to vary the laser pulse intensity (the corresponding damper is part of the laser setup);

4) the ability to precisely vary the position of the sensor to be illuminated with the laser;

5) (optionally) the ability to independently monitor the laser pulse intensity.

The first two were realised using a special electric circuit prepared by the author specifically for this case. The position of the laser was precisely set with the moving stages. The laser pulse intensity was monitored with the help of the beam splitter and a photo-diode. The Mimosa26 sensor was illuminated with the laser from the front side,

since the illumination from the back side will in any case not be possible in the PLUME ladder.

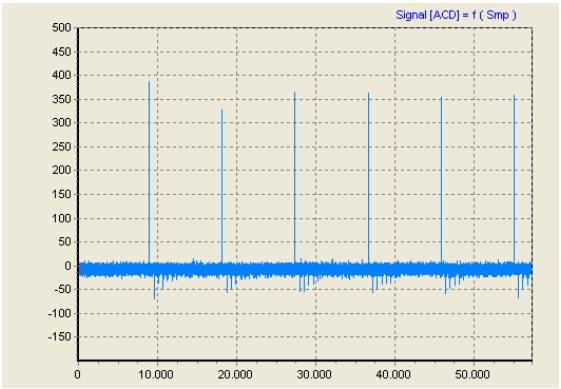

(a) Signal in the 576 pixels of the selected column of the Mimosa26 sensor illuminated with a laser as a function of time. Along the X axis is the number of the pixel and the number of the readout cycle, such that numbers from 0 to 575 correspond to the first frame, 576 to 1151 correspond to the second frame and so on. The laser pulses were sent on each 16th readout cycle, which corresponds to 0.46 ms $\times$ 16 = 7.36 ms between the consequtive pulses.

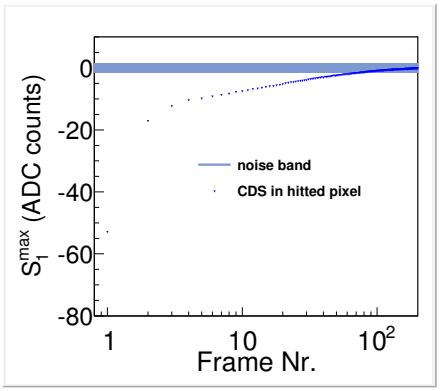

(b) Absolute value of the average signal in the pixel fired by the laser as a function of the frame number, starting from the next frame after the laser pulse. The signal in a given pixel recovers to noise level during about 100 frames ($\approx$ 50 ms) after the laser pulse. The width of the horizontal line at 0 represents the noise in the pixel.

Figure 8.11: Development of the signal in a pixel fired with a laser.

Mimosa26 is operating in the so-called rolling shutter mode and a correlated double sampling is performed in each pixel. This means that there is no dead time and the output signal in each pixel is determined as the difference of two successive read-out pixel signals.

The charge for large signals remains in the pixel for several readout cycles and is reduced from cycle to cycle. Because of this and the CDS procedure described above, the output signal for the few next frames after the laser pulse becomes negative for the fired pixels (since the output pixel signal is determined as a difference of signals for two consecutive read out cycles). This can be seen in Fig. 8.11(a), where the signals collected in the 576 pixels of the selected column are shown as a function of time. Fig. 8.11(b) summarises the example of this effect for one pixel: the signal recovers to the noise level about 50 milliseconds after the laser pulse.

The dependence of the signal on the position of the laser beam was also studied. The scan along the X and Y axes of the sensor was performed using precisely moving stages. The precision was high enough to move the laser beam within a pixel. Figures 8.13(a)-8.13(f) show the results of the scan. The scan was performed strictly within

one column of pixels. Three neighbouring pixels were scanned, as confirmed by Figs. 8.13(a), 8.13(b). The signal varies strongly depending on the part of the pixel which is illuminated, the maximal signal is up to 6 times larger than the minimal signal, as illustrated in Figs .8.13(c), 8.13(d). This is explained by the non-uniform distribution of the dead material within a pixel: some parts of the pixel sensitive volume are covered by the pixel electronics, as shown in Figure 8.12. The ratio of the signal in a pixel with maximal response (hit pixel) to the total signal of the cluster, $F^1_{\max} = S^1_{\max}/A_1$, is shown in Fig. 8.13(e). Together with Fig. 8.13(f) they illustrate that the spread of the charge between neighbouring pixels is also dependent on the position of the registered particle.

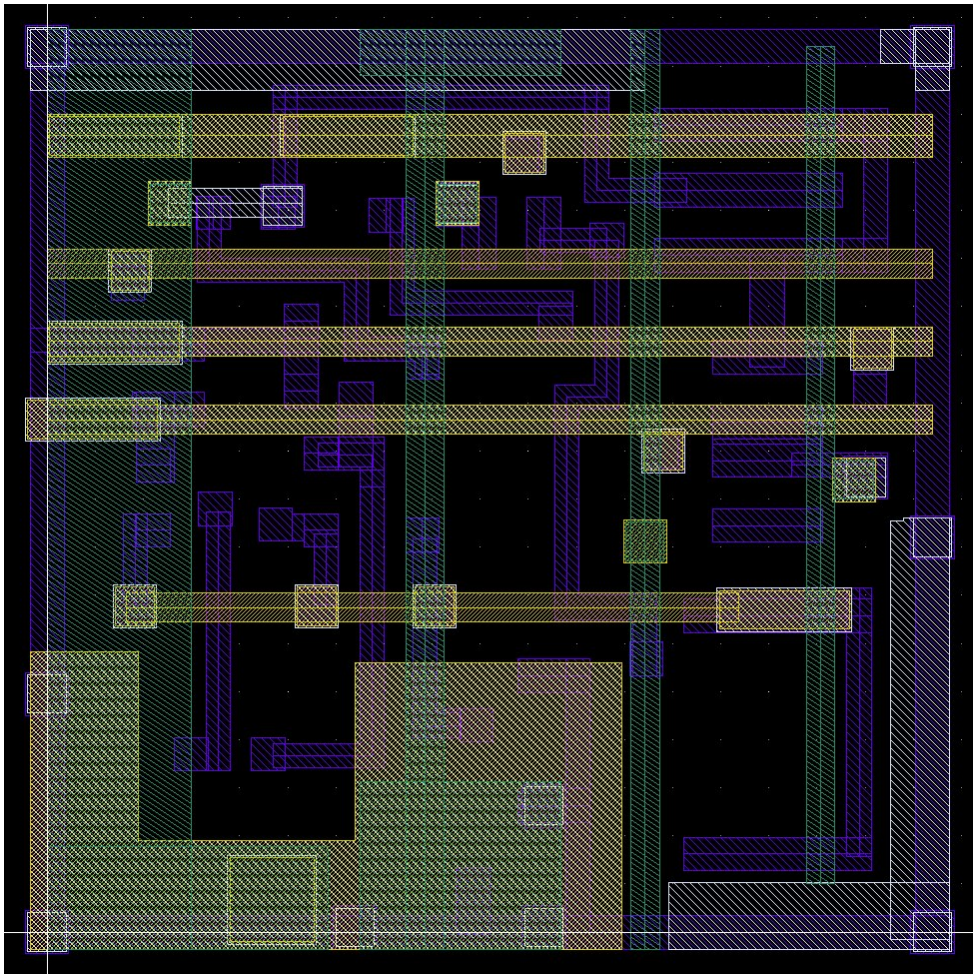

Figure 8.12: Picture of a Mimosa26 pixel. The hatched area represents position of the metal layers (electric circuits) within the pixel.

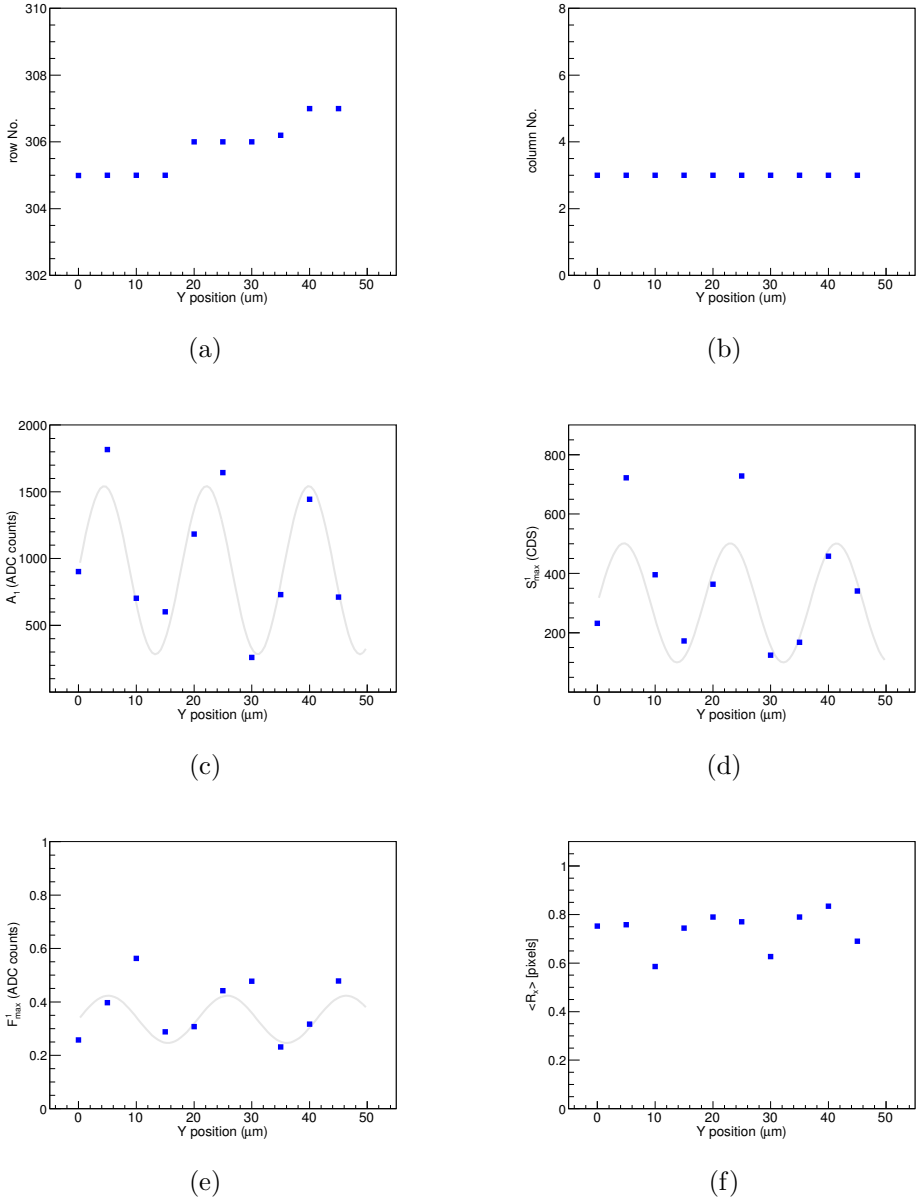

Figure 8.13: Response of the Mimosa26 pixel sensor for different positions of the laser beam. The scan is performed along one column (defined here as Y direction). Periodical structures can be distinguished. The sinusoidal curve of 18.4 μm (pixel width) period is shown to guide the eye. On the plots, as function of the laser beam Y position, are:
(a) Row number of the pixel illuminated by the laser, calculated from the signal-weighted position of the cluster. The scan is performed over three neighbouring pixels;
(b) Column number of the pixel illuminated by the laser, calculated from the signal-weighted position of the cluster. The plot shows that the laser beam stays within the same column during the scan;
(c) Cluster signal;
(d) Hit pixel signal. A hit pixel is defined as the pixel with maximal response inside the cluster
(e) Ratio of the signal in the pixel with maximal response to the total signal of the cluster;
(f) The RMS size of the cluster along the X direction. The RMS size along the Y direction has a similar dependence.

Another method to estimate the time needed for the recovery of the pixel after registering a particle is to study the dependence of the sensor response on the laser pulses frequency. The readout of the sensor is done in series of 455 frames, as explained in subsection 8.2.2. The time between series is limited by the speed of writing the data to a hard drive and is enough for the sensor to recover. Thus, recovery studies are based on series of 455 consequtive frames, and we start counting the laser pulse from one for each new series. It is observed that for high frequencies of the laser pulses, the response to the first laser pulse is slightly larger than to following pulses. Fig. 8.14 shows an example distribution of the ratio of response for two consequtive laser pulses when the pulses are sent with a 30 ms interval. The ratio of the 2nd to 1st pulse is on average about 0.93, while the ratio of the $(n+1)$-th to the n-th pulse, where $n > 1$, is more close to unity. The dependence of the first ratio on the laser pulse intensity is illustrated in Fig. 8.15. The ratio is closer to unity for lower intensities. The same ratio as a function of the laser pulse frequency is shown in Fig. 8.16. The ratio is equal to one if the time between laser pulses is greater than 60 ms, which is in agreement with the value obtained in the studies of negative signals described above (in Figure 8.11).

Figure 8.17 illustrates the high level of correlation between the signals in the photo-diode and Mimosa26 in response to the laser shots. For this case the laser beam was divided into two beams using beam splitter, where the first was directed onto Mimosa26 and second onto the photo-diode.

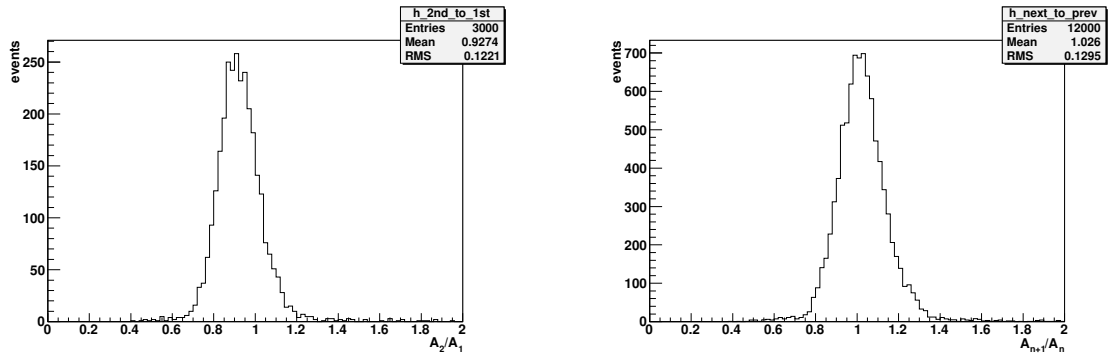

(a) (b)

Figure 8.14: The ratio of Mimosa26 responses for two consecutive, n-th and $(n+1)$-th, laser pulses. Time between laser pulses is 30 ms. The ratio ideally should be equal 1 (since laser intensity was not varied), while for (a) $n = 1$, the average ratio is 0.93 and for (b) $n > 1$, the average ratio is 1.03. The fact that for $n = 1$ the ratio is deviating from 1 stronger than for $n > 1$ may indicate that the time between laser pulses is not enough for the charge collected in pixel to be reduced to a noise level.

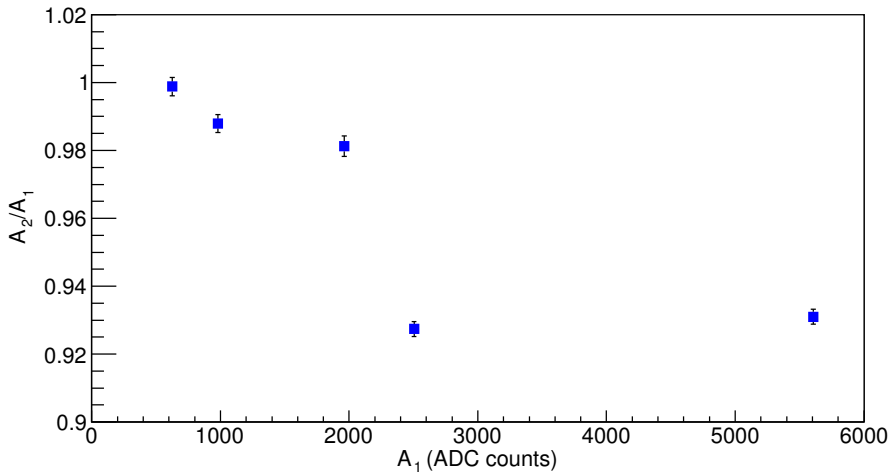

Figure 8.15: Ratio of responses for 2nd and 1st laser pulse as a function of the first pulse intensity.

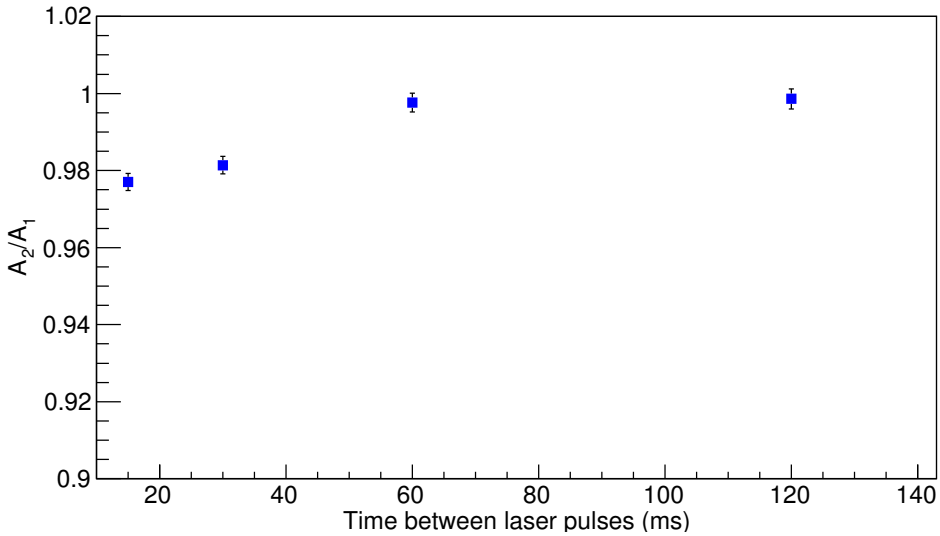

Figure 8.16: Ratio of responses for 2nd and 1st laser pulses as a function of the time interval between pulses.

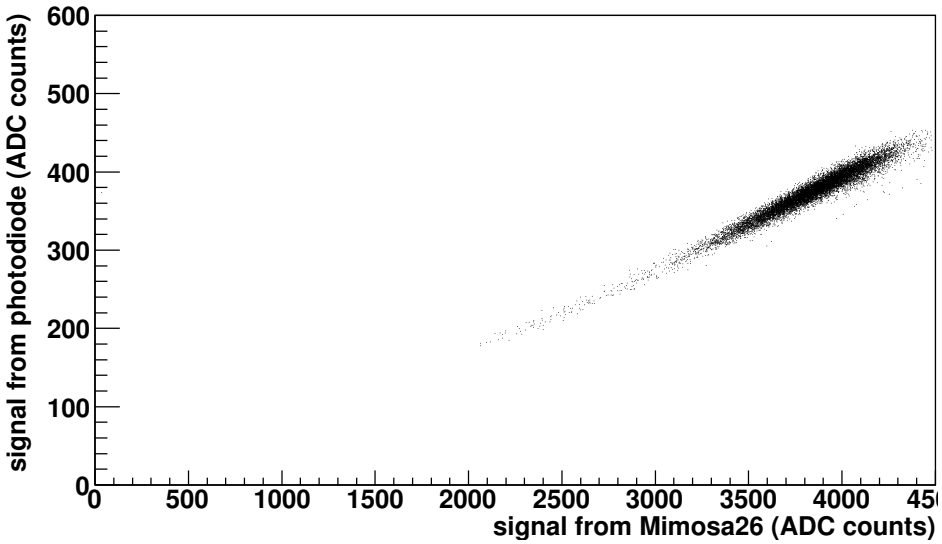

Figure 8.17: Correlation of the Mimosa26 and photo-diode responses to laser shots.

8.4 Power Pulsing Studies Using Digital Output of Mimosa26

In the nominal operation mode, Mimosa26 has a digital output providing only a list of hit pixels without further information on the strength of the signal. The readout of the sensor in this mode takes 115.2 μs (the clock frequency is 80 MHz). This section describes the results of power pulsing studies of Mimosa26 operating in the nominal mode.

8.4.1 Fake Hit Rate Studies

For the fake hit rate measurements, the cooling was connected to the closed aluminium frame which contained a Mimosa26, in order to have a better time stability of the fake hit rate.

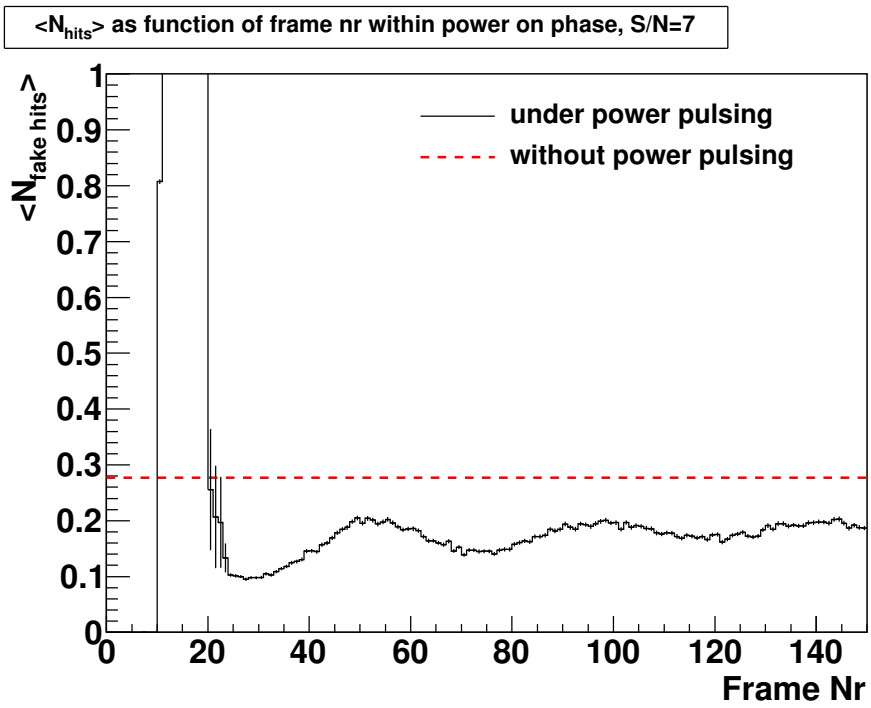

Figure 8.18: Average number of fake hits per frame as a function of frame number within the power on phase, compared to the fake hit rate under normal conditions. The averaging is done over about 1000 power on/off cycles.

The main result of the study is summarised in Fig. 8.18, where fake hit rates under power pulsing conditions and under normal conditions are shown. The solid line represents the dependence of the average number of fake hits on the frame number; frame counting starts after switching the sensor into power on phase. The constant dashed line is the average fake hit rate under normal conditions (no power pulsing). It is seen from the figure that the sensor reaches its reasonably stable operation after about 50 frames, i.e. about 6 ms after switching the power fully on. This limitation stems from the absence of specific power-pulsing management inside the sensor. Nevertheless, the fake hit rates under power pulsing and under normal conditions are of the same order, which proves the reliability of the power pulsing approach.

Damped oscillations of the fake hit rate are visible in Fig 8.18. They are probably related to features of the sensor's electrical circuit. Further studies have to be done in order to know the exact reason.

8.4.2 Studies With a ^{55}Fe Source

The studies of Mimosa26 illuminated with the ^{55}Fe source are done in the same way as described in the previous subsection. The ^{55}Fe source emits photons at an energy

of 5.90 keV with a probability of 24.4% and photons at an energy of 6.49 keV with a probability of 2.86%. The result is shown in Fig. 8.19. The average number of hits per frame during power pulsing becomes constant after about 400 frames (45 ms) after switching the power on. It is close to the average number of hits under normal conditions, however there is still small difference between them, which is probably due to a different average temperature of the sensor during power pulsing and during normal conditions. This result means that the Mimosa26 sensor would need to be switched to the "power ON" phase about 45 ms before the arriving of the bunch train.

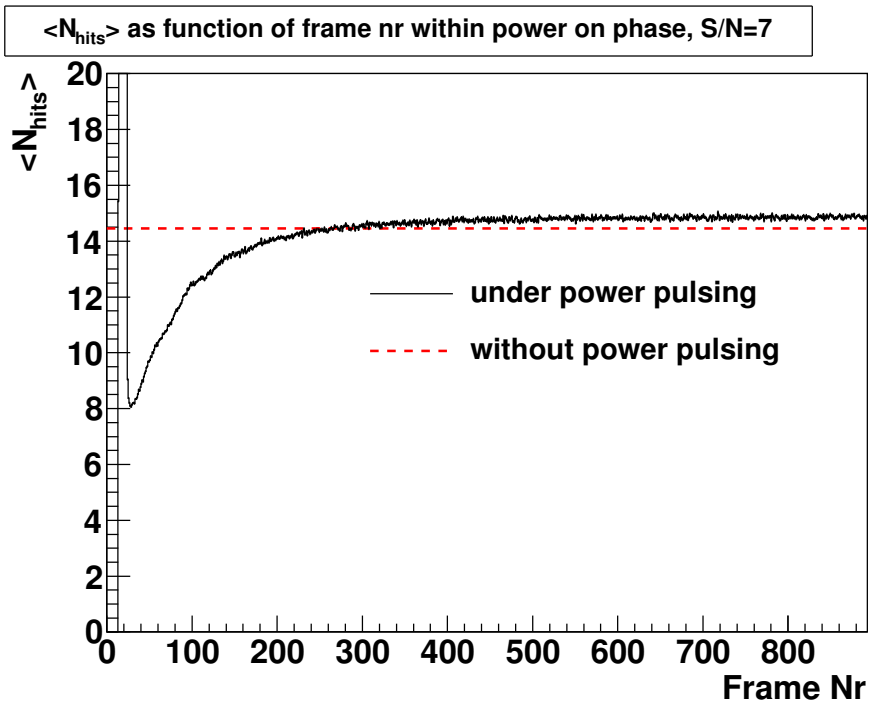

Figure 8.19: Average number of hits per frame as a function of frame number within the power on phase, compared to the hit rate under normal conditions. The hits are due to illumination with X-rays from the ^{55}Fe source. The averaging is done over about 8000 power on/off cycles

This study allows the reduction in power consumption at ILC bunch timing conditions to be estimated, with respect to no power pulsing. The reduction factor is given by the formula

$$f_{\mathrm{ILC}} = \frac{T \cdot P_{\mathrm{ON}}}{T_{\mathrm{ON}} \cdot P_{\mathrm{ON}} + (T - T_{\mathrm{ON}}) \cdot P_{\mathrm{OFF}}} = \frac{T}{T_{\mathrm{ON}} + (T - T_{\mathrm{ON}})/f_{\mathrm{reduction}}}, \tag{8.2}$$

where $T = 200$ ms is the time between arrivings of two consequtive bunch trains at ILC, T_{ON} is the time for which the detector needs to operate at nominal power (power

"ON" phase), and the factor $f_{\text{reduction}} = 6.34$ is given by (8.1). The value of T_{ON} is $T_{\text{ON}} = 45 + 1 = 46$ ms, where 45 ms where read from Fig. 8.19 as explained earlier in this subsection and 1 ms is the time of bunch train collision, i.e. the time of data-taking period. Collecting everything together gives

$$f_{\text{ILC}} = \frac{200 \text{ ms}}{46 \text{ ms} + 154 \text{ ms}/6.34} \approx 2.8.$$

These results present a first "proof of principle" for Mimosa26 working under power pulsing conditions with the nominal digital readout, showing that the sensor performs normally. The results presented here give a first rough estimate of the gain in power consumption. Further laboratory and test beam studies are needed with the full PLUME ladder in order to obtain final numbers on the reduction of the power consumption.

It also needs to be stressed that Mimosa26 is not the final sensor prototype for the ILC vertex detector and it is not optimised for working under power pulsing conditions. Further sensor prototypes with specific power management adapted for power pulsing will allow a further reduction of the power consumption.

8.4.3 Temperature Studies

It is important to know the surface distribution of the temperature of the sensor, because a change of the temperature during power pulsing leads to a corresponding change of the thermal expansion of the chip, which in turn could lead to deformation of the chip. Thus, information about the temperature distribution could be taken into account when mounting (gluing) the sensor on supporting structures, to avoid strong mechanical tensions on the sensor.

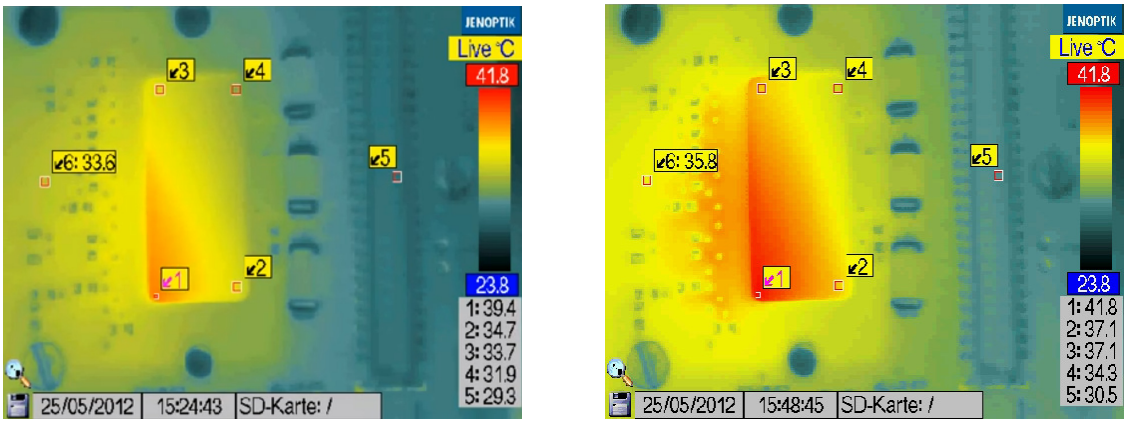

(a) (b)

Figure 8.20: Heating of the sensor during power pulsing: (a) during the power OFF phase, (b) during the power ON phase.

The studies were performed with a thermal imaging camera which allows both video and photographs to be taken. In Figs. 8.20(a) and 8.20(b), photographs of the sensor taken in the infrared range during power pulsing are shown at the end of power phases "off" (160ms) and "on" (40 ms), respectively. The cooling was not applied for this study. Two main conclusions can be made. Clearly, temperature variation is visible during power pulsing. We do not provide a quantitative estimation of the reduction of the heat dissipation here, since part of the energy that comes from the sensor surface is due to the reflection of the surrounding lights. Another conclusion visible from the photographs is that the surface of the sensor is heated non-uniformly; there is a temperature gradient along the diagonal of the sensor surface. This fact should be considered carefully when developing further chip prototypes and support structures for the ladder, since the local characteristics of the glued chip (mechanical tension of the heated silicon, noise in pixels etc) can differ within the chip due to different temperatures in defferent parts of the chip.

8.5 Conclusions for the Mimosa26 Studies

Laser studies using the analogue output of Mimosa26 were performed. The studies show the power of exploiting the laser beam in laboratory tests of the pixel sensor. It was possible to illuminate the sensor in different regions within one pixel, with specified frequency and intensity of the laser pulses. With the laser studies it was found that in the test mode (with analogue readout) of Mimosa26, the signal in the pixel reduces to the noise level after about 40 ms after registering a particle.

The main task of the studies was to investigate the Mimosa26 pixel sensor performance, using digital output, in the power pulsing regime, which is supposed to be the regime for part of detector electronics at the ILC due to sparse bunch filling: 1 ms of intense collisions are followed by 199 ms of no bunch crossing. The voltage supplies during the studies described here thus were lowered to a minimum operating level with a period of 200 ms, which correspond to nominal ILC conditions. Studies with the ^{55}Fe source show that during power pulsing Mimosa26 fully recovers to its stable state, very similar to that observed in the constant power regim, after about 45 ms after switching to the ON phase. The fake hit rate recovers to a reasonable level already after about 6 ms after switching to the ON phase. An estimate for the reduction factor of the power consumption compared to the constant power regime at the ILC conditions, i.e. if a (45+1) ms/200 ms duty cycle is assumed, is: $f_{\mathrm{ILC}} \approx 2.8$. Power pulsing allows a reduction not only of the power consumption, but also of heat dissipation. Temperature studies of the sensor surface during the power pulsing show a reduction of the sensor temperature during the power OFF phase. A temperature gradient along the sensor diagonal was also detected. The gradient is enhanced during power ON phase compared to power OFF phase. Such information could be taken into account when mounting the sensors on the support structure of the PLUME ladder.

The investigations presented in this chapter are an intermediate step on the way to produce a final sensor prototype for the ILC vertex detector. Further studies are needed to be done with a full PLUME ladder, both in the laboratory and at the test beam.

This study shows that so far there is no showstopper for adopting the power pulsing regime for the pixel sensors of the ILC vertex detector.

Summary and Outlook

A QCD analysis of collider cross-section data is a powerful method to measure the parameters of QCD. In particular, parton distribution functions (PDFs) of the proton and the strong coupling constant, $\alpha_s(M_Z)$, can be extracted from deep inelastic scattering and jet data and used as a tool for more sophisticated studies of physics within and beyond QCD. This thesis briefly describes examples of cross section measurements to which the author contributed and presents their consequent QCD analysis in combination with further experimental data. The program used for the proton PDF + α_s fits is called HERAFitter; it was modified to accommodate the developments needed for this thesis.

A dijet measurement is described in this thesis, which was made with the ZEUS detector at HERA, at large virtualities of the exchanged boson, Q^2, between $125 < Q^2 < 20\,000$ GeV^2, where theoretical uncertainties are expected to be small. The dijet cross sections were characterised by a relatively small statistical uncertainty of the order of 2 to 10% depending on the phase space region. Good agreement with the Next-to-Leading Order (NLO) QCD predictions was observed. The results of the measurement were published by the ZEUS collaboration in 2010.

A measurement of isolated photons with an accompanying jet is also presented here. The phase space of the measurement corresponded to low-Q^2 DIS with $10 < Q^2 < 350$ GeV^2. The transverse energy of the isolated photon, E_T^γ, was in the range $4 < E_T^\gamma < 15$ GeV and the transverse energy of the accompanying jet was greater than $E_T^{\text{jet}} > 2.5$ GeV. Perturbative QCD predictions give a reasonable description of the shape of the measured cross sections over most of the kinematic range, but the absolute normalisation is typically deviates by 10-30%. The cross sections were published by the ZEUS collaboration in 2012.

A QCD analysis of the measured isolated photon data was performed, since it was expected that these data could constrain the sea u and d quark PDFs at low values of the proton momentum fraction, x, carried by the quark, due to their different electrical charges. The program EPGJet for NLO predictions for this process was used to produce the table of perturbative coefficients in order to perform a fast calculation of the NLO predictions by its convolution with the proton PDFs and α_s, during the fit. The sea u/d PDF ratio at $x \to 0$ was extracted and found to be consistent with unity, as expected by isospin symmetry. The quantity was mainly constrained by the inclusive DIS data, while

adding the photon data led to a slight increase of the ratio and to a small reduction of the relative uncertainty. Generally, the isolated photon data were found to be perfectly consistent with the inclusive DIS data. The level of presence of additional partons in the proton, apart from quarks and gluons (e.g. photons), was also evaluated, and found to be about or below 1%. Adding more isolated photon data is straightforward with the setup provided, and could potentially lead to a further improvement of the results.

The running of the strong coupling constant, $\alpha_s(\mu)$, was tested in an NLO QCD analysis using jet measurements at LHC, Tevatron and HERA in combination with inclusive DIS data (the dijet measurement at HERA described above was also used). A variant of the Fixed Flavour Number Scheme (FFNS "B") was used for the heavy quark treatment. This scheme was demonstrated to give a better description of the data than the usual FFNS "A". The parameter n_f of the running, which gives the number of active quarks contributing to loop corrections of the jet and DIS cross sections, was replaced by $n_f + \Delta n_f$ at energy scales greater than $\mu > \mu_{\text{thresh}}$, and Δn_f was extracted from the fit. Thereby, Δn_f is used to parametrise potential non-Standard-Model contributions. A series of simultaneous $\alpha_s(M_Z) + \Delta n_f +$ proton PDF fits to world collider cross section data was done, for μ_{thresh} values ranging from 1 GeV to 1 TeV. The fitted Δn_f was consistent with zero at all tested scales, which gives a precise quantitative confirmation of the QCD running of α_s over 3 orders of magnitude in energy scale. The presented method also provides a new way for indirect searches of physics beyond the Standard Model (SM). Constraints are derived on those models suggesting physics beyond the SM, which contain loop corrections to the jet and DIS cross sections, and for which a change of the measured configuration of the final state can be neglected. As an example, a fourth quark generation, with masses of both quarks of the new generation equal to the top mass, was excluded at 95% confidence level. The generic limits obtained are better than those of an earlier similar but somewhat less sophisticated result by a group of theorists. By further improvement of the method and a more detailed study of the respective theory models, a more broad set of models can be tested.

As a technical task, power pulsing studies of the Mimosa26 pixel sensor, which is the first sensor prototype for the vertex detector for International Linear Collider (ILC) were performed. The beam structure of the ILC allows the possibility of power pulsing: only for about the 1 ms long bunch train full power is required, and during the 199 ms long pauses between the bunch trains the power can be reduced to a minimum. Not being adapted for the power pulsing, the Mimosa26 sensor nevertheless shows a good performance under power pulsing in laboratory tests. The power pulsing allows for a significant reduction of the heating of the chip and divides the power consumption approximately by a factor of 3. The results of the studies were reported at the Vienna Conference on Instrumentation in 2013. The studies show that power pulsing operation is possible with no discernible disadvantages.

Appendix A

Breakdown of Systematics

$\frac{d\sigma}{dE_T^\gamma}\left(\frac{\text{pb}}{\text{GeV}}\right)$							
E_T^γ range, GeV	$\frac{d\sigma}{dE_T^\gamma}$	δ_{stat}	δ_1	δ_2	δ_3	δ_4	δ_5
4 ... 6	2.38	0.18	0.11	0.07	0.13	0.07	0.04
6 ... 8	1.28	0.10	0.06	0.06	0.020	0.018	0.03
8 ... 10	0.62	0.08	0.026	0.04	0.029	0.028	0.014
10 ... 15	0.256	0.025	0.021	0.022	0.005	0.010	0.0004

Table A.1: Differential cross section of the isolated photon + jet production in DIS as a function of the transverse energy of the photon. The absolute values of the statistical, δ_{stat}, and systematical, δ_{1-5}, uncertainties are given. The uncertainties δ_1 and δ_2 (correlated) are the downward and upward variations of the cross section, respectively, due to the variation of the energy scales. The uncertainties δ_3 and δ_4 (correlated) are the downward and upward variations of the cross section, respectively, due to variation of the $\langle \delta Z \rangle$ fit range. The uncertainty δ_5 is the variation of the cross section, when no reweighting is applied (for a further use of the data it is suggested to be symmetrised and treated as uncorrelated). There is an additional common uncertainty of 1.8% on the luminosity measurement (correlated across all bins), which is not included in the table.

$\frac{d\sigma}{d\eta^\gamma}$ (pb)							
η^γ range	$\frac{d\sigma}{d\eta^\gamma}$	δ_{stat}	δ_1	δ_2	δ_3	δ_4	δ_5
-0.7 ... -0.3	7.6	0.6	0.6	0.4	0.19	0.22	0.20
-0.3 ... -0.1	6.7	0.5	0.3	0.27	0.05	0.17	0.21
0.1 ... 0.5	5.8	0.6	0.19	0.16	0.3	0.12	0.23
0.5 ... 0.9	5.2	0.5	0.26	0.24	0.5	0.07	0.005

Table A.2: Differential cross section of the isolated photon + jet production in DIS as a function of the pseudorapidity of the photon. The other details are as in caption for Table A.1.

$\frac{d\sigma}{dQ^2}\left(\frac{\text{pb}}{\text{GeV}^2}\right)$							
Q^2 range, GeV^2	$\frac{d\sigma}{dQ^2}$	δ_{stat}	δ_1	δ_2	δ_3	δ_4	δ_5
10 ... 20	0.298	0.024	0.014	0.021	0.003	0.012	0.0014
20 ... 40	0.129	0.012	0.009	0.004	0.010	0.004	0.00020
40 ... 80	0.049	0.005	0.003	0.0016	0.005	0.0017	0.00011
80 ... 150	0.0224	0.0023	0.0008	0.0005	0.0009	0.0008	0.00012
150 ... 350	0.0037	0.0007	0.000009	0.0001	0.00012	0.00028	0.000004

Table A.3: Differential cross section of the isolated photon + jet production in DIS as a function of the Q^2 variable. The other details are as in caption for Table A.1.

$\frac{d\sigma}{dx}$ (pb)							
x range	$\frac{d\sigma}{dx}$	δ_{stat}	δ_1	δ_2	δ_3	δ_4	δ_5
0.0002 ... 0.001	4870	300	230	2700	160	210	90
0.001 ... 0.003	1811	140	110	80	90	4	24
0.003 ... 0.01	278	30	11	7	13	4	8
0.01 ... 0.02	25.1	7	1.7	0.007	1.2	5	3

Table A.4: Differential cross section of the isolated photon + jet production in DIS as a function of the x variable. The other details are as in caption for Table A.1.

$\frac{d\sigma}{d\eta^{\text{jet}}}$ (pb)							
η^{jet} range	$\frac{d\sigma}{d\eta^{\text{jet}}}$	δ_{stat}	δ_1	δ_2	δ_3	δ_4	δ_5
-1.5 ... -0.7	1.53	0.17	0.15	0.13	0.11	0.026	0.009
-0.7 ... 0.1	2.84	0.25	0.12	0.15	0.12	0.15	0.04
0.1 ... 0.9	3.91	0.3	0.15	0.09	0.08	0.08	0.04
0.9 ... 1.8	3.57	0.29	0.20	0.15	0.26	0.007	0.04

Table A.5: Differential cross section of the isolated photon + jet production in DIS as a function of the jet pseudorapidity. The other details are as in caption for Table A.1.

$\frac{d\sigma}{dE_T^{\text{jet}}}\left(\frac{\text{pb}}{\text{GeV}}\right)$							
E_T^{jet} range, GeV	$\frac{d\sigma}{dE_T^{\text{jet}}}$	δ_{stat}	δ_1	δ_2	δ_3	δ_4	δ_5
2.5 ... 4	1.40	0.16	0.023	0.026	0.15	0.009	0.04
4 ... 6	1.19	0.11	0.12	0.06	0.04	0.04	0.023
6 ... 8	1.01	0.10	0.06	0.08	0.011	0.006	0.04
8 ... 10	0.74	0.07	0.05	0.04	0.003	0.03	0.0026
10 ... 15	0.32	0.03	0.003	0.022	0.010	0.012	0.005
15 ... 35	0.031	0.006	0.0028	0.0024	0.00021	0.0003	0.0004

Table A.6: Differential cross section of the isolated photon + jet production in DIS as a function of the jet transverse energy. The other details are as in caption for Table A.1.

Appendix B

Materials for Chapter 7

B.1 Further Models Beyound the SM Which Potentially Can be Tested

Tensor gluons. In Ref. [206] the possibility that inside hadrons there are additional massless partons - tensor gluons - is considered. The tensor gluons have the same properties as normal gluons except spin: the spin of tensor gluons is larger and can be equal to 2, 3, 4, ... In the suggested model, tensor gluons are produced by normal gluon splitting to a tensor-gluon pair but tensor gluons are not radiated by quarks. It is argued that therefore the configuration of the final state in jet events is unchanged. In [206] the density of neutral partons in a proton is given by the sum of the gluon density, $g(x, Q^2)$, and the tensor gluon density, $t(x, Q^2)$. The effect of tensor gluons appears also in coefficients of the beta-function (and therefore in the α_s evolution) [206]:

$$b_0 = \frac{\sum_s (12s^2 - 1)C_A - 4n_f T_R}{12\pi}, \quad s = 1,\ 2,\ 3,\ \ldots\ . \tag{B.1}$$

If one limits oneself to spin-one gluons, the standard formula (1.29) is recovered. If one considers additionally the contribution from spin-2 tensor gluons, the unification scale at which the coupling constants of the Standard Model merge moves to ≈ 40 TeV which is much smaller that the scale $M \sim 10^{14}$ GeV in the absence of tensor gluons.

Since the tensor gluons are massless, the approach presented in the Chapter 7 cannot be readily used to constrain the model. However, with the corresponding extension of the method with help of theorists it may be possible to do it in future.

Extra dimensions. In string theories the appearence of extra spacetime dimensions is expected. The study of the effects of extra dimensions at intermediate mass scales is considered e.g. in [207]. It is shown that extra spacetime dimensions lead to a drastical change of the evolution of the couplings. Thus, in Figure B.1 [208] the effect on the α_s evolution is shown, when new dimensions appear at a scale $\mu_0 = 200$ GeV.

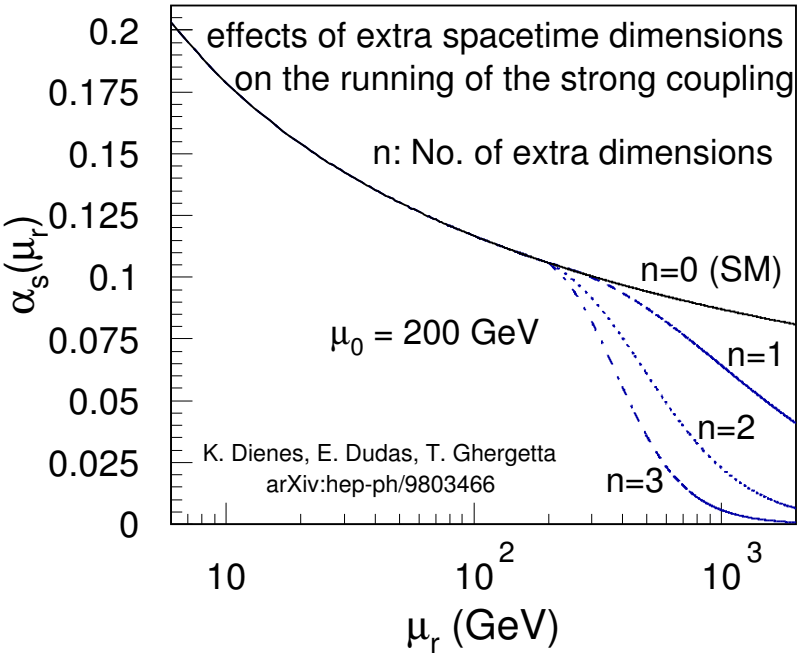

Figure B.1: Running of the strong coupling constant in the absence (SM) and presence of n extra dimensions [208].

If the appearence of extra dimensions does not imply the appearence of new real particles, it can be effectively parametrised as a change of the n_f^{loop} parameter in the α_s running and can be tested with the method used in this thesis.

B.2 HERAFitter Steering Files

steering.txt:

```
&InFiles
    NInputFiles = 26
     InputFileNames(1) = 'data/proc_101.dat'
     InputFileNames(2) = 'data/proc_102.dat'
     InputFileNames(3) = 'data/proc_103.dat'
     InputFileNames(4) = 'data/proc_104.dat'
     InputFileNames(5) = 'data/proc_105.dat'
     InputFileNames(6) = 'data/proc_106.dat'
     InputFileNames(7) = 'data/proc_107.dat'
     InputFileNames(8) = 'datafiles/lhc/cms/InclusiveJets2011v2qed.dat'
     InputFileNames(9) = 'datafiles/tevatron/CDF_JETS2008.dat'
     InputFileNames(10) = 'datafiles/tevatron/D0_JETS.dat'
     InputFileNames(11) = 'datafiles/lhc/atlas/Jets2010/inclusivejets_R06_00_03.dat'
     InputFileNames(12) = 'datafiles/lhc/atlas/Jets2010/inclusivejets_R06_03_08.dat'
     InputFileNames(13) = 'datafiles/lhc/atlas/Jets2010/inclusivejets_R06_08_12.dat'
     InputFileNames(14) = 'datafiles/lhc/atlas/Jets2010/inclusivejets_R06_12_21.dat'
```

```
     InputFileNames(15) = 'datafiles/lhc/atlas/Jets2010/inclusivejets_R06_21_28.dat'
     InputFileNames(16) = 'datafiles/lhc/atlas/Jets2010/inclusivejets_R06_28_36.dat'
     InputFileNames(17) = 'datafiles/lhc/atlas/Jets2010/inclusivejets_R06_36_44.dat'
     InputFileNames(18) = 'datafiles/hera/H1_InclJets_HighQ2_99-00.dat',
     InputFileNames(19) = 'datafiles/hera/H1_InclJets_LowQ2_99-00.dat',
     InputFileNames(20) = 'datafiles/hera/ZEUS_InclJets_HighQ2_96-97_33.dat',
     InputFileNames(21) = 'datafiles/hera/ZEUS_dijet_98-07_33.dat'
     InputFileNames(22) = 'datafiles/bcdms/BCDMS_F2p.100gev.dat'
     InputFileNames(23) = 'datafiles/bcdms/BCDMS_F2p.120gev.dat'
     InputFileNames(24) = 'datafiles/bcdms/BCDMS_F2p.200gev.dat'
     InputFileNames(25) = 'datafiles/bcdms/BCDMS_F2p.280gev.dat'
     InputFileNames(26) = 'datafiles/lattice/HPQCD_alphas_2010.dat'
&End
&InCorr
    NCorrFiles = 1
    CorrFileNames(1) = 'datafiles/lhc/cms/InclusiveJets2011___InclusiveJets2011.corr'
&End
&Scales
    DataSetMuR  = 26*1.0     ! Set muR scale to 1 for all 4 datasets
    DataSetMuF  = 26*1.0     ! Set muF scale to 1 for all 4 datasets
&End
&HeraFitter
  TheoryType = 'DGLAP'
  Order  = 'NLO'
  Q02     = 1.4 ! Evolution starting scale
  HF_SCHEME = 'FF 3,4,5 ABM'
  PDFStyle = 'HERAPDF'
   CHI2SettingsName = 'StatScale', 'UncorSysScale', 'CorSysScale', 'UncorChi2Type', 'CorChi2Type'
   Chi2Settings     = 'Poisson'  , 'Linear',        'Linear'     , 'Diagonal'     , 'Hessian'
   Chi2ExtraParam = 'ExtraSystRescale'
  LDEBUG     = False
&End
&ExtraMinimisationParameters
   name  = 'alphas',   'fs',   'fcharm',  'deltan',  'als_thresh', 'nf_in_als', 'mur_factor'
   value =  0.117766,   0.4,      0.,        0.0,        0.0,       3.0,           1.0
   step  =   0.000405, 0.0 ,      0.,        0.0,        0.0,       0.0,           0.0
&End
&Output
  DoBands = False
  Q2VAL = 1.9, 10., 100., 1000., 10000, 100000
  OUTNX = 101
  OUTXRANGE = 1E-4, 0.9999
&End
&Cuts
   ProcessName(1)     = 'NC e+-p'
   Variable(1)        = 'Q2'
   CutValueMin(1)     = 3.5
   CutValueMax(1)     = 1000000.0
   ProcessName(2)     = 'NC e+-p'
   Variable(2)        = 'x'
   CutValueMin(2)     = 0.000001
   ProcessName(3)     = 'CC e+-p'
   Variable(3)        = 'Q2'
   CutValueMin(3)     = 3.5
   CutValueMax(3)     = 1000000.0
   ProcessName(4)     = 'CC e+-p'
   Variable(4)        = 'x'
   CutValueMin(4)     = 0.000001
   CutValueMax(4)     = 1.0
   ProcessName(5)     = 'CC pp'
   Variable(5)        = 'eta1'
   CutValueMin(5)     = -1.
```

```
   CutValueMax(5)     = 100.
   ProcessName(6)     = 'pp jets APPLGRID'
   Variable(6)        = 'pt1'
   CutValueMin(6)     = 20.
   CutValueMax(6)     = 1000000.
   ProcessName(7)     = 'muon p'
   Variable(7)        = 'Whad2'
   CutValueMin(7)     = 15.
   ProcessName(8)     = 'FastNLO ep jets'
   Variable(8)        = 'ylow'
   CutValueMin(8)     = 0.0
   CutValueMax(8)     = 100.
   ProcessName(9)     = 'NC e+-p charm'
   Variable(9)        = 'Q2'
   CutValueMin(9)     = 3.5
   CutValueMax(9)     = 10000.0
   ProcessName(10)     = 'NC e+-p charm'
   Variable(10)        = 'x'
   CutValueMin(10)     = 0.000001
   CutValueMax(10)     = 1.0
&End
&MCErrors
  lRAND   = False
  lRANDDATA = True
  ISeedMC = 390182678
  STATYPE =  1
  SYSTYPE =  1
&End
&Cheb
   NCHEBGLU = 0   ! number of parameters for the gluon (max 15)
   NCHEBSEA = 0   ! number of parameters for the sea   (max 15)
   ichebtypeGlu = 1
   ichebtypeSea = 1
   chebxmin = 1.E-5
   ILENPDF  = 0   ! use pdf length constraint
   PDFLenWeight = 1., 1., 1., 1., 1.
   WMNLen =  20.
   WMXLen = 320.
&End
&Poly
  NPolyVal = 0
  IZPOPOLY = 1  ! ( times (1-x) for 0 and (1-x)^2 for 1)
  IPOLYSQR = 0  ! ( ensure positivity of PDFs by squaring them )
&End
&HQScale
   scalea1    =  1.
   scaleb1    =  1.
   MassHQ = 'mc' ! (available: mc, mb), relevant for 'FF', 'ZMVFNS', 'ACOT Full' and  'ACOT chi'
&End
&lhapdf
  LHAPDFSET  = 'cteq66.LHgrid' ! LHAPDF grid file
  ILHAPDFSET = 0               ! Set number withing PdfSet
&End
&reweighting
  FLAGRW   = False                ! Should reweighting be done?
  RWPDFSET        = 'NNPDF21_100.LHgrid' ! LHAPDF grid file
  RWDATA     = 'test'              ! arbitrary name for new datasample to be put in
  RWMETHOD  = 1             ! either 1=chi2 or 2=data
  DORWONLY     = True                ! do / do not run usual HERA fit
  RWREPLICAS    = 10              ! Number of input replicas used to build the PDF probability distributions from the Hessian
  RWOUTREPLICAS   = 10              ! how many output replica of the NNPDF should be kept?
&End
```

minuit.in.txt:

```
set title
new 13p HERAPDF
parameters
    2   'Bg'   -0.409301    0.009612
    3   'Cg'    3.534264    0.121066
    7   'Aprig'    0.568210    0.027284
    8   'Bprig'   -0.450923    0.006711
    9   'Cprig'   25.000000    0.000000
   12   'Buv'    0.647089    0.010492
   13   'Cuv'    2.819870    0.069953
   14   'Duv'    2.357708    0.155198
   15   'Euv'   -2.808748    0.173187
   22   'Bdv'    1.003156    0.037975
   23   'Cdv'    4.756963    0.158869
   33   'CUbar'    2.711950    0.263376
   34   'DUbar'   -2.171966    0.206831
   41   'ADbar'    0.246236    0.007198
   42   'BDbar'   -0.127568    0.003736
   43   'CDbar'    9.873431    0.812213

set print 3
migrad 200000
hesse
*iterate
*mystuff 2000
*minos
return
```

ewparam.txt:

```
*  Electroweak parameters
&EWPars
  ! Choice of EW scheme: 0 - alpha(0), 1 - G_mu, 2 - running alpha_EM
  ! EWSchemeFlag = 0
  alphaem = 7.29927d-3
  gf = 1.16637d-5
  sin2thw = 0.2315d0
  convfac = 0.389379323d9
  ! boson masses
  mw = 80.41d0
  mz = 91.187d0
  mh = 120d0
  ! widths
  wz = 2.4935d0
  ww = 2.1054d0
  wh = 1d-3
  wtp = 1.551d0
  ! charges
  ! euq = 0.6666666666667d0
  ! edq = -0.3333333333333d0
  ! CKM ( todo: add Vub & Vcb to DY)
  Vud = 0.97419d0
  Vus = 0.22570d0
  Vub = 0.35900d-2
  Vcd = 0.22560d0
  Vcs = 0.97334d0
  Vcb = 0.41500d-1
  Vtd = 0.867d-2
```

```
  Vts = 0.40d-1
  Vtb = 0.999146d0
  !*** fermion masses
  ! lepton masses
  men = 1d-10
  mel = 0.51099892d-3
  mmn = 1d-10
  mmo = 0.105658369d0
  mtn = 1d-10
  mta = 1.77699d0
 ! Light quark masses:
  mup = 0.06983d0
  mdn = 0.06983d0
  mst = 0.150d0
 ! Heavy quark masses: RT OPT 1.47 4.75 174
  mch = 1.67d0    ! Synchronize with QCDNUM,RT
  mtp = 177.0d0    ! Synchronize with QCDNUM
  mbt = 4.78d0   ! Synchronize with QCDNUM,RT
&end
```

B.3 Extra plots

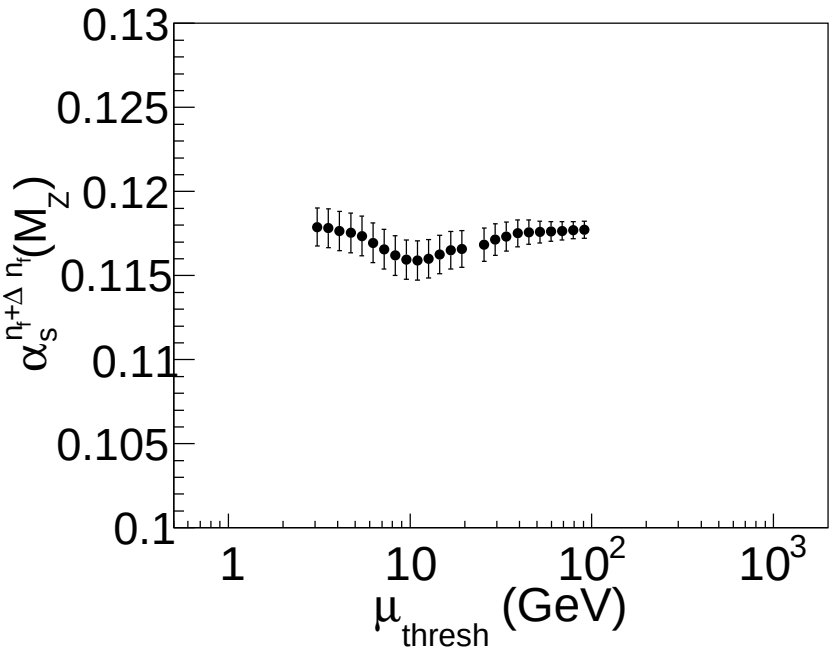

Figure B.2: Dependence of the fitted $\alpha_s^{n_f+\Delta n_f}(M_Z)$ on μ_{thresh}. The error bars correspond to a fit uncertainty. The details are given in Section 7.3.3.

Bibliography

[1] D. Hanneke, S. Fogwell, and G. Gabrielse, *New Measurement of the Electron Magnetic Moment and the Fine Structure Constant*, *Phys.Rev.Lett.* **100** (2008) 120801, [arXiv:0801.1134].

[2] Muon G-2 Collaboration, G. Bennett et al., *Final Report of the Muon E821 Anomalous Magnetic Moment Measurement at BNL*, *Phys.Rev.* **D73** (2006) 072003, [hep-ex/0602035].

[3] R. Bouchendira, P. Clade, S. Guellati-Khelifa, F. Nez, and F. Biraben, *New determination of the fine structure constant and test of the quantum electrodynamics*, *Phys.Rev.Lett.* **106** (2011) 080801, [arXiv:1012.3627].

[4] P. J. Mohr, B. N. Taylor, and D. B. Newell, *CODATA Recommended Values of the Fundamental Physical Constants: 2010*, *Rev.Mod.Phys.* **84** (2012) 1527–1605, [arXiv:1203.5425].

[5] T. Aoyama, M. Hayakawa, T. Kinoshita, and M. Nio, *Tenth-Order QED Contribution to the Electron g-2 and an Improved Value of the Fine Structure Constant*, *Phys.Rev.Lett.* **109** (2012) 111807, [arXiv:1205.5368].

[6] S. Descotes-Genon, J. Matias, and J. Virto, *Understanding the $B \to K^* \mu^+ \mu^-$ Anomaly*, *Phys.Rev.* **D88** (2013), no. 7 074002, [arXiv:1307.5683].

[7] T. Blum, A. Denig, I. Logashenko, E. de Rafael, B. Lee Roberts, et al., *The Muon (g-2) Theory Value: Present and Future*, arXiv:1311.2198.

[8] Particle Data Group Collaboration, J. Beringer et al., *Review of Particle Physics (RPP)*, *Phys.Rev.* **D86** (2012) 010001.

[9] "Particle Data Group." http://pdg.lbl.gov/ [Online; accessed 6-August-2014].

[10] "A Generic Fitter Project for HEP Model Testing." http://gfitter.desy.de/ [Online; accessed 6-August-2014].

[11] M. Baak, M. Goebel, J. Haller, A. Hoecker, D. Ludwig, et al., *Updated Status of the Global Electroweak Fit and Constraints on New Physics*, *Eur.Phys.J.* **C72** (2012) 2003, [arXiv:1107.0975].

[12] CMS Collaboration, CMS, *Precise determination of the mass of the Higgs boson and studies of the compatibility of its couplings with the standard model*, CMS-PAS-HIG-14-009.

[13] C. Burgess and G. Moore, *The standard model: A primer*. Cambridge University Press (2007).

[14] G. Altarelli and K. Winter, *Neutrino mass*, *Springer Tracts Mod.Phys.* **190** (2003) 1–248.

[15] R. Davis, *A review of the Homestake solar neutrino experiment*, *Prog.Part.Nucl.Phys.* **32** (1994) 13–32.

[16] B. Pontecorvo, *Inverse beta processes and nonconservation of lepton charge*, *Sov.Phys.JETP* **7** (1958) 172–173.

[17] B. Pontecorvo, *Neutrino Experiments and the Problem of Conservation of Leptonic Charge*, *Sov.Phys.JETP* **26** (1968) 984–988.

[18] F. Zwicky, *Die Rotverschiebung von extragalaktischen Nebeln*, *Helv.Phys.Acta* **6** (1933) 110–127.

[19] Supernova Search Team Collaboration, A. G. Riess et al., *Observational evidence from supernovae for an accelerating universe and a cosmological constant*, *Astron.J.* **116** (1998) 1009–1038, [astro-ph/9805201].

[20] P. Peebles and B. Ratra, *The Cosmological constant and dark energy*, *Rev.Mod.Phys.* **75** (2003) 559–606, [astro-ph/0207347].

[21] H. Abramowicz and A. Caldwell, *HERA collider physics*, *Rev.Mod.Phys.* **71** (1999) 1275–1410, [hep-ex/9903037].

[22] J. I. Friedman and H. W. Kendall, *Deep inelastic electron scattering*, *Ann.Rev.Nucl.Part.Sci.* **22** (1972) 203–254.

[23] R. Feynman, *Photon-hadron interactions*. Benjamin, New York (1973).

[24] J. Bjorken and E. A. Paschos, *Inelastic Electron Proton and gamma Proton Scattering, and the Structure of the Nucleon*, *Phys.Rev.* **185** (1969) 1975–1982.

[25] R. Devenish and A. Cooper-Sarkar, *Deep inelastic scattering*, .

[26] J. Callan, Curtis G. and D. J. Gross, *High-energy electroproduction and the constitution of the electric current*, *Phys.Rev.Lett.* **22** (1969) 156–159.

[27] J. Collins, *Foundations of Perturbative QCD*, *Cambridge monographs on particle physics, nuclear physics and cosmology* (2011) 1–624.

[28] T. Muta, *Foundations of quantum chromodynamics*, *World Sci.Lect.Notes Phys.* **78** (2010) 1–409.

[29] F. Jegerlehner, "Quantum Chromodynamics and strong interaction physics." http://www-com.physik.hu-berlin.de/ fjeger/QCD-lectures.pdf [Online; accessed 28-September-2014].

[30] R. Ellis, W. Stirling, and B. Webber, *QCD and Collider Physics*. Cambridge University Press (2003).

[31] R. Ellis, W. Stirling, and B. Webber, *Foundations of Perturbative QCD*. Cambridge University Press (2011).

[32] T. Kinoshita, *Mass Singularities of Feynman Amplitudes*, *J. Math. Phys.* **3** (1962) 650.

[33] T. Lee and M. Nauenberg, *Degenerate Systems and Mass Singularities*, *Phys.Rev.* **133** (1964) B1549–B1562.

[34] G. B. West, *An Asymptotic estimate of the nth loop QCD contribution to the total e+ e- annihilation cross-section*, *Phys.Rev.Lett.* **67** (1991) 1388–1391. Erratum *Phys. Rev. Lett.* **67** 3732 (1991).

[35] J. Chyla, J. Fischer, and P. Kolar, *On an asymptotic estimate of the n loop correction in perturbative QCD*, *Phys.Rev.* **D47** (1993) 2578–2587, [hep-ph/9210237].

[36] G. 't Hooft and M. Veltman, *Regularization and Renormalization of Gauge Fields*, *Nucl.Phys.* **B44** (1972) 189–213.

[37] P. M. Stevenson, *Optimized Perturbation Theory*, *Phys.Rev.* **D23** (1981) 2916.

[38] P. M. Stevenson, *Resolution of the Renormalization Scheme Ambiguity in Perturbative QCD*, *Phys.Lett.* **B100** (1981) 61.

[39] G. Grunberg, *Renormalization Group Improved Perturbative QCD*, *Phys.Lett.* **B95** (1980) 70.

[40] K. Chetyrkin, B. A. Kniehl, and M. Steinhauser, *Strong coupling constant with flavor thresholds at four loops in the MS scheme*, *Phys.Rev.Lett.* **79** (1997) 2184–2187, [hep-ph/9706430].

[41] M. Botje, *QCDNUM: Fast QCD Evolution and Convolution*, *Comput.Phys.Commun.* **182** (2011) 490–532, [arXiv:1005.1481].

[42] CTEQ Collaboration, R. Brock et al., *Handbook of perturbative QCD; Version 1.1: September 1994*, *Rev. Mod. Phys.* (1994).

[43] R. K. Ellis, H. Georgi, M. Machacek, H. D. Politzer, and G. G. Ross, *Perturbation Theory and the Parton Model in QCD*, *Nucl.Phys.* **B152** (1979) 285.

[44] G. Curci, W. Furmanski, and R. Petronzio, *Evolution of Parton Densities Beyond Leading Order: The Nonsinglet Case*, *Nucl.Phys.* **B175** (1980) 27.

[45] G. Altarelli and G. Parisi, *Asymptotic Freedom in Parton Language*, *Nucl.Phys.* **B126** (1977) 298.

[46] V. Gribov and L. Lipatov, *e+ e- pair annihilation and deep inelastic e p scattering in perturbation theory*, *Sov.J.Nucl.Phys.* **15** (1972) 675–684.

[47] V. Gribov and L. Lipatov, *Deep inelastic e p scattering in perturbation theory*, *Sov.J.Nucl.Phys.* **15** (1972) 438–450.

[48] Y. L. Dokshitzer, *Calculation of the Structure Functions for Deep Inelastic Scattering and e+ e- Annihilation by Perturbation Theory in Quantum Chromodynamics.*, *Sov.Phys.JETP* **46** (1977) 641–653.

[49] E. Laenen, S. Riemersma, J. Smith, and W. van Neerven, *On the heavy quark content of the nucleon*, *Phys.Lett.* **B291** (1992) 325–328.

[50] E. Laenen, S. Riemersma, J. Smith, and W. van Neerven, *Complete O (alphas) corrections to heavy flavor structure functions in electroproduction*, *Nucl.Phys.* **B392** (1993) 162–228.

[51] S. Riemersma, J. Smith, and W. van Neerven, *Rates for inclusive deep inelastic electroproduction of charm quarks at HERA*, *Phys.Lett.* **B347** (1995) 143–151, [hep-ph/9411431].

[52] C. Ford and C. Wiesendanger, *Multiscale renormalization*, *Phys.Lett.* **B398** (1997) 342–346, [hep-th/9612193].

[53] ZEUS Collaboration, A. T. Doyle, *Highlights and open questions from ZEUS*, hep-ex/9808022.

[54] S. Alekhin, J. Blumlein, S. Klein, and S. Moch, *The 3, 4, and 5-flavor NNLO Parton from Deep-Inelastic-Scattering Data and at Hadron Colliders*, *Phys.Rev.* **D81** (2010) 014032, [arXiv:0908.2766].

[55] J. C. Collins and W.-K. Tung, *Calculating Heavy Quark Distributions*, *Nucl.Phys.* **B278** (1986) 934.

[56] R. Thorne and R. Roberts, *An Ordered analysis of heavy flavor production in deep inelastic scattering*, *Phys.Rev.* **D57** (1998) 6871–6898, [hep-ph/9709442].

[57] R. Thorne, *A Variable-flavor number scheme for NNLO*, *Phys.Rev.* **D73** (2006) 054019, [hep-ph/0601245].

[58] R. Thorne, *Effect of changes of variable flavor number scheme on parton distribution functions and predicted cross sections*, *Phys.Rev.* **D86** (2012) 074017, [arXiv:1201.6180].

[59] M. Aivazis, J. C. Collins, F. I. Olness, and W.-K. Tung, *Leptoproduction of heavy quarks. 2. A Unified QCD formulation of charged and neutral current processes from fixed target to collider energies*, *Phys.Rev.* **D50** (1994) 3102–3118, [hep-ph/9312319].

[60] . Kramer, Michael, F. I. Olness, and D. E. Soper, *Treatment of heavy quarks in deeply inelastic scattering*, *Phys.Rev.* **D62** (2000) 096007, [hep-ph/0003035].

[61] S. Kretzer, H. Lai, F. Olness, and W. Tung, *Cteq6 parton distributions with heavy quark mass effects*, *Phys.Rev.* **D69** (2004) 114005, [hep-ph/0307022].

[62] S. Catani, Y. L. Dokshitzer, M. Seymour, and B. Webber, *Longitudinally invariant K_t clustering algorithms for hadron hadron collisions*, *Nucl.Phys.* **B406** (1993) 187–224.

[63] S. D. Ellis and D. E. Soper, *Successive combination jet algorithm for hadron collisions*, *Phys.Rev.* **D48** (1993) 3160–3166, [hep-ph/9305266].

[64] M. Cacciari, G. P. Salam, and G. Soyez, *The Anti-k(t) jet clustering algorithm*, *JHEP* **0804** (2008) 063, [arXiv:0802.1189].

[65] Y. L. Dokshitzer, G. Leder, S. Moretti, and B. Webber, *Better jet clustering algorithms*, *JHEP* **9708** (1997) 001, [hep-ph/9707323].

[66] K. Streng, T. Walsh, and P. Zerwas, *Quark and Gluon Jets in the Breit Frame of Lepton - Nucleon Scattering*, *Z.Phys.* **C2** (1979) 237.

[67] B. Webber, *Factorization and jet clustering algorithms for deep inelastic scattering*, *J.Phys.* **G19** (1993) 1567–1575.

[68] *HERA - A Proposal for a Large Electron Proton Colliding Beam Facility at DESY*, DESY-HERA-81-10 (1981).

[69] U. Schneekloth, *The HERA luminosity upgrade*, DESY-HERA-98-05 (1998).

[70] M. Seidel, *Luminosity upgrade of hera*, in *Proceedings of the Particle Accelerator Conference, 1999*, vol. 1, pp. 34 – 36, 1999.

[71] Y. Cho, E. Crosbie, M. Foss, H. Walenta, K. Anderson, et al., *Electron - Proton Interaction Experiment*, FERMILAB-PROPOSAL-0708 (1981).

[72] ZEUS Collaboration, K. Edwards et al., *ZEUS, A DETECTOR FOR HERA: LETTER OF INTENT*, DESY-HERA-LI-1 (1985).

[73] ZEUS Collaboration, G. Wolf et al., *THE ZEUS DETECTOR: TECHNICAL PROPOSAL*, DESY-HERA-ZEUS-1 (1986).

[74] ZEUS Collaboration, *The ZEUS Detector. Status Report 1993*, available at `www-zeus.desy.de/bluebook/bluebook.html`.

[75] J. Krüger, *The Uranium scintillator calorimeter for the ZEUS detector at the electron - proton collider HERA: The Heart of ZEUS*, DESY-F35-92-02 (1992).

[76] M. Derrick, D. Gacek, N. Hill, B. Musgrave, R. Noland, et al., *Design and construction of the ZEUS barrel calorimeter.*, *Nucl.Instrum.Meth.* **A309** (1991) 77–100.

[77] ZEUS Calorimeter Group, ZEUS Collaboration, A. Andresen et al., *Construction and beam test of the ZEUS forward and rear calorimeter*, *Nucl.Instrum.Meth.* **A309** (1991) 101–142.

[78] A. Caldwell, I. Gialas, S. Mishra, J. Parsons, S. Ritz, et al., *Design and implementation of a high precision readout system for the ZEUS calorimeter*, *Nucl.Instrum.Meth.* **A321** (1992) 356–364.

[79] M. Forrest, *Isolated photon production in deep inelastic scattering at HERA*, Ph.D. thesis, University of Glasgow (2010).

[80] ZEUS-UK Collaboration, C. Brooks et al., *Development of the ZEUS Central Tracking Detector*, *Nucl.Instrum.Meth.* **A283** (1989) 477–483.

[81] ZEUS Collaboration, B. Foster et al., *The Design and construction of the ZEUS central tracking detector*, *Nucl.Instrum.Meth.* **A338** (1994) 254–283.

[82] B. Foster, G. Heath, T. Llewellyn, D. Gingrich, N. Harnew, et al., *The Performance of the ZEUS central tracking detector z-by-timing electronics in a transputer based data acquisition system*, *Nucl.Phys.Proc.Suppl.* **32** (1993) 181–188.

[83] R. Hall-Wilton, N. McCubbin, P. Nylander, M. Sutton, and M. Wing, *The CTD Tracking Resolution*, ZEUS-99-024 (1999).

[84] ZEUS Collaboration, A. Polini et al., *The design and performance of the ZEUS Micro Vertex detector*, *Nucl.Instrum.Meth.* **A581** (2007) 656–686, [arXiv:0708.3011].

[85] ZEUS Luminosity Group Collaboration, J. Andruszkow et al., *Luminosity measurement in the ZEUS experiment*, *Acta Phys.Polon.* **B32** (2001) 2025–2058.

[86] M. Helbich, Y. Ning, S. Paganis, Z. Ren, W. Schmidke, et al., *The Spectrometer system for measuring ZEUS luminosity at HERA*, *Nucl.Instrum.Meth.* **A565** (2006) 572–588, [physics/0512153].

[87] ZEUS Collaboration, L. Adamczyk et al., *Measurement of the Luminosity in the ZEUS Experiment at HERA II*, *Nucl.Instrum.Meth.* **A744** (2014) 80–90, [arXiv:1306.1391].

[88] W. Smith, K. Tokushuku, and L. Wiggers, *The ZEUS trigger system*, DESY-92-150B, C92-09-21.

[89] ZEUS Collaboration, R. Carlin, W. Smith, K. Tokushuku, and L. Wiggers, *Experience with the ZEUS trigger system*, *Nucl.Phys.Proc.Suppl.* **44** (1995) 430–434.

[90] ZEUS Collaboration, R. Carlin, W. Smith, K. Tokushuku, and L. Wiggers, *The trigger of ZEUS, a flexible system for a high bunch crossing rate collider*, *Nucl.Instrum.Meth.* **A379** (1996) 542–544.

[91] C. Youngman, *The ZEUS data acquisition system*, DESY-92-150A, C92-09-21 (1992).

[92] R. Brun, F. Bruyant, M. Maire, A. McPherson, and P. Zanarini, *GEANT3*, CERN-DD-EE-84-1 (1987).

[93] H. Abramowicz, A. Caldwell, and R. Sinkus, *Neural network based electron identification in the ZEUS calorimeter*, *Nucl.Instrum.Meth.* **A365** (1995) 508–517, [hep-ex/9505004].

[94] J. Behr, *Jets at high Q^2 at HERA and test beam measurements with the EUDET pixel telescope*, Ph.D. thesis, University of Hamburg (2010).

[95] N. Tuning, *ZUFOs: Hadronic Final State Reconstruction with Calorimeter, Tracking and Backsplash Correction*, ZEUS-01-21, internal ZEUS note (2001).

[96] G. C. Fox and S. Wolfram, *A Model for Parton Showers in QCD*, *Nucl.Phys.* **B168** (1980) 285.

[97] T. Sjostrand, *A Model for Initial State Parton Showers*, *Phys.Lett.* **B157** (1985) 321.

[98] G. Gustafson and U. Pettersson, *Dipole Formulation of QCD Cascades*, *Nucl.Phys.* **B306** (1988) 746.

[99] A. Kwiatkowski, H. Spiesberger, and H. Mohring, *Heracles: An Event Generator for ep Interactions at HERA Energies Including Radiative Processes: Version 1.0*, *Comput.Phys.Commun.* **69** (1992) 155–172.

[100] K. Charchula, G. Schuler, and H. Spiesberger, *Combined QED and QCD radiative effects in deep inelastic lepton - proton scattering: The Monte Carlo generator DJANGO6*, *Comput.Phys.Commun.* **81** (1994) 381–402.

[101] G. Ingelman, A. Edin, and J. Rathsman, *LEPTO 6.5: A Monte Carlo generator for deep inelastic lepton - nucleon scattering*, *Comput.Phys.Commun.* **101** (1997) 108–134, [hep-ph/9605286].

[102] L. Lonnblad, *ARIADNE version 4: A Program for simulation of QCD cascades implementing the color dipole model*, *Comput.Phys.Commun.* **71** (1992) 15–31.

[103] T. Sjostrand, S. Mrenna, and P. Z. Skands, *PYTHIA 6.4 Physics and Manual*, *JHEP* **0605** (2006) 026, [hep-ph/0603175].

[104] X. Artru and G. Mennessier, *String model and multiproduction*, *Nucl.Phys.* **B70** (1974) 93–115.

[105] B. Andersson, G. Gustafson, G. Ingelman, and T. Sjostrand, *Parton Fragmentation and String Dynamics*, *Phys.Rept.* **97** (1983) 31–145.

[106] B. Andersson, *The Lund model*, *Camb.Monogr.Part.Phys.Nucl.Phys.Cosmol.* **7** (1997) 1–471.

[107] T. Sjostrand, *The Lund Monte Carlo for Jet Fragmentation and e+ e- Physics: Jetset Version 6.2*, *Comput.Phys.Commun.* **39** (1986) 347–407.

[108] K. Fabricius, I. Schmitt, G. Kramer, and G. Schierholz, *Higher Order Perturbative QCD Calculation of Jet Cross-Sections in e+ e- Annihilation*, *Z.Phys.* **C11** (1981) 315.

[109] G. Kramer and B. Lampe, *Jet Cross-Sections in e+ e- Annihilation*, *Fortsch.Phys.* **37** (1989) 161.

[110] H. Baer, J. Ohnemus, and J. Owens, *A Next-To-Leading Logarithm Calculation of Jet Photoproduction*, *Phys.Rev.* **D40** (1989) 2844.

[111] B. Harris and J. Owens, *The Two cutoff phase space slicing method*, *Phys.Rev.* **D65** (2002) 094032, [hep-ph/0102128].

[112] R. K. Ellis, D. Ross, and A. Terrano, *The Perturbative Calculation of Jet Structure in e+ e- Annihilation*, *Nucl.Phys.* **B178** (1981) 421.

[113] Z. Kunszt, P. Nason, G. Marchesini, and B. Webber, *QCD AT LEP*, ETH-PT-89-39, C89-02-20.1.

[114] M. L. Mangano, P. Nason, and G. Ridolfi, *Heavy quark correlations in hadron collisions at next-to-leading order*, *Nucl.Phys.* **B373** (1992) 295–345.

[115] S. Frixione, Z. Kunszt, and A. Signer, *Three jet cross-sections to next-to-leading order*, *Nucl.Phys.* **B467** (1996) 399–442, [hep-ph/9512328].

[116] S. Catani and M. Seymour, *A General algorithm for calculating jet cross-sections in NLO QCD*, *Nucl.Phys.* **B485** (1997) 291–419, [hep-ph/9605323].

[117] T. O. Eynck, E. Laenen, L. Phaf, and S. Weinzierl, *Comparison of phase space slicing and dipole subtraction methods for $\gamma^* \to Q\bar{Q}$*, *Eur.Phys.J.* **C23** (2002) 259–266, [hep-ph/0109246].

[118] Z. Nagy and Z. Trocsanyi, *Multijet cross-sections in deep inelastic scattering at next-to-leading order*, *Phys.Rev.Lett.* **87** (2001) 082001, [hep-ph/0104315].

[119] Z. Nagy, "NLOJet++: C++ program for calculating LO and NLO jet cross sections." http://www.desy.de/z̃nagy/Site/NLOJet++.html (2010). [Online; accessed 28-July-2014].

[120] P. M. Nadolsky, H.-L. Lai, Q.-H. Cao, J. Huston, J. Pumplin, et al., *Implications of CTEQ global analysis for collider observables*, *Phys.Rev.* **D78** (2008) 013004, [arXiv:0802.0007].

[121] A. Gehrmann-De Ridder, G. Kramer, and H. Spiesberger, *Photon plus jet-cross sections in deep inelastic e p collisions at order O(alpha**2 alpha(s))*, *Nucl.Phys.* **B578** (2000) 326–350, [hep-ph/0003082].

[122] H1 and ZEUS Collaboration, F. Aaron et al., *Combined Measurement and QCD Analysis of the Inclusive e+- p Scattering Cross Sections at HERA*, *JHEP* **1001** (2010) 109, [arXiv:0911.0884].

[123] S. Baranov, A. Lipatov, and N. Zotov, *Deep inelastic prompt photon production at HERA in the kt-factorization approach*, *Phys.Rev.* **D81** (2010) 094034, [arXiv:1001.4782].

[124] M. Kimber, A. D. Martin, and M. Ryskin, *Unintegrated parton distributions*, *Phys.Rev.* **D63** (2001) 114027, [hep-ph/0101348].

[125] T. Kluge, K. Rabbertz, and M. Wobisch, *FastNLO: Fast pQCD calculations for PDF fits*, hep-ph/0609285.

[126] fastNLO Collaboration, M. Wobisch, D. Britzger, T. Kluge, K. Rabbertz, and F. Stober, *Theory-Data Comparisons for Jet Measurements in Hadron-Induced Processes*, arXiv:1109.1310.

[127] fastNLO Collaboration, D. Britzger, K. Rabbertz, F. Stober, and M. Wobisch, *New features in version 2 of the fastNLO project*, arXiv:1208.3641.

[128] T. Carli, D. Clements, A. Cooper-Sarkar, C. Gwenlan, G. P. Salam, et al., *A posteriori inclusion of parton density functions in NLO QCD final-state calculations at hadron colliders: The APPLGRID Project*, *Eur.Phys.J.* **C66** (2010) 503–524, [arXiv:0911.2985].

[129] "HERAFitter." https://wiki-zeuthen.desy.de/HERAFitter [Online; accessed 29-July-2014].

[130] *HERAFitter - Open Source QCD Fit Project*, *paper in preparation.*

[131] H1 and Z. Collaborations, "QCD Analysis of the Inclusive ep Scattering Cross Sections at HERA." ZEUS-prel-14-007, 2014.

[132] H. Pirumov, *QCD Analysis of Neutral and Charged Current Cross Sections and Search for Contact Interactions at HERA (Section 5.1: Definition of the χ^2 function)*, Ph.D. thesis, Ruperto-Carola-University of Heidelberg (2013).

[133] ZEUS Collaboration, H. Abramowicz et al., *Inclusive dijet cross sections in neutral current deep inelastic scattering at HERA*, *Eur.Phys.J.* **C70** (2010) 965–982, [arXiv:1010.6167].

[134] J. E. Huth, N. Wainer, K. Meier, N. Hadley, F. Aversa, et al., *Toward a standardization of jet definitions*, FERMILAB-CONF-90-249-E, FNAL-C-90-249-E.

[135] A. Arbuzov, D. Y. Bardin, J. Blumlein, L. Kalinovskaya, and T. Riemann, *Hector 1.00: A Program for the calculation of QED, QCD and electroweak corrections to e p and lepton+- N deep inelastic neutral and charged current scattering*, *Comput.Phys.Commun.* **94** (1996) 128–184, [hep-ph/9511434].

[136] ZEUS Collaboration, S. Chekanov et al., *Measurement of the neutral current cross-section and F(2) structure function for deep inelastic e + p scattering at HERA*, *Eur.Phys.J.* **C21** (2001) 443–471, [hep-ex/0105090].

[137] ZEUS Collaboration, S. Chekanov et al., *Measurement of high-Q**2 neutral current deep inelastic e- p scattering cross sections with a longitudinally polarised electron beam at HERA*, *Eur.Phys.J.* **C62** (2009) 625–658, [arXiv:0901.2385].

[138] ZEUS Collaboration, J. Breitweg et al., *Measurement of high Q^2 neutral current e^+p deep inelastic scattering cross-sections at HERA*, *Eur.Phys.J.* **C11** (1999) 427–445, [hep-ex/9905032].

[139] ZEUS Collaboration, H. Abramowicz et al., *Measurement of isolated photons accompanied by jets in deep inelastic ep scattering*, *Phys.Lett.* **B715** (2012) 88–97, [arXiv:1206.2270].

[140] O. Kuprash, *Production of isolated photons with jets in deep inelastic ep-scattering at HERA*, Master's thesis, Taras Shevchenko National University of Kyiw (2011).

[141] "Trigger home page of the ZEUS Diffraction and Vector Mesons group." http://www-zeus.desy.de/physics/diff/ZEUS ONLY/trigger/2005/ [Online; accessed 25-September-2014].

[142] ZEUS Collaboration, J. Breitweg et al., *Observation of isolated high E(t) photons in photoproduction at HERA*, *Phys.Lett.* **B413** (1997) 201–216, [hep-ex/9708038].

[143] ZEUS Collaboration, J. Breitweg et al., *Measurement of inclusive prompt photon photoproduction at HERA*, *Phys.Lett.* **B472** (2000) 175–188, [hep-ex/9910045].

[144] ZEUS Collaboration, S. Chekanov et al., *Study of the effective transverse momentum of partons in the proton using prompt photons in photoproduction at HERA*, *Phys.Lett.* **B511** (2001) 19–32, [hep-ex/0104001].

[145] ZEUS Collaboration, S. Chekanov et al., *Observation of isolated high E(T) photons in deep inelastic scattering*, *Phys.Lett.* **B595** (2004) 86–100, [hep-ex/0402019].

[146] ZEUS Collaboration, S. Chekanov et al., *Measurement of isolated photon production in deep inelastic ep scattering*, *Phys.Lett.* **B687** (2010) 16–25, [arXiv:0909.4223].

[147] H. Spiesberger, *Private Communication*.

[148] N.P. Zotov, *Private Communication*.

[149] G. Kramer and H. Spiesberger, *Private Communication*.

[150] "Software packages alphaQED and pQCDAdler by F. Jegerlehner." http://www-com.physik.hu-berlin.de/$\tilde{\text{f}}$jeger/software.html [Online; accessed 5-September-2014].

[151] F. Jegerlehner, *Electroweak effective couplings for future precision experiments*, *Nuovo Cim.* **C034S1** (2011) 31–40, [arXiv:1107.4683].

[152] A. Martin and M. Ryskin, *The photon PDF of the proton*, arXiv:1406.2118.

[153] CMS Collaboration, S. Chatrchyan et al., *Measurements of differential jet cross sections in proton-proton collisions at $\sqrt{s} = 7$ TeV with the CMS detector*, *Phys.Rev.* **D87** (2013), no. 11 112002, [arXiv:1212.6660].

[154] Görner, Martin, *Differential Cross Sections for Top-Quark-Pair Production in the e/μ+Jets Final State at $\sqrt{s} = 8$ TeV in CMS*, Ph.D. thesis, University of Hamburg (2014).

[155] K. Rabbertz, *Private Communication*.

[156] CMS Collaboration, CMS, *Measurement of the 3-jet mass cross section in pp collisions at 7 TeV and determination of the strong coupling constant from 3-jet masses in the TeV range*, CMS-PAS-SMP-12-027.

[157] J. R. Ellis and D. A. Ross, *Virtual-sparticle threshold effects on large E(T) jet cross-sections*, *Phys.Lett.* **B383** (1996) 187–192, [hep-ph/9604432].

[158] J. R. Ellis and D. A. Ross, *Calculations of one loop supersymmetric corrections to large E(t) jet cross-sections*, *Eur.Phys.J.* **C4** (1998) 339–349, [hep-ph/9708312].

[159] E. L. Berger, P. M. Nadolsky, F. I. Olness, and J. Pumplin, *Light gluino constituents of hadrons and a global analysis of hadron scattering data*, *Phys.Rev.* **D71** (2005) 014007, [hep-ph/0406143].

[160] V. D. Barger, M. Berger, and R. Phillips, *Thresholds in alpha-s evolution and the p(T) dependence of jets*, *Phys.Lett.* **B382** (1996) 178–180, [hep-ph/9512325].

[161] C. Kim and S. Alam, *Virtual SUSY threshold effects and CDF large E(T) anomaly*, *Phys.Lett.* **B398** (1997) 110–115, [hep-ph/9610503].

[162] M. Buza, Y. Matiounine, J. Smith, and W. van Neerven, *Comparison between the various descriptions for charm electroproduction and the HERA data*, *Phys.Lett.* **B411** (1997) 211–217, [hep-ph/9707263].

[163] A. Chuvakin, J. Smith, and W. van Neerven, *Comparison between variable flavor number schemes for charm quark electroproduction*, *Phys.Rev.* **D61** (2000) 096004, [hep-ph/9910250].

[164] A. Chuvakin and J. Smith, *MS-bar parton densities with NNLO heavy flavor matching conditions*, hep-ph/9911504.

[165] F. I. Olness and S. T. Riemersma, *Leptoproduction of heavy quarks in the fixed and variable flavor schemes*, *Phys.Rev.* **D51** (1995) 4746–4755, [hep-ph/9409208].

[166] R. Demina, S. Keller, M. Kramer, S. Kretzer, R. Martin, et al., *Heavy quark production and PDF ' s subgroup report*, `hep-ph/0005112`.

[167] M. Gluck, E. Reya, and M. Stratmann, *Heavy quarks at high-energy colliders*, *Nucl.Phys.* **B422** (1994) 37–56.

[168] H1 and Z. Collaborations, "Combined measurement of inclusive ep scattering cross sections at HERA." ZEUS-prel-14-005, 2014.

[169] S. Alekhin, J. Blümlein, and S. Moch, "OpenQCDRad." http://www-zeuthen.desy.de/ãlekhin/OPENQCDRAD/ [Online; accessed 19-September-2014].

[170] H1 Collaboration, ZEUS Collaboration, H. Abramowicz et al., *Combination and QCD Analysis of Charm Production Cross Section Measurements in Deep-Inelastic ep Scattering at HERA*, *Eur.Phys.J.* **C73** (2013) 2311, [`arXiv:1211.1182`].

[171] H1 Collaboration, A. Aktas et al., *Measurement of inclusive jet production in deep-inelastic scattering at high Q**2 and determination of the strong coupling*, *Phys.Lett.* **B653** (2007) 134–144, [`arXiv:0706.3722`].

[172] H1 Collaboration, F. Aaron et al., *Jet Production in ep Collisions at Low Q**2 and Determination of alpha(s)*, *Eur.Phys.J.* **C67** (2010) 1–24, [`arXiv:0911.5678`].

[173] ZEUS Collaboration, S. Chekanov et al., *Inclusive jet cross-sections in the Breit frame in neutral current deep inelastic scattering at HERA and determination of alpha(s)*, *Phys.Lett.* **B547** (2002) 164–180, [`hep-ex/0208037`].

[174] CDF Collaboration, T. Aaltonen et al., *Measurement of the Inclusive Jet Cross Section at the Fermilab Tevatron p anti-p Collider Using a Cone-Based Jet Algorithm*, *Phys.Rev.* **D78** (2008) 052006, [`arXiv:0807.2204`].

[175] D0 Collaboration, V. Abazov et al., *Measurement of the inclusive jet cross-section in $p\bar{p}$ collisions at $s^{(1/2)}$ =1.96-TeV*, *Phys.Rev.Lett.* **101** (2008) 062001, [`arXiv:0802.2400`].

[176] BCDMS Collaboration, A. Benvenuti et al., *A High Statistics Measurement of the Proton Structure Functions F(2) (x, Q**2) and R from Deep Inelastic Muon Scattering at High Q**2*, *Phys.Lett.* **B223** (1989) 485.

[177] ATLAS Collaboration, G. Aad et al., *Measurement of inclusive jet and dijet production in pp collisions at $\sqrt{s} = 7$ TeV using the ATLAS detector*, *Phys.Rev.* **D86** (2012) 014022, [`arXiv:1112.6297`].

[178] CMS Collaboration, S. Chatrchyan et al., *Measurement of the electron charge asymmetry in inclusive W production in pp collisions at $\sqrt{s} = 7$ TeV*, *Phys.Rev.Lett.* **109** (2012) 111806, [arXiv:1206.2598].

[179] CMS Collaboration, S. Chatrchyan et al., *Measurement of the Rapidity and Transverse Momentum Distributions of Z Bosons in pp Collisions at $\sqrt{s} = 7$ TeV*, *Phys.Rev.* **D85** (2012) 032002, [arXiv:1110.4973].

[180] R. Thorne, *The effect on PDFs and $\alpha_S(M_Z^2)$ due to changes in flavour scheme and higher twist contributions*, *Eur.Phys.J.* **C74** (2014) 2958, [arXiv:1402.3536].

[181] A. Kusina, F. Olness, I. Schienbein, T. Jezo, K. Kovarik, et al., *Hybrid scheme for heavy flavors: Merging the fixed flavor number scheme and variable flavor number scheme*, *Phys.Rev.* **D88** (2013), no. 7 074032, [arXiv:1306.6553].

[182] D. Napoletano, *A new hybrid scheme for the treatment of heavy quarks in perturbative QCD*, Master's thesis, Università Di Milano (2014).

[183] V. Radescu, *Private Communication.*

[184] R. Plačakytė, *Private Communication.*

[185] S. Alekhin, *Private Communication.*

[186] C. McNeile, C. Davies, E. Follana, K. Hornbostel, and G. Lepage, *High-Precision c and b Masses, and QCD Coupling from Current-Current Correlators in Lattice and Continuum QCD*, *Phys.Rev.* **D82** (2010) 034512, [arXiv:1004.4285].

[187] CMS Collaboration, S. Chatrchyan et al., *Determination of the top-quark pole mass and strong coupling constant from the t t-bar production cross section in pp collisions at $\sqrt{s} = 7$ TeV*, *Phys.Lett.* **B728** (2014) 496–517, [arXiv:1307.1907].

[188] D. Becciolini, M. Gillioz, M. Nardecchia, F. Sannino, and M. Spannowsky, *Constraining new coloured matter from the ratio of 3- to 2-jets cross sections at the LHC*, arXiv:1403.7411.

[189] CMS Collaboration Collaboration, S. Chatrchyan et al., *Measurement of the ratio of the inclusive 3-jet cross section to the inclusive 2-jet cross section in pp collisions at $\sqrt{s} = 7$ TeV and first determination of the strong coupling constant in the TeV range*, *Eur.Phys.J.* **C73** (2013) 2604, [arXiv:1304.7498].

[190] PLUME Collaboration, O. Kuprash, *Power pulsing of the CMOS sensor Mimosa 26*, *Nucl.Instrum.Meth.* **A732** (2013) 519–522.

[191] "ILC Technical Design Report." http://www.linearcollider.org/ILC/Publications/Technical-Design-Report (2013). [Online; accessed 3-June-2014].

[192] ILD Concept Group - Linear Collider Collaboration, T. Abe et al., *The International Large Detector: Letter of Intent*, arXiv:1006.3396.

[193] M. A. Thomson, *Progress with particle flow calorimetry*, *eConf* **C0705302** (2007) SIM16, [arXiv:0709.1360].

[194] Linear Collider Flavour Identification (LCFI) Collaboration, K. Stefanov, *CCD vertex detector for the future linear collider*, *Nucl.Instrum.Meth.* **A501** (2003) 245–250.

[195] R. Turchetta, J. Berst, B. Casadei, G. Claus, C. Colledani, et al., *A monolithic active pixel sensor for charged particle tracking and imaging using standard VLSI CMOS technology*, *Nucl.Instrum.Meth.* **A458** (2001) 677–689.

[196] Y. Gornushkin, M. Deveaux, A. Gay, A. Himmi, C. Hu, et al., *Tracking performance and radiation tolerance of monolithic active pixel sensors*, *Nucl.Instrum.Meth.* **A513** (2003) 291–295.

[197] P. Fischer, W. Neeser, M. Trimpl, J. Ulrici, and N. Wermes, *Readout concepts for DEPFET pixel arrays*, *Nucl.Instrum.Meth.* **A512** (2003) 318–325, [hep-ex/0209074].

[198] PLUME Collaboration, A. Nomerotski et al., *PLUME collaboration: Ultra-light ladders for linear collider vertex detector*, *Nucl. Instrum. Meth.* **A650** (2011) 208–212.

[199] O. Bachynska, *Measurement of the $D^{*\pm}$ meson production in deep-inelastic scattering at HERA*, Ph.D. thesis, University of Hamburg (2012).

[200] C. Hu-Guo, J. Baudot, G. Bertolone, A. Besson, A. Brogna, et al., *First reticule size MAPS with digital output and integrated zero suppression for the EUDET-JRA1 beam telescope*, *Nucl. Instrum. Meth.* **A623** (2010) 480–482.

[201] EUDET, AID Aconsortia Collaboration, I. Rubinskiy, *An EUDET/AIDA Pixel Beam Telescope for Detector Development*, *Phys.Procedia* **37** (2012) 923–931.

[202] G. Voutsinas, *Optimization of a vertex detector for the ILC and study of Higgs Boson couplings*, Ph.D. thesis, Institut Pluridisciplinaire Hubert Curien, Strasbourg (2012).

[203] G. Claus, W. Dulinski, M. Goffe, K. Jaaskelainen, and M. Specht, "Mimosa 26 Training: Mimosa 26 Analogue Power Pulsing Hardware & DAQ Software." IPHC DRS, Strasbourg, 24 -26 March 2010.

[204] G. Claus, M. Goffe, K. Jaaskelainen, J.-S. Pelle, and M. Specht, "Mimosa 26 Training: Mimosa 26 Digital Power Pulsing Hardware & DAQ Software." IPHC DRS, Strasbourg, 23 -24 February 2012.

[205] "TAPI Analysis Framework (TAF)." http://www.iphc.cnrs.fr/Public-documentation.html (2013). [Online; accessed 10-June-2014].

[206] G. Savvidy, *Proton structure and tensor gluons*, *J.Phys.* **A47** (2014), no. 35 355401, [arXiv:1310.0856].

[207] K. R. Dienes, E. Dudas, and T. Gherghetta, *Extra space-time dimensions and unification*, *Phys.Lett.* **B436** (1998) 55–65, [hep-ph/9803466].

[208] D. Bandurin, "QCD results from the Tevatron." QCD@LHC 2014, August 25-29, 2014, Suzdal, Russia, 2014.

Acknowledgements

I thank PD Dr. Achim Geiser, who suggested me the α_s running topic, for his strong support and encouragement during all stages of this work and for his deep and kind involvement in all its aspects. I especially thank Achim for regular discussions and countless helping advises and remarks. It's impossible to overestimate your help, Achim!

I am very pleased to thank Prof. Brian Foster for providing an objective assessment of the results of this thesis, for scrupulous reading of initial versions of the thesis draft and for helping to improve it.

I would like to seize the opportunity and thank Achim and Brian for agreeing to join the Dissertation Committee.

As for the hardware part of the thesis, I thank Ingrid-Maria Gregor for suggesting me an interesting topic and for constantly monitoring of results. I want to express my special thanks to Ulrich Kötz. Dear Uli, it's a pleasure to discuss the physics results with you and to work under your guidance in the lab.

I want to thank separately Prof. Caren Hagner, Prof. Sven-Olaf Moch, and Prof. Christian Sander for kindly agreeing to join the Disputation Committee.

I thank Thomas Schörner-Sadenius and Jörg Behr with whom I started my way in investigating High-Energy Physics and got first experience of the data analysis.

My sincere gratitude goes to Peter Bussey, David Saxon and Ian Skillicorn for sharing their expertise during the measurement of the isolated photon production.

It would be hard to make progress without feedback from scientific community. I thank participants of the ZEUS physics meetings for sharing their scientific experience. I also thank the ZEUS management for their support. Warm thanks to members of the HERAFitter community and participants of the PROSA meetings. I especially thank Voica Radescu and Ringaile Plačakytė. Many thanks go to Olaf Behnke and to Matthew Wing for numerous valuable comments and advises.

Discussions with theorists are essential for interpreting the results of experiments. I am grateful to Sergey Alekhin, Marco Guzzi, Gustav Kramer, Sven-Olaf Moch, Hubert Spiesberger and Nikolai Zotov. After discussions of physics problems with them, the understanding of what I am actually doing is improved. I thank Prof. Laszlo Jenkovszky for beneficial cooperation and for helping me to promote some of the results of this thesis.

My special thanks goes to Dr. Volodymyr Aushev for opening a possibility to join the ZEUS experiment and supervising me in bachelor and master theses, which were made on the ZEUS topics. I would like to specially thank Volodymyr Aushev for a warm-hearted leading of the ZEUS-Kyiw group. I thank Inna Makarenko who played a significant role and contacted me with Volodymyr Aushev.

I thank my friends in Ukraine and in Germany with whom I had great going to parties, doing sport activities and much more.

The loving thank you is for my Family. I thank H.M. for the constant belief in me.

Dear All, thank you!